

Control of surface graded transformation textures in steels for magnetic flux carrying applications

PhD Thesis

Jaiprakash GAUTAM

The research described in this thesis was performed in the department of Material Science and Engineering, at Delft University of Technology



This research was carried out in the framework of the electrical steels research program at Arcelor Mittal Global R&D (OCAS NV), Ghent, Belgium.

Control of surface graded transformation textures in steels for magnetic flux carrying applications

Proefschrift

ter verkrijging van de graad van doctor

aan de Technische Universiteit Delft,

op gezag van de Rector Magnificus Prof. ir. K.C.A.M. Luyben,

voorzitter van het College voor Promoties,

in het openbaar te verdedigen op dinsdag 8 maart 2011 om 10.00 uur

door

Jaiprakash GAUTAM

Master in Metallurgical Engineering
Institute of Technology, Banaras Hindu University, Varanasi, India
geboren te Lucknow, India

Dit proefschrift is goedgekeurd door de promotor:
Prof. dr. ir. L.A.I. Kestens

Samenstelling promotiecommissie:

Rector Magnificus,	voorzitter
Prof. dr. ir. L.A.I. Kestens	Technische Universiteit Delft, Promotor
Prof. dr.ir. Jilt Sitsma	Technische Universiteit Delft
Prof. dr. B. Thijsse	Technische Universiteit Delft
Prof. dr. ir. H. Terryn	Vrije Universiteit, Brussels, Belgium
Prof. dr. ir. R. K. Ray	Indian Institute of Technology, Kanpur, India
Dr. ir. R. Petrov	Technische Universiteit Delft
Ir. E. Leunis	ArcelorMittal Global R&D, (OCAS NV)Ghent, Belgium

ISBN 978-94-91211-03-4

Keywords: Surface energy anisotropy, Phase transformation, Cube texture

Copyright © 2011 by J. Gautam

All rights reserved. No part of the material protected by this copyright notice may be reproduced or utilized in any form or by any means, electronic or mechanical, including photocopying, recording or by any information storage and retrieval system, without written permission from the author.

Printed in the Netherlands

Contents

Chapter 1

Introduction

1.1. Global importance of energy	1
1.1.1. Grain oriented steels	1
1.1.2. Non oriented fully processed steels	1
1.1.3. Non oriented semi-processed steels	2
1.2. Present scenario	2
1.3. Electrical steel and texture	4
1.4. Cube texture and its importance	6
1.5. Techniques to develop the cube texture in BCC iron	7
1.5.1. Surface energy controlled secondary recrystallisation	8
1.5.1.1. Description of metal surface	9
1.5.1.2. Effect of impurities on surface energy anisotropy	10
1.5.2. Decarburization annealing	11
1.5.2.1. Cube texture development by Mn removal and decarburisation	12
1.5.2.2. Decarburisation by SiO ₂ to promote the cube texture	12
1.5.2.3. Two step decarburisation annealing	13
1.5.3. Two stage cold rolling method	15
1.5.4. Phase transformation	16
1.5.5. Twin roll thin strip casting	18
1.5.6. Cross rolling	22
1.6. Challenges in Cube texture evolution	25
1.7. Surface energy anisotropy controlled phase transformation	25
1.8. Objectives and layout of the thesis	25
1.9. References	28

Chapter 2

Experimental procedure

2.1. Material preparation	31
2.2. Thermo mechanical processing	32
2.3. Heat treatment equipments	33
2.3.1. PYROX annealing furnace	33
2.3.2. Dilatometer	35
2.4. Surface texture analysis techniques	36
2.4.1. X-ray diffraction	36

2.4.1.1. Fundamental principles	36
2.4.1.2. Texture goniometer	37
2.4.1.3. Pole figure measurement	38
2.4.1.4. Evaluation of x-ray texture data	39
2.4.2. Orientation imaging microscopy	41
2.5. Compositional depth profiling techniques	45
2.5.1. X-ray induced photoelectron spectroscopy	45
2.5.2. Glow discharge optical emission spectroscopy	47
2.6. References	50

CHAPTER 3

Surface texture evolution during α - γ - α transformation

3.1. Introduction	53
3.2. Experimental procedure	56
3.3. Results	57
3.3.1. Effect of annealing temperature	58
3.3.1.1. Microstructure and texture after ferrite recrystallisation	59
3.3.1.2. Microstructure and texture after inter-critical annealing	60
3.3.1.3. Microstructure and texture after transformation annealing	61
3.3.2. Effect of soaking time during phase transformation annealing	63
3.3.3. Effect of annealing atmosphere during phase transformation annealing	67
3.3.4. Effect of alloy composition on surface texture evolution	68
3.3.5. Effect of initial texture on surface texture evolution	72
3.4. Discussion	74
3.5. Conclusions	78
3.6. References	79

CHAPTER 4

Role of surface chemistry on surface texture evolution

4.1. Introduction	83
4.2. Experimental procedure	84
4.3. Compositional depth profiling by XPS	85
4.4. Compositional depth profiling before α - γ - α transformation	88
4.4.1. Iron spectra at cold rolled surface	88
4.4.2. Oxygen spectra at cold rolled surface	90
4.4.3. Carbon spectra at cold rolled surface	92
4.5. Compositional depth profiling after α - γ - α transformation	93
4.5.1. Silicon spectra after phase transformation	93

4.5.2. Manganese spectra after phase transformation	94
4.5.3. Iron spectra after phase transformation	96
4.5.4. Aluminium spectra after phase transformation	98
4.5.5. Oxygen spectra after phase transformation	99
4.6. Compositional depth profiling by GDOES	101
4.6.1. GDOES compositional depth profiles before phase transformation	102
4.6.2. GDOES compositional depth profiles after phase transformation	103
4.7. Sub surface comparison before and after phase transformation	105
4.8. Surface chemistry relation with texture	108
4.9 Conclusions.....	110
4.10. References	111

CHAPTER 5

Surface texture evolution during interrupted annealing

5.1. Introduction	113
5.2. Experimental procedure	114
5.3. Results	115
5.3.1. Surface texture and through thickness microstructure before annealing	115
5.3.2. Surface texture and microstructure during interrupted annealing in ULC steels alloyed with manganese and Aluminium	116
5.3.3. Surface texture and microstructure during interrupted annealing in low carbon (LC) steel	120
5.3.4. Surface texture and microstructure during interrupted annealing in ULC steels alloyed with high silicon (Si2)	124
5.3.5. Surface texture and microstructure during interrupted annealing in ULC steels alloyed with low silicon (Si1)	127
5.3.6. Contact annealing experiment	130
5.4. Discussion	132
5.5. Conclusions	137
5.6. References	138

CHAPTER 6

Surface texture and microstructure characterization after transformation annealing

6.1. Introduction	139
6.2. Experimental procedure	140
6.3. Material characterization	141
6.4. Serial sectioning at RD-TD surface	142
6.5. Results	142

6.5.1. Microstructure and texture after transformation annealing	142
6.5.2. Through thickness grain morphology	144
6.5.3. Grain morphology and grain boundary character at the transformed sheet surface	145
6.5.4. Nucleation and growth of surface (cube) texture	150
6.5.5. Simulated texture after double phase transformation	152
6.6. Discussion	153
6.6.1. Bulk texture after α - γ - α phase transformation	154
6.6.2. Surface texture after α - γ - α phase transformation	156
6.6.3. Surface energy anisotropy	156
6.6.4. In grain orientation gradients	158
6.7. Conclusions	160
6.8. References	161

CHAPTER 7

Inward growth of surface texture components

7.1. Introduction	163
7.2. Experimental procedure	164
7.3. Results	166
7.3.1. Effect of decarburisation annealing on surface texture	166
7.3.2. Inward grain growth by strain induced boundary migration	169
7.3.3. Skin pass rolling with 10% cold reduction	171
7.4. Discussion	178
7.4.1. Low carbon steel (LC)	180
7.4.2. Ultra low carbon steels alloyed manganese and aluminium	181
7.5. Conclusions	183
7.6. References	184

CHAPTER 8

General conclusions and suggestion for future work	187
--	-----

Summary	193
Samenvatting	199
List of publications	205
Acknowledgements	207
Curriculum Vitae	208

Chapter 1

Introduction

1.1. Global importance of optimal energy use and electrical steels

The need to change the way energy is used and supplied throughout the world represents the greatest challenge for building a society based on sustainable technologies. The abundant availability of cheap energy is one of the key factors in our high standard of living. The use of energy poses global challenges in terms of available resources, environmental and economic impact. Electrical power in all its facets has become of great concern worldwide for environmental and economic reasons. Perhaps more than any other form of energy, electrical energy is of crucial importance for modern industrial societies.

Electrical steels play a vital role in the generation, transmission, distribution and use of electrical power and are among the most important magnetic materials produced today. Electrical steels have certain magnetic properties which allow them to be employed as the flux carrying core of electrical transformers or electrical motor parts. The constructors of electrical devices use three different grades of electrical steel. The choice among the different materials is made based upon their application.

1.1.1. Grain oriented steels

These are iron- 3% silicon alloys developed with a strong $\{110\} \langle 001 \rangle$ texture also called the Goss-type texture to provide very low power loss and high permeability in the rolling direction. These steels are predominantly employed for transformers of high efficiency.

1.1.2. Non-oriented fully processed steels

These are iron-silicon alloys with varying silicon contents which have similar magnetic properties in all directions in the plane of the sheet. They are principally used for motors, generators, alternators, ballasts, small transformers and a variety of other electromagnetic applications. A wide range of products includes newly developed thin gauge materials for high frequency applications.

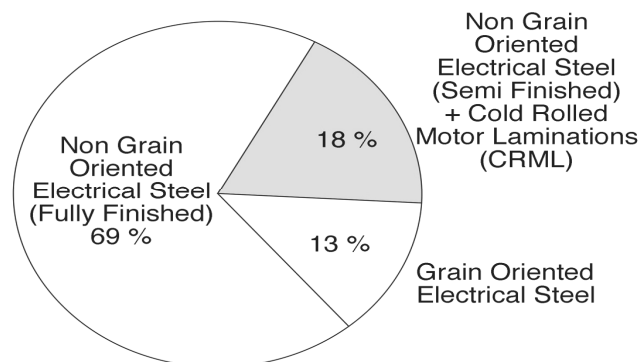
1.1.3 Non oriented semi-processed steels

These products are moderately Si-added (generally less than 1% Si addition) alloys and they are sold in a temper rolled condition to enhance punchability. Low power loss and good permeability properties are developed after final annealing of the punched laminations.

1.2 Present scenario

The world crude electrical steel production is around 14 million metric ton/per year, which was 1 % of total world steel production in 2009[1]. It is interesting to note that among all different kinds of electrical steels non-oriented steels, including fully processed and semi processed grades, share 80% of the total electrical steels production, as shown in figure 1. The effective use of energy and environmental

14.0 million t = appr. 1% of the world crude steel production



Source: ThyssenKrupp Steel, IISI, WV Stahl

Figure 1.1 World production of different types of electrical steel grades [1]

protection has been considered as one of the most important incentives for technological innovation in this area. Industrial motor systems are dominated by induction motors running at effectively constant speed. Variable-speed drives, in which the speed of the machine is controlled by a power electronic converter, are taking an increasing market share and in 2004 accounted for 25% of the new systems [2]. Electric motors and drives become increasingly dominant in various modes of transport. In marine transport electric ship propulsion of military vessels, ferries and cruise liners is now commonplace, with the ships engine driving a generator, which in turn feeds propeller motors. The propeller can now be pod-mounted which results in improved hydrodynamic efficiency, resulting in system gains of up to 15%. [2]

In aircraft vessels hydraulic and mechanical systems are being replaced with electrical alternatives, along with the introduction of electrical climate control. Direct energy savings result from more efficient pumping systems and most important from reduced aircraft mass [3]. In road transport hybrid electric vehicles are able to provide fuel economy advantages over conventional vehicle drive trains [3], whereas most new rail systems worldwide are now electrically driven, with induction motor drives. The efficiency of the drive is high, but could be further increased with permanent magnet drives. Magnetic levitation can be used to reduce drag losses and increase speed [3], but involves very high capital investment.

Current efforts to further improve the quality of electrical steels (magnetic properties and dimensional characteristics) either by optimizing the technology or by more fundamental changes are limited by the fact that electrical steels are commonly manufactured on universal equipment together with stainless, deep-drawing and structural steels. Such severe boundary condition is imposed by the requirements of utilization efficiency of the investment cost and by the comparatively small production volumes of these steels which does not justify specific and separate manufacturing lines. The steels have a crystalline structure and the magnetic properties of a sheet are derived from the individual crystals or grains, which exhibit a pronounced crystalline anisotropy. Therefore, the magnetic properties of the

crystalline aggregate are dependent of the crystallographic texture. The magnetic properties of electrical steel sheet are commonly improved if they have stronger cube fibre textures ($\langle 100 \rangle // \text{ND}$) or a Goss texture ($\{110\} \langle 001 \rangle$) whereas the γ -fibre texture ($\{111\} \langle uvw \rangle$) needs to be avoided. In industrial grades of grain oriented electrical steels (GO) the $\{110\} \langle 001 \rangle$ texture was first time obtained after a very special thermo-mechanical treatment which was patented by **Norman P. Goss** (February 04, 1906 – October 28, 1977) - inventor and researcher from Cleveland, USA. He graduated from Case Institute of Technology in 1925 and made significant contributions to the field of metals research and in 1935 he patented the aforementioned method and published a paper describing a technique to obtain so called grain-oriented electrical steel with strongly improved magnetic properties along the rolling direction. This special "grain-oriented" texture was named after him and referred to as the GOSS texture. In stark contrast to the universally applied Goss patent for the manufacturing of GO electrical steels, a standard reference method for the manufacturing of NO steel grades with a strong cube texture or even a strongly suppressed $\{111\}$ fibre texture does not exist.

1.3. Electrical steel and texture

Production and use of the electrical steel sheets are based on the fact that Fe, the main chemical constituent of steel is ferromagnetic. In electrical steels the magnetic properties of the Fe matrix are improved by the addition of silicon [4] which increases the resistivity of the metal matrix and hence reduces the eddy current losses. Their development can be traced back to this discovery in 1900 by Hadfield et al [4]. The history of electrical steels originated here and its evolution that has started at that time has extended over one hundred years. Later, in 1926, the magnetic anisotropy of iron crystals was discovered by Honda and Kaya [5]. In 1934 N.P. Goss patented an industrial process, with two-stage rolling, for magnetic applications and this material is known as cold rolled grain oriented steel. The GO steel is first hot rolled in the steel mill until a thickness of approximately 2mm. Thereafter, it is further reduced by a

series of cold reductions with intermediate annealing at 900°C to a final thickness of commonly 0.3 mm. During the annealing process the cold rolled sheet is continuously annealed to decarburise the material almost completely. Subsequently, after coiling it is batch annealed in a controlled atmosphere, at 1200°C for several hours. Whilst batch annealing in the temperature range 830-1000°C the material is subjected to a continuous grain growth which develops into a discontinuous growth of $\{110\}\langle 001\rangle$ -oriented grains as soon as the critical temperature is achieved. The discontinuous grain growth is normally referred as *secondary recrystallisation*. The exact moment of secondary growth depends on the previous stages of the process and especially on the amount and kind of grain growth inhibitors.

The $\{110\}\langle 001\rangle$ orientation is normally referred to as the Goss orientation, which is an ideal orientation for the transformer core as it provides magnetic properties in the rolling direction which are very much superior to those in any other sheet direction. The cold rolled Grain Oriented steel containing about 3% silicon replaced the hot rolled silicon steel containing 4 to 4.5% silicon which was used as transformer core-material till 1940s [6].

The magnetic properties of electrical steels strongly depend on their texture. In grain oriented material the marked influence of crystallographic orientation on magnetic properties is utilised in the most effective way. By thermo-mechanical manufacturing, it is intended to produce a highly textured material with directions of easy magnetization $\langle 100\rangle$ lying in the plane of the sheet, parallel to the rolling direction. This is done to take advantage of the fact that in BCC iron the magnetization processes occurs most effectively in the $\langle 100\rangle$ crystal directions and the least effective in the $\langle 111\rangle$ directions. Although favourable textures in non oriented materials are less pronounced, concentrated efforts are made to minimise the incidence of $\{111\}$ planes and maximise the incidence of $\{100\}$ planes parallel to the plane of sheet. This chapter reviews the various strategies and mechanisms involved to enhance the $\langle 100\rangle//ND$ fibre texture, known as the cube fibre or θ -fibre texture.

1.4. Cube texture and its importance

Polycrystalline ferromagnetic materials have anisotropic magnetic properties, which is a consequence of the magnetic anisotropy of the Fe single crystal as shown in figure 1.2. It means that the magnetic properties like the permeability of ferromagnetic sheets will depend on the orientation of crystals in the plane of the sheets. At room temperature, iron has a BCC lattice in which the electron spins are spontaneously aligned resulting in a magnetic domain structure with a spontaneous magnetic moment parallel to one of the $\langle 100 \rangle$ crystal directions in each single domain.

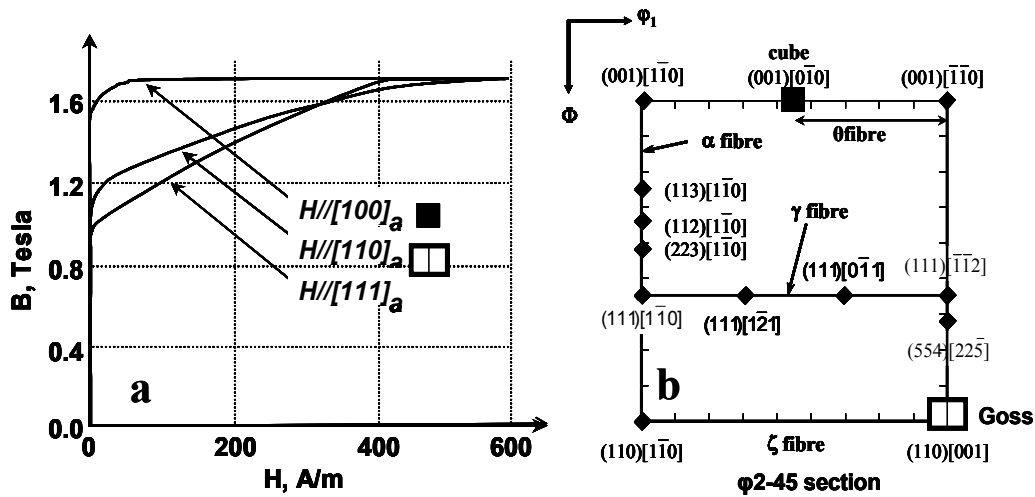


Figure 1.2 (a) The magnetisation curve of the Fe single crystal with an applied magnetic field parallel to various crystal directions; (b) Representation of the main BCC rolling and annealing texture components in the $\phi_2 = 45^\circ$ section of Euler space.

Figure 1.2a shows the magnetisation ability of the Fe single crystal with different orientations. It is understood from figure 1.2a that $\langle 100 \rangle$ crystal orientations are easy axes of magnetisation, i.e. when the crystal is magnetised along one of the $\langle 100 \rangle$ direction the highest permeability is obtained as compared to any other magnetisation direction $\langle hkl \rangle$. As single crystal anisotropy is eventually reflected in the crystallographic texture of the polycrystalline aggregate, it implies that the ideal texture in this case is the one that maximises the density of $\langle 100 \rangle$ crystal directions

parallel to the flux lines of magnetic induction. Because in rotating applications the flux lines have a nearly isotropic distribution in the plane of sheet, the ideal texture is the one that maximises the incidence of $\langle 100 \rangle$ directions in the sheet of the plane. The $\langle 100 \rangle$ fibre texture (also known as θ -fibre) is the texture that best fulfils this condition. All orientations belonging to this fibre provide two $\langle 100 \rangle$ directions in the sheet of the plane. When all fibre components are present with equal intensity then the material will provide the ideal magnetic isotropy. Even after decades of intense research both by academic and applied scientists a standard industrial manufacturing method in perfect control of the θ -fibre texture has not yet been developed. In the next section an overview will be presented of the various methods that have been explored and published in the technical literature. Most often these methods were only applicable on a laboratory scale with serious obstacles preventing industrial upscaling. Even more often the proposed manufacturing scheduled did not provide an ideal θ -fibre but one or other specific component of the fibre, i.e. the $\{100\}\langle 001 \rangle$ (cube) or $\{001\}\langle 110 \rangle$ (rotated cube) orientation, as a 2nd best substitute for the ideal texture..

1.5. Techniques to develop the cube texture in BCC iron

The $\{100\}\langle 001 \rangle$ or cube texture is easily obtained in face centred cubic materials by rolling and recrystallisation. In BCC metals and alloys this cube texture is never obtained unless specific non-conventional processing routes are employed [7]. There are various techniques explored to obtain the cube or cube fibre texture. These are classified according to different physical metallurgical mechanism and discussed separately.

1.5.1. Surface energy controlled secondary recrystallisation

One of the first methods for obtaining a cube texture in 3% Si-Fe sheet by secondary recrystallisation process has been reported by Assmus et al. [8]. Later, Wiener [9] experimentally obtained the cube texture in electrical steels by controlling the secondary recrystallisation through the surface energy. It was based on the principle

that {100} planes have the lowest surface energy in iron under low vacuum or a slightly oxidizing environment. These methods rely on recrystallisation and grain growth in the full ferrite phase domain without phase transformation during the entire annealing treatment. According to various researchers [9,10] the texture of secondary recrystallisation depends on the structure and texture of the primary small-grained matrix material. This matrix contains the nuclei of secondary recrystallisation, which will abnormally grow and eventually consume the entire primary matrix with increasing annealing time or temperature. By appropriate orientation selection only cube orientations will abnormally grow and thus provide a perfect cube texture to the secondary recrystallized material. The driving force is of crucial importance for the orientation selection. At the outer-metal surface the driving force for growth will be affected by the metal-gas surface energy. One grain of certain orientation may grow because of the fact that it exhibits a crystallographic plane to the surface of reduced surface energy¹.

It is a well accepted fact that the surface energy is crystallographically anisotropic. In first approximation, the crystal plane with the least density of broken bonds will exhibit the lowest surface energy. The entire crystallographic anisotropy of the single crystal is reflected in the so-called γ -plot as shown in figure 1.3. The inner-evolvement of this γ -plot determines the equilibrium surface shape of a free growing crystal in equilibrium with the ambient atmosphere. It can be observed that the BCC single crystal will exhibit both {110} and {001} free crystal surfaces but with a larger surface fraction of {110} planes as they display the absolute minimum in surface energy.

¹ Here the term *surface energy* refers to the energy at the gas-metal interface that separates the metal substrate from its gaseous environment. This energy is different from the *grain boundary energy*, which refers to the inter-granular interfaces in the bulk of the material.

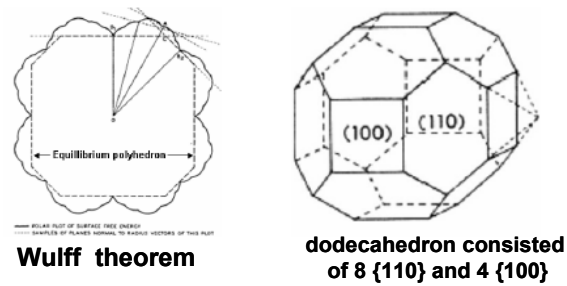


Figure 1.3 Equilibrium shape of a free growing Fe single crystal in vacuum based on Wulff's theorem [11].

In order to increase the surface fraction of $\{100\}$ planes (at the expense of $\{110\}$ planes) attempts were made to affect the crystallographic anisotropy of the surface energy. It is known that the surface energies of different planes change with the annealing atmosphere and chemical composition. Several efforts have been made by various researchers in the past to change the metal surface composition or annealing atmosphere composition in order to maximise the cube orientation [8,9,10,12,13].

1.5.1.1. Description of metal surface

A metal surface represents a portion of the lattice where the surface atoms may have

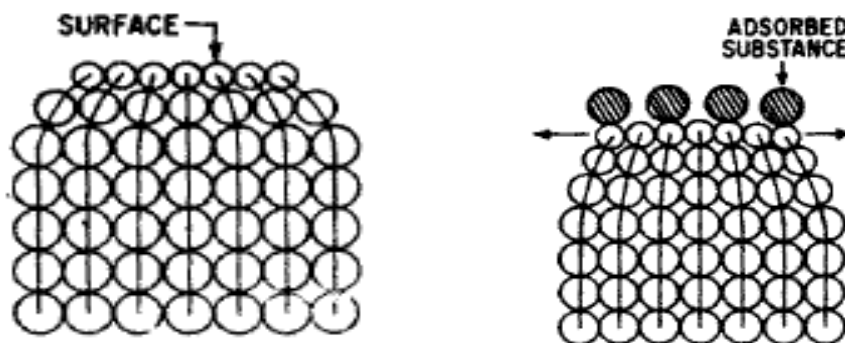


Figure 1.4 Schematic view of metal surface and adsorbed foreign atoms at the surface [13]

only half the usual numbers of neighbours. Therefore, the surface atoms will have half the number of bonds and a higher strength per bond than the lattice average [13] if

one accepts the idea that an electron-shared bond distributes itself among all available positions. With higher bond strength, it follows that the characteristic atomic radius of the surface atoms will be less than the average for the lattice as shown schematically in figure 1.4. Thus, the body of the metal is under compression while the surface is under tension. The surface tension represents the excess energy, per unit area as a result of the presence of the surface as compared with the energy in the absence of the surface. It is obvious that the different crystal faces, having different inter-atomic spacing, have different values of surface energy. Any substance in the environment that shares electrons or forms bonds with the metal surface atoms will, consequently, tend to relieve some of the surface tension as shown in figure 1.4. The reduction of tension may also depend upon the crystal face exposed at the surface and upon the substance. This implies e.g. that the surface energy of dense packed crystal surfaces will be less affected by foreign atoms and thus, as a rule of thumb it can be stated that the crystal surface anisotropy, is reduced by the presence of environmental substances [13].

1.5.1.2. Effect of impurities on surface energy anisotropy

As mentioned previously, adsorption of foreign atoms at the metal surfaces causes changes in the surface energy which, in turn, will affect either the rate of grain growth or the crystallographic orientation of grains that will grow (i.e. $\{100\}$ or $\{110\}$). Walter et al [13] investigated the migration of grain boundaries between $\{110\}$ grains and $\{100\}$ grains in high purity 3% silicon iron sheet at 1,200°C to determine whether or not impurity atoms could affect a reversal in the direction of boundary migration. Boundaries were found that advance into the $\{100\}$ planes in a vacuum anneal, then reverse their direction of migration and advance into the $\{110\}$ grains in a subsequent annealing in an oxygen contaminated argon atmosphere. They explained these results by assuming that impure argon supplied oxygen atoms to the metal surface whereas pure vacuum annealing removes the oxygen atoms. They have drawn the following conclusions from their experimental findings:

- 1) Under proper conditions impurity atoms can effect a reversal in the direction of grain boundary migration.
- 2) $\gamma_{110} < \gamma_{100}$ for annealing in vacuum whereas $\gamma_{100} < \gamma_{110}$ for annealing in an oxygen contaminated argon atmosphere.
- 3) The high density plane is not always the lowest energy plane.
- 4) The impurities reduce the surface energy of $\{100\}$ planes more than the ones of $\{110\}$ planes and thus reduces the surface anisotropy.

For Fe-Si alloys it is probable that sulphur as an impurity substance even can extend the growth of $\{100\}$ oriented grains to the point where they have completely eliminated the $\{110\}$ oriented grains. This would occur because silicon sulphide is less stable than iron sulphide and iron atoms would retain the sulphur as long as it is present in the atmosphere [13].

In the presence of oxygen, or equivalent impurities such as sulphur, in the annealing atmosphere the $\{100\}$ oriented grains would be favoured to grow because of their reduced surface energy as compared to the $\{110\}$ planes or any other orientations.

1.5.2. Decarburisation annealing

A substantial part of the volume of non-oriented electrical steel is manufactured as Semi Processed (SP) sheet meaning that the final step of the thermo-mechanical process is carried out on the punched motor lamella and not on the continuous sheet processing line of the steel manufacturer. Normally the annealing treatment on the punched motor lamella is accompanied with a decarburization and hence it is customary to speak of the decarburization treatment. The decarburizing annealing treatment is conventionally carried out in the intercritical region leading to the development of a microstructure with columnar grains as the ferrite front moves down from the decarburized surface to the bulk of the sheet. By application of such annealing it is possible to obtain the much wanted random cube texture $\{100\} \langle 0vw \rangle$ which cannot be achieved by applying ordinary rolling and annealing processes. Some of the techniques that are based on this methodology are explained below.

1.5.2.1. Cube texture development by Mn removal and decarburisation

An investigation was made by T. Tomida et al [15] to develop the $\langle 100 \rangle // \text{ND}$ textures in silicon steel utilizing a well-defined annealing treatment in a controlled atmosphere. Steel sheets containing 2% Si, 1% of Mn and 0.1 % C were vacuum annealed and subsequently decarburized in a wet atmosphere of hydrogen and argon. During the vacuum annealing in the intercritical ($\alpha+\gamma$) or single γ phase region at temperatures from 950 to 1050°C, because of Mn diffusion and depletion a thin layer at the sheet surface transforms to ferrite with a strong $\{100\}\langle 0vw \rangle$ texture. By subsequent decarburization at 950°C for 30 minutes, the grains within the layer grow inward as columnar grains retaining the initial texture. It has been mentioned that the austenite-to-ferrite transformation occurring near the surface and the removal of manganese during the vacuum annealing provide a selective driving force for forming the strong $\{100\}$ texture which is thought to be owed to the anisotropy of surface energy.

1.5.2.2. Decarburisation by SiO₂ to promote the cube texture

Decarburization of silicon steel sheets by annealing with an oxide separator has been found to cause a high degree of $\{100\}$ -texture development. Cold rolled Fe-3% Si-1.1%Mn-0.05%C sheet of 0.35 mm thickness was laminated with a SiO₂ containing separator. This was done to prevent the samples from sticking but also to react with the samples and to cause decarburisation. The sheet was decarburised down to about 0.001% of carbon concentration without oxidation of silicon and manganese. During lamination annealing a microstructure evolution takes place in the single phase alpha regions which emerges at the surface from the two-phase structure because of surface decarburization. With ongoing decarburization columnar grains start to consume the alpha/gamma two phase regions and gradually invade the bulk of the material.

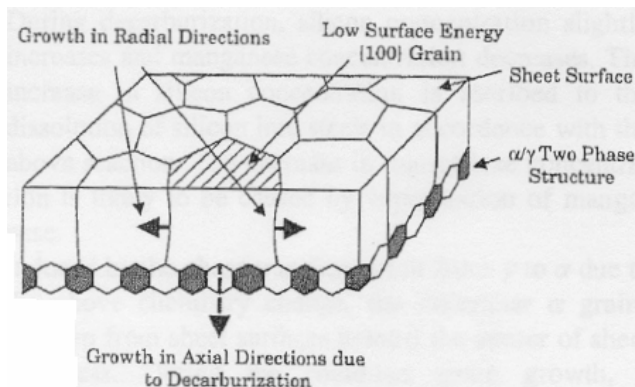


Figure 1.5 Grain growth mechanism during decarburization according to Tomida [15]

Apart from the microstructure, a remarkable feature in columnar grain growth was the $\{100\}\langle 012\rangle$ texture evolution. This texture sometimes is observed in steels after secondary recrystallisation. Also in this case it could be considered as a surface energy related phenomenon. It is obvious that the surface energy of $\{100\}$ oriented grains of the ferrite phase

display the lowest surface energy. Driven by the shifting equilibrium towards ferrite, induced by the ongoing decarburization, the $\{100\}$ oriented alpha islands tend to preferentially grow at the expense of austenite phase grains until the surface is entirely covered by the ferrite phase. In addition, if the radii of columnar grains increase concurrently with the growth in the ND the $\{100\}$ texture may further evolve during columnar grain growth (cf. figure 1.5).

1.5.2.3. Two step decarburisation annealing

In the proposed method by Sidor et al [16.] columnar grain growth is obtained by a two step decarburizing annealing process, without application of the preliminary long vacuum annealing. This annealing process was applied on both semi-processed and fully-processed grades of non-oriented electrical steels. The chemical composition is given in the table below (figure 16a). Both sheets had a thickness of 0.5 mm and were annealed in a decarburising atmosphere consisting of 35% of H_2 and 65% of N_2 with a dew point of $35^\circ C$. The semi-processed steel samples were treated after temper rolling.

(A)-Chemical compositions

Steel	C	Mn	Si	P	Al
SP	0.05	0.36	0.24	0.068	0.109
FP	0.03	0.38	1.01	0.134	0.157

(B)-Parameters decarburisation annealing:

Steel	t1(s)	T1(°C)	t2(s)	T2(°C)
SP	120-140	870-890	210-240	800-820
FP	120-150	900-920	240-270	810-830

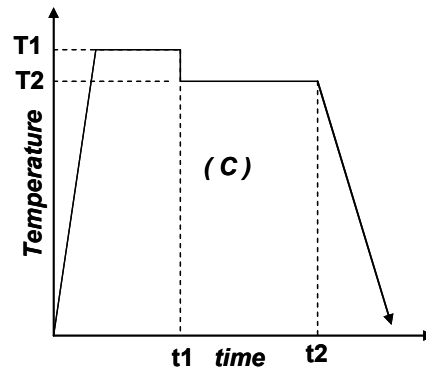


Figure 1.6 Chemical compositions (A) parameters (B) of the decarburisation annealing schedule (C) redrawn from reference [16].

The samples were annealed according to the stepped temperature schedule in the inter-critical region as shown in figure 1.6c. They used three different heating rates $V_1 < V_2 < V_3$ to reach the fixed initial temperature T_1 and the subsequent temperature T_2 with isothermal holding times t_1 and t_2 , respectively. T_1 and t_1 were designed to result in a fine primary recrystallised microstructure and a thin decarburised ferrite region at the sheet surface. Temperature T_2 was chosen with the aim to provide the most efficient decarburisation of the material and this temperature was kept identical for both steels compositions.

According to Sidor et al the columnar microstructure development can be explained as follows: Annealing at temperature T_1 provides a fine homogeneous microstructure with a certain amount of gamma phase at the beginning of the first annealing stage. When the material is heated at an appropriate rate (8.5°C/s in this case) at temperatures lower than A_{c1} the primary recrystallisation occurs simultaneously with intensive decarburisation of the surface. When the material is heated up to temperatures higher than A_{c1} phase transformation occurs inside the sheet, which refines the primary recrystallised ferrite matrix. At the same time the surface layer still remains untransformed due to its lower carbon content. Highly unstable conditions of grain growth near the sheet surface lead to the formation of a thin layer of inhomogeneous relatively fine grains at the sheet surface. In order to obtain a full

columnar microstructure the growing rate of ferrite columnar grains from the surface towards the middle region of the sheet has to be high in order to avoid coarsening of ferrite grains in the mid thickness region. The temperature T_2 in the scheme has to provide conditions for an intensive decarburization that promotes fast growth of the ferrite columnar grains from the surface toward the centre of the sheet. The proposed two step decarburising continuous annealing of non oriented semi processed electrical steels with low carbon and low silicon content leads to a columnar microstructure with a strong rotated cube component in the final sheet.

1.5.3. Two stage cold rolling method

Nakamura et al [17] have patented a method to enhance a $\{001\}\langle 210 \rangle$ texture by a two stage cold rolling process in which the intermediately annealed sheet partially recrystallises. In this study [18] the formation mechanism of the $\{001\}\langle 210 \rangle$ texture by means of the two stage cold rolling method was investigated on steel with 0.024 wt% C, 0.13wt% Si and 0.22wt% Mn. The steel was hot rolled to 22.2mm and later cold rolled to a reduction of 97% to 0.5mm thickness, intermediate annealing at various temperatures from 540°C to 700°C for 30s in an Argon atmosphere and a second cold rolling to a reduction of 12% to 0.44mm in thickness. To simulate continuous annealing, the heating rates in the intermediate and final annealing treatments were adjusted to 10°C/s. After intermediate annealing at 640°C the maximum value of the $\{100\}$ pole intensity is measured in the finally annealed sheet. The $\{001\}\langle 210 \rangle$ texture was enhanced after final annealing but its origin is assumed to be in the sheet annealed at 640°C.

The mechanism of the $\{001\}\langle 210 \rangle$ texture formation in two stage cold rolling is schematically illustrated in Figure 1.7. The intermediately annealed sheet exhibits a mixed structure of recrystallised $\{111\}$ grains and deformed $\{001\}\langle 210 \rangle$ grains. After the second cold rolling and subsequently during annealing the growth of $\langle 111 \rangle$ //ND partially recrystallised grains into the deformed area is suppressed because the second cold rolling decreases the stored energy difference between

$\langle 111 \rangle // ND$ partially recrystallised grains and the remaining deformed grains. In addition, $\langle 111 \rangle // ND$ grains no longer recrystallise during final annealing. Then $\langle 111 \rangle // ND$ partially recrystallised grains are replaced by newly recrystallised $\{001\}$

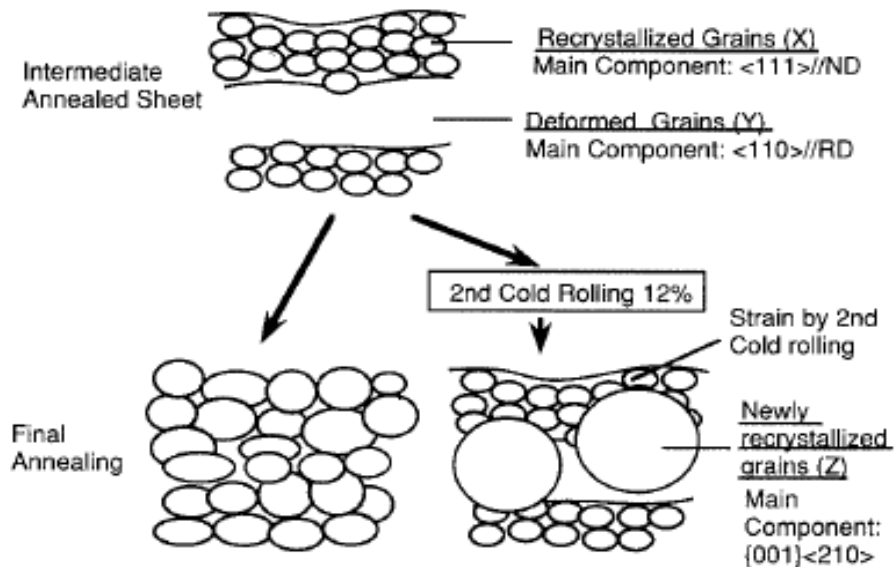


Figure 1.8 Mechanism of $\{001\} \langle 210 \rangle$ texture formation in the two stage cold rolling method according to reference [18]

$\langle 210 \rangle$ grains, which nucleated in the deformed area. The strain in $\langle 111 \rangle // ND$ partially/small recrystallised grain stored by the second cold rolling makes newly recrystallised $\{001\} \langle 210 \rangle$ grains grow into $\langle 111 \rangle // ND$ partially recrystallised grains. Consequently $\{011\} \langle 210 \rangle$ grains dominate the overall texture of the final-annealed sheet.

1.5.4. Phase transformation

Phase transformation is a common and inherent phenomenon in steels. When a phase transformation takes place, an orientation relationship exists between the lattices of the parent and the produced crystals. The relationships that are most frequently cited

are Bain [19], Kurdjumov-Sachs (K-S) [20], Nishiyama [21] and Wassermann [22] (N-W). In steels the most commonly observed relationships are the Young-Kurdjumov-Sachs (YKS) and the Nishiyama-Wasserman (NW) correspondences. In both of these, the respective closed packed planes $\{111\}_\gamma$ in austenite and $\{011\}_\alpha$ in ferrite are parallel. In the YKS correspondence the closed packed directions $[011]_\gamma//[111]_\alpha$ are also parallel while for the NW correspondence the $[112]_\gamma$ crystal direction lines up with the $[011]_\alpha$ direction. Due to crystal symmetry there are possible equivalent product orientations generated by one specific parent orientation, 12 in the case of NW and 24 for YKS. In a treatment that involves a ferrite-austenite-ferrite transformation loop there will be n^2 possible products originating from one parent, with n the number of variants associated with the orientation correspondence under consideration. The principal characteristics of ferrite-austenite orientation relations has been extensively reviewed by R.K Ray and J.J. Jonas [23] with the main emphasis on the control of hot band textures observed obtained after hot rolling of low-carbon steel sheet. However, the α - γ - α phase transformation texture at the steel sheet surface has not been studied in detail.

In a study performed by Aspeden et al [24] the $\{001\} \langle uvw \rangle$ texture was observed after a forward and reverse $\alpha \rightarrow \gamma \rightarrow \alpha$ transformation in electrolytically pure iron. The cold rolled sheets of 0.45 mm in thickness were annealed in a controlled argon atmosphere contaminated with 1% hydrogen sulphide in an alumina tube furnace at 1,050°C for 12 hours. During $\gamma \rightarrow \alpha$ transformation the cooling rate was very slow (4°C/hr.). Preferred nucleation of $\{001\}$ ferrite grains was observed to occur as the $\{001\}$ crystal surface is of the lowest surface free energy by virtue of selective adsorption of a constituents like sulphur. The average alpha grain diameter reported was 0.25 cm. The orientations of 91 grains were determined by the back reflection technique and the texture was $\{001\} \langle uvw \rangle$ as shown by the axial density distribution in figure 1.8. This technique showed that this alloy was highly oriented containing 90 % volume fraction of $\{001\} \langle uvw \rangle$ orientations.

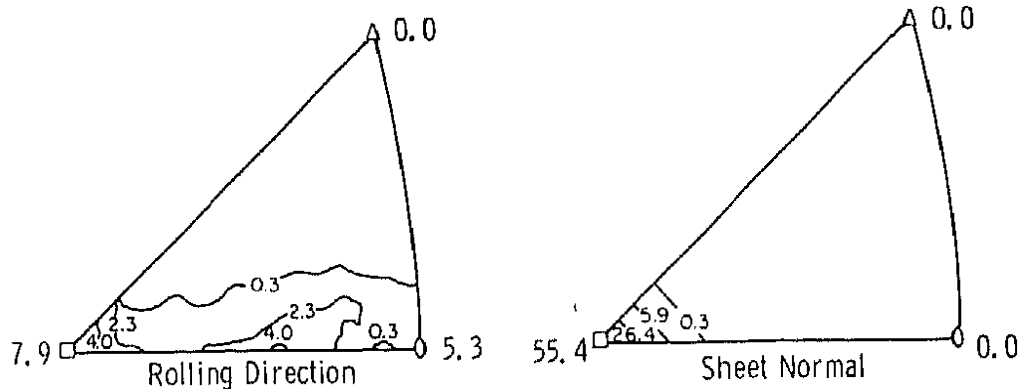


Figure 1.8 Two inverse pole figures of electrically pure iron sample annealed for 12 hrs at 1,050°C and cooled at 4°C/hr through the γ - α phase change. The total numbers of X-rayed grains were 91.

Later, in 1983 Hashimoto et al [25] showed the $\{100\}$ texture or the texture consisting of $\{110\}$ orientations and orientations of 20 to 30° off the $\{100\}$ fibre developed solely in the surface layer of a sheet sample after α - γ - α phase transformation in ultra low carbon steel which was kept 15 minutes in the austenite region. Accordingly the development of such textures is considered to be associated with a certain characteristic of the sheet surface. These authors [25] attribute the selection of $\sim\{001\}$ grains to the anisotropy of transformation strain and the easy release of the strain at a sheet surface, assuming that in the surface layer the perpendicular components of transformation strain are released more readily than the other components. Very similar observations were made by Yoshinaga et al [26] in 1997, i.e. cube texture components were observed at the surface of the steel sheet during a very short annealing treatment. Yoshinaga et al. also considered surface energy anisotropy to explain their findings. In a study performed by Bodin et al has also shown the cube texture development after γ - α transformation in low carbon steels [27].

1.5.5. Twin-roll thin strip casting

The progress in strip casting technology provides a possibility to manufacture silicon steel sheet by simpler processes than the conventional ones because the strip casting process can supply the silicon steel strip with the same thickness and width as of hot rolled strip. This process offers the possibility to eliminate the continuous casting and hot rolling steps in the conventional manufacturing route of electrical steels.

The challenge here is to obtain an appropriate texture and microstructure through the innovative technological process. A study [28] on 4.5wt % of silicon steel strips shows the cube orientation formation with varying temperatures of superheating of the melt pool. Figure 1.9 shows a schematic of the vertical type twin roll caster in which the Fe-4.5wt % silicon strips were produced with 100mm width and 1.5mm gauge.

C	Si	Al	Mn	S	N	Fe
<0.001	4.46	0.014	0.054	0.013	0.015	bal.

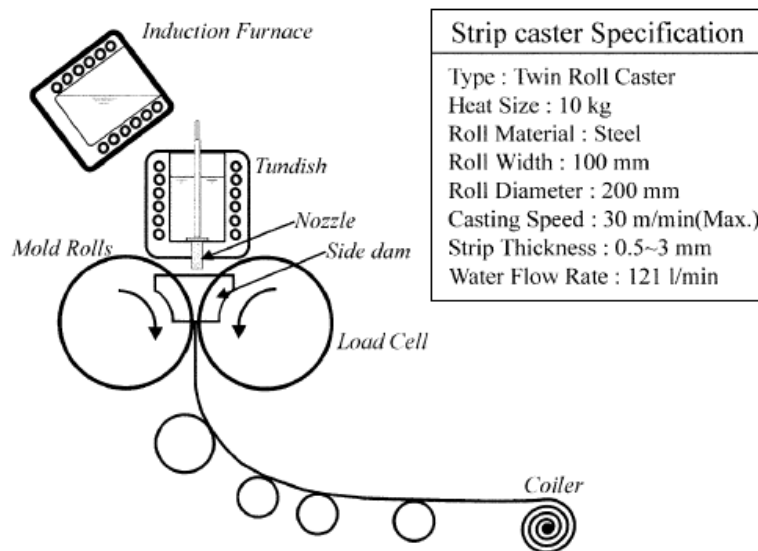


Figure 1.9 Schematic diagram of the vertical type twin-roll caster [29].

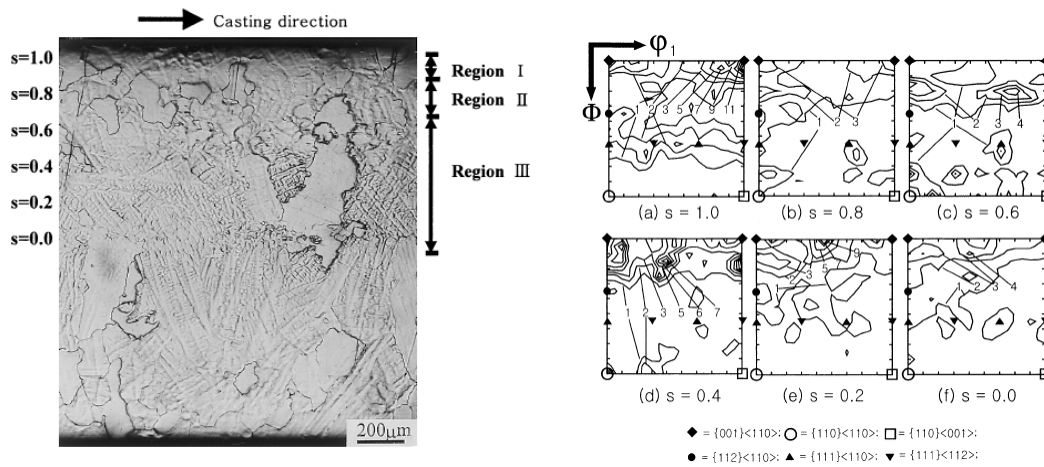


Figure 1.10 Microstructure of as-cast strip solidified from a melt at a superheating temperature of 30°C and $\varphi_2=45^{\circ}$ sections of the ODF in various thickness layer of strip.[29]

The through thickness microstructures and textures are shown in figure 1.10. The microstructure of the strip displays heterogeneous zones across the thickness of the sheet which can be distinguished in region I, region II and region III. The rapidly solidified thin layer at the surface was named Region I. An equiaxed dendritic layer and a columnar dendritic layer were named Region II and Region III, respectively. A strong $\{001\}\langle uvw\rangle$ fibre texture is present from the surface to the centre layer of the sheet cast [28], cf. figure 1.10.

Further cold reduction of the thin strip cast sheet destroys the cube texture which renders this process difficult to apply in industrial operations.

Yonamine et al. [29] have simulated the strip-casting process by carrying out directional solidification experiments in a vacuum induction furnace. A Fe- 3.0 % Si alloy was cast in a heated ceramic mould at $1,400^{\circ}\text{C}$, with a diameter of 57 mm and equipped with a water-cooled copper chill in the bottom. At a casting temperature of $1,620^{\circ}\text{C}$ an ingot was produced with columnar grains of approximately 50mm length and with a diameter of $\sim 1\text{mm}$. For magnetic measurements a ring of 1.53 mm thickness was machined from the ingot and submitted to heat treatment at 760°C for

3 hours, in a 88%N₂ - 9%H₂ - 3%H₂O atmosphere to decarburize and eliminate residual stresses. The carbon concentration of the ring decreased from 260 to 38 ppm. Figure 1.11 shows the microstructure and texture results after cold rolling and annealing and the effect of second cold rolling followed by annealing on the texture evolution.

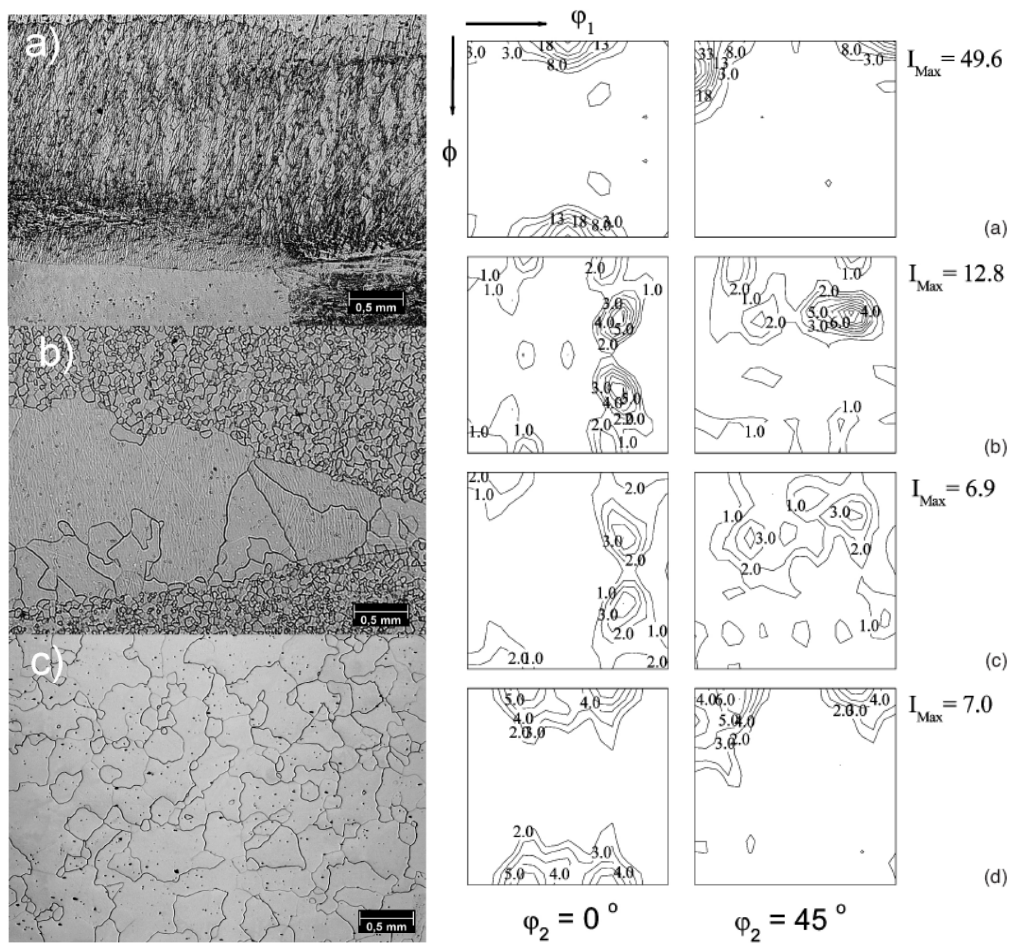


Figure 1.11 Microstructure (left) after first cold rolling (a), intermediate annealing (b), final annealing (c), and on the right side ODFs in the $\phi_2=45^\circ$ sections of the first cold rolling (a), intermediate annealing (b), second cold rolling (c), and final annealing (d) [29].

The microstructure of figure 1.11a shows the inhomogeneity after cold deformation where two large grains show in-grain shear bands parallel to TD while one bottom grain remains virtually unaffected by the deformation. They have attributed this heterogeneity to different initial grain orientations. The microstructure of figure 1.11b is partially recrystallised and presents regions with different grain sizes varying from 45 to 150 μm . Comparing figures 1.11a and b, it seems reasonable to conclude that the grains with deformation bands, probably close to the initial $\{001\}\langle 100\rangle$ orientation, give rise to the small recrystallized grains after intermediate annealing. The microstructure of figure 1.11c, which is obtained after a 2nd cold rolling reduction and final annealing, exhibits recrystallised grains of approximately 400 μm . The $\varphi_2 = 45^\circ$ section of the ODF for the first stage of cold rolling, shown in figure 1.11a, presented the maximum intensity of almost 50 times the random at the $\{117\}\langle 110\rangle$ position near the rotated cube $\{001\}\langle 110\rangle$. After intermediate annealing (figure 1.11b), the intensity of almost 8 times random was observed at $(114)\langle 1\ 3\ 1\rangle$ in the $\varphi_2 = 45^\circ$ section. In this case, the ODF maximum intensity of almost 13 times random was observed at position $\{392\}\langle 776\rangle$ in the $\varphi_2 = 20^\circ$ section, or, equivalently, at position $(239)\langle 6\ 17\ 7\rangle$, $\varphi_2 = 30^\circ$ section. The decrease of intensity from 13 to 7 times random was the main effect observed after the second cold rolling (figure 1.11c). After final annealing (figure 1.11d), the maximum intensity of 7 times random was observed at orientations $\{001\}\langle 120\rangle$ and $\{116\}\langle 110\rangle$ (near the rotated cube component). These orientations are components of the cube fibre $\langle 001\rangle // \text{ND}$. Therefore, the two-stage cold rolling method resulted in obtaining components of the ideal texture for magnetic properties.

From these results of Yonamine et al [29] concluded that high intensities of $\{00\}\langle 120\rangle$ and $\{116\}\langle 110\rangle$ (near rotated cube) components were repeatedly obtained after double stage rolling of directionally solidified iron 3% silicon steels. The heterogeneous deformation structures observed after the first cold rolling were attributed to the orientation difference between grains. The first stage as-deformed texture showed a strong rotated cube component, as expected. Intermediate annealing

systematically produced an uncommon component, $\{114\}\langle 131 \rangle$. Only after second stage cold rolling and final annealing part of the ideal fibre texture was achieved. It is obvious that by the 2-stage cold rolling and annealing process a favourable (partial) cube fibre texture could be obtained, albeit with much reduced intensity as compared to the initial twin-roll cast texture.

1.5.6. Cross rolling

In order to obtain the $\{001\}$ fibre by control of the annealing texture, one has to bear in mind that during recrystallisation of the cold-rolled sheet a selection will be made of orientations which have developed during the cold rolling process. Therefore, it should be attempted to form as few as possible unfavourable orientations of α and γ fibres as a result of the rolling strain. Unfortunately, these are the stable end orientations which appear after conventional rolling reductions of 60 to 80% [30]. By changing the orientations of the rolling-mill rolls with respect to the sheet, the rotation paths of the orientation flow during plastic deformation can be affected. In a study conducted by Kestens and Jacobs [30], a laboratory scale experiment was carried out in which the hot-rolled sheet was 90° rotated before cold rolling. In doing so the RD of hot rolling turns into the TD of cold rolling and vice versa. Hence, the hot band texture, with its characteristic strong α fibre is transformed into a texture with a strong $\langle 110 \rangle$ //TD fibre by simply substituting the hot rolling by the cold rolling reference frame. Because the latter fibre is highly unstable for cold rolling, all its components

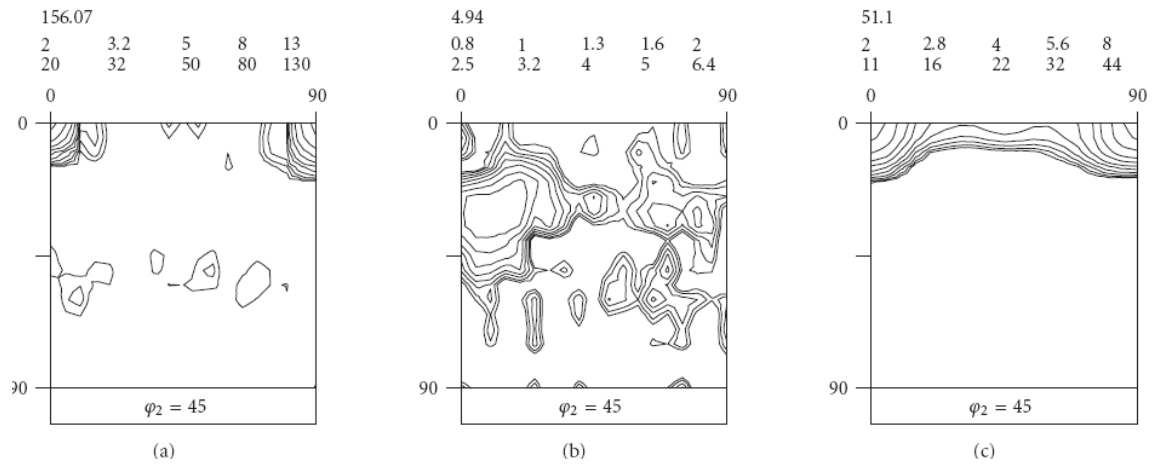


Figure 1.12 ODFs observed after cross rolling: (a) rolling texture, (b) primary recrystallization texture, and (c) after additional annealing treatment [30]

will rotate toward the semi-stable $\{001\}\langle 110\rangle$ orientation. This procedure will give rise to an extremely strong rotated cube component $\{001\}\langle 110\rangle$ with an extraordinary intensity of more than 150 times of random levels, cf. figure 1.12a, which offers the advantage that it does not introduce the unfavourable α and γ fibre components during cold reduction. This favourable texture is not preserved, though, after the primary recrystallisation treatment which produces a rather weak texture with a maximum in the vicinity of $\{311\}\langle 136\rangle$ (cf. figure 1.12b).

When this material is cold rolled to a reduction of 4 to 8% and submitted to an additional annealing treatment, comparable to the one which is applied to semi-processed products, the rotated cube component spectacularly reappears in the material and even other components of the $\{001\}$ fibre are formed. The texture presented in figure 1.12c is the result of such an additional annealing treatment. It displays a maximum of $>50x$ on the rotated cube component and $<10x$ on the cube component. In summary, it is worth noting that during cross rolling there is an evident weakening of the $\{111\}$ fibre texture compared to the conventional rolling process. Indeed, it can be seen from figure 1.12b that the unfavourable α and γ fibres were not introduced during the cold roll reduction of the cross rolled hot band. Another observation associated with the cross rolling is the development of the $\{311\}\langle 136\rangle$

component which appears to be an essential prerequisite to obtain the favourable ideal {100} fibre component.

In a recent study, an innovative method for texture control during the processing of NO electrical steel by severe plastic deformation (SPD) is investigated. The proposed hypothesis is inspired by reported textures after accumulative rolled bonding (ARB) and recrystallization annealing in IF steel. The ARB technique, developed by Saito et al. [31], provides a mode of applying excessive rolling reductions to sheet material but without excessively thinning the sheet. The primary aim of this study was to explore the effect of excessive rolling strains, within the industrial relevant range, in producing non-conventional recrystallization texture components in NO Fe-Si steel with promising potential for magnetic applications.[32]

1.6 Challenges in cube texture evolution

The cube fibre texture is of essential importance to achieve isotropic and efficient magnetization of electrical steels in arbitrary directions in the plane of the sheet. A considerable amount of research efforts have been spent in the past, and several techniques have been reported in the literature as explained in the previous sections of this chapter but none of the mentioned concepts or techniques have reached to the level of a reference and generally accepted industrial process.

Among the existing techniques the potential of the α - γ - α phase transformation needs further investigation as it is among the least explored paths so far. This research is focussed on the systematic study of surface texture evolution during phase transformation annealing based on the concept of surface energy anisotropy.

1.7 Surface energy anisotropy controlled phase transformation

It is well known that surface energy anisotropy is the driving force for the orientation selection at the metal-vapour interface. This affects the microstructure and texture evolution at the surface during phase transformation. Although, the exact value of the interfacial energy between the atmosphere and the steel surface is largely unknown, it

is widely accepted that the bcc {100} and {110} planes have a relatively low surface energy [9,10,11,12,13]. The surface textures reported in the literature [19,20,21,22] do not include a systematic description of their evolution along with the grain morphology and grain structure at the surface.

1.8 Objectives and layout of the Thesis

In the present study an attempt has been made to represent a comprehensive view on the surface texture evolution in ultra low carbon steel alloyed with Mn, Al and Si in various amounts. Cold rolled sheets of different compositions were subjected to phase transformation annealing in a protective atmosphere as mentioned in figure 1.13. Various parameters have been investigated in a systematic manner to investigate their effect and to a certain extent also to optimize the concept. The general line that is applied here, based on the literature findings, consists of a number of consecutive thermo-mechanical processing steps including a transformation annealing treatment aiming to create the appropriate surface texture and followed by a cold rolling and recrystallisation annealing treatment. In the latter processing step it is intended to grow the surface layer of crystals across the entire thickness of the sheet. These processing steps will be dealt with in detail in the next chapters of this thesis.

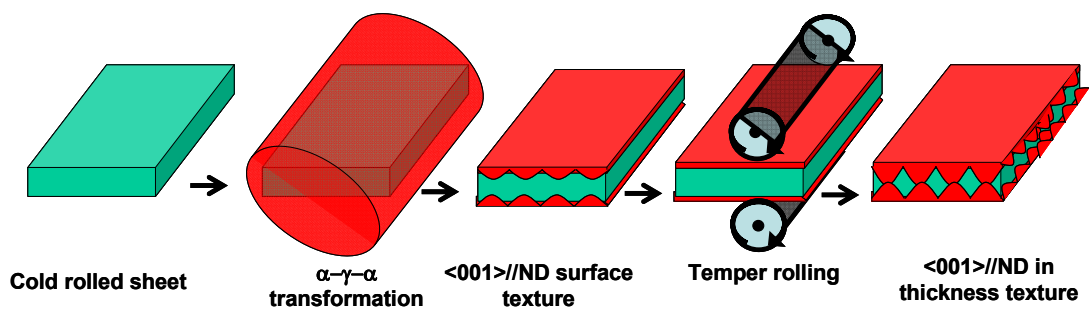


Figure 1.13 Schematic concept of surface texture evolution during phase transformation annealing and its inward growth across the thickness of the sheet.

Chapter 2 describes the material selection and the thermo mechanical history of the iron alloys under consideration as well as the experimental strategy and important experimental tools employed in this investigation. Special attention was paid to the techniques for characterization of the exact chemical composition, the microstructure and the texture of surface and bulk of the sheet material.

In Chapter 3 several parameters which may be of importance such as steel composition, annealing characteristics (time, temperature and atmosphere) or the initial material condition prior to annealing. This chapter reports an extensive investigation on the influence of these parameters on the characteristics of the surface texture and microstructure.

Chapter 4 considers the investigation on the possible role of the surface chemistry during phase transformation annealing. The steel sheet surface chemistry was investigated on the cold rolled surface before annealing and also subsequently on the annealed surface with dedicated analysis techniques: X-ray Photoelectron Spectroscopy and Glow Discharge Optical Emission Spectrometry. X-ray photo electron spectroscopy is unique in revealing the surface contamination in terms of peak shift of binding energy, whereas GDOES gives the larger in-depth profiles of individual elements before and after annealing. The results confirm that the chemical composition of the steel and the precise features of the oxide layer play a crucial role in the formation of the surface texture during transformation annealing.

Chapter 5 reports the interrupted annealing experiments in better quality vacuum in the dilatometer. The experiments were intended to observe the surface texture evolution systematically within a narrow range of temperatures and also the effect of better vacuum on surface texture.

Chapter 6 reports a detailed study on the surface microstructure, i.e. the very outer surface layer of grains, appearing after phase transformation annealing. These surface layer grains and their grain boundary properties were analysed in detail by orientation imaging microscopy to reveal their crystallographic features.

Chapter 7 includes the potential processing strategies by which the surface texture components could be grown through the thickness of the sheet so as to consume the entire bulk. Skin pass rolling (temper rolling) with different light rolling reductions has been tried to induce strain in the surface of the transformation annealed sheets which have surface texture with specific components. Subsequently, these temper rolled sheets were annealed at different temperature and time to investigate the possible growth of the specific surface texture components.

Chapter 8 includes the general conclusions and some suggestions for future work.

1.9. References

- [1] CD Wupperman, HJ Wieland and S Geisler: WMM 2010 proceedings, Ghent University, Belgium
- [2] A T Almeida, F J T E Ferreira, and D. Both, IEEE Transactions on Industry Applications, 41(1) (2005) p188
- [3] S S Williamson, S M. Likic, and A Emadi, IEEE Transactions on Power Electronics, 21(3) (2006) p730
- [4] WF Barret, R.A Hadfield Sci. Trans. Roy.Dublin Soc. 1(1900), p 67
- [5] Honda K, Kaya S : Sci.Rep. Touhoku Univ.,15(1926) p 721.
- [6] N P Goss,U.S. patent no. 1965559 (1934).
- [7] L Kestens, J J Jonas, P Van Houtte and E Aernoudt Textures and Microstructures, 26-27(1996), p. 321.
- [8] F Assmus, R Bull, D Ganz and F F Pfeifer, Zs. Metallkunde, 48 (1957)
- [9] G Wiener and M Littman, J. Appl. Phy. 29, No.3 (1958)
- [10] J L Walter and W. Hibbard, H.C. Fiedler, H.E. Grenoble, RH Pry and PG Frishmann Journal of Applied Physics Vol. 29 No. 3 (1958) p 363
- [11] D A Porter and K.E. Easterling, Phase transformation in metals and alloys, Chapman and Hall, London.
- [12] D M Kohler, Journal of applied Physics, Suppl.to Vol 31, No.5, (1960) 408S

- [13] J L Walter, Journal of applied physics, 39, 3 (1965).
- [14] M Godec, M Jenko, H J Grabke and R Mast, ISIJ International, Vol.39 (1999) No.7, p 742
- [15] T. Tomida, JMEPEG, 5 (1996) p 316
- [16] Yuri Sidor, F.Kavac and M Djubinsky Thermomechanical processing conference proceedings (2004) p 514
- [17] Nakamura and K. Matsumura: Japanese Patent No, 1899382.
- [18] Minoru Takashima , Michiru Komatsubara and Nobuyuki Moritu. ISIJ vol 37, (1997) No. 12 p 1263
- [19] E.C. Bain Trans. AIME, 70 (1924), p. 25.
- [20] G. Kurdjumov and G. Sachs, Z. Phys., 64 (1930), p. 325.
- [21] Z. Nishiyama, Sci. Rep. Tohoku Imp.Univ. 23 (1934/1935), p. 638.
- [22] G. Wassermann, Arch. Eisenhüttenwes, 16 (1933), p. 647.
- [23] R.K. Ray and J.J.Jonas, International Materials Reviews, 35, 1 (1990)
- [24] RG Aspeden, JA Berger, HE trout Acta Met. 16 (1968) p 1027
- [25] O Hashimoto, S Satoh, T Tanaka, Transactions ISIJ 23 (1983) p 1028
- [26] N. Yoshinaga, L.Kestens, BC de Cooman; Material science forum vol 495-497 (2005) p 1267-1272
- [27] A. Bodin, L Woning, J. Sietsma, S vander Zwaag, ISIJ international, 42, (2002) p 94
- [28] J Y Park, Kyu Hwan OH and Hyung Yong RA ISIJ Vol 41, (2001) p 70
- [29] Taeko and Yonamine, Nicolou A. Castro, Fernando JG Landgraf; steel research international no.6, 461-463; 2005
- [30] L. Kestens and S. Jacobs, Texture, Stress and Microstructure, Vol. 2008,
- [31] Y. Saito, H. Utsonomiya, N.Tsuji and T. Sakai, Acta Mater. 47 (1999) p 579
- [32] P. Governado, Phd Thesis, Ghent University, Ghent, Belgium (2009) p 100

Chapter 2

Experimental procedure

This chapter includes the description about materials selection, thermo-mechanical processing and various experimental techniques which have been used to carry out the investigations on the surface texture evolution.

2.1. Material preparation

Although an ultra low carbon steel was selected as a base composition for the present study, most of the observations were carried out on two other alloys, denominated as MnAl1 and MnAl2, with minute and increased additions of manganese and aluminium, respectively. These MnAl1 and MnAl2 alloys were casted in a Pfeiffer VSG100 vacuum melting and casting unit operated under an argon protective atmosphere in the laboratory. The weight of the charge was 100 kg with alloying additions of Mn, Al and Si to ultra low carbon steel as a base melt. The chemical compositions of the cast alloys are shown in table 2.1 together with the chemistries of a number of commercial grades of non-oriented electrical steels received as hot rolled sheet from the industrial partner (Arcelor Mittal Global R&D, Ghent, Belgium) of this research program. Two ultra low carbon steel alloys denominated as Si1 with low silicon (0.5wt %) and Si2 with high silicon (1.38wt %) are fully processed grades. The third alloy denominated as LC with low carbon (0.05wt%) is a semi-processed grade with a Si-content of 0.17 wt%.

Table 2.1 Chemical composition (wt %)

	C	Mn	Si	Al
ULC	0.002	0.15	0.005	0.055
MnAl1	0.003	0.75	0.23	0.12
MnAl2	0.002	1.28	0.22	0.29
Si1	0.002	0.33	0.510	0.13
Si2	0.002	0.34	1.38	0.11
LC	0.047	0.46	0.17	0.037

2.2. Thermo mechanical processing

The casting ingots of alloys MnAl1, MnAl2 and the base material ultra low carbon steel were cut in the shape of a plate of 25 mm thickness and these plates were pre-rolled till a thickness of 10 mm. Afterwards the pre rolled sheets were hot rolled till a thickness of 1.5 mm under different schemes as shown in figure 2.1.

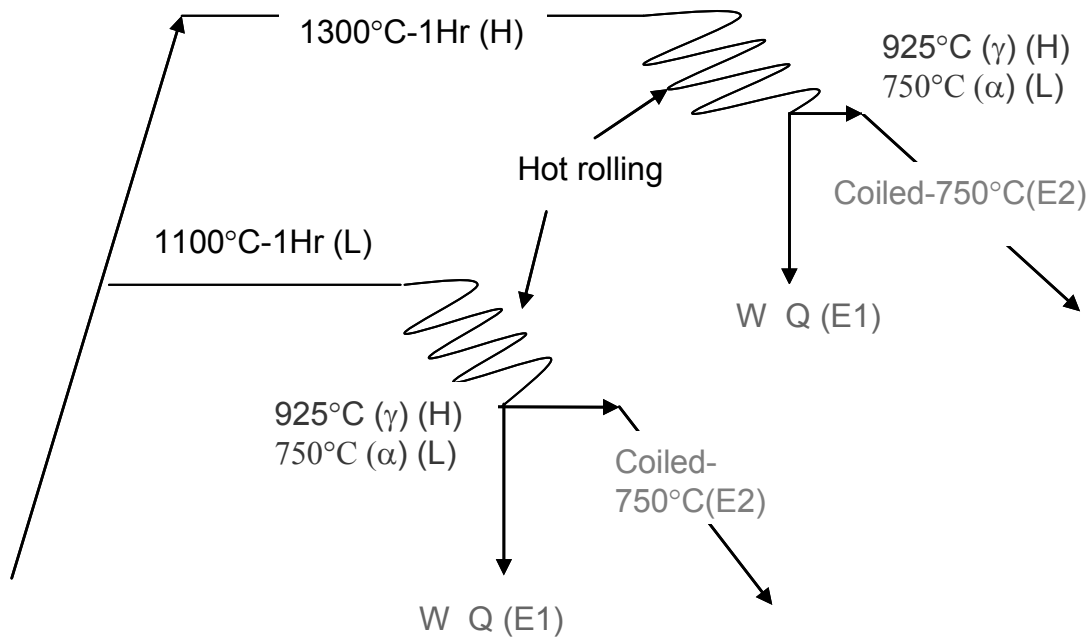


Figure 2.1 Schematic flow diagram applied in material processing.

The schematic plan (figure 2.1) shows two slab reheating temperatures 1,300°C and 1,100°C. Subsequently, after the final pass of hot rolling two different treatments were performed. In one case a coiling simulation was applied at 750°C for 24 hours and in the other case the hot rolled sheet was water quenched after the final pass of hot rolling. This selection was done in order to allow for comparison with the industrial materials Si1, Si2 and LC that have undergone a similar type of hot rolling history. In the present study the sheets that were processed at the high slab reheating temperature (1,300°C) and the high finishing temperature (925°C) followed by coiling are the ones that were investigated most intensively. After hot rolling the material was further cold rolled to a thickness of 0.5 mm, which is a very conventional thickness for non oriented electrical steel laminates. Cold rolled sheets of 0.5 mm thickness from all alloy compositions were used for further sample preparation required for different experimental studies including various types of annealing treatments. Two types of sample dimensions were selected depending on the furnace type employed for annealing. For the Pyrox tube furnace a sample size of 20 mm x 30 mm was employed whereas for the dilatometer furnace the smaller sample size of 6 mm x 12 mm was used. The samples were very well degreased and subsequently cleaned by acetone before the annealing experiments.

2.3. Heat treatment Equipment

2.3.1. PYROX annealing furnace

Some of the annealing tests were performed in the Pyrox tube furnace with graphite resistance heating (figure 2.2). The samples were introduced in a quartz tube of 30 mm diameter, closed on one side and on the other side a cross shaped vacuum piece was fitted. Three more components were attached to this piece: one pipe and a valve connecting to the vacuum pump, a thermocouple with vacuum proof fitting and

one more valve connecting to a N_2 gas supply. The furnace was heated up to a temperature slightly higher than the targeted annealing temperature.

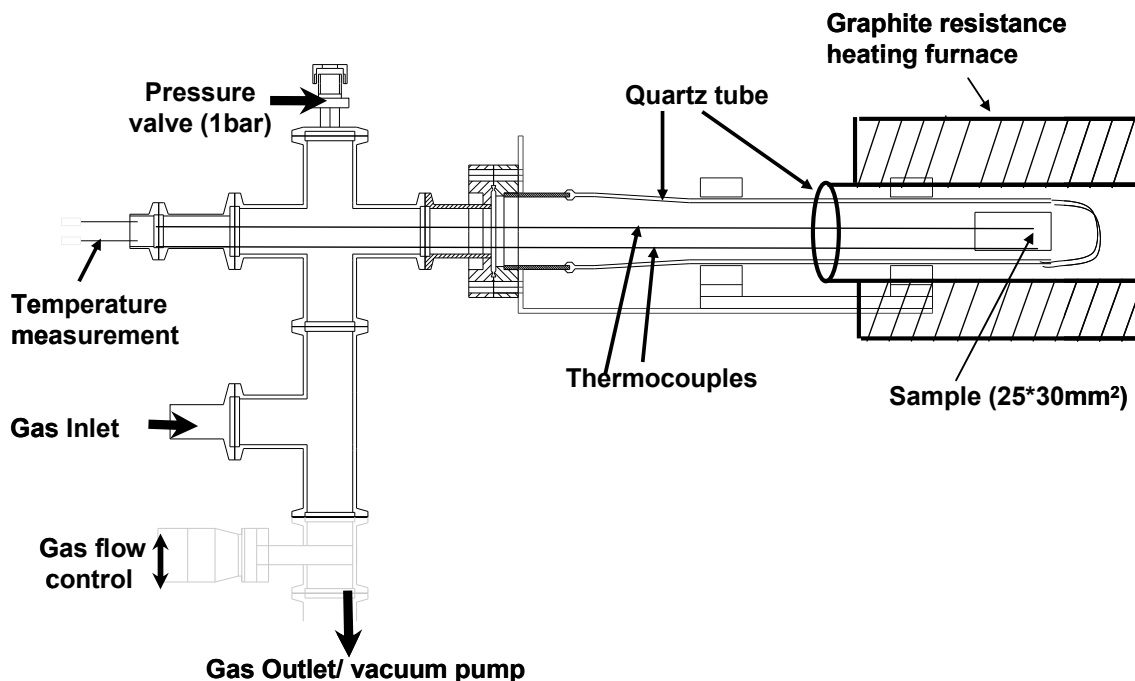


Figure 2.2 Schematic drawing of the pyrox tube furnace.

The sample was kept in the quartz tube at room temperature until the furnace had reached the set temperature by the controlling device. The vacuum pump was coupled with the supply of N_2 , Ar or a mixture of gases required to provide the desired protective or reactive annealing atmospheres. The quartz tube containing the sample was moved into the furnace using a guiding system. The temperature reading from the thermocouple was used as feedback information for the temperature controller of the furnace and it was also recorded in a computer. Using this procedure, the sample was heated to the required annealing temperature with controlled average heating rate of 15°C/s and subsequently after finishing the soaking time the quartz tube along with the sample was withdrawn from the tube furnace and air cooled with an average cooling rate of 30°C/s . The heating rate and cooling rate were kept identical for all the experiments presented in this thesis.

2.3.2. Dilatometer

The phase transformations were experimentally studied by means of a dilatometer. The technique is based on monitoring the length change of the sample during heating, cooling or isothermal holding. The lattice parameter for both ferrite and austenite of a given composition varies linearly with temperature in the temperature range 300-1200°C. The ferrite lattice contains 2 atoms in one cubic unit cell with a unit lattice parameter of 0.289 nm in pure iron at 727°C, whereas the austenite lattice contains 4 atoms in the cubic unit cell with a lattice parameter of 0.36309nm in pure iron at 727 °C. The specific volume (nm^3/at) is therefore higher for ferrite than for austenite and therefore, at the transformation temperature when the ferrite phase transforms to austenite or vice versa, the steel exhibits a dilatation, due to its volume change.

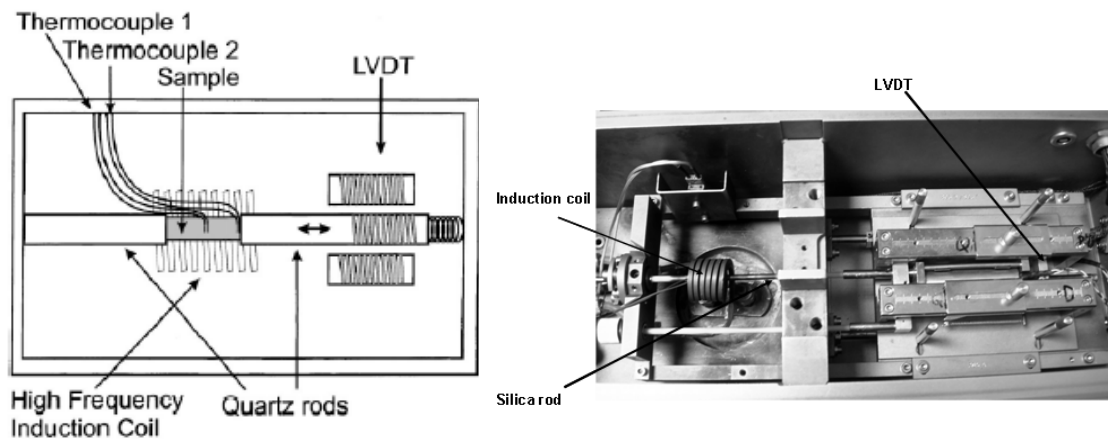


Figure 2.3 Schematic top view of the dilatometer (left) and employed equipment in this work (right).

The samples used in dilatometric studies are cylindrical samples of 10 mm in length and 5 mm in diameter. In the present study, the standard cylindrical samples were prepared for the laboratory cast alloys MnAl1 and MnAl2. The rectangular samples with 6 mm width and 12 mm length were prepared from 2 mm thick hot rolled steel sheet received from the industrial partner. The Linear Variable Displacement Transducer (LVDT) transforms the length displacement of the sample to an electrical

signal, which is digitally recorded and recalculated into a relative dilatation. $\Delta l/L_0$. Because of its high quality vacuum the furnace of the dilatometer was also used as an annealing tool ignoring the dilatation signal (figure 2.3).

2.4. Surface texture analysis techniques

In the present study the very surface of the steel sheet samples were investigated by X-ray diffraction and orientation contrast microscopy attached to an environmental scanning electron microscope. The fundamental details of these equipments and their relevance in the surface texture analysis are described below.

2.4.1. X-ray Diffraction

X-ray diffraction is the most established technique for bulk texture measurements as it reveals the macro texture of a volume of material from a flat specimen by measuring the intensities of the diffraction maxima.

2.4.1.1. Fundamental principles

If a flat sample of a polycrystalline material of known lattice parameter and crystal structure is rotated in space, whilst preserving constant $\theta/2\theta$ Bragg conditions for a specific crystal plane $\{hkl\}$, the intensity of the diffracted beam will be proportional to the volume fraction of sample crystallites which exhibit the considered $\{hkl\}$ plane in the proper position for Bragg diffraction. The raw output from the X-ray texture goniometer is a chart showing the diffracted intensity with respect to rotation angles of the specimen which determine the sample position with respect to the laboratory reference system. The latter can be precisely characterized by an inverse pole figure which represents the distribution of polar coordinates of the sample normal directions with respect to the crystal pole $\langle hkl \rangle$ of the diffracting planes $\{hkl\}$ and an arbitrary chosen azimuthal direction. Inversely, the $\langle hkl \rangle$ can be represented in polar coordinates with respect to the sample coordinate reference system, conventionally

denominated by the RD, TD and ND sample directions. The latter representation is called the $\{hkl\}$ pole figure.

2.4.1.2. Texture goniometer

An overview of the D5000 diffractometer with the open eulerian cradle is shown in figure 2.4, displaying the individual components in the diffraction path. In order to determine the orientation of a given lattice plane $\{hkl\}$, of a single crystallite, the detector is first set to the proper Bragg angle 2θ of the diffraction peak of interest and then the sample is rotated in the goniometer so as to give the possibility of all grains in the polycrystalline aggregate to comply with the Bragg condition. The intensity recorded at a certain sample orientation is proportional to the volume fraction of crystallite with their lattice plane in diffraction condition. The systematic change in angular orientation of the sample is normally achieved by utilizing a four-circle diffractometer. We collect the intensity data for various settings of χ and φ whereby, χ is the angle between the sample normal and the diffraction vector and φ is the rotation angle of the sample around its perpendicular. In a concentric circle measuring setup we measure all PHI values ($0 < \varphi < 360^\circ$) for a given χ value, then χ is increased with a value $\Delta\chi$ (e.g. $\Delta\chi = 5^\circ$) and the process is repeated. The mechanical assembly that makes up the sample holder, detector arm and associated gearing is referred to as the texture goniometer whereas the particular mechanical device which implements the χ rotation required to measure a pole figure is called an Eulerian cradle.

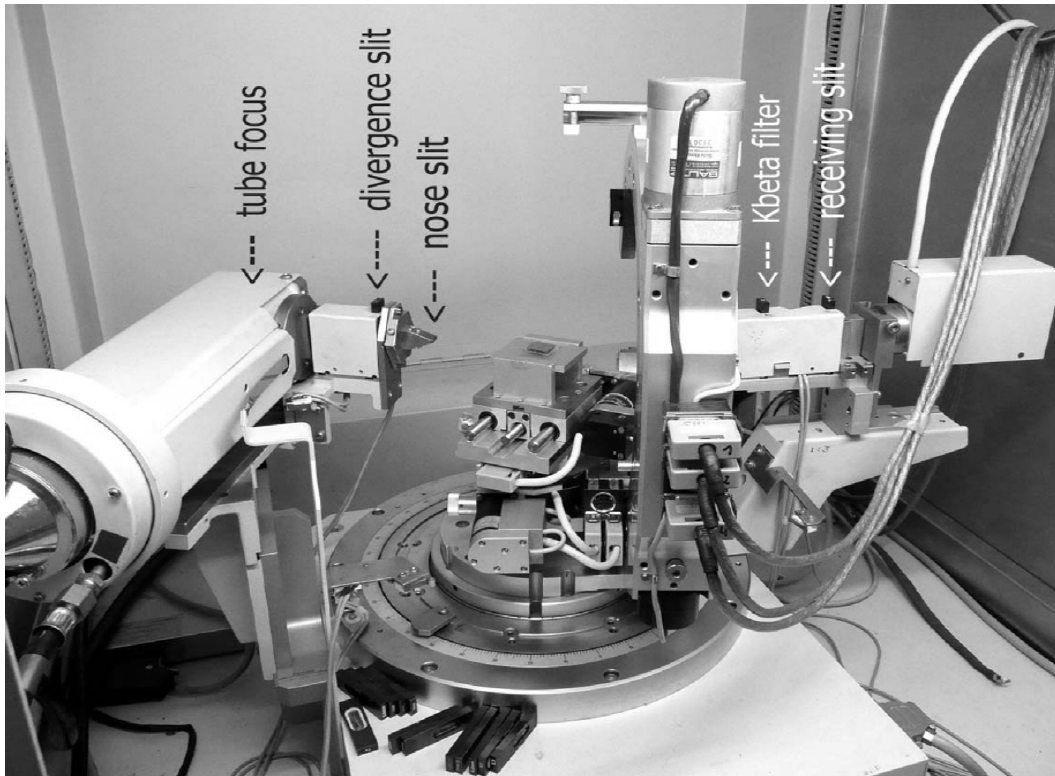


Figure 2.4 The D5000 X-ray texture goniometer with different parts.

In the present study materials with BCC crystal structure at room temperature were measured with Mo $K\alpha$ radiation ($\lambda = 0.07107$ nm) at 40kV and 50mA. In a conventional measuring setup four pole figures (110), (100), (211) and (310) were measured at the corresponding Bragg angles as listed in table 2.2. Per pole figure 15 circles were measured along the χ -range between $\chi = 0$ and 70° and the circles are 5° apart from each other ($\Delta\chi = 5^\circ$). On each circle data are collected in a continuous mode with a ϕ -resolution of 4° so there are 90 segments per circle.

Table 2.2 also shows the penetration depth of the beam in the steel sheet during the measurement. It can be seen that in general the depth of penetration is increasing with the diffraction angle. As in the present study particular attention was paid to the outer surface texture right at the metal/vapour interface it is important to note that the diffracted data are not collected from the surface only but rather they are coming from a certain depth under the surface.

Table 2.2 Penetration depth (μ) underneath the metal surface with Mo ($K\alpha$) X-rays.

Pole figure	2θ	90%contribution to the diffracted beam	70%contribution to the diffracted beam
110	22.34	7.94μ	4.14μ
100	32.55	11.49μ	6.02μ
211	41.23	14.44μ	7.55μ
310	58.26	19.99μ	10.44μ

2.4.1.3. Pole figure measurement

The principle of pole figure measurement by means of diffraction techniques is based on Bragg's diffraction law. As each set of lattice planes has a different lattice spacing d , reflections from various sets of lattice planes can be distinguished by setting the detector to the corresponding 2θ angle with respect to the incident radiation. To derive the crystallographic orientation of a given crystallite, the arrangement with respect to an external reference frame, of a set of lattice planes (hkl), has to be determined. First we consider the reflection at a single crystallite as schematically shown in figure 2.5. The crystal is irradiated with monochromatic radiation at the proper Bragg angle for reflection and the detector is set at an angle 2θ with respect to the primary beam. Of course a reflected intensity is measured only when the reflecting lattice planes are arranged such that they are perpendicular to the diffraction vector which bisects the incident and reflected beam (cf. figure 2.5) which means that in most cases no reflection is obtained for a single crystal. In order to ensure reflection from arbitrarily oriented lattice planes the sample has to be rotated and tilted until lattice planes are in reflection conditions. The necessary rotation and tilt angles are measured for the arrangement of lattice planes within the crystal, which means that they represent the orientation characteristic of the crystal with respect to external sample frame.

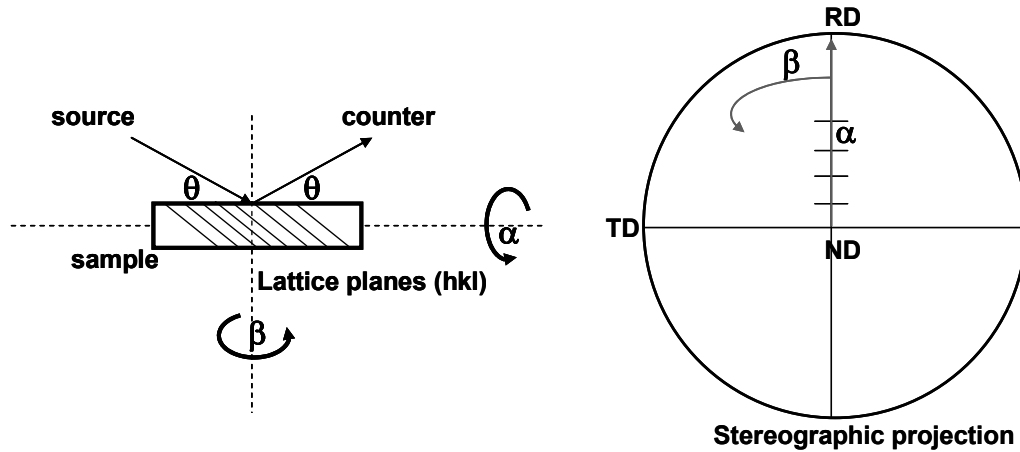


Figure 2.5 scheme of pole figure measurement [1].

When the Goss orientation ($\{110\} \langle 001 \rangle$) is irradiated in a crystal at the Bragg angle for $\{200\}$ reflection, the reflected intensities will be obtained at a sample tilt of $\chi=45^\circ$ plus an additional rotation of $\varphi=90^\circ$ or 270° .

For the polycrystalline samples, which are composed of an array of single crystallites, the intensity recorded at a certain sample orientation is directly proportional to the volume of diffracting crystals which currently is in reflection condition for a specific sample position. Thus the pole figure of a crystalline sample reflects the distribution of orientation in that sample i.e. its *crystallographic texture*.

2.4.1.4. Evaluation of x-ray texture data

The raw output of an X-ray texture measurement is the diffracted $\{hkl\}$ intensity in the form of two pole figure angles α and β , which can be converted readily in a conventional $\{hkl\}$ pole figure. Hence the pole figure is the obvious choice for a critical assessment of experimental texture results. However, the full texture information as represented by the orientation distribution $f(g)$ is of a 3-dimensional nature and therefore the pole figure can be considered as a 2D projection of a 3D object. Therefore, the pole figure representation implies unavoidably a loss of

information, and thus it is not possible to determine the ODF from one single experimental pole figure without ambiguity. Mathematical conversion techniques have been developed which can derive an approximation of the ODF from a number of N measured pole figures. For practical purposes in the present work 4 pole figures are measured on each sample: the $\{220\}$, $\{200\}$, $\{211\}$ and $\{310\}$ pole figures with $\Delta\varphi$ and $\Delta\chi$ values of 4° and 5° , respectively. The ODF calculation from measured pole figures was carried out with the ODF software package developed by Van Houtte [2] which is based on the conventional Bunge method of pole figure inversion, coupled with a Ghost correction procedure by Van Houtte et al [2]

2.4.2. Orientation imaging microscopy

Electron back scattering diffraction (EBSD) produces a band-like diffraction pattern when the primary electron beam interacts with the outer surface atomic layers of a bulk sample in a scanning electron microscope (SEM). These diffraction bands bear a direct connection with the crystal planes of the sample. In fact, they may be considered as macroscopic extensions of the crystal planes (hkl) which leave the sample and intersect with a 2D detection screen. The first observations of similar high-angle patterns were made by Kikuchi in the transmission electron microscope in the 30's [4], and therefore the apparently similar diffraction patterns in the SEM were coined (pseudo-) Kikuchi patterns. In the 70's, the first EBSD patterns were recorded in the SEM and computer routines for interactive EBSD pattern evaluation were developed for the first time in the early 80's [5]. In the late 80's and early 90's the indexation of EBSD patterns was fully automated and, later on in the mid-90's, gradually developed into the orientation mapping tool as we know it today [2,6-8].

Two steps were crucial to improve the EBSD technology and use it as a metallographic imaging technique. First, there is the automated pattern collection and indexation without operator interference [9,10] and, second, the coupling of this feature to the beam and/or stage control which completely automates the EBSD operation leading to the orientation mapping facility [9]. An EBSD system, operating

automatically on a conventional SEM with W-filament provides a pattern solving algorithm which takes a fraction of a second, an angular accuracy better than 1° , a spatial resolution of $\sim 200\text{-}500\text{nm}^2$ (with a Field-Emission filament this can be improved to approximately $40 \times 100\text{nm}^2$) and an angular width of approximately 60° .

Since the early days of the application of EBSD technology, a typical EBSD system consisted of a light-sensitive CCD camera, a phosphor screen and a computer [11]. In order to maximize the yield of backscattered electrons a glancing incidence of the primary beam is preferred. In practice, most EBSD setups work with a specimen tilt angle of 70° to 75° as shown in figure 2.6, i.e. the angle between the sample surface and the primary e-beam is 20° to 15° .

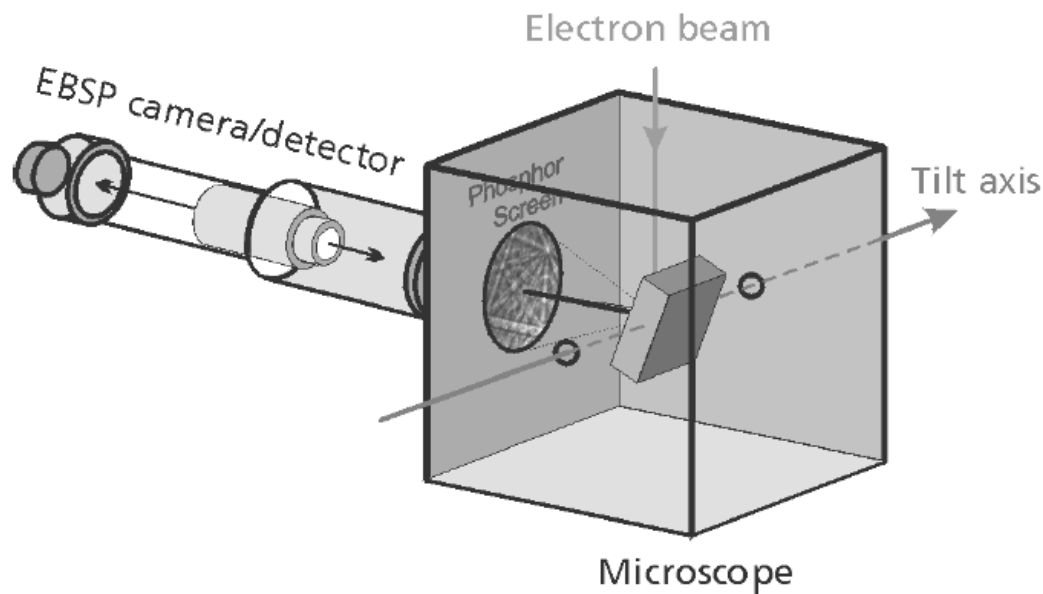


Figure 2.6 Schematic of EBSD attachments in scanning electron microscope [2].

Under such condition the microscope hardware may require that the camera which records the diffraction pattern cannot always be positioned in a simple geometrical relationship with respect to the specimen – only rarely is the camera parallel to the specimen surface as for TEM. These additional considerations for EBSD imply that

distances in the pattern cannot be transformed into angles by a simple relationship. The diffraction pattern is captured by a fluorescent phosphor screen which is commonly perpendicular to the horizontal direction within $\pm 10^\circ$. Through a lead-glass window which separates the vacuum chamber from the outside world, the pattern of the fluorescent phosphor is captured by a light sensitive video camera. The image is digitalized by a video grabber card which feeds the pattern pixel by pixel to the data collection computer. In the present study, digital cameras have been used in the EBSD hardware. Digital cameras offer the advantage that they are a factor 10 to 50 as fast as the analog ones because the image does not need to be converted anymore from analog to digital. All these subsequent steps of the data collection system are schematically represented in figure 2.7. Orientation contrast microscopy is one of the most powerful tools for the determination of the local correlation between microstructural features and crystallographic orientation.

Some systems work in stage control mode which requires that the electron beam remains in a fixed position while the stage of the microscope moves the specimen relative to the beam by means of the EBSD acquisition software. Within this mode, the problems observed in beam mode are eliminated as the beam stays in a stationary position. Hence, there is no risk of beam deflection out of the optic axis which will result in a better accuracy on the determination of the absolute orientations and if the sample surface is accurately parallel to the x-y plane of the moving stage, the problem of the beam defocus is also avoided. The disadvantage of this method is that it is slower than the beam control, the typical displacement time being around 1 s and the displacement accuracy is not very high making it only interesting to be used with large a step size, i.e. at the low-end tail of the resolution spectrum.

Orientation scans are the basic output of the collected EBSD data which are used to quantitatively analyse the crystallography and the microstructure of the sample. In order to provide such amount of data, the scans have to be collected as fast as possible and critical parameters such as spatial and angular resolution should be taken into consideration. These parameters depend on the type of filament (W, LaB6 or FEG),

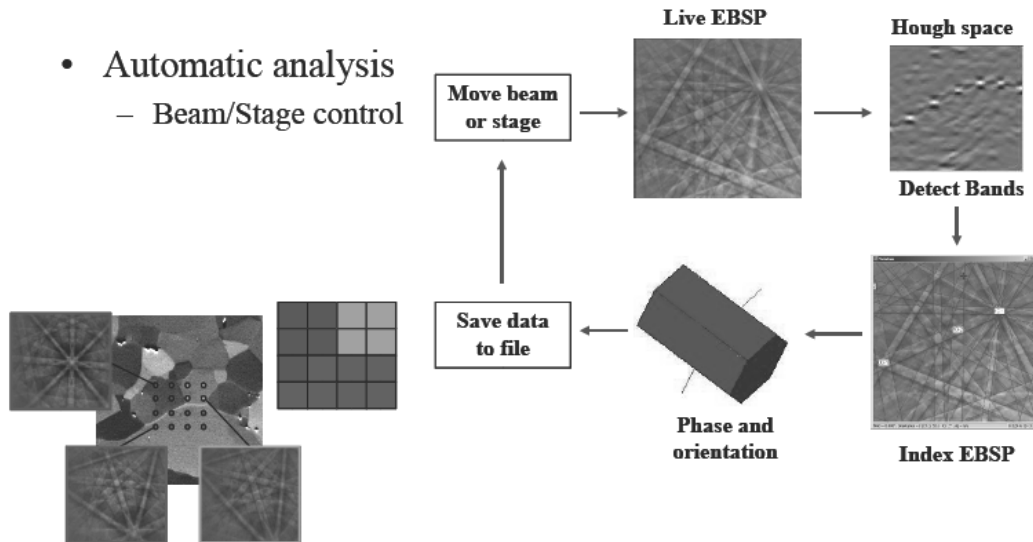


Figure 2.7 Data collection system in orientation imaging microscopy [2].

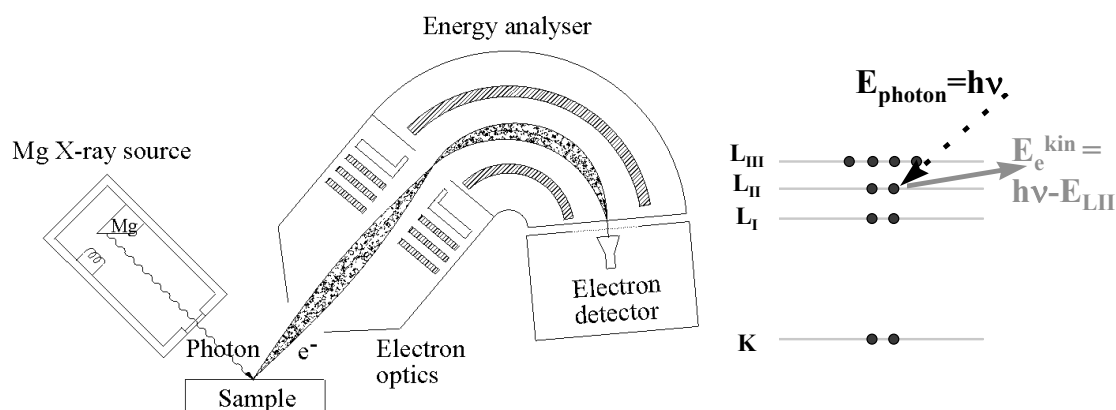
the crystal structure of the sample (mono-phase, single phase, cubic or lower symmetry), sample preparation (mechanical or electrochemical), camera (analog vs. digital) and the input parameters of the data acquisition software (e.g. detect 5 or 13 Kikuchi lines). The data presented in this work were collected with the FEI XL-30 ESEM microscope with LaB6 filament of the Department of Materials Science Engineering at Ghent University. The microscope is equipped with a TSL[®] type EBSD system which consists of a digital camera and data-collection software which takes over the beam control when a measurement is in progress. In addition to the data collection software the system also includes the data processing software which offers a broad range of post-processing facilities. In the EBSD configuration samples were tilted 70° along with the stage. Data acquisition was performed with a step size ranging from 0.1 to of 1.0 μm, depending on the required resolution, scanning over an area of approximately 500μm x 500μm for most of the measurements. The accelerating voltage of the beam was set to 20 kV for all measurements.

2.5. Compositional depth profiling techniques

The composition at the surface of the steel sheet before and after annealing was analyzed by the surface analyzing techniques X-ray induced photoelectron spectroscopy (XPS) and Glow Discharge Optical Emission Spectroscopy (GDOES). The fundamental principles and application of these techniques are discussed separately in the following sections.

2.5.1. X-ray induced photoelectron spectroscopy (XPS)

XPS is one of the main surface analytical techniques that have become widely available for material research since the seventies. In XPS the primary excitation is accomplished by illuminating the specimen with a monochromatic Mg or Al K_{α} X-ray beam. These X-rays cause photo-ionisation of atoms in the specimen which triggers the emission of photo-electrons and auger-electrons. These photo-electrons have a kinetic energy that is characteristic of the element by which they are emitted, cf. figure 2.8b. By registering the energy spectrum of the emitted electrons the chemical elements which are responsible for their emission can be identified. Additional information about the binding condition or chemical state of that element can be obtained as pronounced shifts can be observed in the position of the peaks in the spectrum. XPS can be applied on virtually all vacuum compatible samples since the incident X-rays normally do not cause surface damage.



(a) Schematic of the basic apparatus used in X-ray photoelectron spectroscopy. X-rays with energy $h\nu$ are produced at the Mg anode by bombardment of electrons created at the filament. The X-rays impinge on the sample producing photo-electrons, which are detected after analysis in the electron analyzer.

(b) Principle of XPS on an atomic scale.

Figure 2.8 Schematic of x-ray photo-electron spectroscopy.

The typical schematic setup of an X-ray photo electron spectroscope is shown in figure 2.8a. The main components of the setup include a source of X-rays, an ultrahigh vacuum stainless steel chamber, an electron collection lens, an electron energy analyzer, an electron detector system and a moderate vacuum sample introduction chamber.

XPS is routinely used to quantitatively determine the presence of elements within a distance of ~ 10 nm of the sample surface being either material proper or contamination elements. By consequence, it is possible to identify empirically the chemical formula of a material that is free of excessive surface contamination together with the chemical state of one or more of the elements in the sample. The spectral resolution is sufficient to yield precise information on the binding energy (BE) of one or more electronic states and the thickness of one or more thin layers (1–8 nm) of different materials within the top 10 nm of the surface.

An additional advantage of the XPS is that it produces minimal beam damage because of the comparatively low beam energies and minimal sample charging; hence the technique can be used with very delicate materials. The spectra collection speed is

high (typically less than five minutes) and quantitative to better than $\pm 10\%$ using calibration standards.

XPS measurements were carried out on a PHI Quantera SXM apparatus using a monochromatic AlK α anode (1486.6eV) at 26.1Watt and with a beam diameter of 100 μm . The take off angle was 45 $^\circ$ and an area of $\sim 1\text{mm}^2$ was analysed over the sample surface. The analyzer was operated under the fixed analyzer transmission (FAT) anode. Sample charging during the measurement was avoided by application of an electron flood gun, operating at 1.2V and 10 μA . The analysis parameters for all elements studied with this technique and assumed to be of importance in this work are shown in table 2.3.

Table 2.3 XPS analysis parameters used in present study.

Spectrum	Range (eV)	Step energy (eV)	No. sweeps	Pass energy (eV)
O1s	525-545	0.1	6	55
Fe2p	700-740	0.13	6	69
Mn2p	632-672	0.1	6	55
C1s	278-298	0.1	4	55
Si2p	95-115	0.1	6	55
Al2p	68-88	0.13	3	69
Survey	00-900	0.13	3	69

The spectra obtained were quantified by performing a peak fitting for all the elements, using the Multipak V8.0[®] software. XPS depth profiling was performed on the samples using a 3keV Ar⁺ gun with a calibrated sputter rate of 4.4 nm/min on thermally grown SiO₂ on a silicon substrate.

2.5.2. Glow Discharge Optical Emission spectroscopy (GDOES)

Glow Discharge optical Emission Spectroscopy is an analytical method for the determination of elemental composition in bulk samples for broad area measurements. GDOES also offers the capability of surface depth profiling. Glow discharges (GD)

have been studied for many years now [12] as they are used for analytical purposes for about 100 years [13]. Today we know of many different glow discharges [14–16] and even in the analytical field the variety of glow discharges is very wide [17]. In this review, however, we will concentrate on the properties of the hollow *anode–flat cathode* glow discharge introduced by Grimm [18] in 1967 and now commonly called the *Grimm* source. In the following we use the term glow discharge to mean a “Grimm-type” glow discharge operating at typical conditions of 5–10 hPa pressure and usually at powers of less than 100 W.

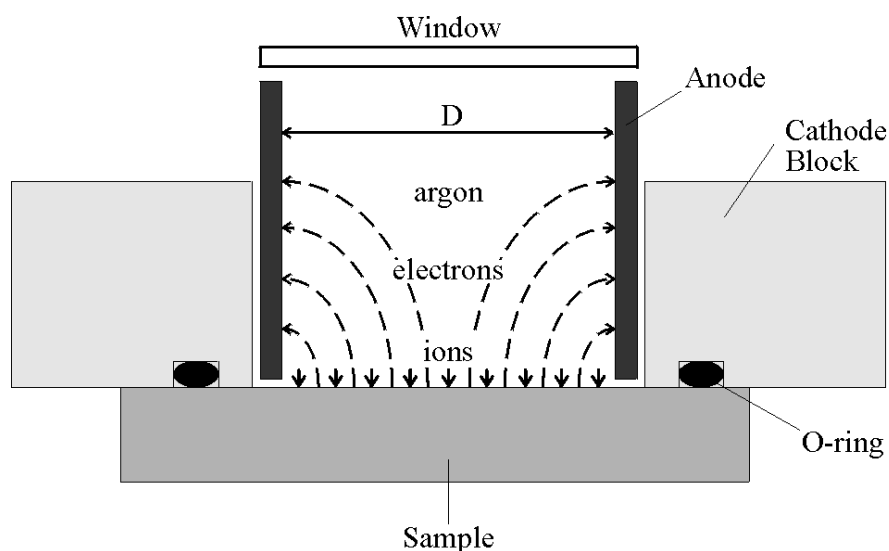


Figure 2.9 Schematic of the Glow Discharge Optical Emission Spectroscopy (GDOES) operating principle.

The GDOES equipment consists of a tubular copper anode, which is brought very close to the solid sample to be analysed. The copper tube is filled with low pressure argon and a voltage is applied between the anode and the sample. The sample is negatively biased relative to the anode i.e. it acts as a cathode. Electrons leave the more negative surface of the sample towards the anode and collide with argon atoms creating positively charged Argon ions and high energy meta-stable argon atoms. The positively charged argon ions are attracted to the negatively biased sample surface. Along the way they have many low energy collisions with other argon atoms, losing

about half of their original energy. Many of the ions are neutralised by collisions but continue travelling towards the sample. When the Ar^+ ions and the Ar atoms strike the sample surface they impart sufficient energy ($>100\text{eV}$) to disrupt atomic bonds and eject atoms and electrons. This process is called *sputtering*. The sputtered atoms fly away from the sample surface and coat themselves on the anode or are removed by vacuum pumps. Away from the sample some of the sputtered atoms have collisions with high energy electrons or meta-stable argon atoms and are excited to high energy states. When they de-excite, they emit characteristic photons normally called as *Glow*. This radiation is analysed with one or more optical spectrometers. By measuring the photon intensities at specific energies, characteristic for electronic transitions between energy levels for a specific atom, the relative amounts of the different atoms can be determined.

The process by which atoms are sputtered from the sample into the discharge where they may be ionised and excited is absolutely fundamental to the utility of glow discharges in quantitative analysis. Key to the success of the technique is that the sputtered material has the same composition as the bulk sample. This is normally true, even though different elements or regions of the sample may be sputtered at different rates, because as sputtering progresses the available area of more easily sputtered species decreases and for bulk samples a steady state is reached in which the sputtered fluxes of various elements have the same stoichiometric ratios as the bulk material.

In a glow discharge, cathode sputtering is used to remove material layer by layer from the sample surface. The atoms removed from the sample surface migrate into the plasma where, they are excited through collisions with electrons or metastable carrier gas atoms.

The technique can provide continuous qualitative and quantitative profiles from the surface ($\sim 10\text{nm}$) down to the substrate (tens of μm). Only a few minutes are needed to obtain the chemical composition of each layer with a depth resolution of some nanometres in ideal conditions.

The characteristic spectrum emitted by these excited atoms is measured by the spectrometer. In this study GDOES in depth concentration profiles were recorded using a LECO 750A spectrometer to examine the subsurface composition of sheet samples in addition to XPS to confirm the depth profiles and precise quantitative measurement over large areas of over 5 mm². The GDOES measurements were performed in corrosion and metal research institute known as Swerea KIMAB AB, in Stockholm, Sweden.*

2.6. References

- [1] V Randle, and O Engler, *Texture Analysis-Macrotecture, Microtexture & Orientation Mapping*, ed Taylor & Francis, (2003).
- [2] P. Van Houtte: *The MTM-FHM Software system Version2 Users Manual* (1995)
- [3] M.N., Blackman, M. and Pashley, D.W.. *Proc. Royal Soc. London. A221*, (1954) p.224
- [4] D J Dingley and Randle, V. J. *Mater.Sci.27*, (1992), p. 4545
- [5] V.Randle, V. *Microtexture Determination*, Institute of Materials, London, 1992.
- [6] B L Adams, *Ultramicroscopy* 67, 1997, p.11
- [7] D P. Field, *ibid.* 67, 1997, p.1
- [8] S I Wright, and B L Adams, *Metall. Trans* 23A, 1992, p.759
- [9] BL Adams, S I Wright, and K Kunze, *Met.Mat.Trans.* 24A, 1993, p.819
- [10] D J Dingley, M Longden, J Weinbren and J Alderman, *Scan Micros.*1, 1987, p.451
- [11] J Mahiu, PhD thesis, Department of materials science and engineering, UGent
- [12] W R Grove, *Philos Trans R Soc* 142, (1852) p 87
- [13] F Paschen *Ann Phys* 50 (1916) p 901
- [14] B Chapman, *Glow discharge processes*. Wiley, New York (1942)
- [15] Marcus RK, *Glow discharge spectroscopies*. Plenum, New York (1942)

* Author would like to acknowledge the support of Prof B. Hutchinson in carrying out these tests.

[16] RK Markus, JAC Broekaert *Glow discharge plasmas in analytical spectroscopy*, Wiley, Chichester, UK (2003)

[17] NH Bings, A Bogaerts, JAC Broekaert *Anal Chem* 76, (2004) p 3313–3336

[18] W. Grimm, *Natur Wiss* 54 (1967) p586

Chapter 3

Surface texture evolution during α - γ - α transformation

In this chapter the possible role of surface energy anisotropy on surface texture evolution is studied. The texture and microstructure of a surface at equilibrium may be related to the behaviour of the surface energy per unit area as a function of crystal orientation. An attempt has been made to show that the surface energy affects the surface texture evolution during transformation in ULC steel alloyed with Si, Mn and Al. Several experimental parameters which could affect the surface texture evolution and its characteristics will be considered. Very little is known about the precise details of the emerging surface texture and microstructure at the metal/vapour interface during α - γ - α phase transformation. This chapter presents an investigation of a number of processing parameters including annealing temperature and time, chemical composition, annealing atmosphere and initial texture.

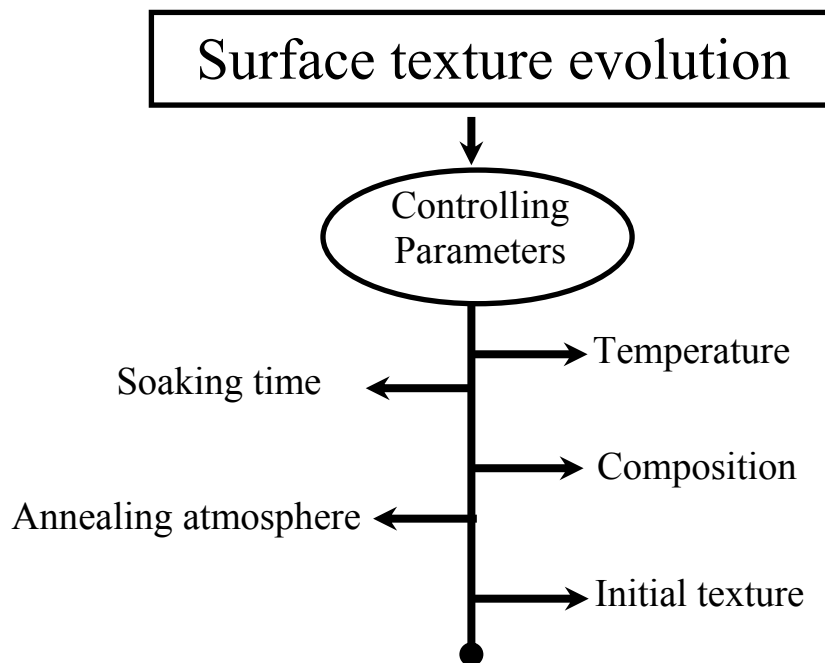


Figure 3.1 Different parameters possibly controlling surface texture evolution.

3.1. Introduction

Phase transformation is a very common and inherent phenomenon in iron and its alloys. Many investigations [1-33] on structure and texture formation associated with austenite (γ) to ferrite (α) transformation have been performed in steels and they can approximately be divided into the following categories:

- (1) Textures developed in columnar ferrite grains [12-16] which are formed by the γ to α transformation due to the decreased transformation temperature during decarburisation or the penetration of foreign atoms from surface to mid section.
- (2) Textures developed on the run-out table of hot rolling in an industrial process [17-22].
- (3) Textures which are formed in cold rolled sheet during annealing in α and γ dual phase region to improve deep drawing properties [23-25]

In category (1), which is of relevance for the present research, a number of results were reported. A single fibre texture with $\langle 001 \rangle$ or $\langle 012 \rangle$ orientations parallel to the ND was developed [12] together with a columnar grain structure after a decarburization treatment of carbon steels. The developed texture was dependent [13-16] on carburizing, decarburizing or surface conditions during transformation. In another study, the texture with $\{100\}$ component produced during $\gamma \rightarrow \alpha$ transformation was reported by applying a H_2S partial pressure during transformation annealing [15]. It has also been reported that the transformation texture with a $\{111\}$ component was formed [14-16] by diffusion of Zn or Al into the steel.

The formation mechanisms of the γ - α transformation texture described above were explained basically by the following theories. One theory considers that in order to decrease the surface energy γ grains of higher metal/vapour interface energy preferentially transform to α and alternatively α grains with the lower surface energy are preferentially formed, thereby developing the texture with $\{100\}$, $\{110\}$ or their neighbouring orientations.

The other theory assumes that the texture develops with a definite orientation relationship between α and γ crystals during transformation, such as e.g. the Young-

Kurdjumow-Sachs relationship which implies the following correspondence $\{111\}_\gamma // \{110\}_\alpha$ — $\langle 110 \rangle_\gamma // \langle 111 \rangle_\alpha$. Either theory has to explain the common phenomenon that the texture of $\{100\}$, $\{110\}$ or their neighbouring orientations develops by γ - α transformation.

However, in another investigation, Hashimoto et al [36] reported a $\langle 100 \rangle //$ ND texture was formed rather than the usual $\langle 111 \rangle //$ ND fibre texture, during α - γ - α phase transformation in an ultra low carbon cold rolled steel sheet. They interpreted this experimental result by assuming that the elastic work in the ND direction associated with the transformation could be larger than that in any other direction.

In a study, performed by Yoshinaga et al [31,32] on α - γ - α transformation in ultra low carbon steel and IF steel with and without manganese, two important results were observed. A stronger γ fibre was observed in the final texture in the bulk of the sheet in comparison with the samples that were simply recrystallisation annealed in the full ferrite domain. This was attributed to the *texture memory effect* which was further developed by Hutchinson et al [33]. According to the texture memory phenomenon the high temperature austenite phase abounds in neighbouring grains that have nucleated in one common parent ferrite grain. Afterwards, on back transformation from austenite to ferrite, the new ferrite nuclei, which predominantly appear at the austenite GBs, will revert to the *common* ferrite parent orientation of the two austenite grains because only this specific ferrite nucleus orientation allows for a double YKS interface with the two neighbouring austenite grains. That a double YKS interface at either side of the austenite grain boundary is a facilitating factor in nucleation during phase transformation has been demonstrated in great detail by Landheer et al [34].

In the same report Yoshinaga et al [31] also noticed an outer surface texture with a strong rotated cube orientation which was completely different from the γ fibre in the bulk texture. Although this phenomenon was attributed to a surface energy effect at the metal vapour interface, detailed features and parameters of this phenomenon have not been explored extensively. In the present study an attempt has been made to

explore the controlling parameters for surface texture and microstructure evolution during α - γ - α transformation.

3.2. Experimental procedure

Seven different chemical compositions were investigated which include pure iron and six other iron alloys listed in table 3.1. The first alloy is ultra low carbon steel which is the base alloy named as ULC. In addition the alloys MnAl1 and MnAl2 are ULC base compositions alloyed with low and high manganese and aluminium respectively. The other two alloys named as Si1 and Si2 are also ULC base compositions alloyed with low and high amounts of silicon. The last steel composition, denominated LC, is a low carbon steel (with higher carbon concentration than the other alloys) alloyed with comparatively minute concentrations of Mn, Si and Al, cf. table 3.1. The critical temperatures are listed in table 3.2 which were derived from the dilation curves obtained after several heating and cooling experiments performed in dilatometer for heating rate 15°C/s and 30°C/s.

Table 3.1 The chemical compositions (wt.%)

	C	Mn	Si	Al
ULC	0.002	0.15	0.005	0.055
MnAl1	0.003	0.75	0.23	0.12
MnAl2	0.002	1.28	0.22	0.29
Si1	0.002	0.33	0.510	0.13
Si2	0.002	0.34	1.38	0.11
LC	0.047	0.46	0.17	0.037

Table 3.2 Critical temperatures (°C)

Alloys	Ac1	Ac3	Ar3	Ar1
MnAl1	949	1000	910	845
MnAl2	940	990	884	832
Si1	1070	1100	940	880
Si2	1030	1050	975	940
LC	850	925	825	650

The alloy MnAl1 and MnAl2 were casted and hot rolled in the laboratory, whereas the alloys Si1, Si2 and LC were received as a hot rolled sheet from the industrial partner. The hot rolled sheets of all the alloys were further cold rolled till 0.5mm in final thickness with 75% cold reduction. The samples were prepared for several experiments from the properly degreased and acetone cleaned cold rolled steel sheets of all alloy compositions. Afterwards, these samples were subjected to different transformation annealing experiments carried out mainly in the pyrox tube furnace

(cf. Chapter 2). Figure 3.2 shows five parameters which have been selected to investigate their potential to control the surface texture. A number of steel sheets were heated to different temperatures: (i) below the Ac1 temperature, (ii) in between Ac1 and Ac3 temperatures and (iii) above the Ac3 temperature. In addition to that, different annealing atmospheres and various soaking times above the Ac3 temperatures were also investigated. Different initial textures were also prepared to investigate their effect on surface texture evolution.

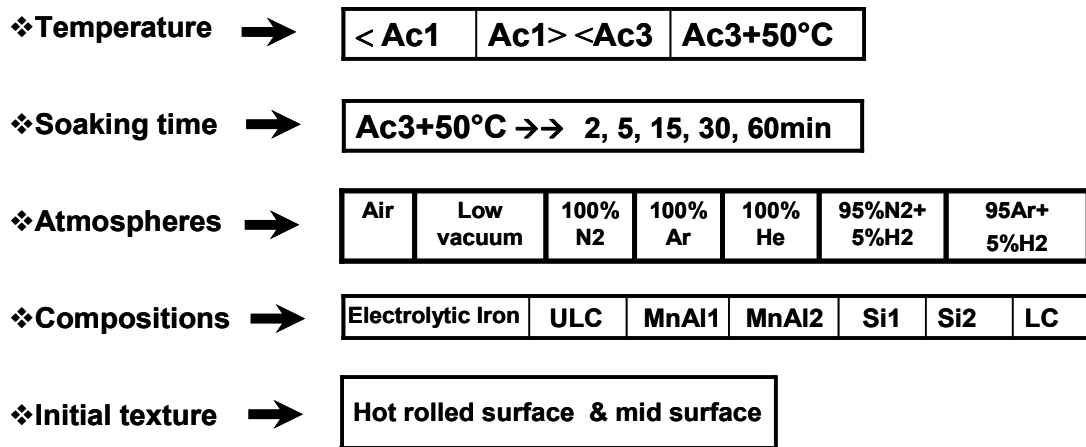


Figure 3.2 Different parameters studied to control surface texture evolution during annealing of a cold rolled sheet.

3.3. Results

X-ray diffraction texture analysis is well known and widely accepted for bulk texture measurements in steel. This technique was employed to measure the texture on the outer surface of the cold rolled sheet subsequently after transformation annealing. X-ray texture data analysis was performed and orientation distribution functions were calculated with the help of the MTM-FHM software [35]. Orientation imaging microscopy was also performed on the through thickness section of the annealed sheet of selected samples to observe changes in the grain structure on the edge and in the bulk of the samples.

3.3.1. Effect of annealing temperature

Different annealing temperatures were investigated corresponding to the recrystallisation, intercritical and fully austenite zone of the laboratory cast alloys MnAl1 and MnAl2. For these steels the critical temperatures during heating (Ac1 and Ac3) and cooling (Ar3 and Ar1) were determined by dilatometer tests on standard cylindrical steel samples with 5 mm in diameter and 10 mm in length. Subsequently, these cylindrical samples were heated with a heating rate of 10°C/s in the dilatometer under vacuum conditions of 10⁻⁶ Torr. The dilatation curve for the alloys MnAl1 and MnAl2 obtained during heating are shown in figure 3.2. These curves show a decrease of length at 939°C for the alloy AlMn1 and at 946°C for the alloy MnAl2. This is the Ac1 temperature at which phase transformation has started in these alloys. The same dilatation curves show that the full austenite phase is achieved at 1,000°C which is well above the Ac3 temperature for these alloys. Based on these critical temperatures three annealing experiments were performed in the pyrox tube furnace under low vacuum condition of 10⁻⁴ Torr at three different temperatures representing the three different phase domains as shown in the schematic figure 3.2

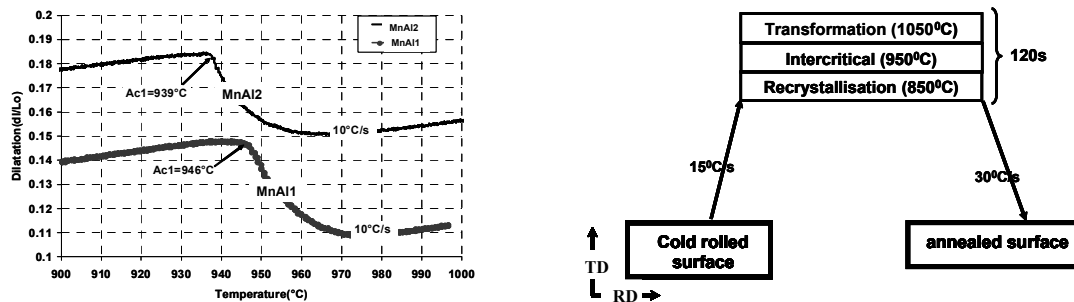


Figure 3.3 The dilation curves during heating for the alloy MnAl1 and MnAl2 (left) and schematic of annealing treatment at different temperatures (right).

3.3.1.1 Microstructure and texture after ferrite recrystallisation

The two alloy composition MnAl1 and MnAl2 were subjected to a ferrite recrystallisation annealing treatment at 800°C. Figure 3.4 shows the bulk microstructure consisting of a single ferrite phase with equi-axed grains with an average grain size of approximately 15 μm . Figure 3.4 also shows the texture measured at the sample surface after cold rolling and the annealing textures at the surface and in the midlayer section. The cold rolled sheet exhibits the conventional α ($\langle 110 \rangle // \text{RD}$) / γ ($\langle 111 \rangle // \text{ND}$) -fibre texture which is commonly observed after cold reductions of the order of 70 to 80% as in the present case. After annealing, the bulk texture observed in the mid thickness layer has converted to the typical γ -fibre recrystallization texture which is characteristic for deep drawing steels. Small differences have been observed between the high and low Mn steel as the latter exhibits an increased residual intensity on the α -fibre and a maximum on the $\{111\} \langle 110 \rangle$ component at the cross section of the α and the γ -fibres while the former displays a more isotropic γ -fibre with less residual intensity on the α -fibre. The surface textures are somewhat weaker than the bulk textures. The low Mn material (MnAl1) is still characterized by a predominant γ -fibre with a wide intensity spread towards the α -fibre, though. The high Mn material (MnAl2), on the other hand, displays a slightly stronger α -fibre intensity and additionally some intensity spread towards the Goss component ($\{110\} \langle 001 \rangle$)

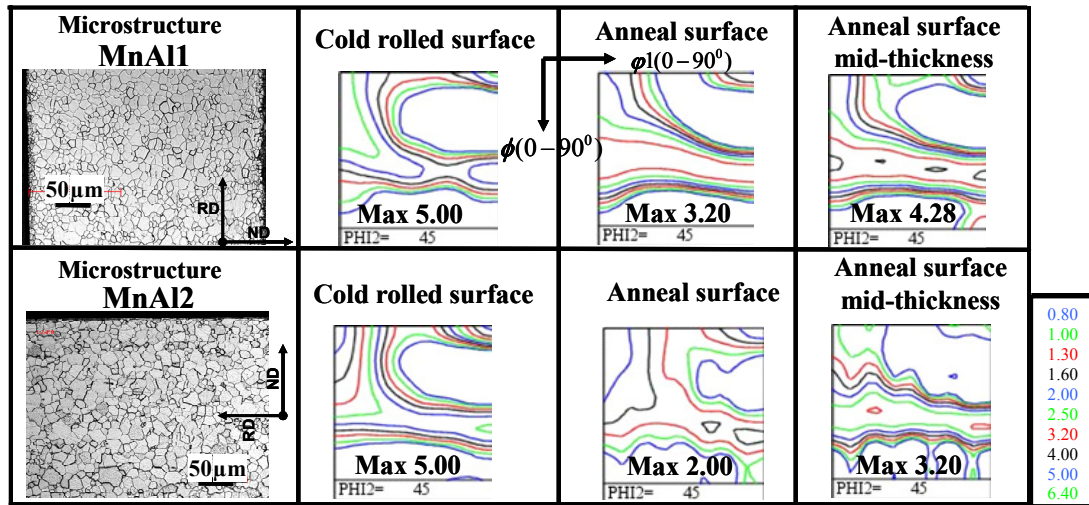


Figure 3.4 Optical micrographs and $\phi_2=45^\circ$ sections of textures recorded on RD-TD surface after recrystallisation of the alloy MnAl1 (top) and MnAl2 (bottom).

3.3.1.2. Microstructure and texture after inter-critical annealing

Figure 3.5 shows the microstructures and textures obtained after inter-critical annealing of alloy MnAl1 and MnAl2. The optical micrographs of figure 3.5 show the partially transformed microstructure for both alloys. The grains size is $\sim 40 \mu\text{m}$ and these grains show protrusions at grain boundaries which may have partially transformed to austenite and later, during reverse transformation have transformed back to ferrite. Figure 3.5 also displays the X-ray textures measured on the sheet surface after cold rolling and the texture measured at the surface, sub-surface (i.e. 5% underneath the outer surface) and in the mid-plane after intercritical annealing. The cold rolled surface texture shows the typical α/γ fibre which is the conventional texture fibre after 70% cold rolling. After inter-critical annealing at 970°C the texture measured at the annealed surface of both alloys MnAl1 with low manganese and MnAl2 with high manganese show weak textures with maxima of approximately 2 levels of random intensity. The $\phi_2=45^\circ$ section contains a wide spread of all the major texture components in both alloys. The $\phi_2=45^\circ$ section of the annealed subsurface of alloy MnAl2 with high manganese exhibits a strong γ -fibre with a maximum intensity

of 5 times random. The other alloy MnAl1, with low manganese, also shows a γ -fibre but of slightly weaker intensity. The $\phi_2=45^\circ$ sections of the annealed subsurface of both alloys also show the presence of a weak cube fibre and a slightly stronger Goss component. The textures measured at the mid thickness plane of both alloys show a stronger γ -fibre than the subsurface. The alloy MnAl2 with higher Mn content exhibits a slightly stronger γ -fibre at the subsurface and in the mid plane in comparison to alloy MnAl1 with lean Mn and Al.

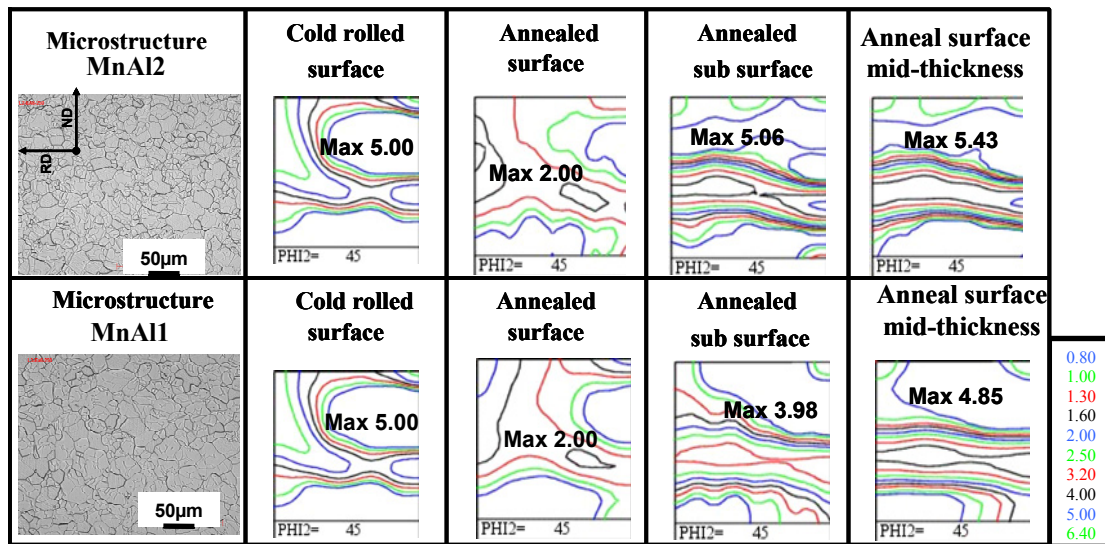


Figure 3.5 Optical micrographs and $\phi_2=45^\circ$ sections of textures examined on RD-TD surface of intercritically annealed sheet of alloy MnAl2 (top) and MnAl1 (bottom).

3.3.1.3. Microstructure and texture after transformation annealing

The alloy composition MnAl1 and MnAl2 were subjected to transformation annealing in the full austenite domain at 1,050°C. Figure 3.6 shows the bulk microstructure consisting of a single ferrite phase with an average grain size of approximately 50 μm which is larger than the recrystallised ferrite grain size (15 μm). Figure 3.6 also shows the texture measured at the sample surface after cold rolling and at the surface, subsurface and in the midlayer section after transformation annealing. The cold

rolling exhibits the conventional α/γ -fibre texture which is commonly observed after cold reductions 75% as in the present case.

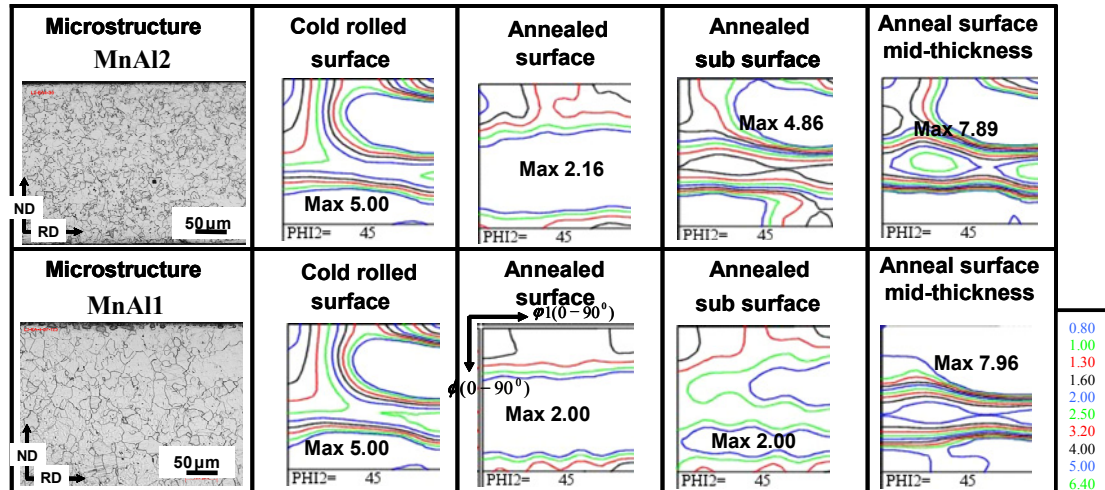


Figure 3.6 Optical micrographs and $\phi_2=45^\circ$ sections of textures examined by XRD on the RD-TD surface of transformation annealed sheet of alloy MnAl2 (top) and MnAl1 (bottom).

After complete transformation annealing, the $\phi_2=45^\circ$ section of the measured surface texture shows components like cube and Goss in both alloys with low and high manganese additions. Contrastingly, the γ -fibre is completely absent from the surface after complete transformation which is an obvious difference from the samples observed after recrystallisation and after intercritical annealing. The intensity of the surface texture components is weak, though, exhibiting a maximum of ~ 2 times random. After removing 5% material from the surface, the sub-surface was examined and the measured texture shows a strong γ fibre in the alloys MnAl2 with high manganese content. On the other hand, in the alloy MnAl1 with low manganese the measured subsurface texture shows that the cube and Goss components are still present, together with a weak γ fibre. This suggests that the surface texture in alloy MnAl1 (with low Mn) has a deeper penetration than the alloy MnAl2 with higher manganese. Because removing 5% from the surface of a 500 μm thick sheet

corresponds to $25\mu\text{m}$ it can be concluded that in the MnAl2 alloy the cube/Goss dominant texture extends to $25\mu\text{m}$ away from the surface. The detailed characterization of the surface texture is discussed separately in Chapter 6. The texture measured in the mid plane surface shows a strong γ -fibre in both alloy compositions MnAl1 and MnAl2, which reflects the typical texture memory effect observed by Yoshinaga et al [31, 32] and Hutchinson et al [33].

3.3.2. Effect of soaking time during phase transformation annealing

The effect of different soaking times during phase transformation annealing was investigated only in alloy MnAl1. Five different annealing times (120s, 300s, 900s, 1800s and 3600s) were applied at a temperature of 50°C above A_{c3} . Five samples listed in table 3.1 were prepared from the cold rolled sheets with initial surface texture as shown in figure 3.7.

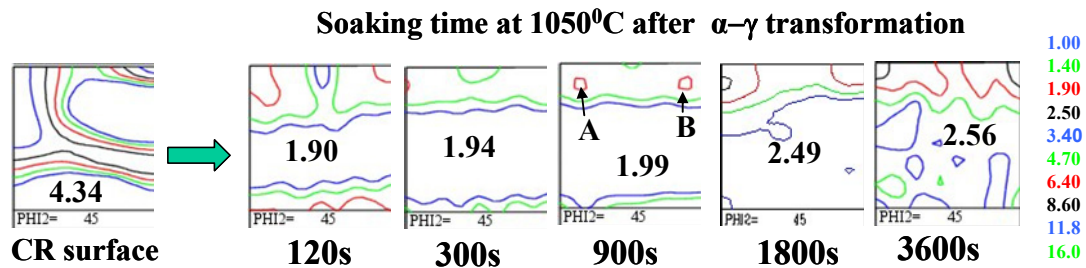


Figure 3.7 $\varphi_2=45^\circ$ sections of surface textures examined by XRD on the RD-TD surface of cold rolled sheets and annealed sheets of alloy MnAl1 annealed at $A_{c3}+50^\circ\text{C}$ for different soaking time.

After phase transformation with different soaking time the annealing textures were measured by conventional XRD and the results are presented in figure 3.7. The $\varphi_2=45^\circ$ sections reveal that the surface textures persistently consist of cube fibre and Goss fibre components with minor intensity variations. It is important to note that the intensity of the Goss fibre components decrease slightly up to 900s of soaking time and then disappear after 1,800s and 3,600s of soaking time. In general it can be seen that the surface texture appears with an intensity of approximately 2 times random on

the cube and Goss fibre after 120s of soaking time, whereas on extended annealing the Goss fibre components start to disappear and after 3,600s other components start appearing on various locations of Euler space, although there does not seem to be much of a pattern and the intensities remain very weak. Something which may be of significance, in light of the analysis that is presented in Chapter 6, are the small local maxima that are present after 900s of annealing some 10° away from the cube fibre at $\Phi = 10^\circ$ (indicated, A, B in Figure 3.7)

3.3.3. Effect of annealing atmosphere during phase transformation annealing

The cold rolled sheets from the alloys MnAl1 and MnAl2 were annealed under controlled atmosphere according to the thermal cycle shown in figure 3.3 with two different heating rates and cooling rates as different types of furnaces were employed to allow for an optimum atmosphere control. Particularly the use of a resistance heating muffle furnace allows only for rather small heating and cooling rates.

Table 3.3 Different annealing atmospheres with different furnace types and corresponding heating and cooling rates.

Furnace	Heating mode	Annealing atmosphere	Cooling atmosphere
Rhesca (A)	Infrared radiation	Vacuum	Nitrogen(95%)+ Hydrogen (5%)
Pyrox (A)	Graphite resistance	Vacuum	vacuum
Pyrox (A)	Graphite resistance	Air	Air
Pyrox (A)	Graphite Resistance	Argon	Argon
Gleeble simulator (A)	Resistance	Nitrogen	Nitrogen
Gleeble simulator (A)	Resistance	Argon(95)+ Hydrogen (5)	Argon(95)+ Hydrogen (5)
Muffle furnace(B)	Resistance	Nitrogen	Nitrogen
Muffle furnace (B)	Resistance	Nitrogen (95)+ Hydrogen (5)	Nitrogen (95) +Hydrogen (5)

(A) Heating rate @15 °C/sec
(A) Cooling rate @ 30 °C/sec

(B) Heating rate 2 °C/min
(B) Cooling rate 4 °C/min

Table 3.3 includes the various employed furnace types, the applied annealing atmosphere during heating, soaking and cooling and the mode of heating. Cold rolled sheets of alloys MnAl1 and MnAl2 were transformation annealed in atmospheres containing nitrogen (neutral gas), argon (inert gas) or hydrogen (reducing gas). The gases used in this annealing experiments were either pure, or mixed in the proportions shown in Table 3.3. Initially, the furnace annealing atmosphere was kept under a vacuum of 10^{-4} Torr. Later, gases were introduced in dry conditions. Hence, according to theoretical calculations, the dew point for all transformation annealing was approximately -54°C .

The annealed surfaces were examined in the X-ray texture goniometry. The $\varphi_2=45^{\circ}$ sections of the ODF's are shown in figure 3.8. In this figure the first three ODFs of samples MnAl1 and MnAl12, denominated as "A" display the surface texture after fast heating ($15^{\circ}\text{C}/\text{sec}$) and cooling ($30^{\circ}\text{C}/\text{sec}$) whereas the last two ODFs, denominated as "B", show the surface texture after a slow heating ($2^{\circ}\text{C}/\text{min}$) and cooling rate of ($4^{\circ}\text{C}/\text{min}$). The surface textures denoted as A in figure 3.8 after fast heating and cooling in controlled atmospheres (nitrogen, argon and argon mixed with 5% hydrogen) are quite similar with minor variation in the surface texture components and in their intensity. The $\varphi_2=45^{\circ}$ sections of the measured surface texture for both alloys MnAl1 and MnAl2 exhibit a cube fibre along with the Goss orientation. It is also important to note that cube fibre is slightly stronger than the Goss components.

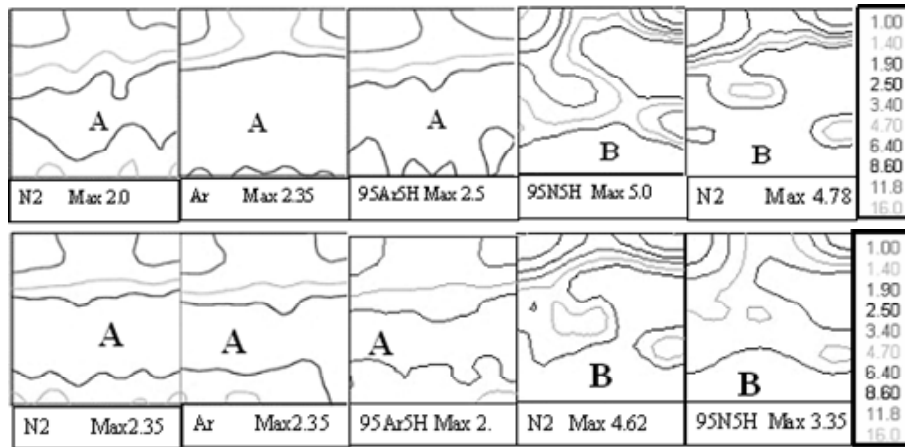


Figure 3.8 ODFs in $\varphi_2=45^\circ$ sections of alloys MnAl1 (top) and MnAl2 (bottom) Samples marked with A are obtained during transformation annealing in controlled atmosphere with fast heating and cooling and ODFs marked with B are processed with slower heating and cooling rates.

Figure 3.8 also shows the $\varphi_2=45^\circ$ sections, denoted as B, measured after transformation annealing in controlled atmosphere (nitrogen and nitrogen with 5% hydrogen) but with slower heating and cooling rates. The surface texture displays a relatively strong cube component along with a weak γ -fibre and without Goss components. In the previous experiments with longer soaking times (1,800s or 3,600 min) of transformation annealing it was observed that the Goss components disappears and simultaneously other components start appearing. Hence, in the same fashion in the present experiment the appearance of the γ -fibre and the loss of the Goss component may be due to the very slow heating and cooling rate. In a similar experiment with much slower heating and cooling rate (50°C/hr) performed by Hashimoto et al and only the cube fibre has been reported [36].

To the purpose of a more complete characterization, the samples (denoted as B) were further examined by orientation imaging microscopy. The through thickness microstructures, in form of inverse pole figure maps, are shown in figure 3.9. These through thickness microstructures show two distinct grain structures and morphologies.

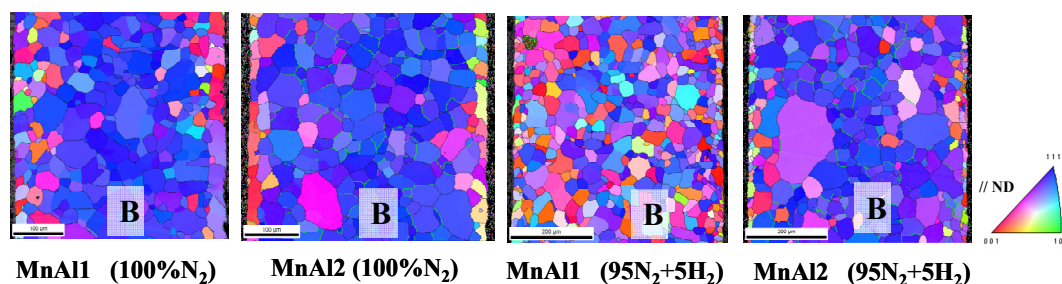


Figure 3.9 Inverse pole figure maps after annealing with slow heating ($2^{\circ}\text{C}/\text{min}$) and cooling rate ($4^{\circ}\text{C}/\text{min}$) in controlled atmosphere (nitrogen and nitrogen mixed with hydrogen).

The grains along the edge show a rather red colour whereas the rest of the grains in the bulk (i.e. away from the surface) are rather blue. The red grains are linked to cube fibre grains whereas the blue coloured grains represent the $\{111\}$ fibre grains. The grain morphology at the edge as well at the RD-TD surface is very unique and discussed in more detail in chapter 6. It can also be observed that some red grains are present in the bulk of the sheet if annealed under a 95N_2 - 5H_2 atmosphere. This, however, cannot be responsible for the increased intensity of the cube type surface texture in slowly heated material (B samples) because all B samples exhibit this increased intensity, also the ones that were annealed in the neutral nitrogen atmosphere. Under the present experimental conditions it can be concluded that the effects of annealing atmosphere on the development of the surface texture are outweighed by the effect of the heating rates and soaking times.

3.3.4. Effect of alloy composition on surface texture evolution

Seven alloy compositions, including pure iron (electrolytically deposited) and a base alloy of ultra low carbon steel, cf. Table 3.1, were selected to investigate the effect of alloy composition on surface texture evolution. The cold rolled steel surfaces of all the selected alloys were subjected to a similar thermo-mechanical history. The cold rolled sheets of these alloys were subjected to a similar transformation annealing at the $\text{Ac}_3+50^{\circ}\text{C}$ temperature of the alloy composition under investigation. The

laboratory cast alloys MnAl1, MnAl2 and base materials (pure iron and ultra low carbon steel) were transformation annealed at 1050°C because these alloys exhibit a narrow range of critical temperatures. The sheet surface texture before and after annealing was examined by X-ray diffraction. Subsequently, the same sheet sample was also characterized by orientation contrast microscopy (EBSD-OIM). The $\varphi_2=45^\circ$ sections and inverse pole figure maps are shown in figure 3.10a and 3.10b.

The $\varphi_2=45^\circ$ ODF sections measured on the cold rolled surface of all alloys are shown in figure 3.10a. These $\varphi_2=45^\circ$ sections show the typical α/γ fibre rolling components which normally appear after 70 to 80 % of rolling deformation, although they are of somewhat weaker intensity than what is normally observed in the bulk of the sheet. The maximum intensity of the α fibre lies on the $\{001\} \langle 110 \rangle$ component. After transformation annealing the $\varphi_2=45^\circ$ sections of the first four alloys, i.e. pure iron, ULC steel, MnAl1 and MnAl2, show the specific surface texture with cube fibre with the maximum intensity of ~ 3 times random. The inverse pole figure maps of the corresponding four alloys display a remarkable difference in the grain structure across the thickness of the annealed sheet. For the pure composition (electrolytically pure and ULC) it appears that surface grains have grown inwards and consumed the bulk of the sheet in a columnar fashion.

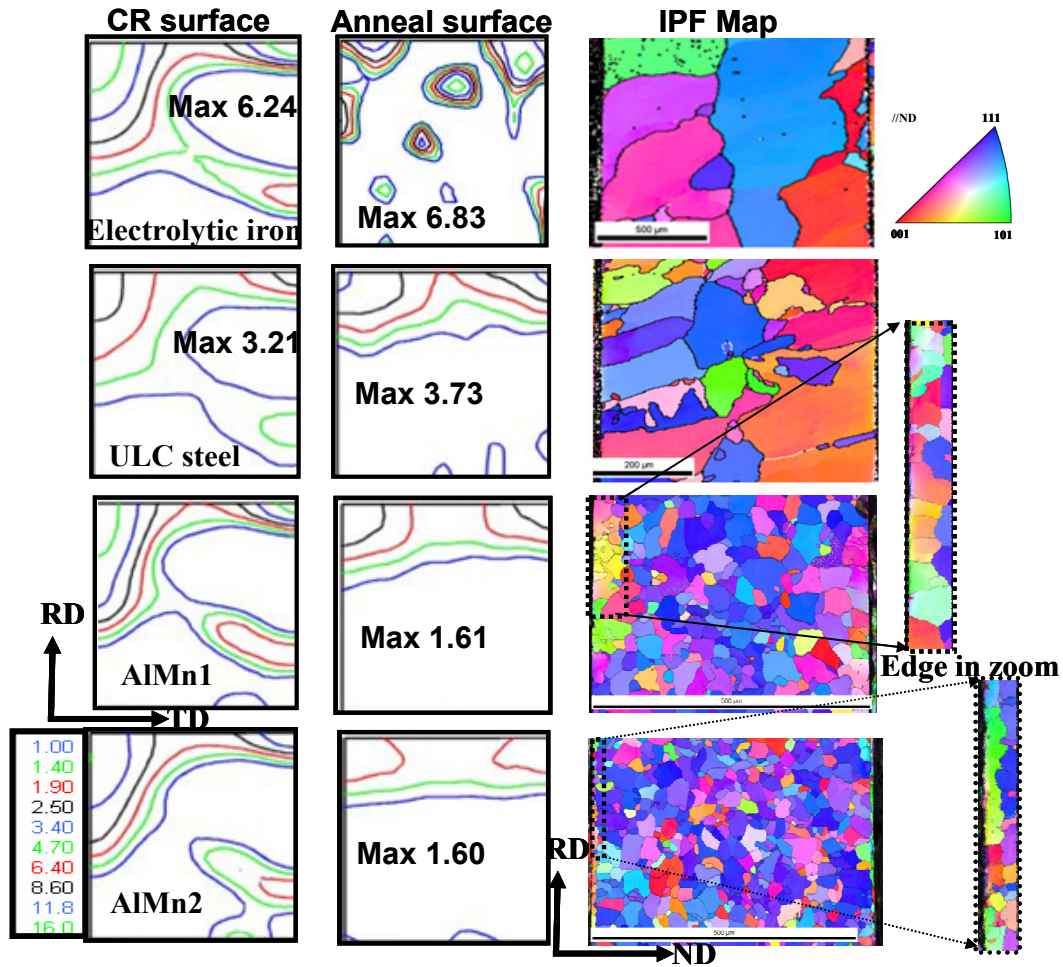


Figure 3.10a $\varphi_2=45^\circ$ sections of x-ray measured textures and inverse pole figure maps obtained from EBSD analysis on samples of different alloys.

In the laboratory cast alloys MnAl1 (low Mn) and MnAl2 (high Mn) a similar columnar grain structure appears, but it remains confined to the surface extending only down 15 to 30 microns towards the bulk.

The industrial alloys Si1 with low silicon, Si2 with high silicon and LC (low carbon) were subjected to different transformation annealing temperatures (1100, 1150 and 950°C). These annealing temperatures were well above the A_{c3} temperatures as listed in table 3.2. The $\varphi_2=45^\circ$ sections in figure 3.10b display the γ fibre texture for alloys Si1 and Si2, which is contrary to all other ultra-carbon alloys, whether or not Mn/Al

alloyed. The low-carbon steel, alloy LC, shows a mixed behaviour with a strong cube fibre together with the γ -fibre. The corresponding inverse pole figure maps of these Si alloys do not reveal special edge grains as is the case for the first four alloys.

The seven alloy compositions can be classified in four types. The first two alloys, electrolytically pure iron and the ULC steel are base alloys without intended alloying elements. These alloys display a surface texture with a cube fibre which has extended across the entire thickness of the annealed sheets, growing inwards from both surfaces and thus having produced a truly columnar structure. The following two alloys are Mn and Al added ultra-low carbon steels. After transformation annealing these alloys display a surface texture with a cube fibre but also with a unique surface grain structure which is confined to a single mono-layer of grains near the edge of the sheet. It is also noteworthy that alloy MnAl1 with less manganese and aluminium has a thicker edge layer that extends over approximately 30 μ m as compared to alloy MnAl2 with more added manganese and aluminium produced a thinner layer of monolayer cube fibre grains only spreading ~ 15 into the bulk. The monolayer surface grains seem to extend in the through thickness during annealing with increasing Ac3 temperatures.

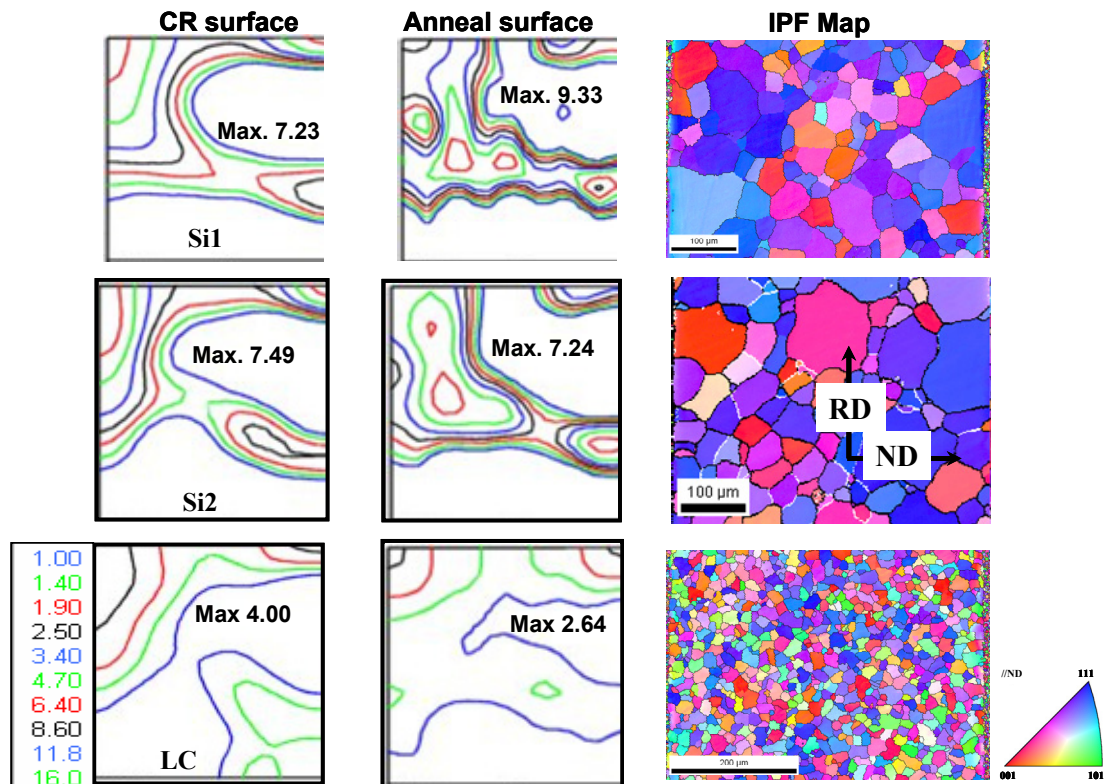


Figure 3.10b $\phi_2=45^\circ$ section of x-ray measured textures and inverse pole figure map obtained from EBSD analysis on transformation annealed samples of different alloys.

The third set of alloys includes the Si added ULC steels Si1 (low silicon) and Si2 (high silicon). They do not show the surface texture with cube fibre grains and there is no distinct monolayer of surface grains at the edge. The low carbon steel with 0.05wt % of carbon content, alloyed with low manganese (0.46wt %) and less silicon (0.17 wt %) represents a separate case. It shows a mixed surface texture with γ -fibre and cube fibre grains and it is difficult to assert whether or not the cube fibre grains are present as a monolayer of surface grains as was the case for the Al/Mn added ULC steels.

3.3.5. Effect of Initial texture on surface texture evolution

So far the transformation annealing was performed on the cold rolled steel surface with typical rolling textures exhibiting α/γ fibre morphology. This was the initial texture prior to transformation annealing but in this section an attempt was made to create different initial textures prior to transformation annealing. To this purpose different sheets samples of alloy MnAl1 were selected which were obtained after different thermo-mechanical treatment.

The hot rolled sheet of 2 mm in thickness was employed to prepare two different types of initial surface textures. Hot rolled sheets, in general, have a heterogeneous texture across the thickness. Figure 3.11 shows the inverse pole figure map of the entire through-thickness section of the hot rolled sheet of alloy MnAl1 with low manganese and aluminium. Three samples were prepared by removing 10, 15 and 50% of the steel sheet from one side by mechanical polishing as shown in figure 3.11. Subsequently, these sheets were subjected to typical phase transformation annealing after the surface texture was examined by XRD.

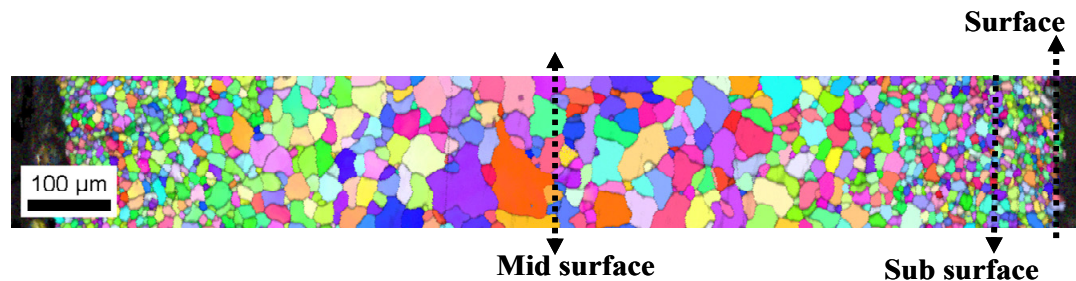


Figure 3.11 Inverse pole figure map across the thickness of a hot rolled sheet of alloy MnAl1.

Figure 3.12 shows the $\varphi_2=45^\circ$ sections of the ODF calculated from the measured pole figure before and after transformation. The hot rolled sheet sample with 10% and 15 % of the initial thickness removed exhibit shear components at the *new* surface texture, whereas the sheet with 50 % of the initial thickness removed exhibits a more conventional hot band texture. After transformation the X-ray texture results exhibit the typical surface textures with cube fibre as shown in the figure 3.12. The $\varphi_2=45^\circ$

sections of figure 3.12 reveal that the initial shear texture transforms to the surface texture with stronger cube fibre (i.e. with higher intensity of 3 to 4 times random) in comparison to the product texture observed in the material of initial γ fibre texture. The latter only gives rise to a surface texture with cube fibre intensity of ~ 2 times random. It is well-known that by applying the YKS orientation relations the BCC shear texture (with $\{110\}$ and $\{112\}\langle 111\rangle$ components) reverts to the FCC $\langle 111\rangle//ND$ and $\langle 110\rangle//RD$ fibre texture, whereas the BCC γ -fibre texture is transformed to the $\langle 110\rangle//ND$ fibre texture upon phase transformation.

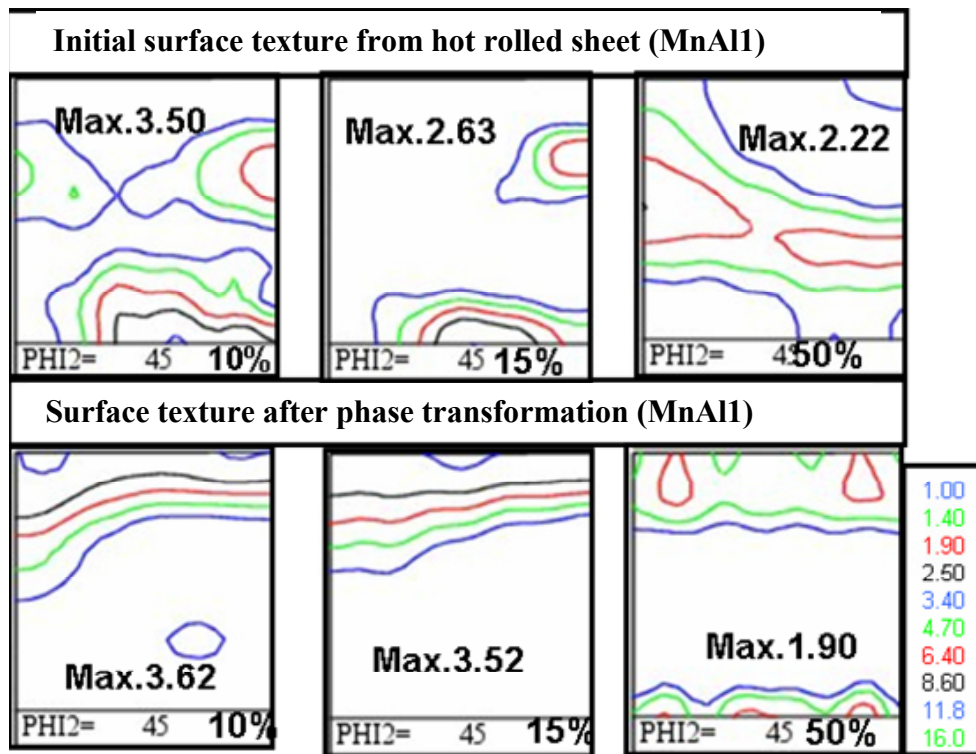


Fig.3.12 The $\varphi_2=45^\circ$ sections (top) with different initial textures obtained from hot rolled sheet sections mechanical polished 10, 15 and 50% of alloy MnAl1 and the $\varphi_2=45^\circ$ sections measured by x-ray diffraction on the same surface after transformation annealing.

3.4. Discussion

It is obvious from the literature data that the development of the surface texture during transformation annealing is strongly affected by the anisotropy of the metal/vapour interface energy in such a way that low energy surfaces are selected during back transformation from austenite to ferrite and this fact has been reported by several authors [26-33] but there is no clear evidence about the parameters, which could be responsible for surface texture evolution and its characteristics.

It has been identified that a complete phase transformation is necessary for specific surface texture evolution instead of recrystallisation or intercritical annealing. The complete phase transformation offers an additional degree of freedom for orientation selection in the sheet sample as the orientation selection during phase transformation is of considerably larger variability than the orientation selection during recrystallization. Whereas during nucleation of newly recrystallized grains in the deformed matrix there is a one-to-one relation between the nucleation site and the newly formed nucleus, this is not the case for a phase transformation as one parent grain may give rise to 24 potential product nuclei when the YKS orientation relations are considered (and 12 product equivalents for the NW correspondence). It is clear that this wider variability is required in order to introduce sufficient random orientations so that the mechanism of surface texture anisotropy can play its role.

The fact that the $\{100\}$ and $\{110\}$ oriented grains are only observed as a monolayer of (outer) surface grains represents convincing evidence that these grains are the results of a typical metal/vapour interface phenomenon and not a (sub-) surface effect which gradually plays its role from the bulk towards the surface such as the release of transformation stresses in the vicinity of the surface. The latter phenomenon should also play a role in grains that are immediately underneath the outer surface monolayer.

The outer surface grains tend to grow towards the bulk of the material and extend the specific surface texture towards the bulk. This is particularly the case for the very pure chemical compositions such as the electrolytic pure iron and the ULC steel

(commercially pure iron). The fact that surface grains rapidly grow towards the bulk of the sheet during back transformation indicates that the growth of surface ferrite into bulk austenite is the dominant (back) transformation mechanism rather than nucleation of new ferrite grains in the bulk of the sheet. This is only possible when the activation energy for interface migration is lower than the activation energy for nucleation of new ferrite grains. In general it could be observed that the surface grains showed an increasing tendency to grow towards the bulk with an increasing Ar3 temperature and thus back transformation occurring at increased temperatures where the interface mobility (which is exponentially temperature dependent following Arrhenius behaviour) is much higher than in the less pure compositions with a more extended intercritical domain. This tendency is confirmed for the laboratory processed grades electrolytic pure iron, ULC, MnAl1 and MnAl2 (with decreasing extension of the surface layer), but not for the Si added steels Si1 and Si2. The latter behaviour may have its specific reasons which are presumably related to internal oxidation at subsurface layers which is a well-known property of Si added alloys (cf. chapter 4).

Another peculiarity of the observed surface texture is that in most cases the cube fibre is the stronger one, whereas the Goss fibre represents the weaker part. According to the Wulff diagram of the iron crystal surface anisotropy the {110} planes have the lowest energy whereas {001} planes exhibit somewhat larger energy. Thus, one would expect a more dominant {110} surface texture. The fact that this was not observed may have been caused by various reasons. First of all, the presence of adsorbed impurity elements at the surface may have reversed the order of lowest surface energy. We do not have proof that this has played a role here, although we observed very little effect of the annealing atmosphere which may indicate the role of impurity elements is limited in this case.

The 2nd factor that might have played a role in the balance between the {110} and {001} fibre texture is the nature of the initial texture prior to transformation. As already mentioned the appearance of transformation textures is generally explained in terms of specific orientation correspondences between parent and product orientations

such as e.g. the YKS orientation relation. The appearance of a product texture is the result of the activation of a selection mechanism on a parent texture. It might be possible that orientation A is heavily favoured by the selection mechanism at the expense of orientation B, but if the genetic precursor of orientation B is a majority component compared to the genetic precursor of orientation A then orientation B still may be dominant in the product texture, even though it was less favoured. It is difficult, though, to quantify this concept in the present experiment as one ignores the high temperature austenite surface texture which is the parent texture of the ferrite surface texture.

Figure 3.12 represents a model calculation which simply reproduces the texture evolution during α - γ - α transformation if only the YKS rules are active. By applying the YKS transformation operator ($\{111\}_\gamma // \{110\}_\alpha$ and $\langle 110 \rangle_\gamma // \langle 111 \rangle_\alpha$ which is equivalent to $\langle 112 \rangle_{90^\circ}$ on the initial ferrite the high temperature austenite texture can be modelled and subsequently, by applying the same operator on the austenite texture, the product ferrite texture can be modelled. It can be seen on figure 3.13 that this double YKS transformation (i) gives rise to a weakening of the texture and (ii) reproduces the initial ferrite texture, but with reduced intensities. For the model calculations of figure 3.13 the initial textures were used of the hot band MnAl1 steel, cf. figure 3.12.

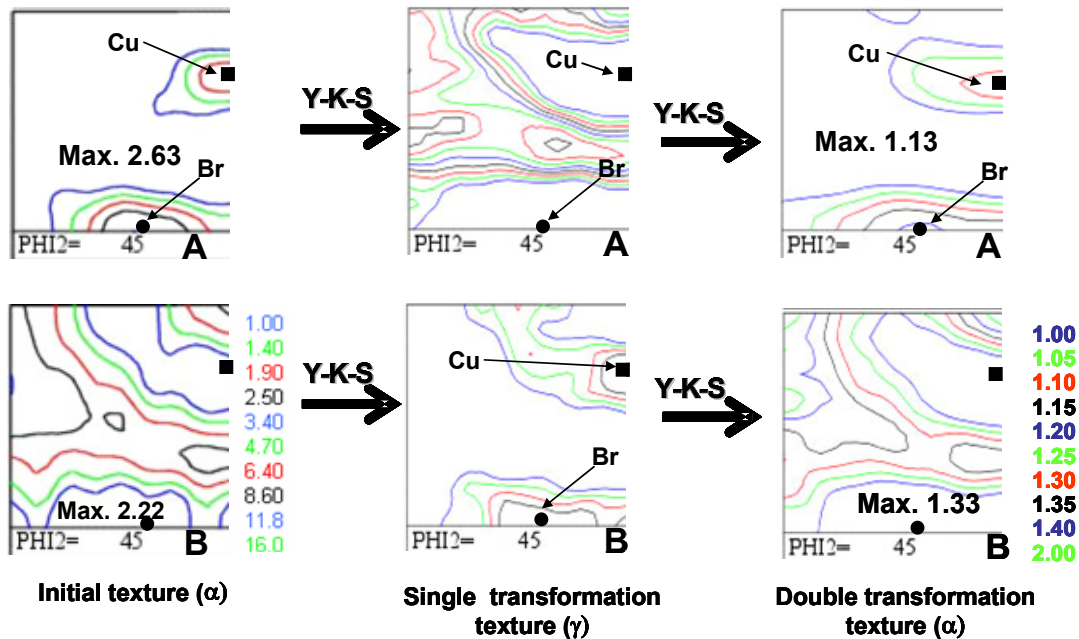


Figure 3.13 Two different initial textures from the hot band of the alloy MnAl1 for sub surface (top) and the mid thickness (bottom) modelled for double phase transformation by applying the Y-K-S relations.

As it has already been mentioned before various sources of variant selection might drastically change the orientation selection as predicted by the YKS orientation relationships. In the present case the following mechanisms of variant selection might have played a role:

- (i) Surface energy anisotropy. This may have affected both the forward (α - γ) and the backward (γ - α) transformation. During forward transformation it may have favoured the nucleation of $\{111\}$ austenite grains as the FCC $\{111\}$ planes exhibit the lowest surface energy;
- (ii) Texture memory during γ - α back transformation [31-34]. The texture memory effect generally enhances a return to the initial ferrite texture;
- (iii) Release of elastic strains associated with the phase transformation [36]. As the newly formed product orientation is embedded in an elastic anisotropic matrix, the elastic strain energy resulting from the transformation eigenstrain is different

for individual variants and moreover this variant selection may operate differently in the (sub-) surface layers of the sheet as the boundary conditions are different at the surface as compared to the bulk of the sheet.

On the basis of the present data it is impossible to derive a general account of all the phenomena that may have been involved in the shaping of the final surface texture. Nevertheless, it seems very probable that the appearance of $\{001\}$ and $\{110\}$ surface textures is the results of variant selection by surface energy anisotropy energy as these specific orientations are only present in one monolayer of outer surface metal grains. It should be mentioned, though, that the first layer of metal crystals are in contact with the metal-oxide thin film and not with the vapour atmosphere. Such consideration might change the balance between the selection of $\{001\}$ vs $\{110\}$ grains.

The fact that $\{001\}$ ferrite product grains increase their intensity at the expense of $\{110\}$ grains during extended high temperature holding time should be associated with a process that occurs in the high temperature austenite. One might think of texture change in the parent phase as a result of austenite grain growth. Some indication to support this assumption might be found in the fact that the ferrite product grain size increases with increasing austenite holding time, which may be considered as reminiscent of the increasing parent grain size.

3.5. Conclusions

Several parameters have been explored and it has been observed that a surface texture appears with specific texture $\{001\}$ and $\{110\}$ fibre components like after complete phase transformation annealing in the full austenite domain. This specific surface texture was observed on the following compositions: electrolytically pure iron, ultra-low carbon steels and ULC steel alloyed with manganese and aluminium. However, annealed under the same conditions, the ULC steels alloyed with silicon do not show

the typical $\{001\}/\{110\}$ surface texture, whereas a low carbon steel alloy (with 0.05 wt% C) exhibits a mixed texture with a strong cube fibre and a weak γ -fibre.

Orientation imaging microscopy analysis reveals that the specific texture components appear only at the metal-vapour interface in the form of a monolayer of grains, which grows readily inwards along the sheet's ND direction in pure iron and ultra low carbon steel. On the other hand, the monolayer of grains in ULC steel alloyed with manganese and aluminium is restricted to the edge extending only 15 μm in alloy MnAl2 and 30 μm in the case of alloy MnAl1. Hence, a columnar grain structure was observed for the non-alloyed compositions which exhibit higher transformation temperatures than the alloyed grades, exception made for the Si-alloyed grades which belong to another category because of internal oxidation (cf. chapter 4). The occurrence of inward growth during the α - γ - α annealing treatment could be linked to the (back) transformation mechanism and the Ar3 temperature of γ - α transformation during cooling. Transformation by growth, which is enhanced at higher temperatures, is considered to be of crucial importance for the occurrence of a columnar structure.

The selection of different annealing atmosphere during transformation annealing does not modify the surface texture orientations. The intensity of surface texture components varies somewhat by changing the annealing atmosphere particularly with inert gases like argon, nitrogen and helium. Also the initial surface texture prior to annealing only had a minor effect on the resulting transformation surface texture after α - γ - α transformation. It appeared that the $\{001\}$ specific surface fibre was somewhat enhanced by an initial BCC shear type surface texture (dominated by $\{110\}\langle 001\rangle$ and $\{112\}\langle 111\rangle$ components), albeit the effect is not very strong.

3.6. References

- [1] K. W. Andrews: JISI, 184 (1956) p 274.
- [2] S. R. Goodman and H. Hu: Trans. Met. Soc. RIME, 230(1964) p 1413.
- [3] S. R. Goodman and H. Hu: Trans. Met. Soc. AIMS, 233(1965) p 103.

- [4] H. Neerfeld and K. Mathieu : Arch. Eisenhuttenw., 20 (1949) p 69.
- [5] E. B. Kula and S. L. Lopata: Trans. Met. Soc. AIME, 215(1959) p 980.
- [6] G. Wassermann: Arch. Eisenhiittenw., 6 (1932/33) p 347.
- [7] J. Grewen and G. Wassermann: Arch. Eisenhuttenw., 32(1961) p 863.
- [8] H. Abe, K. Ito and R. Fukumoto: J. Japan Inst. Metals, 31 (1967) p 37.
- [9] H. Abe and K. Ito: J. Japan Inst. Metals, 31 (1967) p 1300.
- [10] V. V. Sagaradze, Y. A. Vasera and K. A. Malyshev:Fizika Metal., 40 (1975) p 1037.
- [11] H. P. Sattler and G. Wassermann : J. Less-Common Metals,28 (1972) p 119.
- [12] H. Abe and K. Ito: J. Japan Inst. Metals, 32 (1968) p 927.
- [13] K. Ito: Trans. ISIJ, 11 (1971) p 86.
- [14] K. Azuma, H. Abe, S. Goto, K. Ito and Y. C. Wu: J.Japan Inst. Metals, 31 (1967) p 1034.
- [15] R. G. Aspden, J. A. Bergen and H. E. Trout: Acta Met., 16 (1968) p 1027.
- [16] G. T. Higgins, M. Fang and R. De Young: Proceedings of the 4th International Conference on Texture, Metals Soc., London, (1976) p 54.
- [17] H. Kubotera, K. Nakaoka and T. Nagamine : Tetsu-to-Hagane, 52 (1966) p 1171.
- [18] A. Jones and B. Walker: Metal Sci. J., 8 (1974) p 397.
- [19] A. Jones and B. Walker: British Steel Corporation Report SM/612/A, (1974).
- [20] U. Lotter, L. Meyer and R. D. Knorr: Arch. Eisenhiittenw., 47 (1976) p 289.
- [21] I. Kozasu and H. Inagaki : Bull. Japan Inst. Metals, 15 (1976) p 261.
- [22] H. Inagaki : Trans. ISIJ, 17 (1976) p 166.
- [23] R.M.S.B. Horta, D. V. Wilson and W. T. Roberts: JISI, 210 (1972) p 42.
- [24] R. D. Jenkins and D. V. Wilson : JISI, 209 (1971) p 805.
- [25] K. Saiki: J. Japan Soc. Tech. Plasticity, 9 (1968) p 108.
- [26] G. Kurdjumov and G. Sachs: Z. Phys., 64 (1930) p 325.
- [27] Z. Nishiyama: Sci. Rep. Tohoku Univ., 23 (1934/35) p 637.
- [28] G. Wassermann: Stahl u. Eisen, 55 (1935) p 1117.
- [29] R. G. Aspden: J. Appl. Phys., 37 (1955) p 1195.

- [30] R. C. Sharma and G. R. Purdy: *Met. Trans.*, 4 (1973),
- [31] N. Yoshinaga, K. Ushioda, A Itami and O. Akisue, *ISIJ International* 34, (1994) p 33
- [32] N Yoshinaga, N inore, H Kawasaki, L Kestens and B. de Cooman, *Material transactions*, 48 (2007), p 2036
- [33] B. Hutchinson and L.A.I Kestens Applications of texture analysis, *Ceramic transactions* vol. 201 ed by AD Rollet. (2008) p 281
- [34] H Landheer H., PhD thesis, Delft university of Technology, Delft, the Netherlands
- [35] P. Van Houtte: *The MTM-FHM Software system Version2 Users Manual* (1995)
- [36] O Hashimoto, S Satoh, T Tanaka, *Transactions ISIJ* 23 (1983) p 1028

Chapter 4

Role of chemistry during surface texture evolution

One of the main issues under discussion is the role of chemistry on the surface texture evolution during α - γ - α transformation. The alloys used in the present research have different chemistries and this may influence the characteristics of the metal vapour interface during transformation annealing which also may have consequences for the orientation selection during transformation. Compositional depth profiling was performed on the steel surface in both the cold rolled and transformed condition. Two techniques namely X-ray Photoelectron Spectroscopy (XPS) and Glow Discharge Optical Emission Spectroscopy (GDOES) were used to perform compositional depth profiling (CDP). The results of these experiments will be discussed in this chapter.

4.1. Introduction

In the previous chapter various parameters affecting the surface texture evolution has been discussed in detail and it was found that only under certain conditions the surface texture evolution appears with characteristic low energy orientations $\{001\}$ and $\{110\}$. Various compositions like pure iron, ultra low carbon steels and ULC steels alloyed with Mn and Al show the specific surface texture with predominant $\{001\}$ and $\{110\}$ surface orientation, whereas the ULC steel alloyed with silicon does not exhibit these specific surface components. The α - γ - α phase transformation annealing was performed in a vacuum atmosphere with a pressure of 10^{-4} Torr. During the process of vacuum acquisition the amount of air inside the furnace volume is reduced although it is still not completely free from impurities and reactive gases like oxygen and sulphur. The normal air composition contains 21% volume of oxygen, cf. Table 4.1. The oxygen partial pressure (p_{O_2}) is an important physico-chemical characteristic of the atmosphere used in the heat treatment of many

materials. Alloying elements like Mn, Al, Si and Fe have a strong affinity towards the available oxygen in the atmosphere.

Table 4.1 Air composition

Component	Symbol	Volume	Total air volume = 99.998
Nitrogen	N ₂	78.084%	
Oxygen	O ₂	20.947%	
Argon	Ar	0.934%	
Carbon Dioxide	CO ₂	0.033%	

Impurities in the annealing atmosphere play a vital role on the surface energy of low index planes, as described in the first chapter of this work [1]. As a result of that, if there is any oxygen or impurities left in the annealing atmosphere then the surface texture could be influenced by different types of oxide formation at the metal-vapour interface. Compositional depth profiling was performed on the steel surface before and after annealing in order to detect the change in chemistry at the surface and underneath the annealed sheet surface.

4.2. Experimental procedure

Table 4.2 shows the five steel compositions which were selected for compositional depth profiling by X-ray photo electron spectroscopy and glow discharge optical emission spectroscopy. Table 4.2 includes two types of alloy compositions: the first two, denominated as MnAl1 and MnAl2 are ULC steels alloyed with manganese and aluminium, the next two, denominated as Si1 and Si2, are ULC steels alloyed with silicon.

Table 4.2 Chemical compositions of different cold rolled steel sheets

Alloys	C	Mn	Si	Al
MnAl1	0.003	0.75	0.23	0.12
MnAl2	0.002	1.28	0.22	0.29
Si1	0.002	0.33	0.51	0.13
Si2	0.002	0.34	1.38	0.11
LC	0.047	0.46	0.17	0.037

The fifth composition, denominated as LC, is a low carbon (0.05wt %) steel lightly alloyed with silicon. Four sets of cold rolled sheet surfaces were degreased and acetone cleaned from all five steel compositions listed in table 4.2. Two sets of the cold rolled sheets of all the alloys were used for compositional depth profiling in GDOES and XPS separately. The other two sets were used to perform the typical transformation annealing experiment according to the schedule shown in figure 3.1. After transformation annealing these two sets were analysed for compositional depth profiling by both surface analyses techniques under consideration.

4.3. Compositional depth profiling by X-ray photo electron spectroscopy

XPS is a surface chemical analysis technique that can be used to analyze the surface chemistry of a material in its *as received* state, i.e. without any other surface preparation than degreasing and acetone rinsing. In the present study the cold rolled sheets and the transformation annealed sheets were analysed in as received condition. The instrumental details of X-ray photo electron spectroscopy have been explained in chapter 2.

A typical XPS spectrum as shown in figure 4.1 is a plot of the number of detected electrons (Y-axis) versus the binding energy of the electrons (X-axis). Each element produces a characteristic set of XPS peaks at characteristic binding energy values that

directly identify this element that is present on the surface. These characteristic peaks correspond to the electronic configuration of the electrons within the atoms, e.g. Fe $1s^2 2s^2 2p^6 3s^2 3p^6 4s^2$. The number of detected electrons in each of the characteristic peaks is directly related to the amount of the element within the irradiated volume. It is important to note that XPS detects only the electrons that have actually escaped into the vacuum of the instrument. XPS measurements were carried out with the generous technical support of industrial partner associated with this research project. The PHI Quantera SXM apparatus has been used with a monochromatic Al-K α anode (1486.6eV) at 26.1 Watt with a beam diameter of 100 μm . The details of the experimental condition for the measurements have been discussed in chapter 2.

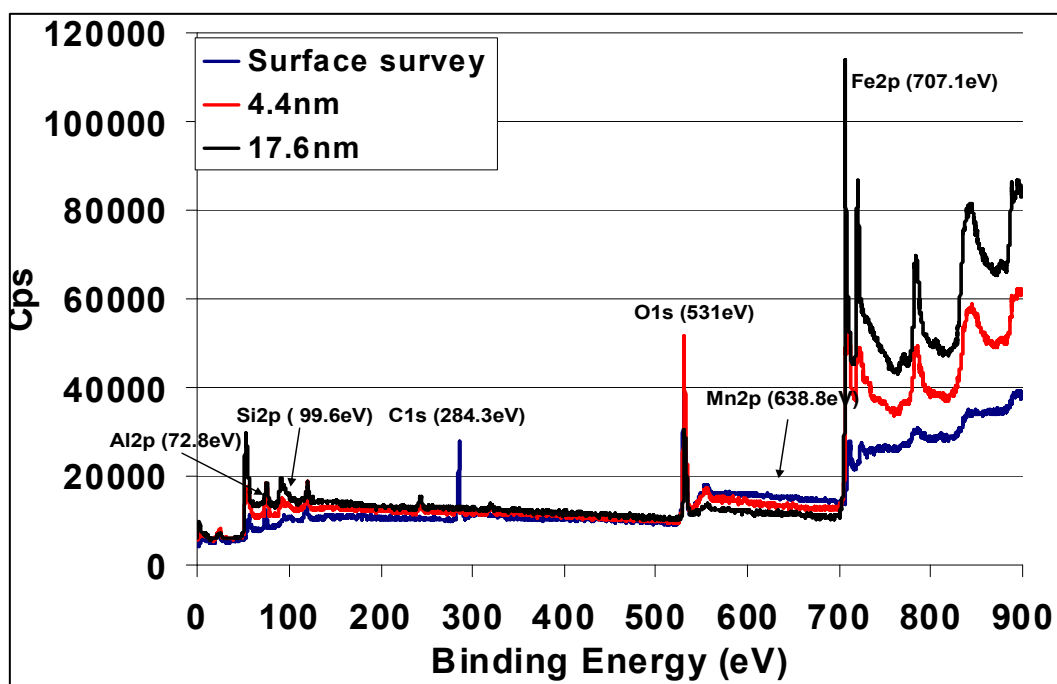


Figure 4.1 Example of compositional depth profiles with complete raw data

The photo-emitted electrons that have escaped into the vacuum of the instrument are those that originated from within the top 10 to 12 nm of the material. Figure 4.1 shows three spectrum plots of different depth levels (surface, 4.4 nm and 17.6 nm underneath the surface) received from XPS analysis of material MnAl₂. The surface

layers were removed by Ar sputtering at a rate of 4.4 nm/min. The XPS spectrum in figure 4.1 shows peaks associated with the alloying elements iron, manganese, aluminium, silicon, carbon and oxygen at specific points on the X-axis corresponding to their binding energy. Table 4.3 shows the reported values of binding energies of different elements in pure state (2p electrons) and their shift in the molecular state. Each element in a molecular configuration has a characteristic binding energy and it gets a characteristic shift in the binding energy values depending on the type of molecular binding. The specific binding energy of each element allows identifying its chemical state which may be compared before and after transformation for all alloy compositions listed in table 4.2

Table 4.3 Characteristic values of electron energies for the most relevant alloying elements either in pure elemental or molecular condition [6].

Element	Compound	Most reported value, eV	Range, eV
Fe	Fe2p spectra	707.1	706.5 - 709.4
	FeO	709.6	709.3 - 710.7
	Fe ₂ O ₃	710.8	709.9 – 711.6
	Fe ₃ O ₄	710.8	708.1 – 711.4
Mn	Mn2p spectra	638.8	638.8– 641.0
	MnO	641.3	640.4 – 642.5
	MnO ₂	642.2	641.1 – 643.4
	MnFe ₂ O ₄	-	639.8 – 641
	MnAl ₂ O ₄	641.3	-
Si	Si2p spectra	99.6	98.7 – 99.6
	SiO ₂	103.6	103.0 – 104.0
	Al ₂ SiO ₅	-	102.6 – 103.0
Al	Al2p spectra	72.8	-
	Al ₂ O ₃	74.3	72.0 – 74.93
	Al [*] ₂ O ₃ /Al	75.8	74.8 - 76.19
	Al ₂ SiO ₅	-	74.6 – 74.8
	AlN	-	74.0 – 74.4
	MnAl ₂ O ₄	74.2	-

Figure 4.1 shows different peaks for different elements like Si, Al, Mn, C and O in the XPS spectra. The positions of binding energy peaks of the different elements shown in figure 4.1 are very much in accordance with their reported value as listed in table 4.3. These high resolution peaks of the individual elements Fe, Mn, Si, Al, C, and O will be discussed below.

4.4. Compositional depth profiling before α - γ - α transformation

The compositional depth profiling (CDP) was performed on cold rolled sheet samples before annealing with the aim to investigate the chemical state of the most important alloying elements particularly iron, manganese, aluminium and silicon as well as carbon and oxygen. It is important to note that cold rolling was performed on the pickled hot rolled sheets to avoid any oxides retained from hot rolling treatment. The XPS spectra of manganese, aluminium and silicon are not shown because they do not reveal any peak therefore only iron, carbon and oxygen are shown and discussed below.

4.4.1. Iron spectra at cold rolled surface

The atomic concentration and chemical state of the iron atoms is determined by fitting of the Fe2p spectrum. Figure 4.2 shows the iron spectra of three high resolution compositional profiles measured at the outer surface, at 4.4 nm and at 17.6 nm underneath the surface on a cold rolled sheet of the five alloys under investigation. The considered electron spectroscopy range is between 702 and 718 eV which includes the pure elemental Fe2p range as well as the binding states of relevance in the present study (cf. Table 4.3) [2-5].

The characteristic Fe peak in the pure chemical state has a reported energy of 707.1 eV [2] and the binded Fe peaks in the various Fe-oxide states have a reported energy close to 711 eV [3]. These peak positions have been shown as dotted black

lines in figure 4.3. The iron spectra collected at the very surface on all five compositions are shown in blue. The iron spectra identified at the surface exhibits a diffuse peak at 711eV which corresponds to the iron oxide binding energy. The iron spectra collected from 4.4 nm and 16.4 nm underneath the surface for all five alloys MnAl1, MnAl2, Si1, Si2 and LC is matching with the reference energy of 707 eV of iron in its elemental chemical state.

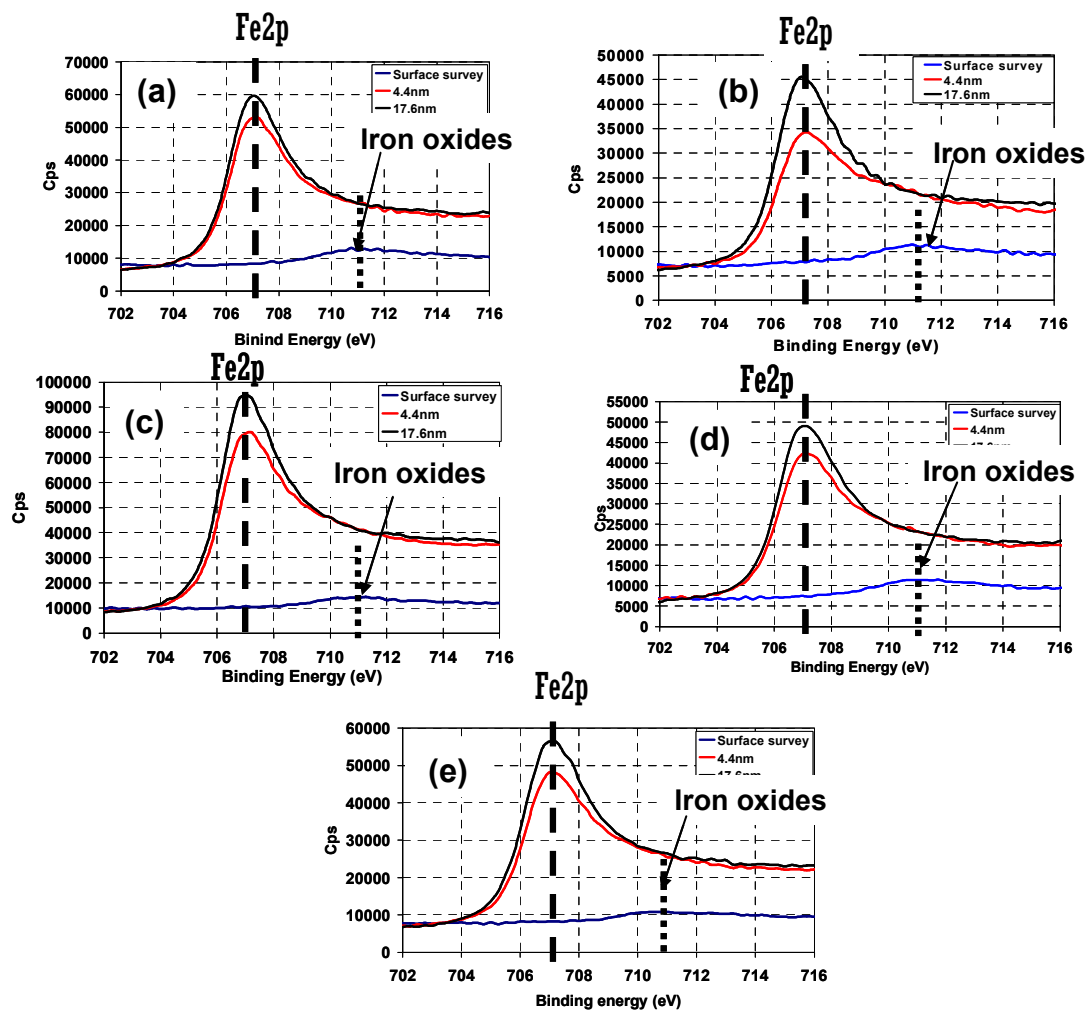


Figure 4.2 Iron spectra at three different depth levels including the surface of cold rolled sheet samples of all five alloy compositions (a) MnAl1, (b) MnAl2, (c) Si1, (d) Si2 and (e) LC.

4.4.2. Oxygen spectra at cold rolled surface

Figure 4.3 shows the high resolution oxygen (O1s) spectrum in the range between 526 and 540 eV at the surface, at 4.4 nm and at 17.6 nm underneath the surface of the cold rolled sheet of the five alloys under investigation. Table 4.4 shows the most reported O1s peak energy values for oxygen in atomic state and in binded condition in various oxides.

Table 4.4 Most reported O1s peak energy values for oxygen containing compounds

Compounds	Reported values
Adsorbed atomic O	531.6 eV
Adsorbed OH	531.5 eV- 532.1 eV
Lattice O from FeO, Fe ₃ O ₄ or FeOOH	530 eV
C-O and O-C=O	532.5 eV
H ₂ O	533.9 eV
MnO	530-531eV
Mn ₂ SiO ₄	531.5 eV
SiO ₂	532.5-533.5eV
SiO _x (x<2)	532.4 eV

The characteristic oxygen peak in the atomic state appears at 531.6 eV [6]. The oxygen spectra recorded at the surface (blue in fig 4.4) shows a wide peak intensity at 530.5eV irrespective of the composition. The oxygen spectra recorded at 4.4 nm underneath the surface (red in fig 4.3) show a broad peak intensity @530.5eV similar to the surface for all compositions. At 16.6 nm underneath the surface (black colours in fig 4.4) a very shallow and broad peak is observed at 530.5eV. The intensity of the oxygen peak has steadily decreased to a minimum value at a depth of 16.6 nm. The width of the oxygen peaks at different depths could be attributed to a combination of different types of Fe-oxides (FeO, Fe₃O₄, Fe₂O₃) in association with manganese silicon and aluminium. These complex oxide peak intensities decrease with successive

depth profile underneath the surface revealing that the oxidation layer extends only to the very surface of the cold rolled sheets and gradually disappears underneath the surface. These characteristics are very similar for all alloys under investigation in this study.

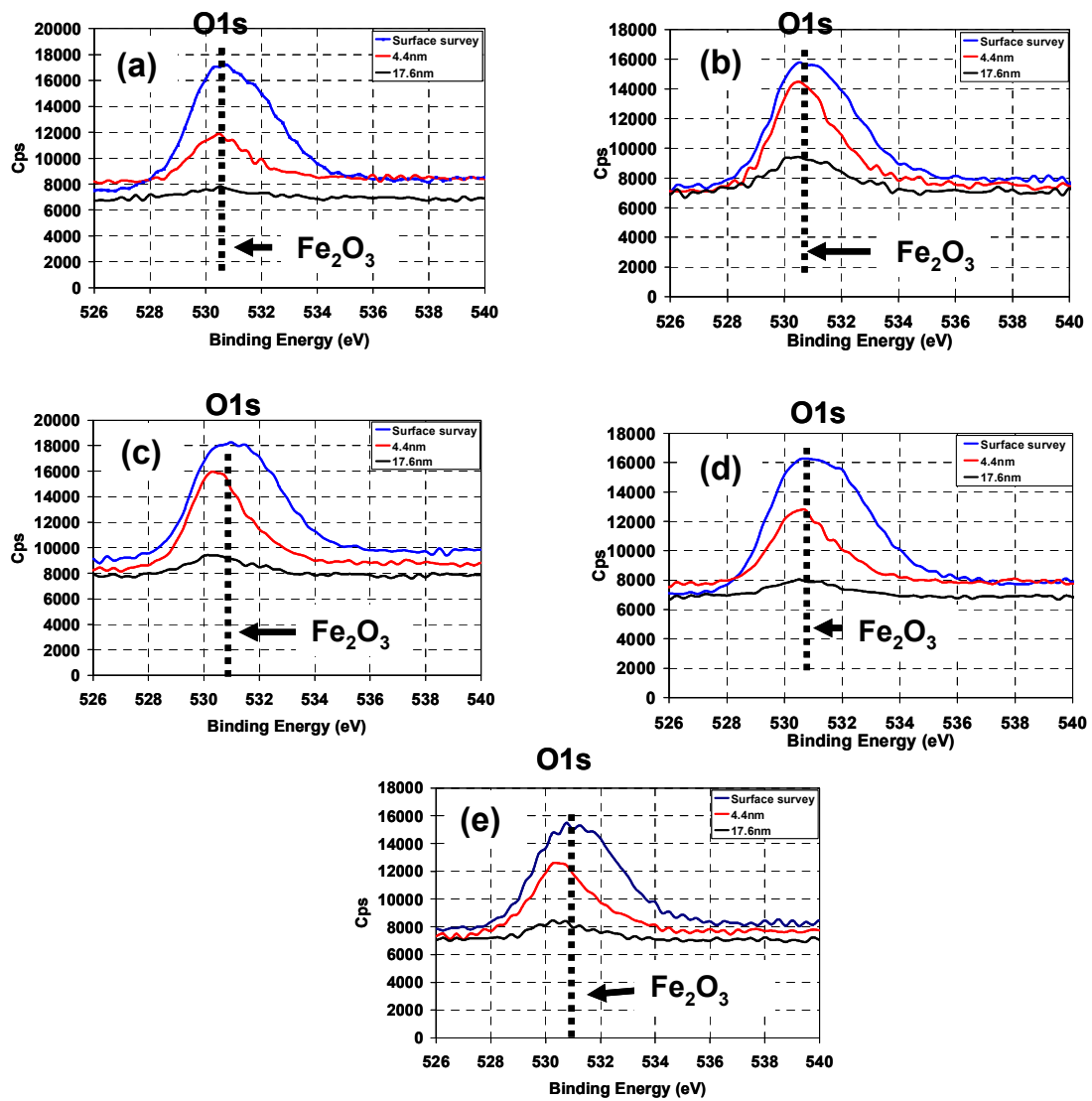


Figure 4.3 Oxygen spectra at three different depth levels including the surface of cold rolled sheet samples of all five alloy compositions under investigation (a) MnAl1, (b) MnAl2, (c) Si1, (d) Si2 and (e) LC.

4.4.3. Carbon spectra at the cold rolled surface

Figure 4.4 shows the high resolution compositional depth profiles of carbon in the spectral range between 280 and 290 eV at the reference distances and for the materials mentioned before. Carbon is always present at surfaces that have been exposed to ambient air. It is even present on surfaces produced in ultra clean (UHV) environments [6].

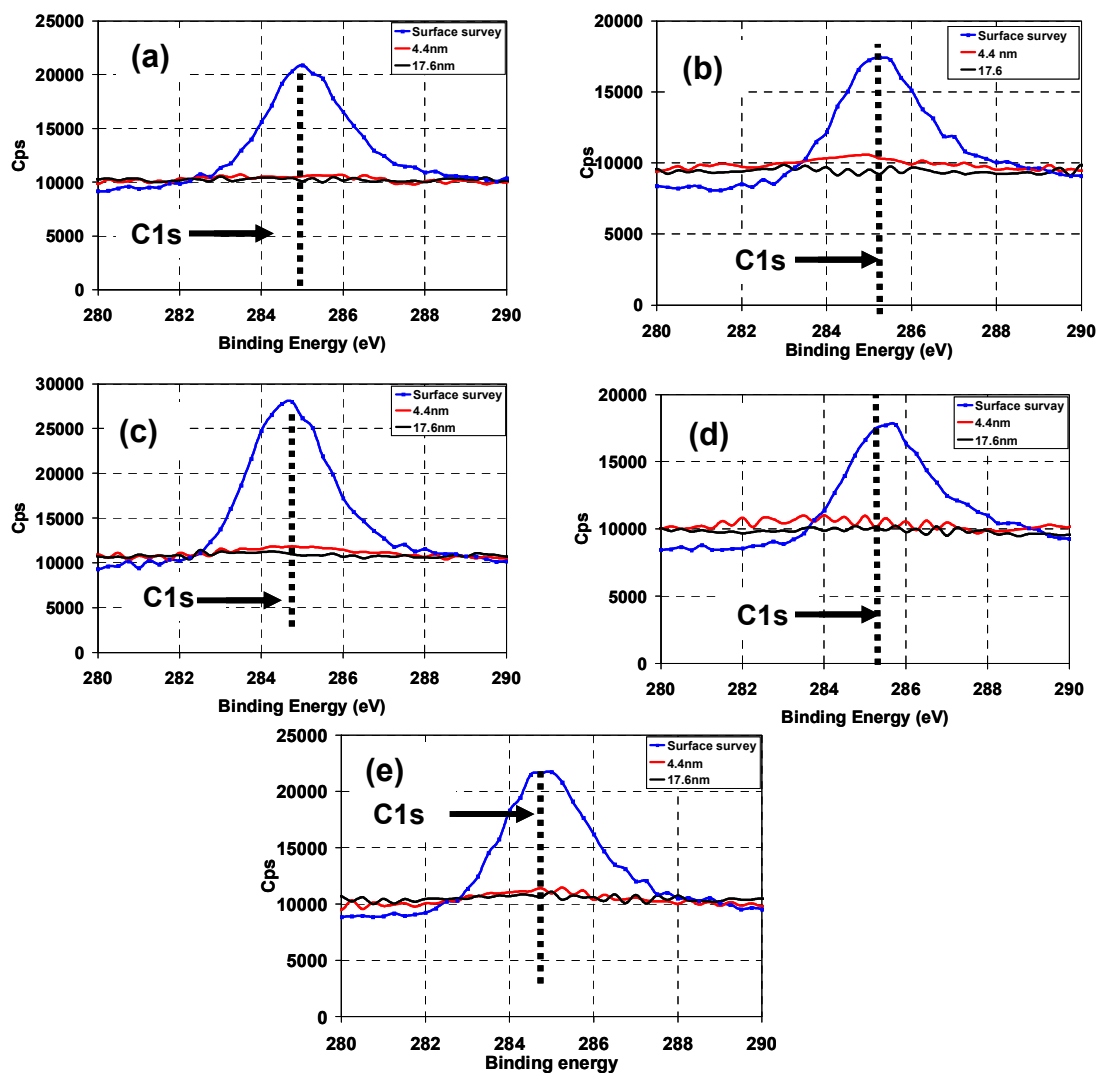


Figure 4.4 Carbon spectra at three different depth levels including the surface of cold rolled sheet samples of all five alloy compositions under investigation (a) MnAl1, (b) MnAl2, (c) Si1, (d) Si2 and (e) LC.

Adventitious carbon is therefore often used as a reference peak to quantify and account for sample charging during XPS measurements. The C1s peak of adventitious carbon is situated at 284.5 eV. The carbon spectra recorded at the surface (blue in figure 4.4) shows its peak intensity at 285eV with a broad range for all five compositions. It can be observed that this peak disappears underneath the surface (red and black in figure 4.4).

4.5. Compositional depth profiling after α - γ - α transformation

The compositional depth profiling by XPS was also performed on the annealed sheet samples after phase transformation. Also here the compositional depth profiling was performed at the same reference sections, i.e. at the outer surface, at 4.4 nm and at 17.6 nm underneath the annealed surface. The same chemical elements were considered as for the alloying elements: Fe, Al, Mn Si, and elemental oxygen in all the five alloy compositions listed in Table 4.3.

4.5.1. Silicon spectra after phase transformation

Figure 4.5 shows the silicon spectra for the reference depths in the spectral range from 96 to 110 eV [7-9]. The characteristic Si peak in the pure chemical state (Si2p) has a binding energy of 99.6 eV (7). The compositional depth profiling was performed on the annealed outer surface, at 4.4 and 17.6 nm underneath the surface of all the five alloy compositions. Figure 4.5 reveals the entire spectrum which is very flat without any pronounced peak in none of the surface profiles for all alloys. Only the high silicon alloy Si2 exhibits a faint appearance of a pure metallic silica peak at 99 eV at 17.6nm underneath the surface (black line). It might be that the level of Si is too low to be recorded in the present composition ranges.

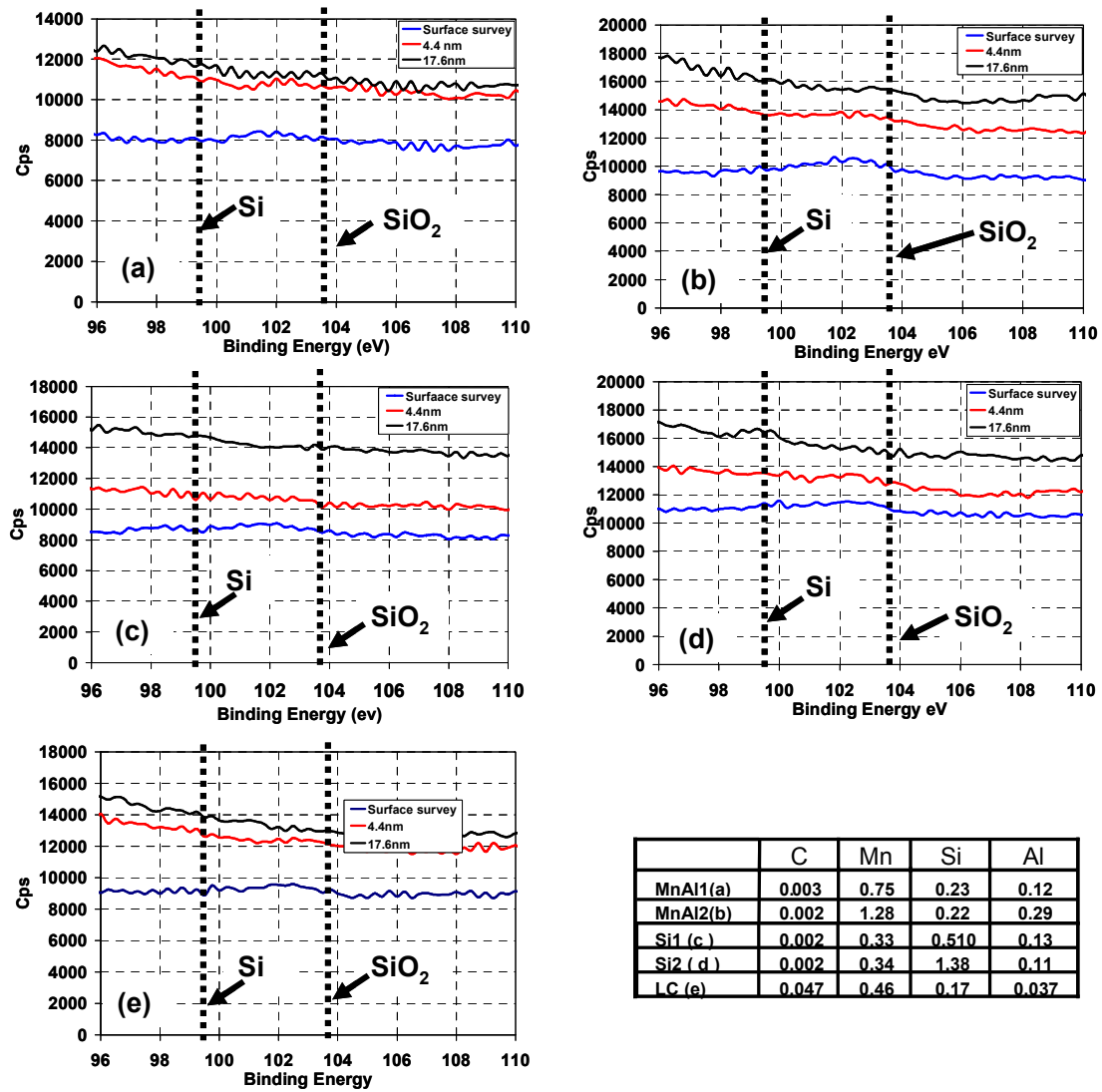


Figure 4.5 Silicon spectra at three different depth levels including the surface of annealed sheet samples of all the five alloy compositions under investigation (a) MnAl1, (b) MnAl2, (c) Si1, (d) Si2 and (e) LC.

4.5.2. Manganese spectra after phase transformation

Figure 4.6 shows the high resolution compositional depths profile of manganese in the spectral range from 634 to 652eV [15-19] recorded at the surface, at 4.4 nm and at 17.6 nm underneath the surface of the annealed sheet of the five alloys listed in table

4.2. Table 4.3 shows the most common peak energy values for metallic manganese and its oxides. The metallic manganese peak in the pure state appears at 638.8 eV [15]. The manganese spectra recorded at the surface (blue in fig 4.6) exhibit a flat line over the entire spectrum for alloys MnAl1, Si1, Si2 and LC whereas the alloy MnAl2 with the highest amount of manganese reveals a broad peak with low intensity at 641 eV. The Mn peak is absent in the spectra recorded at a surface distance of 4.4 nm (red in figure 4.6) on the annealed sheets of alloys denominated as MnAl1, Si1, Si2 and LC. The MnAl2 alloy, on the other hand, reveals a diffuse peak at 643 eV with a slightly stronger intensity than the spectrum recorded at the surface. The manganese spectra recorded at 17.6 nm underneath the surface of the annealed sheets of all the five alloys display a flat profile over the entire range shown by the black lines of figure 4.6. The observed peaks for the high Mn alloys MnAl2 with a manganese content of 1.28 wt% can be attributed to manganese oxides like MnO or MnO₂ or also oxide complexes or iron or aluminium containing oxides. This result indicates that, at least in the high Mn alloy MnAl2, a certain degree of Mn diffusion has taken place from the bulk to the surface. This has given rise to a surface oxide layer, but also may have locally changed the critical transition temperature of the γ - α phase transformation.

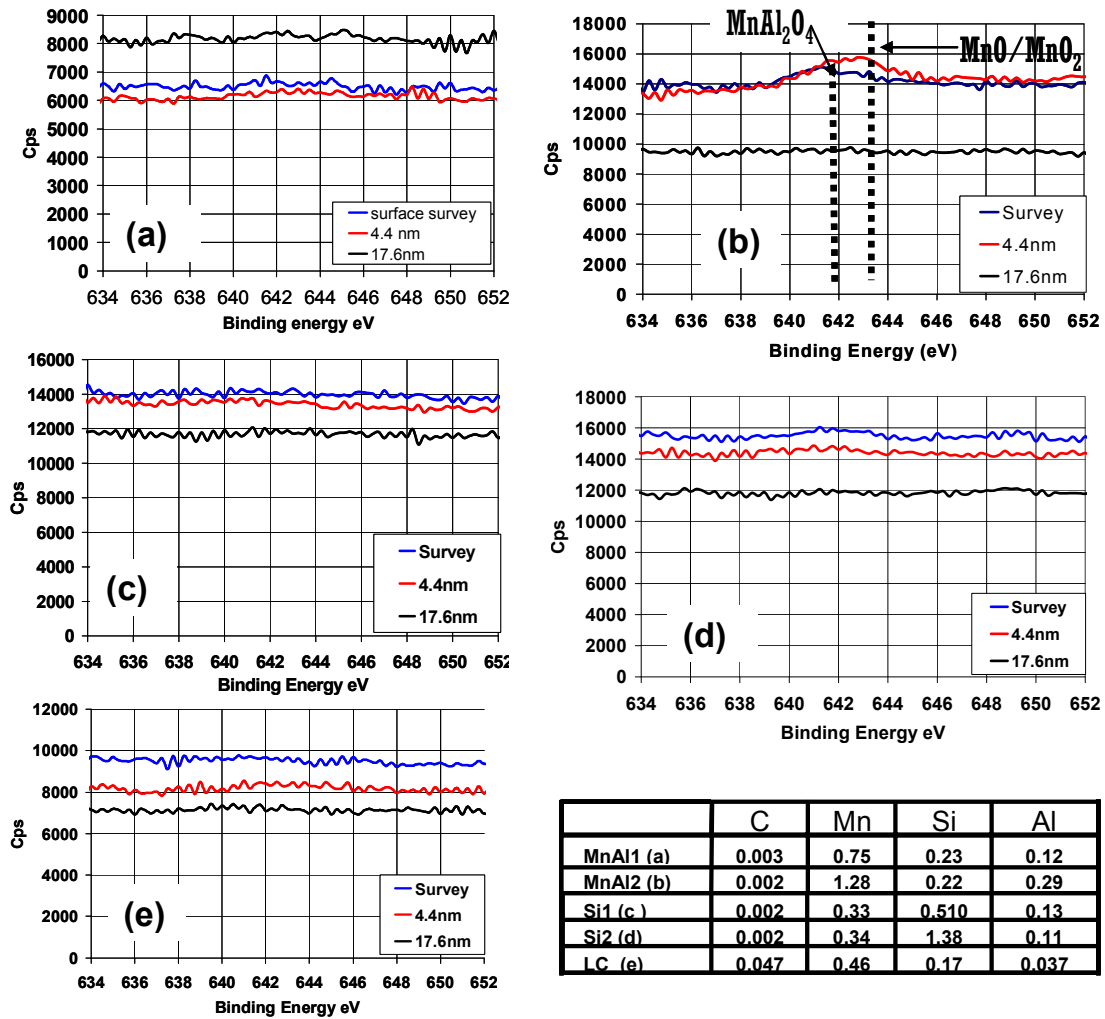


Figure 4.6 Manganese spectra at three different depth levels including the surface of the annealed sheet samples of all the five alloy compositions (a) MnAl1, (b) MnAl2, (c) Si1, (d) Si2 and (e) LC.

4.5.3. Iron spectra after phase transformation

Figure 4.7 shows the iron range of three high resolution compositional depths profiles in the iron range (surface, 4.4nm and 17.6 nm underneath the surface) on the transformation annealed sheet of all five alloys. The iron spectrum is considered in the range between 702 to 716eV with the characteristic Fe peak in the pure chemical state appearing at 707.1eV. [3].

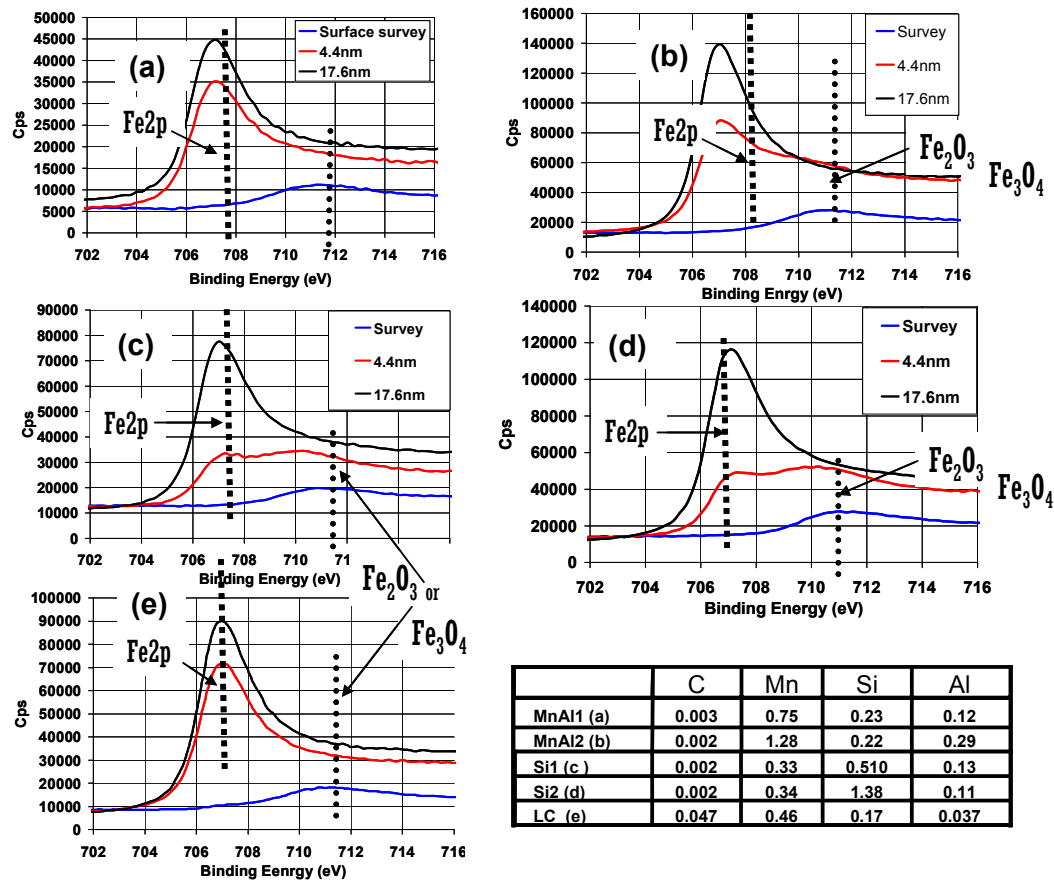


Figure 4.7 The iron spectra at three different depth levels including the surface of annealed sheet samples of all the five alloy compositions (a) MnAl1, (b) MnAl2, (c) Si1, (d) Si2 and (e) LC.

The blue lines, which represent the spectra recorded at the outer surface, exhibit diffuse peaks with very low intensity at 711eV. This intensity value could be related to iron oxides or more complex iron oxides. The spectra recorded at 4.4 nm underneath the surface (red lines in figure 4.7) shows a strong peak at 707.1eV which is the reported value for iron in its pure elemental state. This peak is very strong for the alloys LC, MnAl1 and MnAl2, whereas it is rather diffuse with a plateau extended up to 711eV for alloys Si1(c) and Si2(d). The plateau type of iron spectra in the latter alloys is indicative of a different depth and different type of oxidation binding behaviour as compared to alloys MnAl1, MnAl2 and LC. This difference might be

expected because of the differences in alloy compositions. The plateau type iron Fe2p spectrum in Si1 and Si2 consists of two shallow peaks: one may be referred to as a metallic peak and the other could be referred to as an iron oxide peak. These data suggest that the surface oxidation could be slightly deeper in these alloys. The iron spectra recorded at 17.6 nm underneath the surface are shown as black lines in Figure 4.7. All spectra exhibit a very distinct peak at the pure elemental value of 707.1 eV. The compositional depth profiles at three levels, which are very close to surface, reveal two types of contamination and at two different depths. These different types of surface oxidation could be related to the very thin layer of oxides which might be affecting the surface texture evolution.

4.5.4. Aluminium spectra after phase transformation

The composition depth profiles in the energy range of the aluminium peaks are shown in Figure 4.8. The energy range between 70 and 80eV is considered which includes the characteristic aluminium peak in the pure elemental state at 72.8eV [19] which does not appear in none of the five alloys. For alloys MnAl1 and MnAl2 with an Al content of 0.12 and 0.29 wt%, respectively, a flat spectrum is observed without peak in none of the three sampled levels. On the other hand marked peaks with different chemical shifts can be noticed in alloys LC, Si1 and Si2 with an aluminium content of 0.03, 0.12 and 0.11wt%, respectively. At the outer surface (blue lines) a peak shift from the pure elemental state is observed which can be related to a complex oxide formation at the outer-surface. The LC alloy exhibits a peak around 74 eV which could be linked to a complex oxide of Mn and Al. Underneath the surface, at 4 nm and 17.6 nm, the peak has shifted to 75eV which could be attributed to complexes of aluminium and silicon oxides. A similar characteristic is observed on the alloys Si1 and Si2 with the higher amount of silicon of 1.38 and 0.5wt%, respectively.

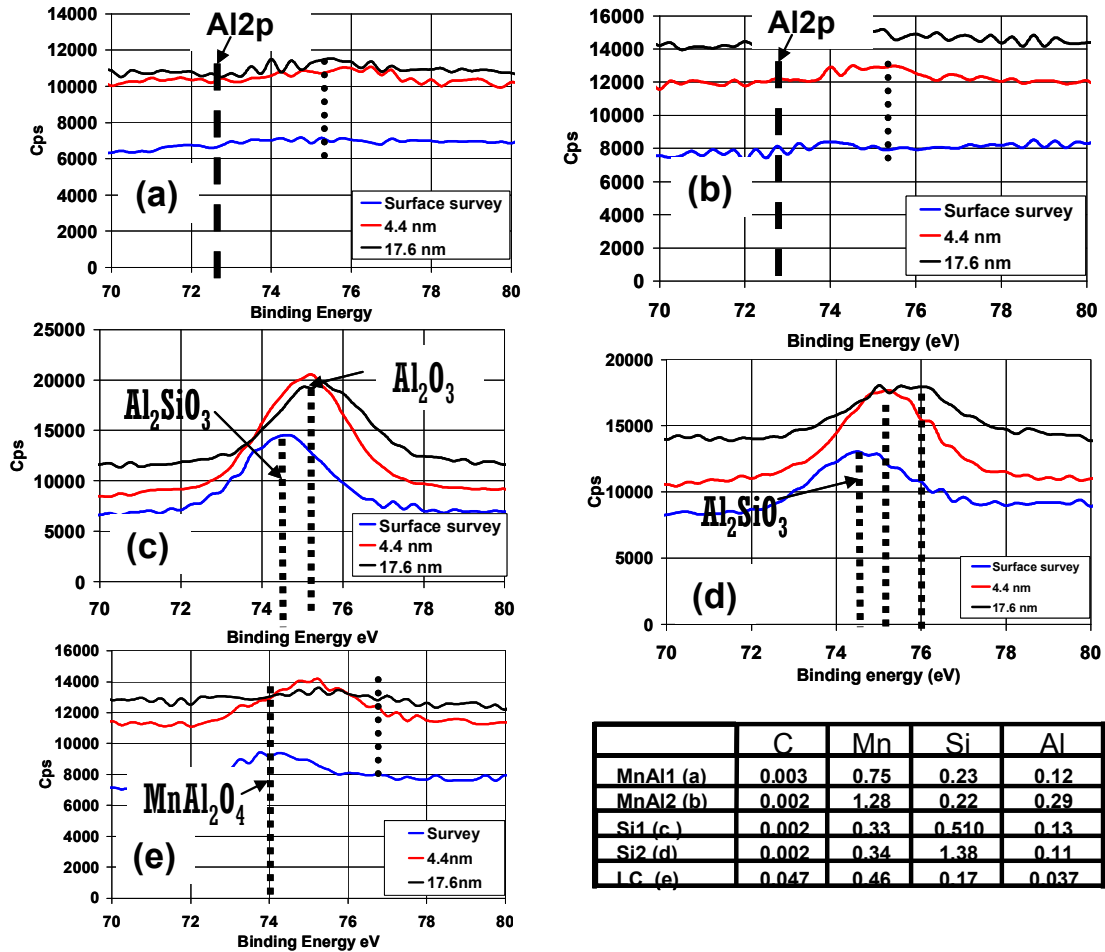


Figure 4.8 Aluminium spectra at three different depth levels including the surface of annealed sheet samples of all the five alloy compositions (a) MnAl1, (b) MnAl2, (c) Si1, (d) Si2 and (e) LC.

4.5.5. Oxygen spectra after phase transformation

The oxygen (O1s) spectral peaks are shown in figure 4.9 in the range between 526 to 540 eV, recorded at the surface and at 4.4nm and 17.6 nm underneath the surface of the transformation annealed sheet. Table 4.4 shows the most common O1s peak energy position for a series of oxides. The characteristic oxygen peak in the atomic state appears at 531.6 eV [6]. The oxygen spectra recorded at the annealed surface (blue in figure 4.9) shows high peak intensities at 530.5eV in alloys MnAl1, MnAl2

and LC, whereas alloys Si1 and Si2 exhibit the lower peak intensity. This could be related to iron oxide peak position according to literature data [6]. So, at the the outer-surface all the alloys have an identical activity of oxide. Subsequently, the oxygen spectra recorded at 4.4 nm underneath the surface (red in figure 4.9) exhibit reduced peak intensity in alloy MnAl1 at 530.5eV, whereas alloy MnAl2 exhibits a similar intensity as it is observed in the surface survey spectra.

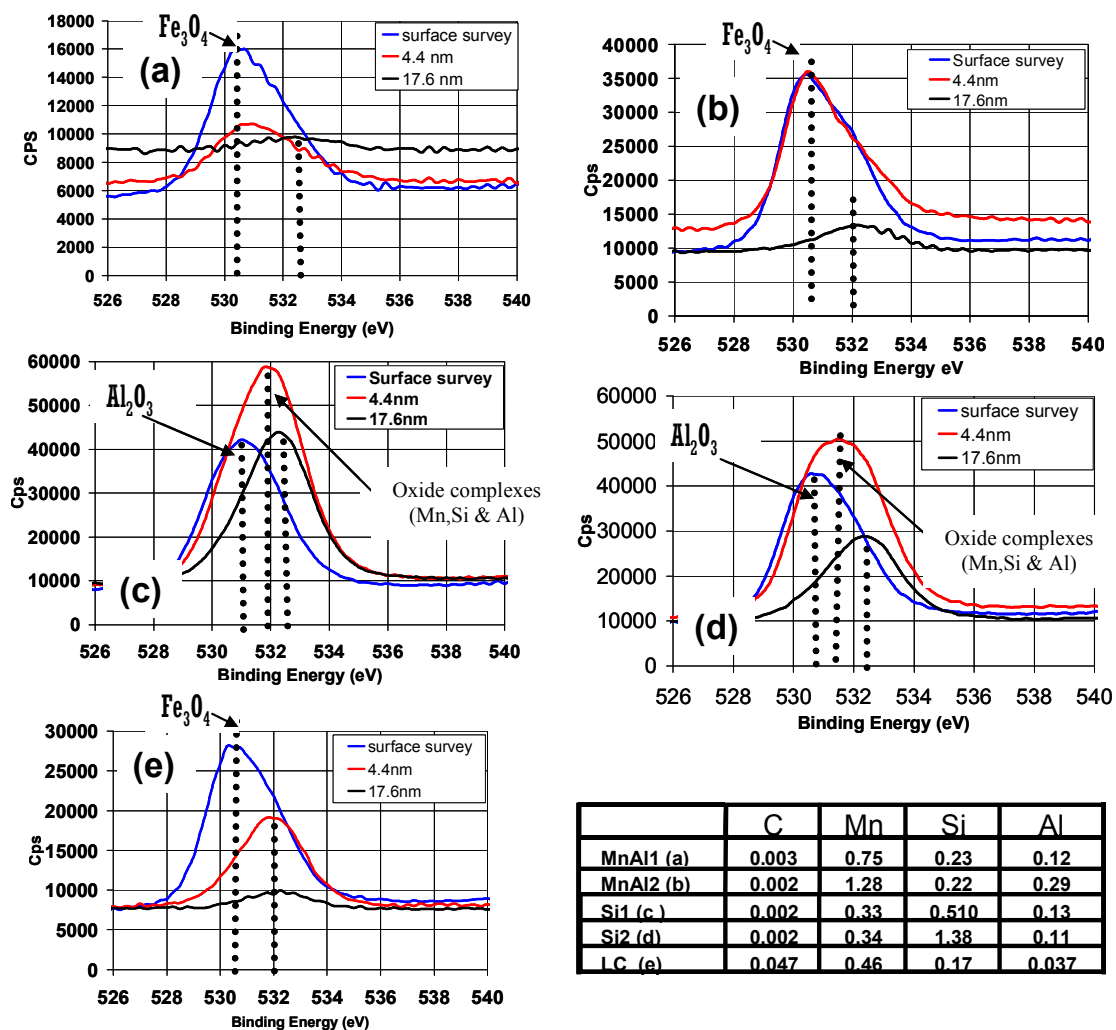


Figure 4.9 Oxygen spectra at three different depth levels including the surface after transformation annealing in the alloys (a) MnAl1, (b) MnAl2, (c) Si1, (d) Si2 and (e) LC.

However, in alloys Si1, Si2 and LC, the oxygen spectra recorded at 4.4nm underneath the surface (red in figure 4.9) shows a strong peak at 532 eV. Most probably, the peak shift observed in these Si-alloyed ULC steels could be attributed to the different nature of oxide binding, which could be related to complex oxides of iron, silicon and aluminium [6] which are of a different nature than the simple iron oxides observed in the other alloys with manganese and aluminium. Further, the oxygen spectra recorded at 17.6 nm underneath the surface (black colour in figure 4.9) shows a weak intensity peak at 532.5eV with a very broad range in alloys MnAl1, MnAl2 and LC. Conversely, the alloys Si1 and Si2 show a strong peak at 532.5eV. These results suggest that selective oxidation is occurring with shallow depth in the ULC steels alloyed with manganese and aluminium whereas a more extensive oxidation layer of a different nature has formed in the ULC steels alloyed with increased silicon. The low carbon steel alloy (LC) shows a mixed behaviour. In order to understand the oxidation depth profile for increased depth beyond 20 nm underneath the surface GDOES is an alternative technique, which has been applied on the samples and results are discussed in the next further section.

4.6. Compositional depth profiling by GDOES

The very surface (extending to 17nm underneath) of the steel sheets was investigated with X-ray photoelectron spectroscopy (XPS). In addition to surface characterization by XPS, the glow discharge optical emission spectroscopy (GDOES) technique was used to obtain supplementary information on the actual concentration of the main alloying elements in the sub-surface region (until 100 nm underneath the surface). The GDOES technique is specifically used for depth-profiling which gives the information on absolute concentrations in wt% of each element of interest which is difficult with XPS. The change in concentration of important elements like iron, manganese, aluminium and silicon has been recorded during depth profiling as shown hereafter.

This change in concentration can be easily compared to their respective bulk compositions, which are already known.

4.6.1. GDOES Compositional depth profiles before phase transformation

Compositional depth profiles were acquired on the cold rolled sheet samples of the five alloys under investigation. The results are shown in figure 4.10 for each alloy separately. Each of the five diagrams of figure 4.10 represents the concentrations as function of depth for different alloying elements of particular interest in this study such as iron manganese, aluminium, silicon, oxygen and carbon. The compositions under consideration in this study are iron based and other elements are less than 2wt% of the total. The concentration depth profiles of Figure 4.10 reveal that irrespective of the nominal chemical composition, the iron concentration starts to decrease in the vicinity of the surface whereas the opposite is true for the oxygen concentration.

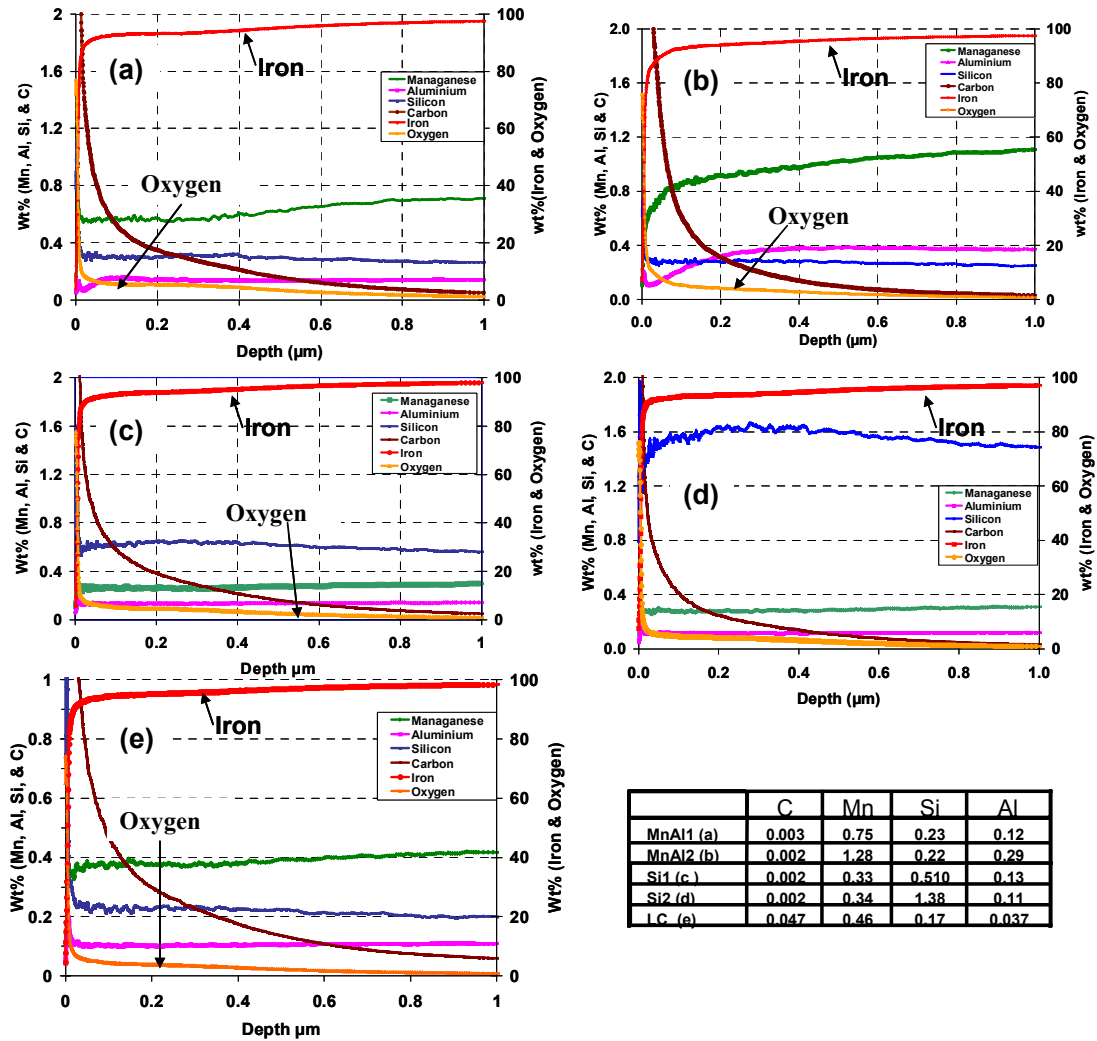


Fig 4.10 Compositional depth profiles obtained from GDOES for all the five alloy compositions (a) MnAl1, (b) MnAl2, (c) Si1, (d) Si2 and (e) LC before transformation annealing.

4.6.2 GDOES Compositional depth profiles after phase transformation

The compositional depth profiles that were acquired on the transformation annealed sheet samples are presented in figure 4.11. The top two figures correspond to the Si and Mn alloyed ULC steels denominated MnAl1 and MnAl2. Both alloy compositions contain slightly different amounts of manganese and aluminium content but the rest of the composition is the same. It can be seen in figure 4.11 that both

alloys show similar chemical activity of the elements under consideration. At the very surface extending to 100 nm the iron activity is decreasing and simultaneously the activity of Mn, Al, and Si is increasing along with the oxygen. In the underlying layers from 100 nm to beyond, the surface activity of the alloying elements Mn, Al and silicon decreases along with the oxygen activity and simultaneously the iron concentration is increasing to the nominal bulk concentration. This behaviour suggests the selective oxidation of these elements preferentially at the surface.

The concentration plots of the Si alloyed ULC steels Si1 and Si2 are also shown in figure 4.11. These plots show an increased activity of silicon, oxygen and iron at the surface and down to 500 nm underneath the surface. These results suggest the presence of complex oxides of iron silicon and oxygen at the metal-vapour interface. The oxygen has diffused much deeper, though (up to 500nm), and has caused internal oxidation as compared to the Mn/Al added ULC steel. Figure 4.11 also exhibits the concentration profile of the LC alloy with low carbon (0.05wt %) content and minute additions of Mn and Si. This profile reveals that oxygen and iron have produced internal oxidation up to 400 nm underneath the surface. The concentration profiles shown in figure 4.14 confirm the behaviour observed in the profiles obtained with X-ray photo spectroscopy. The concentration profile of different elements analysed in GDOES reveals that the extension of the thin oxide film depends on the alloying element at the metal vapour interface. The ULC steel alloyed with Mn and Al show a very thin oxide film of approximately 100 nm, whereas the ULC steel alloyed with silicon only and the LC steel exhibits a much thicker oxide film of approximately 500nm.

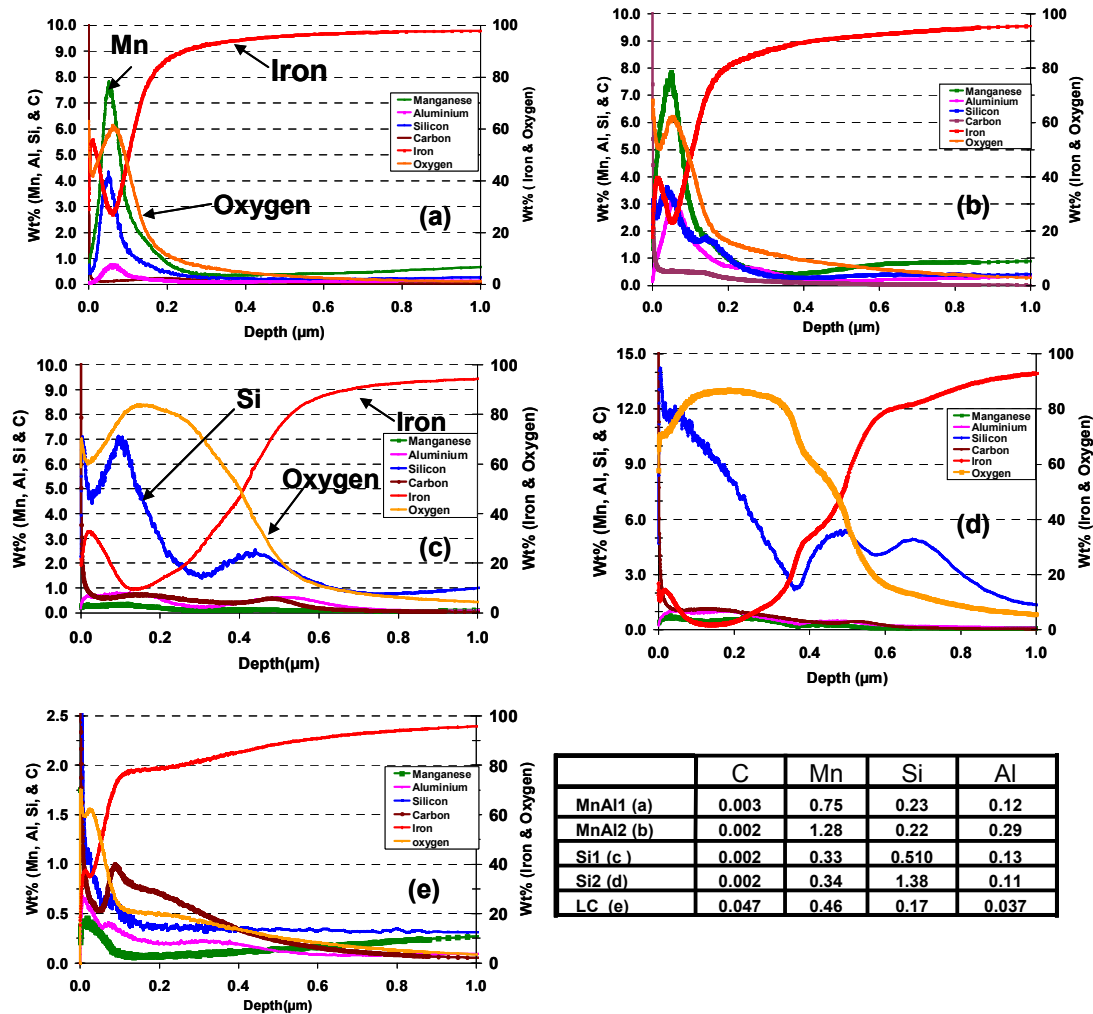


Fig 4.11 Compositional depth profiles obtained from GDOES for the all the five alloy compositions (a) MnAl1, (b) MnAl2, (c) Si1, (d) Si2 and (e) LC after transformation annealing.

4.7. Sub-surface comparison before and after phase transformation

In the previous section the results show the surface analysis which is confined to only 1 μm underneath the surface. In continuation, the sub surface was also examined up to 5 μm underneath the surface for all five alloy compositions but only two very distinct cases are shown for the alloy MnAl2 and Si2. Figure 4.12 shows the compositional depth profiles for the alloy MnAl2 with high manganese and aluminium for both

conditions before and after annealing. This figure represents a detailed view of the chemical compositional changes (wt %) for the main alloying elements Fe, Mn, Si, and Al. These concentrations can be directly compared to the bulk compositions of these alloys. The compositional depth profile before annealing reveals that the surface contains lower manganese, aluminium and silicon in comparison to the bulk composition and also a significant increase in oxygen content. These compositional changes are stabilised below 1 μm underneath the surface. The sub surface composition of the main alloying elements is quite close to the bulk composition of the particular alloy (MnAl₂). After annealing the surface composition has changed dramatically. It is interesting to note that just below the surface, as mentioned before figure 4.12, a hump is present with increased concentration of manganese (up to 8% wt%), silicon (up to 3% wt%) and aluminium (2.5%wt%). Further underneath the surface, the manganese concentration has decreased down to 0.5wt% at $\sim 500\text{nm}$ while the other alloying elements aluminium and silicon gradually stabilize to their bulk composition limits. On the other hand manganese gradually approaches the bulk composition (1.28wt%) at $\sim 3\text{microns}$ underneath the surface.

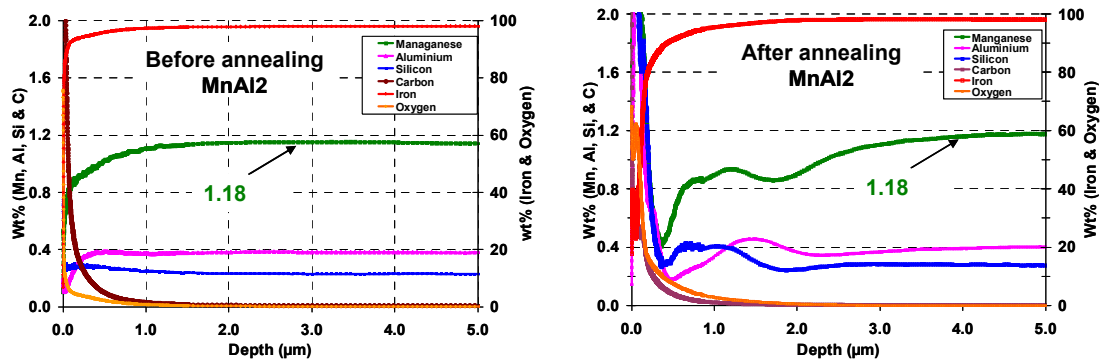


Figure 4.12 GDOES compositional depth profile for the MnAl₂ alloy before and after transformation annealing.

In a similar way figure 4.13 shows the compositional depth profile before and after annealing for the Si₂ alloy with high silicon content (1.38wt%). Before annealing a stable composition profile is shown for the main alloying elements like silicon,

manganese and aluminium. These compositions are very comparable to the bulk composition listed in table 4.2. It is obvious that an oxygen layer is present with gradually decreasing oxygen content towards the bulk, displaying only 50% of the outer surface concentration at a depth of 0.5 μm . Figure 4.13 also shows the composition depth profile after annealing. It can be observed that the iron activity has drastically decreased in the vicinity of the surface, whereas the activity of silicon is as high as 10 wt % and continues to be high until 0.5 μm depth. At $\sim 1.0\mu\text{m}$ below the surface there is a Si depleted layer with a concentration of ~ 1.0 wt%, which is somewhat less than the bulk concentration. In deeper layers beyond 1.0 μm the Si concentration gradually increases and remarkably seems to stabilize at a level of ~ 2.0 wt%, which is well beyond the bulk concentration of 1.38 wt%. The concentrations of Mn and Al exhibit a rising tendency when approaching the surface. From $\sim 1.0 \mu\text{m}$ inwards the concentrations gradually approach the bulk nominal values. The oxygen activity has drastically increased, but decays sharply in a near exponential manner in the sample ND direction. At a depth of 2 μm , the oxygen concentration is 1.8 wt.% after annealing as compared to 0.25 wt.% before.

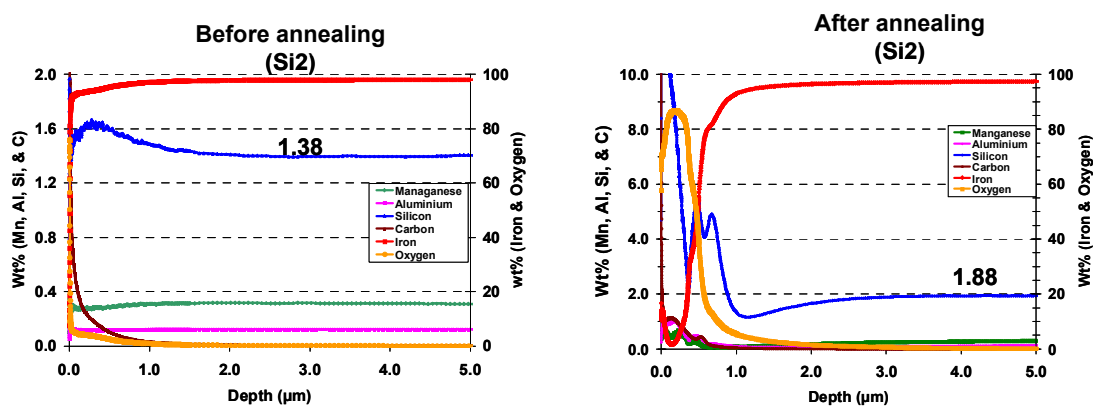


Figure 4.13 Compositional depth profile (GDOES) before annealing (left) and after annealing (right) for the Si2 alloy.

4.8 Surface chemistry relation with texture

The present data suggest that the chemical reactivity of alloying elements like Al, Mn and Si at the metal-vapour interface may have played an important role in the surface texture evolution. As reported in chapter 3 the annealing under medium vacuum conditions has produced the {001} surface texture in the two alloys MnAl1 and MnAl2 with higher manganese whereas the {111} surface texture was observed in the silicon alloyed LC, Si1 and Si2 samples that were annealed under similar conditions. The GDOES experiments have revealed a much more extensive oxidation zone in the Si1 and Si2 alloys as compared to the MnAl1 and MnAl2 steels, whereas the LC alloy shows a mixed oxidation behaviour. Hence it can be concluded that oxidation plays a negative role in the surface orientation selection mechanisms that produces the favourable {001} texture. When the external and internal oxidation process can be reduced by decreasing the vacuum pressure to a level of 10^{-8} Torr, the favourable {001} surface texture also appears in the high silicon industrial alloys as shown in figure 4.14. The ULC steel alloyed with high silicon (1.38wt%) was transformation annealed in two different levels of vacuum with identical experimental conditions. After the transformation annealing the surface was measured by X-ray diffraction. The texture results are shown in the form of $\phi=45^\circ$ sections in figure 4.14. A remarkable texture change is observed due to the vacuum quality. When the vacuum is low, a surface texture appears with typical α/γ -fibre morphology. However, after high vacuum annealing a surface texture appears with a much stronger cube fibre, a weak α -fibre and a minor γ -fibre component. The effect of vacuum has been noteworthy for other alloy compositions as well and full results are described in chapter 5.

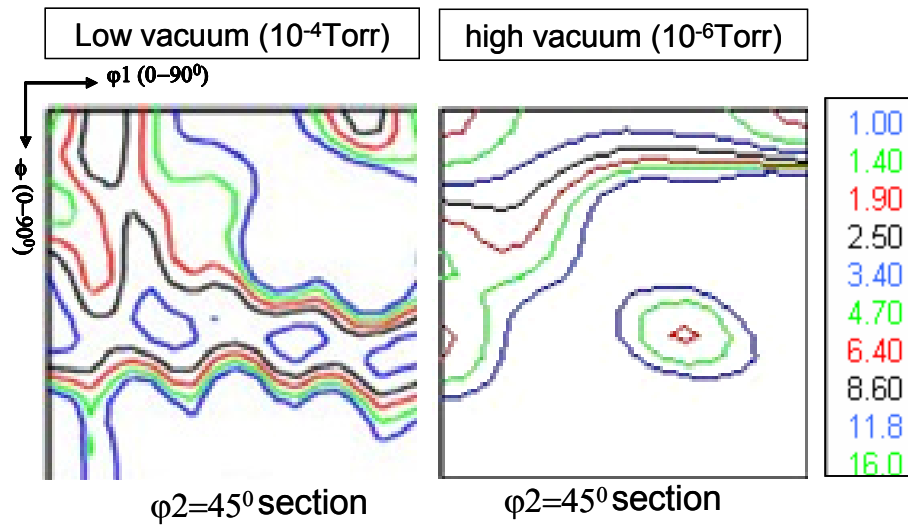


Figure 4.14 Effect of different low vacuum (left) and high vacuum (right) on surface texture after phase transformation annealing for alloy Si2.

It is well understood that the selection of $\{001\}$ orientations at the surface is triggered by the reduced surface energy of these orientations in BCC iron. The present results appear to indicate that this mechanism only seems to play its role when it is not inhibited by the presence of oxide particles. The fact that Si exhibits a stronger affinity for oxidation than Mn explains why the Mn rich alloy displays a shorter oxidation affected zone than the Si rich alloy.

According to the Ellingham-Richardson diagram the calculated partial pressure of oxygen at a temperature of 1,000°C for silicon ($p_{O_2}=7.75 \times 10^{-35}$ bar) is more negative in comparison to manganese ($p_{O_2}=7.75 \times 10^{-30}$ bar) [12, 13]. In the fast heating cycles like the ones applied in this study, the oxide growth is controlled by kinetics. The initial stages of metal-oxygen reaction involve a sequence of adsorption of oxygen and surface reaction leading to oxide nucleation and growth. The outward diffusion of cations and/or the inward diffusion of oxygen ions are responsible for the oxide growth. A number of investigations have been performed on oxides and it was shown that some oxide films grow predominantly by inward diffusion of oxygen: SiO₂, Al₂O₃ and Cr₂O₃, whereas others by outward diffusion of cations: ZnO, MnO, FeO and Fe₃O₄ [14].

Because of these chemical data the ULC steels alloyed with manganese exhibit a very thin oxide layer (~100nm) which apparently allows the surface energy anisotropy to play a decisive role in orientation selection at the interface. Contrastingly, the ULC steel alloyed with silicon shows a wider oxide film layer extending to approximately 1 μm with a dense structure which apparently inhibits the role of surface energy anisotropy. Also the fraction of surface metal grains that is covered by oxide is of relevance with regard to the issue of orientation selection. In the present study this quantity could not be determined.

4.9. Conclusions

The compositional depth profiles obtained from XPS and GDOES after investigation of cold rolled steel sheet confirm that the initial chemical state is very similar for all five alloy composition. After transformation annealing the compositional depth profiles of ULC steels alloyed with Si (Si1 and Si2) shows a very distinct chemical activity from the ULC steels alloyed with Mn and Al (MnAl1 and MnAl2) due to the oxygen pick up from vacuum and its interaction with alloying elements at the metal vapour interface .

XPS analysis performed on the annealed surface of ULC steel alloyed with manganese reveals the formation of manganese oxide complexes, whereas in the steel alloyed with silicon (Fe,Si,Al) oxide complexes have formed. The oxidation layer is only superficial in all alloys, although the Si alloyed samples exhibit comparatively stronger XPS oxygen peaks which indicate that these samples may have oxidized to a larger extent.

The oxygen profiles from XPS as well as from GDOES indicate that selective oxidation takes place due to the outward diffusion of manganese in ULC steel alloyed with manganese, whereas more inward diffusion of oxygen has occurred in the silicon alloyed ULC steel. The latter phenomenon has produced the well-known *internal*

oxidation of Si. The manganese alloys exhibit a very thin oxide layer (~100nm), whereas in the Si alloys a much thicker oxide layer has been observed (~microns).

By combining the present surface chemistry data with the surface texture characteristics (cf. chapter 3) it was shown that the typical {001}/{110} surface texture, emerging as a result of metal/vapour interface energy minimization, only appears in the absence of a thick internal oxidation layer as present in the Si alloyed steels. The latter was confirmed by an experiment in which the surface texture could be reversed in the Si alloyed samples by increasing the vacuum quality of the annealing atmosphere.

4.9. References

- [1] D Kohler, Journal of applied physics, 31, (1960) p 5
- [2] J Mahieu, PhD thesis Ghent University, Ghent, Belgium (2004)
- [3] D.J. Joyner, O. Johnson and D.M. Hercules, J. Am. Chem. Soc. 102, (1980), p. 1910.
- [4] P. Mills and J.L. Sullivan, J. Phys. D. 16, (1983), p 723.
- [5] H.J. Mathieu and D. Landolt, Corrosion Science 26, (1986), p 547.
- [6] D. Brion, Appl. Surf. Sci. 5, (1980), p 133.
- [7] Tom van de Putte, Phd thesis, Ghent University, Ghent, Belgium (2009)
- [8] E. Paparazzo, J. Phys. D. 20, 1987, p 1091
- [9] F.G. Bell and L. Ley, Phys. Rev. B 37, (1988) p 8383.
- [10] J. Finster, Surf. Interface Anal. 12, (1988) p 309
- [11] H.-K. Hu and J.W. Rabalais, Surface Science 107, (1981) p 376
- [12] A.B. Mandale, S. Badrinarayanan, S.K. Date and A.P.B. Sinha, J. Electron Spectrosc. Relat. Phenom. 33, (1984) p 61.
- [13] A. Aoki, Jpn. J. Appl Phys. 15, (1976) p 305.

- [14] B.N. Ivanov-Emin, N.A. Nevskaya, B.E. Zaitsev and T.M. Ivanova, *Zh. Neorg. Khimii* 27, (1982) p 3101.
- [14] H.F. Franzen, M.X. Umana, J.R. McCreary and R.J. Thorn, *J. Solid State Chem.* 18, (1976) p 363
- [15] Y. Umezawa and C.N. Reilley, *Anal. Chem.* 50, (1978) p 1290.
- [16] G.C. Allen, S.J. Harris, J.A. Jutson and J.M. Dyke, *Appl. Surf. Sci.* 37, (1989) p 111.
- [17] V.A.M. Brabers, F.M. Van Setten and P.S.A. Knapen, *J. Solid State Chem.* 49, (1983) p. 93.
- [18] B.R. Strohmeier, D.M. Hercules, *J. Phys. Chem.* 88, (1984) p 4922.
- [19] K. Domen and T.J. Chuang, *J. Chem. Phys.* 90, (1989) p 3318.
- [20] N.H. Turner, *Surf. Interface Anal.* 15, (1990) p 215

Chapter 5

Surface texture evolution during interrupted annealing

Under equilibrium conditions, certain aspects of the surface microstructure are determined by the anisotropy of the surface energy at the metal-vapour interface. Surface energy anisotropy plays a major role in orientation selection during solid-state transformation processes in addition to other driving forces which also occur in the bulk of the material such as the occurrence of preferred crystallographic correspondences associated with a phase transformation. The surface energy is of particular importance in all interface controlled processes such as nucleation and growth of new crystal nuclei in a parent matrix. This chapter includes the results which highlight the effect of the vacuum quality on the metal–vapour interface and also monitors the systematic surface texture evolution with increasing temperature.

5.1. Introduction

It is generally known that silicon iron with cube texture cannot be easily produced. It also has been known that the lower surface energy increases the driving force for the growth of grains having the {100} plane parallel, or within less than 5° from the sheet surface. A clean surface in ultra-high vacuum has a higher free energy than an oxidized (or contaminated) surface because the surface chemical reaction has occurred under the (partial) driving force of the surface energy and as a consequence the resulting Gibbs free surface energy has reduced. For solid surfaces the surface energy is clearly a function of the crystallographic orientation and as a consequence the surface energy plot (γ -plot) will not be spherical but polyhedral with the polyhedron sides parallel to the low energy crystal planes. The effect of surface energy [1-3] on grain growth in tertiary recrystallisation of electrical steel has been confirmed by experiments showing the variation of the texture with the annealing

atmosphere [4, 5] and the variation of the surface energy with the crystallographic orientation in the surface of the electrical steel strip [6].

In the previous chapters it has been reported that a complete forward and reverse ($\alpha \rightarrow \gamma \rightarrow \alpha$) phase transformation in a controlled annealing atmosphere is instrumental for the development of a surface texture with cube fibre orientations. In chapter 3 it was reported, however, that the characteristic $\{001\}/\{110\}$ surface texture could not be observed in ultra low carbon steel alloys with higher silicon and lower manganese content. Compositional depth profiling performed on these sheets has revealed that these alloys have suffered a higher degree of (internal) oxidation as compared to the other alloys with high manganese and aluminium, cf. chapter 4.

In this chapter a more profound investigation will be reported on the surface texture development of all the alloy compositions annealed in a high-quality vacuum with precise control of the temperature cycle.

5.2. Experimental method

The entire process of α - γ - α transformation annealing includes four important stages which lead to structural changes at the surface and in the bulk of the sample. These are (i) recrystallisation below A_{c1} , (ii) the $\alpha \rightarrow \gamma$ phase transformation in the intercritical heating stage starting at A_{c1} and finishing at A_{c3} , (iii) the austenite grain growth stage during isothermal holding above the A_{c3} temperature and (iv) the reverse $\gamma \rightarrow \alpha$ phase transformation during cooling between A_{r3} and A_{r1} . The evolutionary process of the structural and textural formation was monitored by heating the samples to various temperatures (with a step size of 25°C) immediately succeeded by helium gas quench. In the flat soaking stage of the annealing cycle samples were quenched after holding times of 8s for all the different temperatures and additional 30, 60 and 90 s at 1050°C. The schematic representation of this interrupted annealing cycle is shown in figure 5.1.

These annealing experiments were performed in a dilatometer so as to have optimum control over the furnace atmosphere and sample temperature during the entire

annealing cycle. The furnace atmosphere was kept under a high vacuum of 10^{-6} Torr (1.33×10^{-6} Pa) during the entire annealing experiments. Small sheet samples of 0.5mm thickness with dimensions of 5 mm x 10 mm have been used for these annealing experiments. After annealing, the sample surface (RD-TD) was analysed in the X-ray texture goniometer and subsequently the same sample after mechanical and electrochemical polishing was investigated by orientation imaging microscopy in a scanning electron microscope. Utmost care was taken to remove as little as possible material from the outer surface for sample preparation with the purpose of observing the microstructure of the true metal/vapour interfaces.

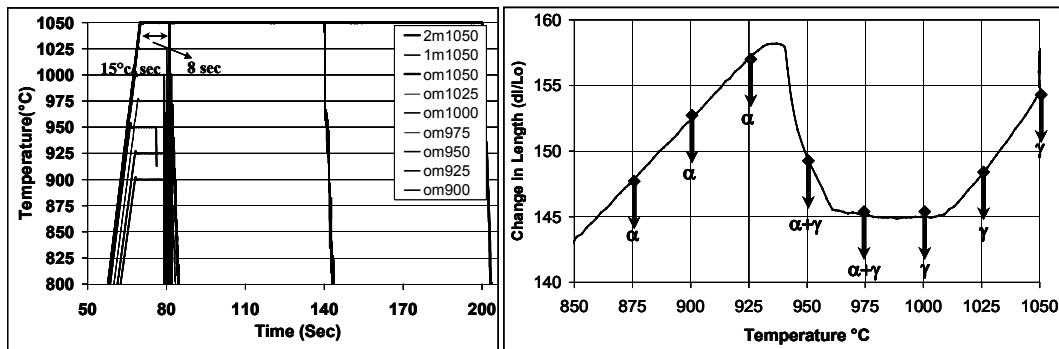


Figure 5.1 Scheme of interrupted annealing experiments performed in dilatometer.

5.3. Results

5.3.1. Surface texture and through thickness microstructure before annealing

The cold rolled sheets of the five alloys, MnAl1, MnAl2, Si1, Si2 and LC were observed in the optical microscope and the through-thickness microstructures are shown in figure 5.2. The cold rolled microstructures are very homogeneous across the thickness. Figure 5.2b shows the $\varphi_2=45^\circ$ sections of the ODFs measured on the samples RD-TD surface sections. The cold rolled surface textures exhibit the typical L-shape morphology of the cold rolling texture as they are composed of the alpha and gamma fibre ($\langle 110 \rangle // RD$ and $\langle 111 \rangle // ND$, respectively). It is noticed that the alpha

fibre is much stronger than the gamma fibre, which is even more pronounced for the Si added steels [7]

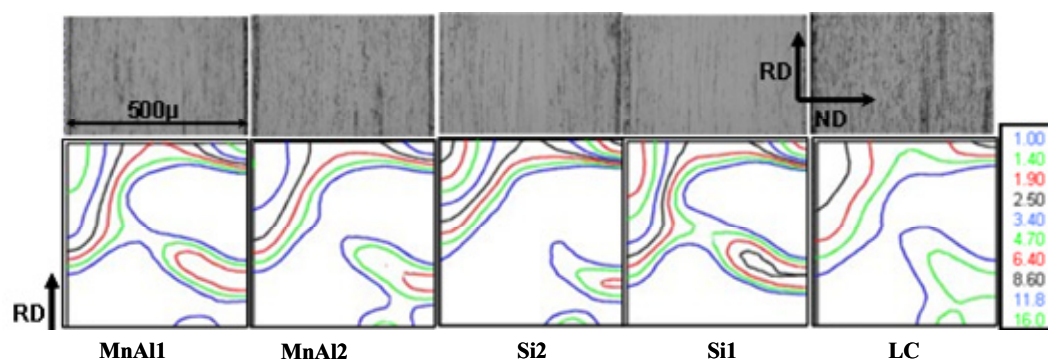


Figure 5.2 Through thickness microstructures (top) of the cold rolled sheet and X-ray measured texture (bottom) observed on the RD-TD surface of alloys.

5.3.2. Surface Texture and microstructure during interrupted annealing in ULC steels alloyed with high manganese and aluminium

The laboratory cast, ultra low carbon steels alloyed with manganese and aluminium and denominated as MnAl1 and MnAl2 will be considered more in detail in the present section. The alloy MnAl2 has the higher manganese and aluminium content in comparison to alloy MnAl1. Both alloys have similar dilatation profile during heating as shown in Figure 5.3. The critical temperature A_{c1} ($\approx 940^\circ\text{C}$) is almost identical for both alloy compositions. So, three temperatures (875°C , 900°C , 925°C) have been selected to observe the surface texture during recrystallisation. The alloy with low manganese and aluminium (MnAl1) exhibits an A_{c3} temperature of $1,005^\circ\text{C}$ which is slightly higher as compared to the value of A_{c3} of 990°C for the high Mn and Al alloy MnAl2. Three temperatures have been selected to observe the texture and microstructure formation in the two-phase domain: 950°C right at the onset of transformation, 975°C in the middle of the two-phase domain with approximately 50% transformed volume fraction and a third one of $1,000^\circ\text{C}$ close to A_{c3} .

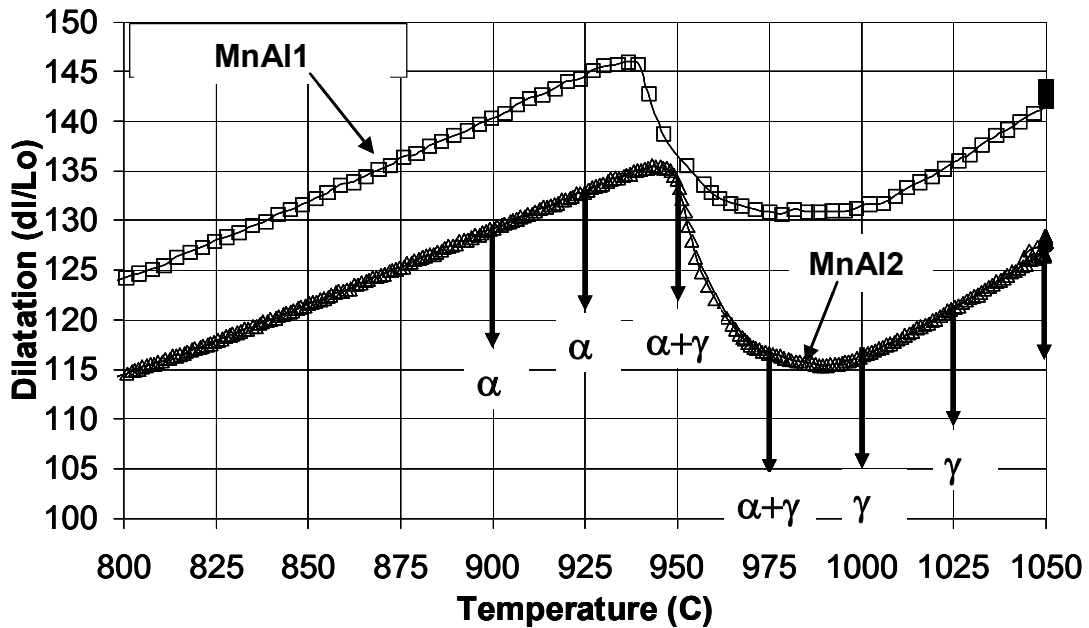


Figure 5.3 Dilatation curves of the alloys MnAl1 and MnAl2 during heating with the successive annealing interruption points up to 1050°C.

Subsequently 2 temperatures were selected above the A_{c3} temperature corresponding to 1,025°C and 1,050°C with holding times of 0, 60 and 120 s followed by helium quench. Afterwards the samples were characterized for texture by XRD and the micro-texture analysis was carried out by EBSD.

The X-ray texture results of the selected samples of both alloys MnAl1 and MnAl2 are shown in figure 5.4. The first $\varphi_2=45^\circ$ sections in figure 5.4 represent the surface textures observed after recrystallisation at the temperature of 925°C. These $\varphi_2=45^\circ$ sections show different recrystallisation texture components: a rather strong α -fibre as well as a weak γ fibre. Conventionally, the γ fibre of cold rolling is retained and becomes stronger after recrystallisation in ULC steels. In the present case the cold rolled texture exhibits a stronger rotated cube component as well as a strong α fibre, cf. figure 5.2.

Figure 5.4 also includes the $\varphi_2=45^\circ$ sections of the samples that were annealed in the two-phase domain and quenched at 950°C and 970°C with 10% and 50% of transformed volume fraction, respectively. These $\varphi_2=45^\circ$ sections show an overall increase in the intensity of the surface texture but the texture components are essentially the same as the ones observed in the recrystallisation texture consisting of a strong rotated cube component, a partial α -fibre and a γ - fibre of weak intensity.

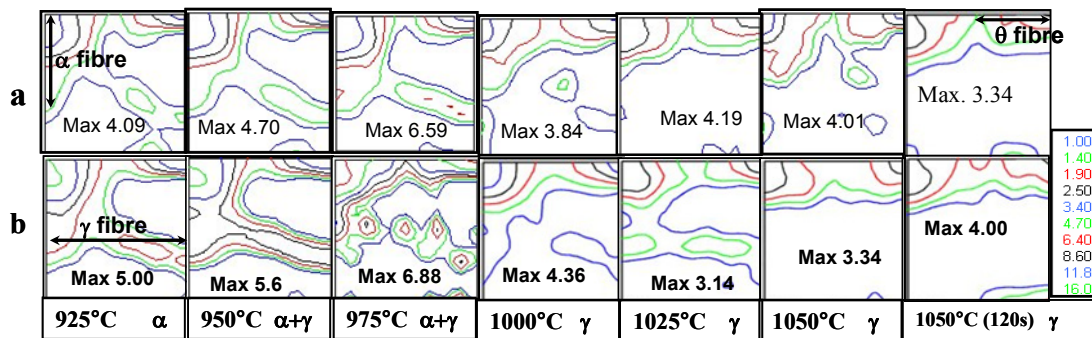


Figure 5.4 $\varphi_2=45^\circ$ sections of ODFs measured after interrupted annealing at different temperatures for alloys MnAl1 (a) and MnAl2 (b).

The $\varphi_2=45^\circ$ sections observed after annealing at 1000°C, 1025°C and 1050°C represent the textures after complete austenitization and subsequent Helium quenching. The surface textures after complete transformation display only a cube fibre with traces of the gamma fibre. The last $\varphi_2=45^\circ$ section shown in figure 5.4 displays the effect of a soaking time of 120s. After soaking it could be seen that the Goss component starts to appear which was not present in the $\varphi_2=45^\circ$ sections without soaking. Both compositions MnAl2 with higher manganese and MnAl1 with lower manganese show a similar surface texture evolution at each reheating stage. It is important to note that in these experiments with a high quality vacuum (10^{-6} Torr.) and helium quenching the intensity of the cube fibre (~ 3 to 4 random levels) in the surface texture has improved in comparison to the surface texture (~ 2.0 random levels) observed in the previous short phase transformation annealing under low vacuum (10^{-4} Torr.) and air cooling (cf chapter3, figure. 3.4).

In addition to the X-ray texture examination the same samples were also characterized by orientation imaging microscopy over the entire cross-section, i.e. on the ND-RD section in the alloys MnAl1 with low manganese and aluminium content and on the RD-TD surface sections in the alloys MnAl2 with high manganese and aluminium content. Figure 5.5 shows a few selected inverse pole figure maps of the alloys MnAl1. The first inverse pole figure (IPF) map shows the homogeneous recrystallised microstructure with polygonised grains across the entire thickness of the measured sample. The next inverse pole figure map shows the intercritical annealed microstructure which consists of a mixture of transformed grains which are larger in size with irregular grain boundaries and also recrystallised grains which are smaller in size with polygonal shape. The third inverse pole figure shows the complete transformation structure observed on the sample annealed at 1050°C with 120s of soaking time. The surface grains exhibit a columnar morphology just at the edge of the sample.

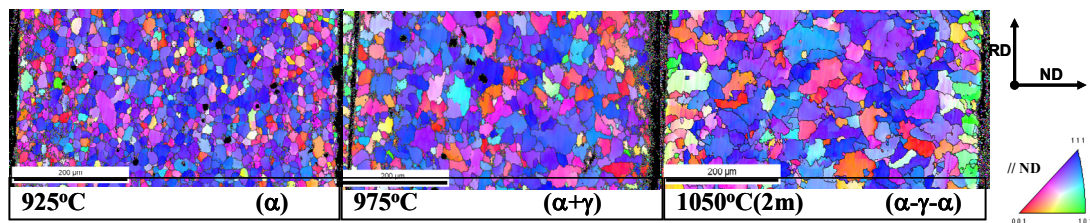


Figure 5.5 Inverse pole figure map of alloy MnAl1 with low Mn and Al measured after interrupted annealing at different temperatures.

Underneath the surface grains the bulk texture with blue coloured grains is observed representing the strong γ fibre texture which is typically observed after complete phase transformation in manganese alloyed ultra low carbon steels [12] and which is attributed to the texture memory effect. Equally common for the texture memory effect is the appearance of rather large grains with very irregular grain boundaries [13]. The other laboratory cast material MnAl2 with high alloying content of Mn and Al was orientation imaged on the RD-TD surface of the annealed samples after quenching at different temperatures. The inverse pole figure maps of some selected

samples are shown in figure 5.6. The grain orientation and grain size in the RD-TD surface varied with the temperature during heating. The structure observed after quenching at 925°C clearly indicates that the surface has undergone recrystallisation before the onset of transformation. After quenching at 950°C and 975°C in the inter-critical range, the OIM scans represent a partially transformed structure. Above 1,000°C a complete forward and reverse transformation loop takes place and the samples quenched at 1000, 1025, 1050°C + 120 s soaking time show a very similar and unique microstructure with large and irregularly shaped grains. It can be observed that the grains are comparatively large (~150 μm), i.e. much larger than in the two-phase or the ferrite recrystallisation domain. More importantly, the grains exhibit an internal orientation gradient which accumulates from the centre towards the edge of the grain misorientation as high as 15°. The surface texture measured from these surface grains is in good correspondence with the X-ray texture, i.e. it shows that the dominant colours are red and green corresponding to the {110} and {001} grains. For a more detailed analysis of this peculiar surface structure the reader is referred to Chapter 6.

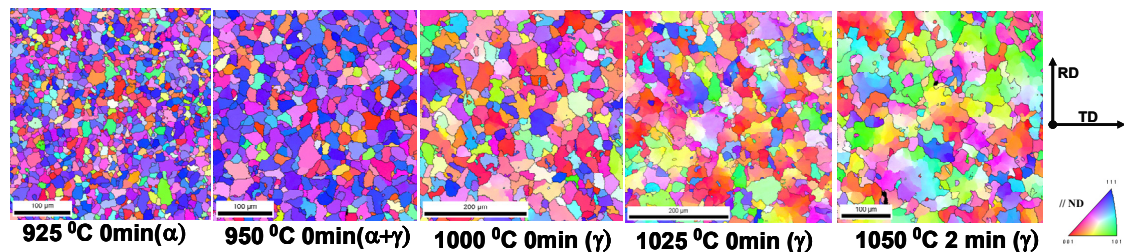


Figure 5.6 Inverse pole figure maps of alloy MnAl2 measured after interrupted annealing at different temperatures.

5.3.3. Surface texture and microstructure during interrupted annealing in the low carbon steel (LC)

The low carbon steel was also used to investigate the surface texture evolution during interrupted annealing. Small samples (5mmx10mm) were prepared from the cold

rolled sheet of the low carbon alloy (LC) with 0.047 wt% carbon and 0.17wt% silicon content. Later these samples were heated to a particular temperature and immediately quenched with helium gas. Different temperatures were selected to cover the various structural stages of the annealing treatment corresponding to the ferrite recrystallisation, the intercritical and the complete transformation stage. Figure 5.7 shows the dilatation curve during heating with the transformation start temperature $A_{c1} = 875^{\circ}\text{C}$ and the finish temperature $A_{c3} = 925^{\circ}\text{C}$. Three quench temperatures (800, 825 and 850°C) are below A_{c1} and thus lie in the ferrite recrystallisation region. The quench temperatures 875, 900 and 925°C cover the intercritical range whereas samples were quenched from the full austenite range with corresponding quench temperatures 950, 975 and 1000°C , well above the A_{c3} temperature.

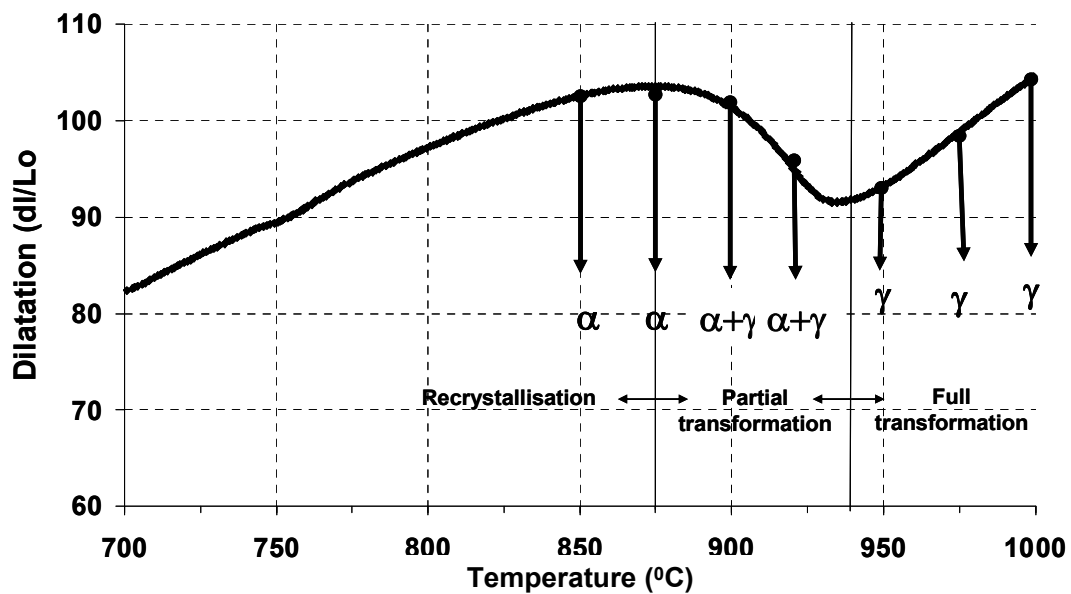


Figure 5.7 Dilatation curve during heating. Selected quench temperatures are indicated with an incremental change of 25°C for LC alloy.

The texture of the quenched sample was determined both by X-ray diffraction measurements (pole figures) and orientation imaging microscopy in the scanning electron microscope. Figure 5.8 shows the surface texture in the $\varphi_2 = 45^{\circ}$ sections of Euler space. The first two $\varphi_2 = 45^{\circ}$ sections show the recrystallisation texture of the samples quenched at 800°C and 850°C . The overall intensity of the surface texture

after recrystallisation is weak (2 times random). The rotated cube texture component in the recrystallisation texture is slightly stronger than the gamma fibre. Figure 5.8 also shows the surface texture evolution after intercritical annealing at 875, 900 and 925°C which corresponds to approximately 10%, 50%, and 95% of phase transformation. Also these ODFs reveal overall weak textures irrespective of the degree of transformation. The surface texture components after intercritical annealing are similar to the ones found in the recrystallisation texture, even with similar intensities which is different from the ULC alloys MnAl1 (low Mn, Al) and MnAl2 (high Mn, & Al) which exhibit an increasing texture strength with increasing annealing temperature.

Figure 5.8 also includes the surface textures after reheating to the full austenite phase domain (above the Ac3 temperature) corresponding to quench temperatures 975, 1000°C and 1000°C + 120s holding time. The ODFs after complete transformation appear to be quite similar to the surface textures obtained after recrystallisation and intercritical annealing. In contrast to the alloys MnAl1 and MnAl2 the present low carbon steel alloy does not develop an explicit <100>//ND fibre texture and (weak) <110>//ND fibre after full austenite annealing. In the present case the surface texture seems to be less affected by surface anisotropy effects and less sensitive to the forward and reverse phase transformation during annealing. The present alloys LC has a much higher carbon content of 470 ppm as compared to the ULC steel alloys with 20 ppm carbon, which could lead to decarburization and might influence the variant selection mechanism of texture evolution leading to an overall weak texture at all stages of phase transformation annealing.

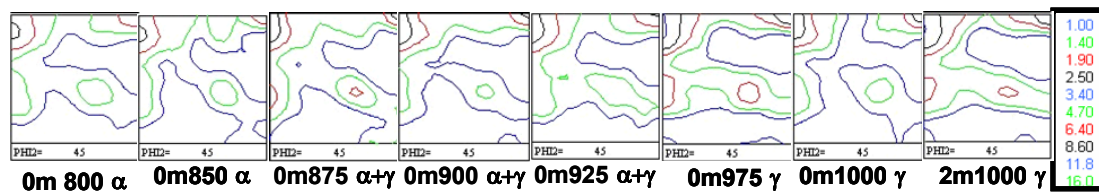


Figure 5.8 $\varphi_2=45^\circ$ sections of ODFs measured after interrupted annealing at different temperatures for low carbon steel (LC) alloy.

Figure 5.9 shows the inverse pole figure maps recorded by orientation imaging microscopy after recrystallisation, intercritical and transformation annealing without and with soaking time of two minutes. The first inverse pole figure map shown in figure 5.9 represents the recrystallisation microstructure with polygonal equi-axed small grains of average diameter of 20 μm . The OIM maps also show that the majority of the orientations belong to the $\langle 111 \rangle // \text{ND}$ fibre (bluish grains) and the $\langle 100 \rangle // \text{ND}$ fibre (reddish grains) which corresponds to the observations of the XRD measured ODFs. The second inverse pole figure map, collected on an intercritically annealed sample (quenched from 900°C), also shows a rather fine grain structure ($d = 15 \mu\text{m}$) with orientations similar to the recrystallisation ones.

Textures and microstructures are very little affected by the forward and reverse transformation loop as can be observed from the inverse pole figure maps recorded after complete transformation at 1000°C without soaking and with a soaking time of 120 s, respectively (cf. figure 5.9). The grain size of the LC alloy remains comparatively small (20 μm) in comparison to the ULC steels alloyed with manganese and aluminium (MnAl1 and MnAl2) which exhibited a much large grain size (150 μm) after complete phase transformation. The small grain size could be due to the high carbon content which might have hindered grain growth. Moreover, the surface grain morphology is also completely different with neither irregular grain boundaries nor ingrain orientation gradients which were observed on ULC steels alloyed with manganese and aluminium.

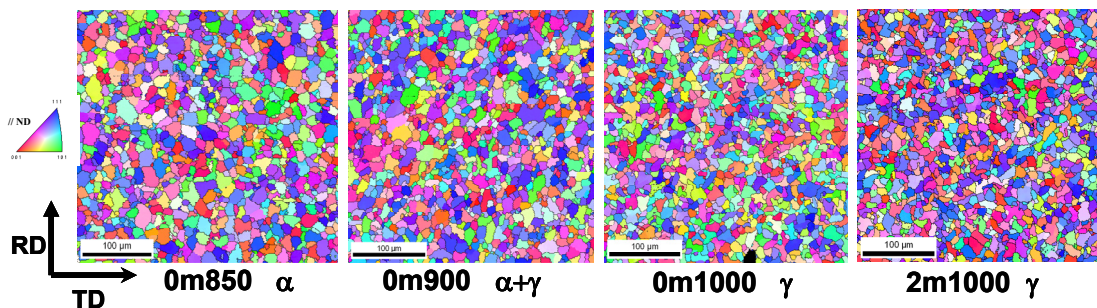


Figure 5.9 Inverse pole figure maps of alloy LC after interrupted annealing.

5.3.4. Surface texture and microstructure during interrupted annealing in ULC steel alloyed with high silicon (Si2)

This steel is an industrially hot rolled grade of fully processed non oriented electrical steel. It is basically a ULC steel alloyed with 1.38 wt% silicon that was investigated in the present study to see the surface texture evolution under high vacuum (10^{-6} Torr) annealing. Small size samples (5mm x 10 mm) were prepared from the cold rolled (75%) sheet of these alloys and then heated to different temperatures up to a maximum of 1,125°C with incremental steps of 25°C according to the dilatation curve as shown in figure 5.10. The complete dilation heating curve was divided in three parts corresponding to the full ferrite (recrystallisation) phase, the two-phase domain and to the full austenite range. The dilation curve during heating shows that $Ac1 = 1050^{\circ}C$ which is the transformation start temperature and $Ac3 = 1075^{\circ}C$, the temperature at which the transformation completes from ferrite to austenite. From the successive reheating temperatures the samples were quenched to room temperature with helium gas. The surface texture was determined by X-ray diffraction on the RD-TD surface and by orientation contrast microscopy on the same section, which was prepared by gentle mechanical polishing (so as to avoid removing the critical surface layer of the sheet sample).

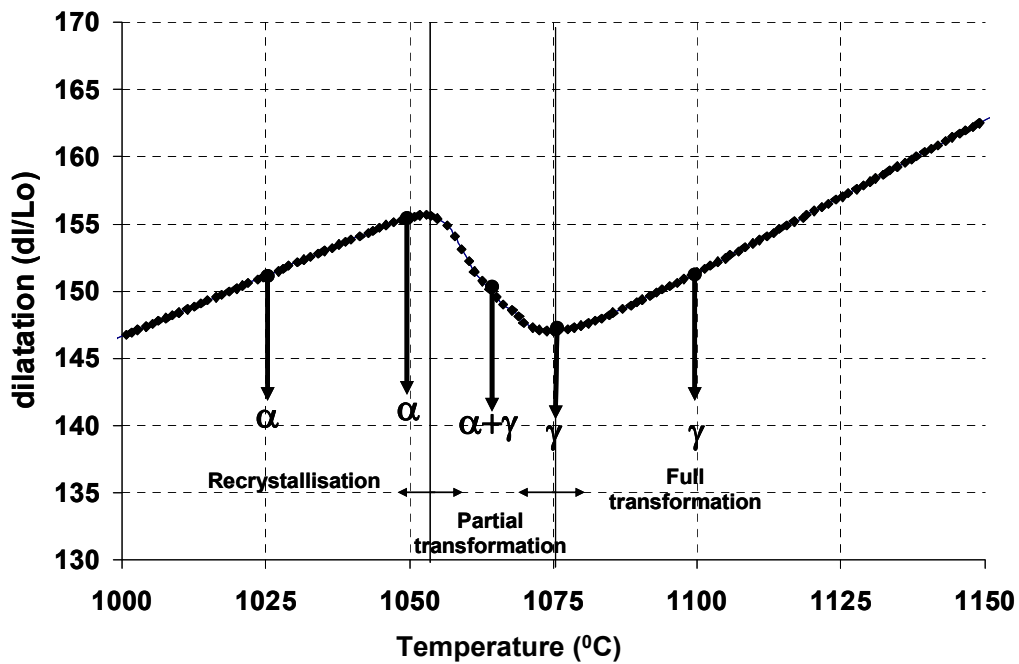


Figure 5.10 Dilatation curve during heating with selected temperatures at which the annealing treatment was interrupted for the alloy Si2.

Figure 5.11 shows the $\varphi_2=45^\circ$ sections revealing the surface texture evolution as determined by X-ray pole figure inversion. The first $\varphi_2=45^\circ$ section shows the surface after recrystallisation annealing which is dominated by a maximum on the α -fibre in the vicinity of the rotated cube component. Together with this maximum some scattered intensity is present along the γ -fibre and the $\langle 100 \rangle // ND$ fibre. The second $\varphi_2=45^\circ$ section of figure 5.11 represents the texture that was obtained after helium quenching at 1,050°C which corresponds to the A_{c1} temperature. It still very much resembles the recrystallization texture of the previous sample quenched at 1,025°C. The third $\varphi_2=45^\circ$ section shows the surface texture recorded at the end of the intercritical stage, corresponding to a quench temperature of 1,075°C. The surface texture components found in this section are few but prominent. These components belong to the $\{h11\} \langle 1/h,12 \rangle$ fibre[15]. Some residual intensity on the gamma fibre is also present after intercritical annealing. These texture components could be

considered as an indication of a gradual transition towards the surface type texture typically observed after annealing in the full austenite region of the lower Si grades MnAl1 and MnAl2. The fourth $\varphi_2=45^\circ$ section of figure 5.11 shows the surface texture after complete transformation at 1,100°C which reveals a stronger rotated cube component and a further weakening of γ -fibre.

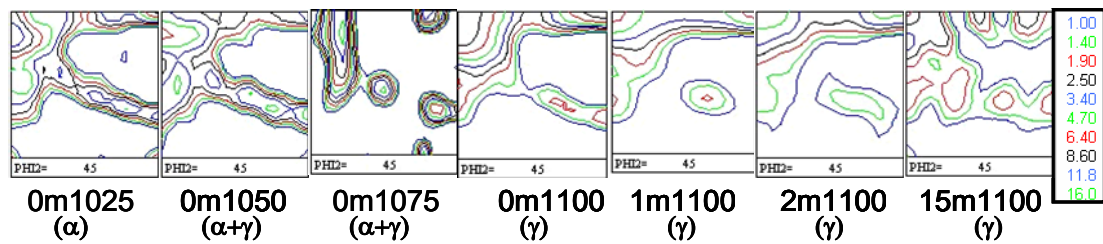


Figure 5.11 $\varphi_2=45^\circ$ sections of ODFs measured after interrupted annealing at different temperatures on sample Si2.

The last three $\varphi_2=45^\circ$ sections show the effect of extended holding at 1,100°C for 60, 120 and 900s, respectively. It could be seen that with increasing soaking time up to 120s the intensity of the cube fibre has increased (5 times random) whereas the intensity of the gamma fibre has decreased. However, the ODF of the sample that was held for 900s (15 min) at 1,100°C exhibits a decrease of cube fibre intensity whereas the γ -fibre components start to re-appear. This gradual change in surface texture during transformation annealing could not be observed in the previous experiments which were performed on the ULC steel alloy with high silicon content, but under low vacuum (10^{-4} Torr.) and with air cooling. The same alloy (Si2) in the present experiments with high vacuum (10^{-6} Torr) and helium quenching has led to a dramatic change in orientation selection during transformation which produces a strong surface texture with predominant cube fibre.

The inverse pole figure maps and corresponding $\varphi_2=45^\circ$ sections of the OIM measurements are shown in figure 5.12 below. The first inverse pole figure shows a recrystallised microstructure with polygonised grain structure with an average grain size of 20 μm . The second inverse pole figure map of figure 5.12, collected on a

sample quenched at 1,050°C (=Ac1), shows that the structure was partially transformed as some grains could be observed of increased size. The third inverse pole figure gathered after quenching at 1,075°C shows the nearly fully transformed structure with predominantly large grains. The fourth inverse pole figure map of figure 5.12 represents the microstructure quenched at 1,100°C, i.e. after complete transformation more than 100°C above Ac3. This map shows an increased amount of cube grains (reddish colour) and a reduced number of gamma fibre grains (bluish in colour). The grain size is large ($d \approx 100 \mu\text{m}$) in comparison to recrystallised or intercritically annealed grains. The last two inverse pole figure maps show the effect of soaking at 1,100°C in the full austenite region. It can be seen that with an increase in soaking time after transformation extensive grain growth has occurred which has given rise to a microstructure with an average grain size of 150 μm . The grain growth process has also produced an intensification of the texture with a more pronounced maximum on the $\langle 100 \rangle // \text{ND}$ fibre. However, it is important to note that the characteristic in-grain orientation gradient is absent in these grains as it is present in alloys MnAl1 and MnAl2.

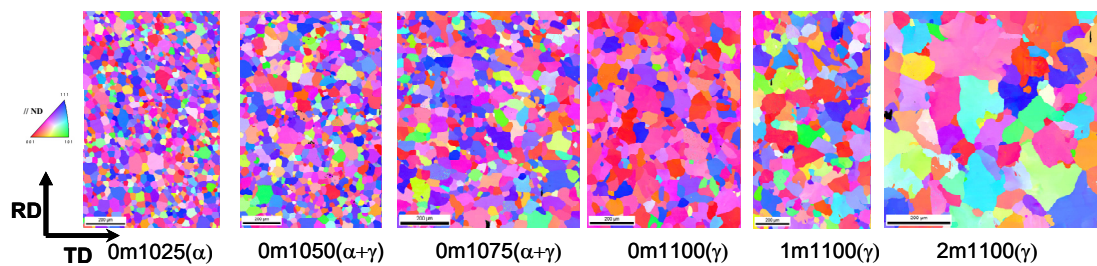


Figure 5.12 Inverse pole figure maps of alloy Si2 measured after interrupted annealing at different temperatures.

5.3.5. Surface texture and microstructure during interrupted annealing in ULC steel alloyed with low silicon (Si1)

The non oriented fully processed electrical steel denominated as Si1 alloyed with 0.5 wt% silicon was annealed in a similar manner under high vacuum (10^{-6} Torr) in

the dilatometer. The samples were prepared from the cold rolled sheet of 0.5 mm thick. Later, these samples were heated to different temperatures up to 1,200°C in incremental steps of 25°C represented as dark triangle in the dilatation curve in figure 5.13. The sample of the alloy Si1 shows the transformation start temperature Ac1 at 1,050°C and the transformation finish temperature at 1,100°C.

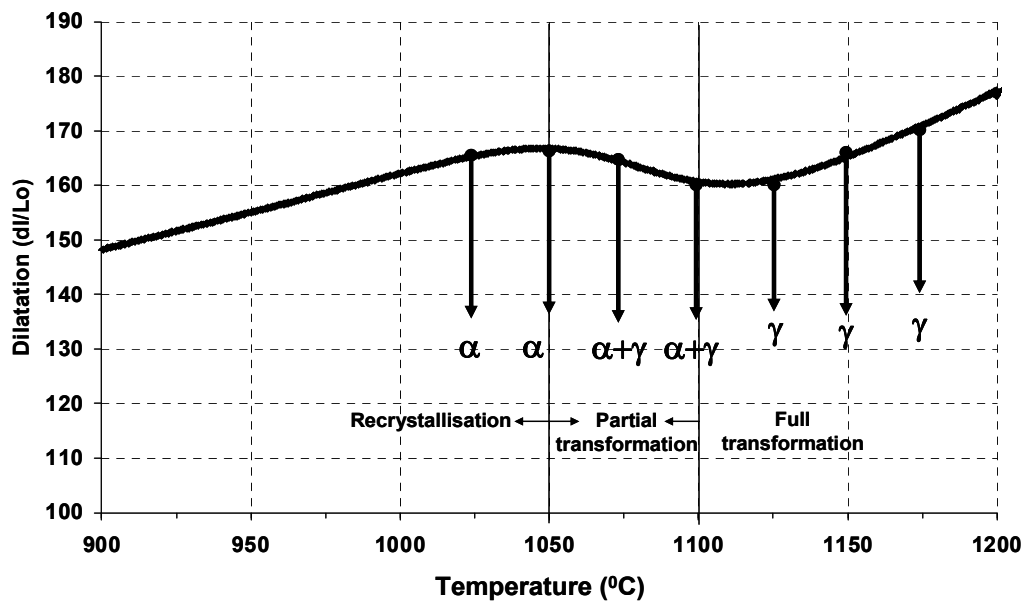


Figure 5.13 Dilatation curve during heating with the temperatures at which the annealing treatment was interrupted for the alloy Si1.

The surface texture evolution at different temperatures is illustrated by the $\varphi_2=45^\circ$ sections of the Euler space in figure 5.14. The first $\varphi_2=45^\circ$ section at 1,050°C shows the surface texture formed after recrystallization annealing in the full ferrite domain. The ODF shows weak texture intensity with a typical γ -fibre and residuals of other texture components. The second and third $\varphi_2=45^\circ$ section in the figure 5.14 represents the product surface texture obtained after annealing in the partially transformed domain by interrupted annealing at 1,075 and 1,100°C. The overall intensity of the surface texture after partial transformation has increased in comparison to the recrystallisation surface. It is remarkable to observe that these textures exhibit a

maximum on the $\langle 100 \rangle // \text{ND}$ fibre, although there is plenty of residual intensity on α and γ -fibre components.

The $\varphi_2=45^\circ$ sections of the ODFs observed on samples that were quenched at 1125°C, 1175°C and 1200°C show the surface texture after complete transformation. These surface textures exhibit a similar trend as the one already emerged on the samples annealed in the two-phase domain, i.e. the overall ODF maximum is located on the $\langle 100 \rangle // \text{ND}$ fibre with a broad intensity spread towards the α and γ -fibres. The same texture morphology can be observed on the samples that were annealed over an extended time lapse of 60 and 120 s at 1,200°C. It could be seen that, in general, the surface texture after has not changed, although there is a gradual development of a new fibre which is apparently parallel to the alpha fibre on a $\varphi_2=45^\circ$ section but which in reality represents a $\{h11\} \langle 1/h,1,2 \rangle$ fibre. This is an entirely new texture fibre which could not be observed in the previous experiments on the same alloys heated to the same temperatures and soaking times but under low quality vacuum.

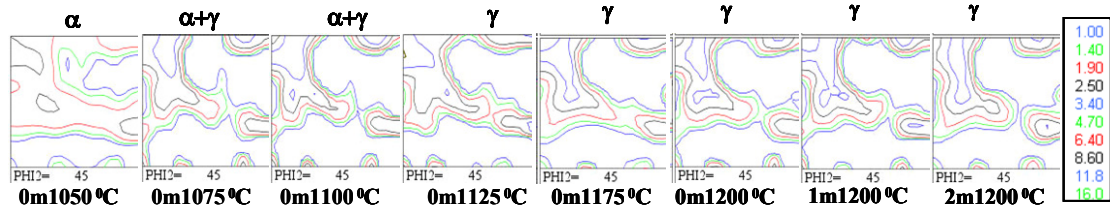


Figure 5.14 $\varphi_2=45^\circ$ section at different temperatures during heating up to 1200°C for the alloy Si1.

The inverse pole figure maps of selected samples from each separate zone of the dilation heating curve are shown in figure 5.15. The first inverse pole figure map represent the surface texture after recrystallisation annealing interrupted at 1,050°C. It shows the recrystallised grains of a polygonal and equi-axed shape (average grain size 30 μm). The second inverse pole figure shown in figure 5.15 represents the surface texture after partial transformation. There is not much change in the microstructure

and in the average grain size (30 μm). The last two inverse pole figure maps of figure 5.15 show the surface microstructure after complete phase transformation at 1,150°C and after 120 s of soaking time at 1,200°C. The inverse pole figure maps after complete transformation without soaking and with soaking do not show much difference in grain structure as well as in the grain size. It can be noticed that grains remain nearly equi-axed, also above the A_{c3} temperature, and also in-grain orientation gradients as observed in samples MnAl1, MnAl2 are totally absent in this case. Therefore, it can be concluded that for the lower Si grades the appearance of a characteristic surface type texture with a $\{001\}$ fibre (and to a lesser extent also $\{110\}$ fibre) is structurally accompanied by large grains with irregular grain boundaries and a significant internal grain orientation gradient. In case the specific texture is absent also these accompanying structural features have not emerged.

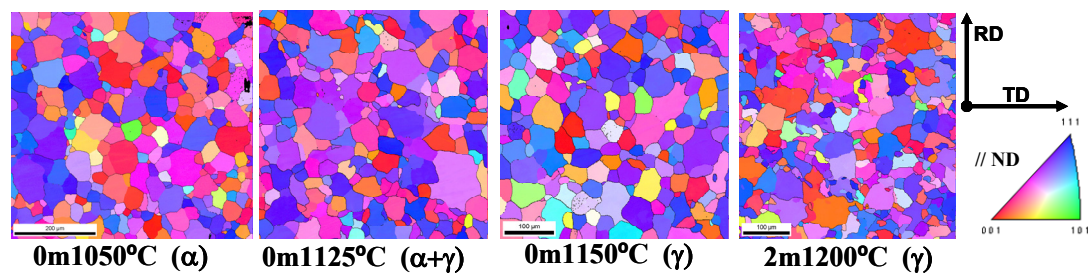


Figure 5.15 Inverse pole figure maps obtained after interrupted annealing at different temperatures in the alloy Si1.

5.3.6. Contact annealing experiment

The compositional depth profiles obtained by XPS and GDOES suggest two different types of oxidation that take place during annealing due to different chemistries of the alloys. The ULC steel alloyed with high silicon did not reveal the specific surface texture with cube fibre under low vacuum annealing conditions, whereas the ULC alloys with manganese and aluminium did show the surface texture with cube fibre and Goss components under identical annealing conditions. The compositional depth profiles have shown that the Si alloyed compositions exhibit an internal oxidation

layer of Si oxides which extends over a much wider range than the internal oxidation layer in the Mn/Al alloyed steels. This has led to the assumption that the internal oxidation layer is detrimental for the development of the appropriate {001} surface texture.

With this thought in mind an additional experiment was designed which aimed to carry out a transformation annealing treatment with less internal oxidation of the Si alloyed steel. To this purpose two cold rolled sheets of alloys Si1 and Si2 were sandwich stacked between two Mn/Al ULC steels. In this way the Si alloyed steel surface could be protected against over-exposure to the O₂ contaminated vacuum of the furnace. The schematic of the setup is shown in figure 5.16. These tied up sheets were annealed under low vacuum conditions (10⁻⁴ Torr) at 1,200°C which is well above the Ac₃ temperature of alloys Si1 and Si2. The heating rate was 15°C/s and after annealing the sheets was air cooled in low vacuum.

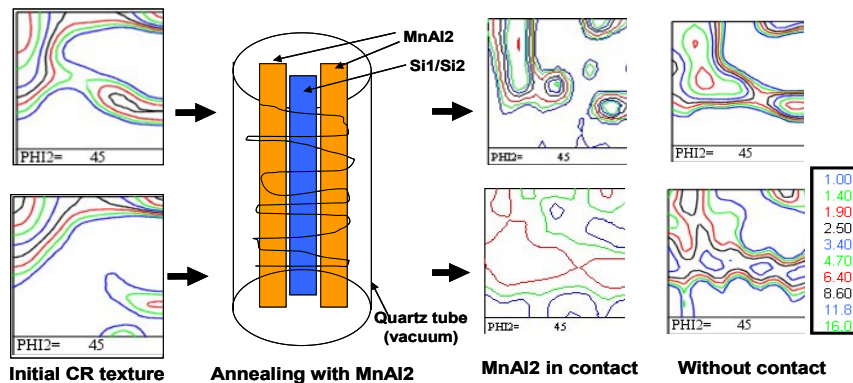


Figure 5.16 The initial surface texture of cold rolled sheets, scheme of contact annealing and final x-ray texture results of alloys Si1(top) and Si2 (bottom).

Figure 5.16 shows the $\phi_2 = 45^\circ$ sections of the Si alloyed ULC steel after annealing in contact with MnAl₂ and without contact which were measured by X-ray diffraction. The $\phi_2 = 45^\circ$ sections of the high Si alloy Si₂ shows a weak almost random surface texture on the annealed sheet surface. The low Si alloy Si₁ shows a surface texture with a strong {h11}<1/h,1,2> fibre which is very much similar to the surface texture

exhibited by the same alloy after transformation annealing under high vacuum conditions at 1,200°C with a soaking time of 120s, cf. figure 5.14.

5.4. Discussion

On the basis of these findings we can come up with a list of parameters that need to be optimized in order to obtain the strongest $\{001\}$ ($\{110\}$) surface texture:

1. Complete transformation is necessary during annealing with the annealing temperature well above A_{c3} ;
2. The chemical composition of the steel should be closely monitored. With higher Si content it gets more difficult to obtain a better surface texture;
3. A clean environment, i.e. better quality vacuum, is instrumental to stimulate the wanted $\{001\}$ ($\{110\}$) surface texture. This is particularly true for the high Si alloyed grades;
4. The austenitic soaking time appears to have an optimum value which was for the current tests determined at ~ 120 s. At lower holding times the $\{001\}$ surface texture has not gained its optimum strength whereas at increased holding times the $\{001\}$ fibre intensity decreases at the expense of $\{110\}$ and γ -fibre intensity.
5. The initial texture prior to α - γ - α does not seem to play a crucial role in determining the strength of the $\{001\}$ ($\{110\}$) surface texture (cf. chapter 3 , figure 3.12).

The requirement of a complete α - γ - α transformation can be understood from the viewpoint of texture variability that is introduced by the double phase transformation. The orientation relation between parent and product orientations in a ferrite-austenite phase transformation is generally described by specific orientation relations of the type YKS ($\{111\}_{\gamma} // \{110\}_{\alpha}$ and $\langle 110 \rangle_{\gamma} // \langle 111 \rangle_{\alpha}$ with 24 variants) or NW ($\{111\}_{\gamma} // \{110\}_{\alpha}$ and $\langle 112 \rangle_{\gamma} // \langle 110 \rangle_{\alpha}$ with 12 variants), cf. figure 5.17. With the YKS correspondence a double α - γ - α transformation would entail $24^2=576$ product orientations originating from one single parent orientation.

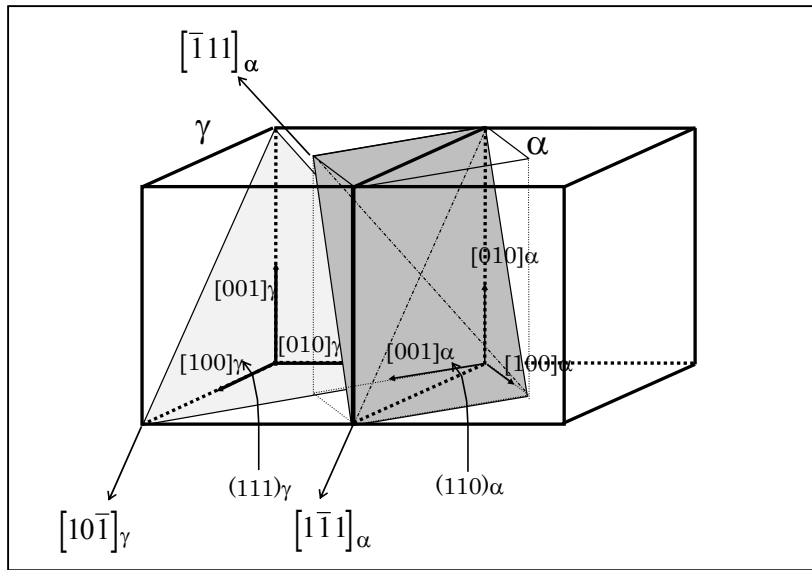


Figure 5.17 Kurdjumov-Sachs relationship between γ and α showing the parallelism between $(111)[01\bar{1}]_\gamma$ and $(110)[1\bar{1}\bar{1}]_\alpha$.

Fig. 5.17 represents the product ferrite texture that is produced by a double transformation with the initial texture either a α/γ fibre texture, as represented by Fig.5.17b or a ferrite surface shear texture as represented by Fig. 5.17a.

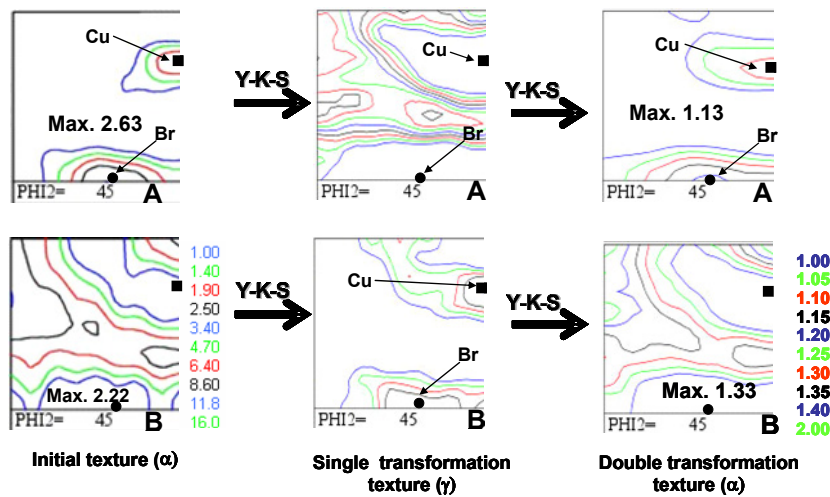


Figure 5.18 Simulated texture evolution after α - γ - α transformation with different initial ferrite texture.

It can be noticed that the YKS correspondence transforms the low-temperature ferrite texture in a high-temperature austenite texture with a dominant Cu component, a Br component and orientation spread towards the Goss component and the cube. When the low-temperature ferrite texture consists of a $\{110\}$ fibre with maximum at the Br component and a Cu component, the austenite transformation texture exhibits the α/γ fibre morphology. After back transformation to the low-temperature ferrite, a product texture is obtained with essentially the same morphology as the original parent ferrite texture, but of much weaker intensity (compare e.g. max. of 2.63 random levels of figure 5.18a to 1.13 random levels after double transformation and max. of 2.21 random levels to 1.33 random levels of figure 5.18b).

This simple calculation proves the point of *texture variability*, i.e. a larger random texture component is introduced by forward and reverse phase transformation as compared to the random component produced by other solid state transformation processes such as recrystallisation and grain growth occurring at lower temperature. It is this random texture component that provides room to select alternative components (such as $\{001\}$ and $\{110\}$ fibre components) by the additional selection mechanism of surface energy minimization.

The role of the vapour environment becomes clear, when the present results are considered in combination with the results of Chapter 4. In chapter 4 it was demonstrated that particularly the Si bearing grades are susceptible to internal oxidation. In the grades Si1 and Si2 an oxidation layer was formed at the surface during annealing under low-vacuum conditions, cf. figure 4.11. This oxidation layer expands over 0.2-0.4 μm away from the surface. In the Mn and Al added steels the oxide layer was of more moderate extension ($< 0.1 \mu\text{m}$). This explains why the cleanliness of the annealing atmosphere is more important for the Si alloyed grades than for the Mn/Al bearing steels. The present results also indicate that by increasing the vacuum level (cf. results presented in figure 5.11) the surface texture also can be positively affected in the Si bearing grades.

Figure 5.19 illustrates that by increasing the surface adsorption of contaminating elements the surface energy anisotropy is drastically reduced [6]. With severe surface contaminations there is almost no surface energy anisotropy left, whereas at intermediate levels of contamination the surface energy of $\{001\}$ and $\{110\}$ crystal planes is reversed. The latter phenomenon might be responsible for the irregular observations about the ratio of the $\{110\}/\{001\}$ fibre intensities. In most cases it was found that the $\{001\}$ fibre exhibits the larger strength 2.16 times random in low vacuum and 3.34 with high vacuum (cf. figure. 5.4 and 3.6) whereas the strength of the $\{110\}$ fibre varied from non-existent to 1.60 times random in low vacuum and 1.40 times random in high vacuum. This would imply that even under high vacuum conditions, the sample surface still could be considered as slightly contaminated.

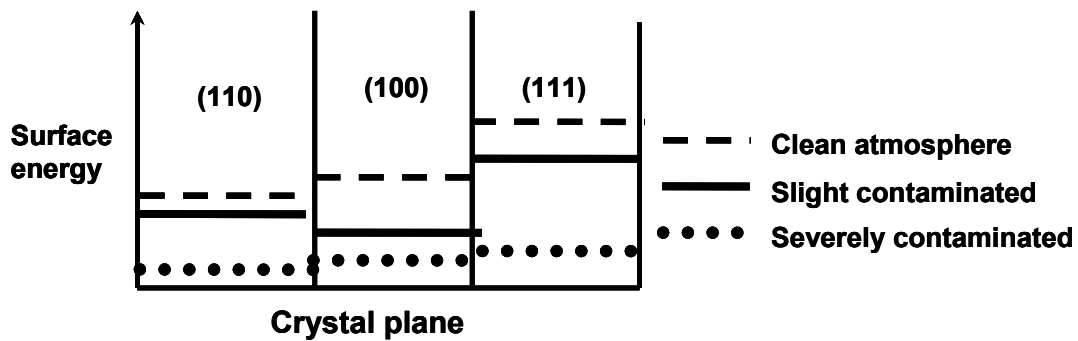


Figure 5.19 Schematic of surface energy anisotropy variation with different annealing atmosphere [6].

Observations reported in chapter 3 (cf. figure. 3.12) also have revealed the limited effect of the initial texture, although the simulation result of Fig. 5.17 might suggest otherwise. Accordingly to these simulations there is a slight preference of the initial texture in the final product texture after double transformation. One might expect e.g. that the potential presence of $\{110\}$ fibre orientations in the product texture in a sheet with a starting ferrite shear texture (cf. figure. 5.17), might give rise to an enhanced selection of this component as a result of surface energy anisotropy. The fact that this was not observed (cf. figure. 3.12), however, suggests that the random component

prevails in the selection mechanism and that the surface energy anisotropy mechanism basically acts on a random nucleation texture.

In some instances a different type of product texture is observed with exhibits a maximum along the $\{h11\}\langle 1/h\ 1\ 2\rangle$ fibre, cf. figure. 5.20.

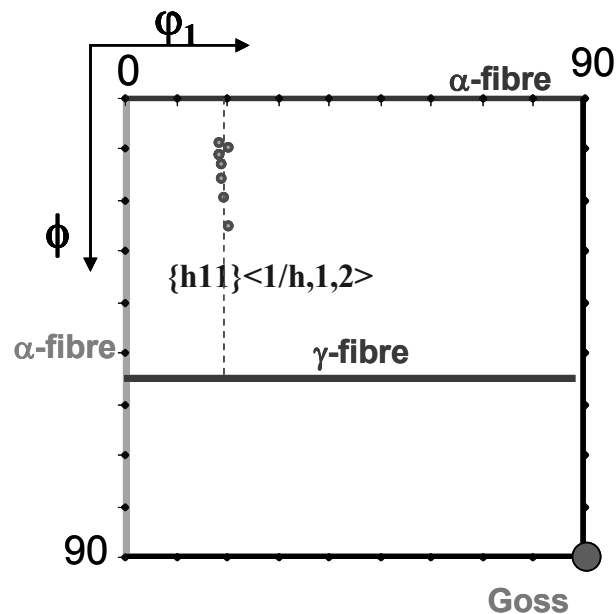


Figure 5.20 The $\phi_2=45^\circ$ section with $\{h11\}\langle 1/h,1,2\rangle$ fibre [15].

This fibre was extensively discussed by Gobernado et al [15, 16] and was considered as a recrystallization component appearing after annealing of a material of which the texture was dominated by a very strong rotated cube component after cold rolling. Some arguments were formulated to suggest that this $\{h11\}\langle 1/h\ 1\ 2\rangle$ fibre with the emblematic $\{311\}\langle 136\rangle$ component is the result of an oriented nucleation process in rotated cube orientations. In the present case this component shows up after transformation annealing of the low Si alloyed steel (Si1), cf. figure 5.14. Although the origin of this component under the present experimental circumstances remains largely unknown, it can be observed that also in this case the cold deformation texture exhibited a relatively strong rotated cube component, which is a point of similarity with the case reported by Gobernado et al. [15, 16]

5.5. Conclusions

The XRD texture investigations performed on the ultra low carbon steel alloyed with manganese and aluminium (MnA11 and MnA12) and alloyed with silicon (Si and Si2) reveal a noticeable change surface texture after α - γ - α transformation annealing in the dilatometer under high vacuum (10^{-6} Torr.). The effect of the vacuum quality became particularly obvious when observing the surface texture of the alloy with 1.38 wt% Si (Si2). In contrast to the low vacuum annealing conditions, after high vacuum annealing the characteristic {001} surface texture emerged on this material. It is concluded that the increased vacuum quality might have reduced the amount of surface oxidation and therefore, has led to a more pronounced surface energy anisotropy at the metal vapour interface which eventually has triggered the {001} orientation selection.

The orientation imaging microscopy performed on the RD-TD surface of the transformation annealed materials of the three ultra low carbon steels alloyed with manganese and aluminium (MnA11 and MnA12) and alloyed with silicon (Si2) exhibit a surface texture with cube fibre orientated grains confirming the X-ray texture results. The alloys MnA11 and MnA12 exhibit in-grain orientation gradients for the surface grains, whereas the alloy Si2 does not.

An increase in soaking time to more than 120s at above Ac3 triggers the appearance of other texture components like Goss or γ -fibre in the three ultra low carbon steel alloyed with manganese and aluminium (MnA11 and MnA12) and alloyed with 1.47wt% silicon (Si2).

The ULC steel alloyed with 0.51 wt% Si (Si1) exhibits a strong {h11}<1/h,1,2> fibre texture after transformation annealing, very much similar to the conventional recrystallization texture observed in ultra low-carbon steels of which the cold rolling texture is dominated by a strong rotated cube component. The origin of this {h11}<1/h,1,2> fibre texture after a forward and reverse α - γ - α transformation could not be traced here, but it was observed that also in this case the cold rolling texture is dominated by a strong {001}<110> (rotated cube) component.

The accurate control of the annealing atmosphere offers an important tool for texture control for the development of steel textures and offers an additional degree of freedom that cannot be obtained by conventional thermo-mechanical processes.

5.6. References

- [1] F. Assmus, K. Detert and G. Ibe, *Z. Metallkd.*, 48 (1957) p 341
- [2] S. Taguchi and A. Sakakura, *Kinzoku Butsuri*, 7 (1968) p 221
- [3] K. Detert, *Acta Metall.*, 7, (1959) p 589
- [4] J. L. Walter, *Acta Metall.*, 7, (1959) p 424
- [5] J. L. Walter and C. G. Dunn, *Trans. Metall. Soc. AIME*, 218, (1960) p 914
- [6] D Kohler *Journal of applied physics*, 31, (1960) p 5
- [7] L Kestens and S Jacobs, *Texture, Stress, and Microstructure Volume 2008* (2008)
- [7] O. Hashimoto, S. Satoh and T. Tanaka, *Tetsu-to-Hagane*, 66, (1980) p 102
- [8] O. Hashimoto, S. Satoh and T. Tanaka, *Tetsu-to-Hagane*, 66, (1980) p 112
- [9] R G Aspden, J. A. Berger and H. E. Trout, *Acta Metall.*, 16, (1968) p 1027
- [10] J. Gautam R. Petrov and L. Kestens, *Materials Science Forum*, 550, (2007) p 503
- [11] P. Van Houtte, *The MTM-FHM Software system Version2 Users Manual* (1995)
- [12] B. Hutchinson and L.Kestens, *Application to texture analysis, Ceramic transactions*, 48 (2007) p 2036
- [13] AC C Reis, L Bracke, R Petrov, W. J. Kaluba, and L. Kestens, *ISIJ International*, Vol. 43 (2003), No. 8, p. 1260
- [13] B. E. Sundquist *Acta Metallurgica*, Vol. 12, (1964)
- [14] B. Mills, M. Mclean, and E. D. Hondros, *Philosophical Magazine*, 27: 2, (1973) p 361
- [15] P. Gobernado, R. Petrov, D. Ruiz, E. Leunis, and L.A.I. Kestens, *Materials Science Forum Vols. 638-642* (2010) p 2829
- [16] P. Gobernado, R. Petrov, D. Ruiz, E. Leunis, and L. A. I. Kestens, *Adv. Eng. Mater.* Vol. 12 No.10 (2010) p 1077

Chapter 6

Surface texture and microstructure characterisation

It is well understood that surface energy anisotropy at the metal–vapour interface may have an impact on orientation selection during solid-state-transformation processes at the surface. This chapter reports a detailed characterization of the surface texture and microstructure using orientation contrast microscopy.

6.1. Introduction

The austenite-to-ferrite phase transformation, which is an inherent feature of low-alloyed low-carbon steels, has scarcely been investigated at the metal-vapour interface of a metal sheet. Hashimoto et al [1-3] investigated the α - γ - α phase transformation texture at the surface of an ultra low carbon cold rolled steel sheet and reported that a $\langle 100 \rangle // ND$ texture was formed rather than the usual $\langle 111 \rangle // ND$ texture. They interpreted this experimental result by assuming that the elastic work relaxation in the ND direction associated with the transformation could be larger than that in any other direction. Aspeden et al. [4] reported that an annealing treatment in the austenite phase followed by slow cooling in an ultra low carbon steel resulted in a stronger $\langle 100 \rangle // ND$ texture. They attributed this to the fact that this surface texture produces the lowest surface energy.

The surface textures reported in the literature do not include a precise description of the grain morphology and grain structure at the surface. Results in previous chapters reported a monolayer of surface grains after a short phase transformation annealing which produces a surface texture with $\{100\}$ and $\{110\}$ orientations very different from the conventional $\{111\}$ bulk texture. In this chapter the morphological and crystallographic nature of the surface texture and surface grains will be further explored and compared with the features of bulk metal grains.

6.2. Experimental

The ULC steel alloyed with manganese and aluminium denominated MnAl1 and MnAl2, with the chemical composition listed in Table 1 were hot rolled above the Ar3 temperature, air cooled and annealed at 700°C in order to simulate the slow cooling trajectory of the industrial hot band coiling process. After surface de-oxidization (pickling) the hot rolled sheets were cold rolled to a reduction of 70%.

Table 6.1 Chemical composition

Alloys	C	Mn	Si	Al
MnAl1	0.003	0.75	0.23	0.12
MnAl2	0.002	1.28	0.22	0.29

Table 6.2: Critical temperatures

	MnAl2	MnAl1
Ac1(°C)	940	949
Ac3(°C)	990	1000
Ar1(°C)	832	845
Ar3(°C)	884	910

In order to determine the critical transformation temperatures various heating and cooling experiments were performed in a dilatometer and the critical temperatures were derived from the dilatation curves, cf. table 6.2. A pyrox tube furnace was used for the transformation annealing treatment at 1,050° C under low vacuum (10^{-4} Torr.) as shown in figure 6.1 The cold rolled sheet samples were heated at the rate of 15°C/s to the temperature of 1,050°C; samples were held at this temperature for 120 s and subsequently cooled down to room temperature at a cooling rate of 30°C/s which is equivalent to air cooling.

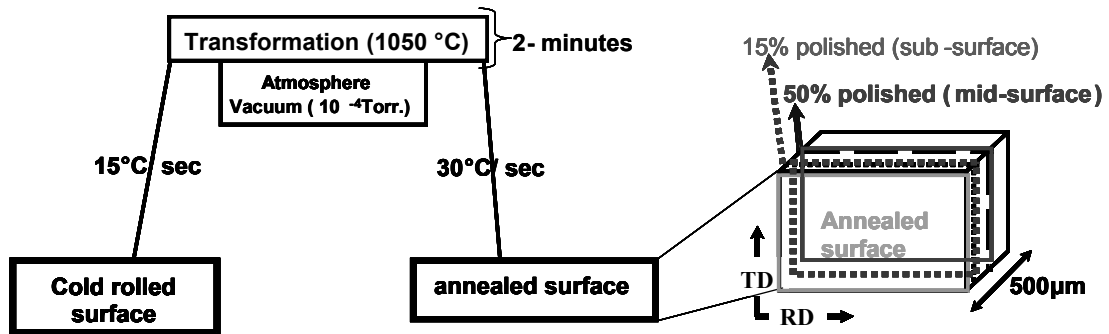


Figure 6.1 Schematic of transformation annealing and sample section for x-ray texture analysis.

6.3. Material characterization

First the surface textures were measured by X-ray diffraction on the clean cold rolled sheets. Afterwards these samples were subjected to the transformation annealing treatment and cooled down to room temperature. After annealing, the texture measurement was again performed on the sample surface and at 15 and 50% underneath the surface as well. The conventional X-ray diffraction method was used to measure the {100}, {110}, {211} and {310} pole figures. The orientation distribution function (ODF) was determined with the software developed by Paul Van Houtte [8]. Scanning electron microscopy observations were made on a FEI XL-30 microscope equipped with an EBSD detector that was used to perform orientation imaging microscopy (OIM) aiming to characterize the cross sectional texture gradient as well as the surface of the samples. The EDAX-TSL[®] software was used for data acquisition and post-processing of the grain orientation data.

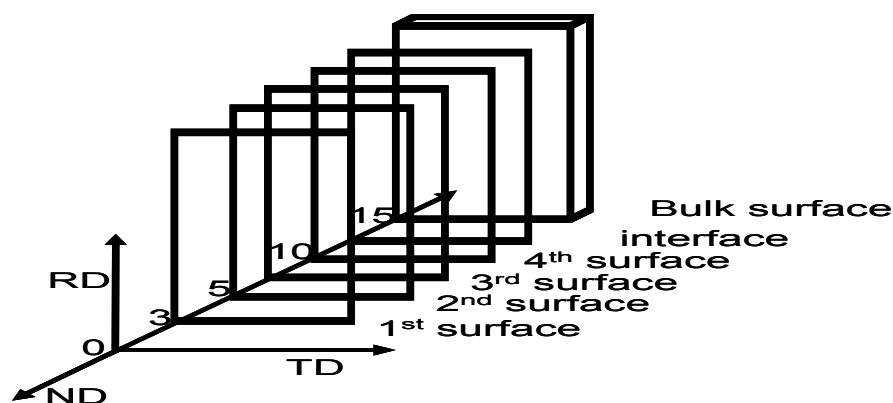


Figure 6.2 Schematic of serial sectioning underneath RD-TD surface for orientation contrast microscopy.

6.4. Serial sectioning of RD-TD surface

In an attempt to further characterize the surface details of the microstructure, serial sectioning was carried out as shown in figure 6.2. To the purpose of removing surface material in a semi-controlled manner the RD-TD surface was carefully mechanically polished with a cloth of fine grain silica emulsion till 5 μm underneath the first surface and this step of depth (5 μm) was kept constant for subsequent serial sections. During polishing the sheet thickness was regularly measured with a screw gauge with a precision of 1 μm . In between the polishing the same RD-TD surface cross sections were examined by orientation contrast microscopy for the materials MnAl1 and MnAl2.

6.5. Results

6.5.1. Microstructure and X-ray texture after transformation annealing

The two alloy compositions denominated as MnAl2 (high Mn and Al) and MnAl1 (low Mn and Al) were subjected to transformation annealing at 1,050°C. Figure 6.3 shows the bulk microstructure consisting of a single ferrite phase with grains of an average size of approximately 20 μm for the alloy MnAl1 and 17 μm for the alloy MnAl2. Figure 6.3 also shows the texture measured at the sample's RD-TD surface after cold rolling and the transformation annealing textures at the surface, sub surface

and in the mid section of the sheet. Cold rolling produces the conventional α/γ -fibre texture, which is commonly observed after rolling reductions of the order of 70 to 80% as in the present case. The intensity of the alpha and gamma fibre after cold reduction is around 5 times random which is weaker than the intensity of the bulk cold rolling texture after a cold rolling reduction of 70%.

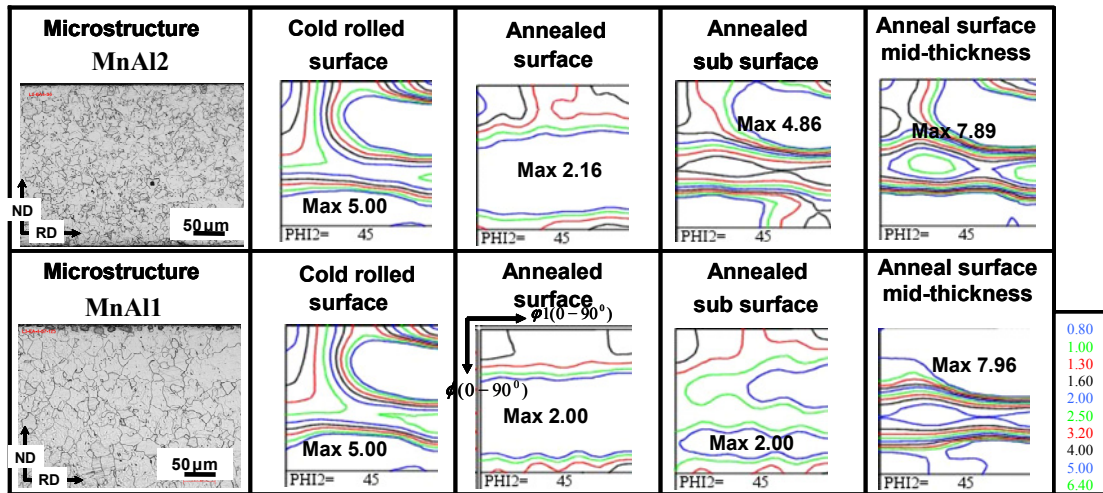


Figure 6.3 Through thickness optical microstructures and X-ray textures on the RD-TD surface and underneath the surface after phase transformation annealing for the alloys MnA2 (top) and MnA11 (bottom).

After complete transformation annealing, the $\phi_2 = 45^\circ$ section of the measured surface texture shows relatively weak (<2 random levels) $\{100\}$ and $\{110\}$ fibre components in both alloys with high and low manganese whereas the $\{111\}$ gamma fibre is completely absent after complete transformation. The subsurface, 15% underneath the outer surface layer, shows a much stronger γ fibre (8 times random) in the alloy MnAl2 with high manganese, whereas in alloy MnAl1 with low manganese content the sub-surface texture still exhibits the $\{110\}$ and $\{001\}$ fibres in combination with a weak γ -fibre. This suggests that surface texture in the low Mn alloy has extended further towards the bulk than in the high Mn alloy.

The mid-plane texture in both alloys exhibits a strong γ -fibre. In principle, the intensity of the bulk texture resulting from a double transformation may lead to a weak product texture due to the occurrence of many different symmetrically equivalent product orientations considering the YKS correspondence between parent and product orientations. However, strong bulk textures with intense gamma fibres have been widely reported in the literature [6]. This is generally attributed to the variant selection mechanism of *texture memory* [17,18].

6.5.2. Through thickness grain morphology

Although the X-ray texture analysis is statistically of excellent quality because of the large irradiated sample surface (commonly $> 1 \text{ mm}^2$) it does not contain any structural information.

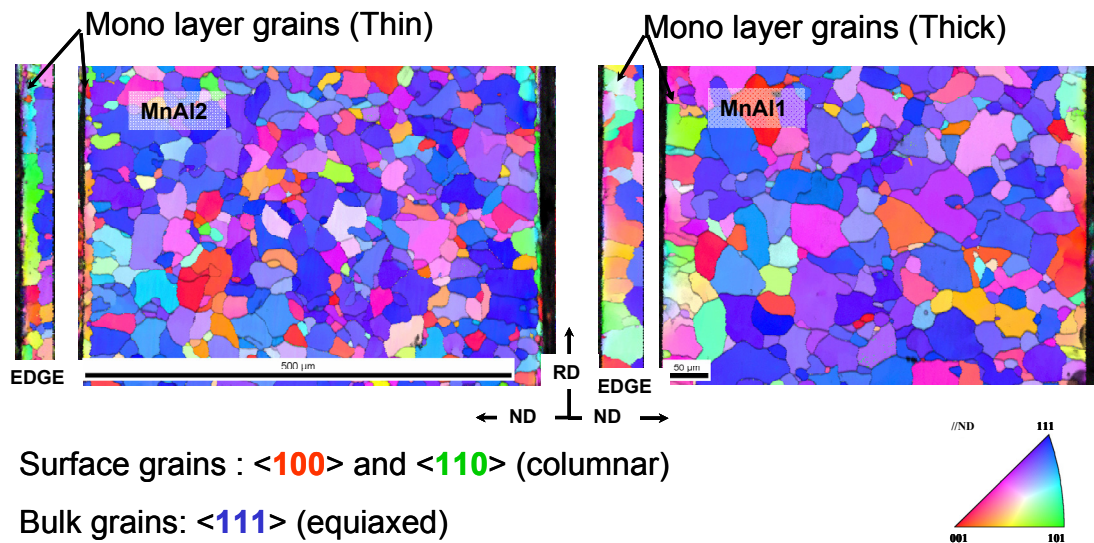


Figure 6.4 Inverse pole figure map after α - γ - α transformation in the RD-ND plane for materials MnAl2 (left) and MnAl1 (right).

Therefore, orientation imaging microscopy was carried out on the RD-ND sections of the samples MnAl1 and MnAl2 to investigate the microstructural and/or textural gradients across the thickness of the sheet. Figure 6.4 shows the inverse pole figure map of both alloys. A single layer of surface grains with specific orientations (predominantly $\langle 100 \rangle$ and $\langle 110 \rangle$ fibre grains) and morphology (columnar structure)

is present in both samples. It was noticed that material MnAl2 displays a thinner layer of surface grains (~15 microns) compared to material MnAl1 with a lower Mn and Al content (~30 microns). The bulk grains underneath the surface are typical equi-axed polygonal grains appearing after transformation with a predominantly blue colour, i.e. predominantly of $\langle 111 \rangle // \text{ND}$ orientations.

6.5.3. Grain morphology and grain boundary character at the transformed sheet surface

Orientation imaging microscopy was also performed on the RD-TD surface of the transformation annealed sheets. The inverse pole figure map recorded at the surface and subsurface of sample MnAl2 is shown in figure 6.5. Both inverse pole figure maps of figure 6.5 show that the majority of grains are of red or green colour. The red colour represents the $\{001\}$ orientations whereas green corresponds to $\{110\}$ orientation. This inverse pole figure map represents a similar texture as the one observed with X-ray texture analysis on the RD-TD surface. The first inverse pole figure map measured at the surface displays large grains, of approximately 200 μm in diameter, with irregular grain boundaries. The cube oriented grains appear to exhibit an X-shaped morphology which is the result of an in-grain orientation gradient. These shapes are even more prominent in the subsurface region which was recorded 5 μm underneath the outer surface.

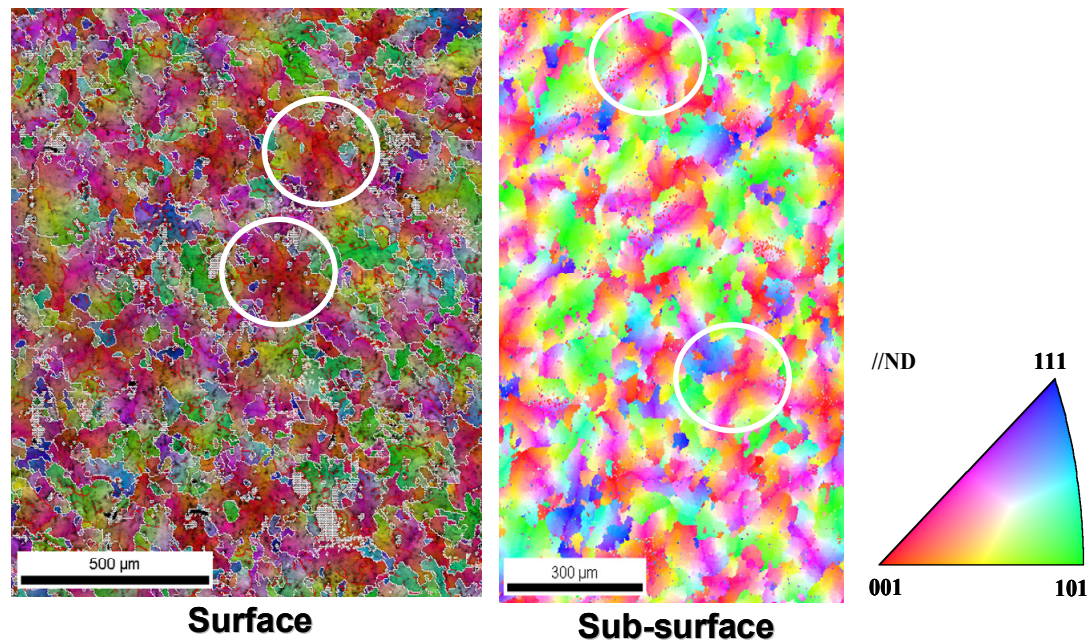


Figure 6.5 The inverse pole figure map measured at the outer-surface and sub surface (5 μm underneath the RD-TD surface) of sample MnAl₂.

Some of these cube grains were cropped out and investigated more in detail. The cube grain structure observed at the surface is very unique in terms of internal structure as revealed by the orientation contrast images. Figure 6.6 shows the inverse pole figure map of one cropped cube oriented grain with apparent X-shape morphology.

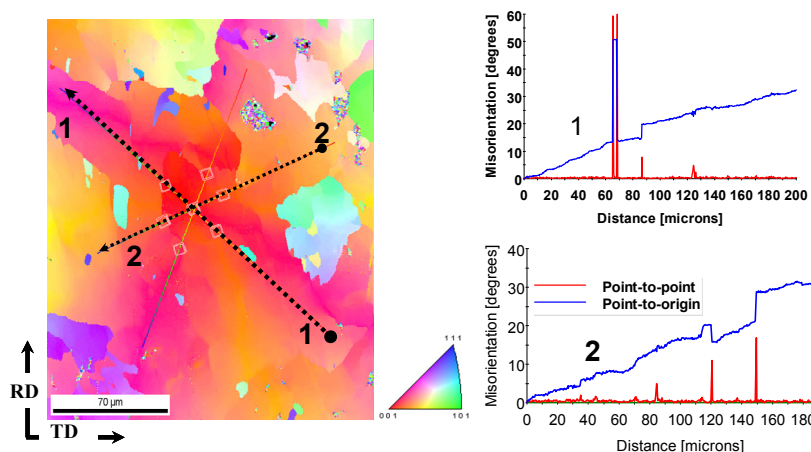


Figure 6.6 Orientation gradients inside a grain with apparent X-shaped morphology.

The cropped area was analysed for point-to-point and point-to-origin misorientation profiles across the grain and the results are equally shown in figure 6.6. This misorientation analysis shows a gradual and linear orientation change across the grain irrespective of the precise position of the line-scan (inside or outside the *legs* of the X-shape). The linear misorientation across the grain mounts up to 40° from one end to the other.

Another misorientation analysis was also considered and is presented in figure 6.7. The crystallographic misorientation was evaluated with increments of 5degree starting from the ideal cube orientation at the centre. It can be observed that the misorientation gradually builds up from the centre to the outer rim of the grain. The outer rim has accumulated a misorientation of ~40 with reference to the centre cube orientation. The X-shaped or flower like pattern arises in an ND inverse pole figure representation because the rotation axis is not constant but exhibits in-plane anisotropy and thus the crystal planes that are parallel to the surface of observation (RD-TD plane) also vary along a circular path inside the grain (cf. figure 6.7). It also could be observed that the misorientation accumulates linearly from the centre to the edge of the grain, cf. figure 6.7.

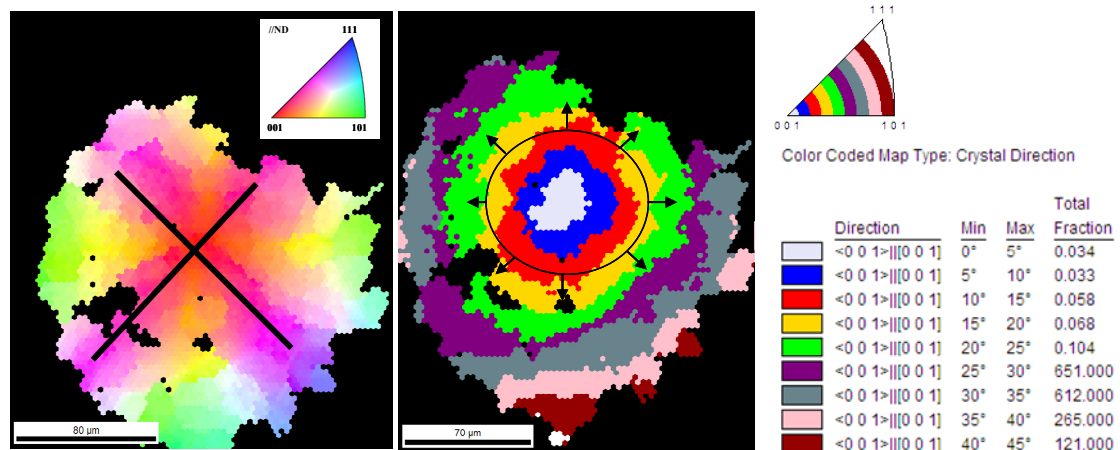


Figure 6.7 One cropped cube oriented grain with X-shape (left) and misorientation spread in concentric circles indicating an approximate linear accumulation of misorientation (right).

In an attempt to characterise the GB boundary character of the monolayer surface grains at the RD-TD surface, the CSL[†] criterion was applied. Figure 6.8 shows the frequency of $\Sigma 3$ ($\langle 111 \rangle > 60^\circ \pm 5^\circ$) boundaries observed on a series of RD-TD sections at various distances from the outer surface. The sections were mechanically polished and prepared for EBSD observation with an incremental step size of 5 μm along the ND direction. A very significant amount of $\Sigma 3$ CSL boundaries (38-45%) was observed at the RD-TD surface. It is important to note that the distribution is independent of the size of the scanned area of the surface grains for both alloys MnAl1 and MnAl2 which shows that a satisfactory statistical relevance is obtained. The analysis shows a fraction of approximately 40% for alloy MnAl1 and 45% for alloy MnAl2 of $\Sigma 3$ boundaries. This number is far beyond the random fraction of 10% for the given texture, if orientations would be arbitrarily paired together.

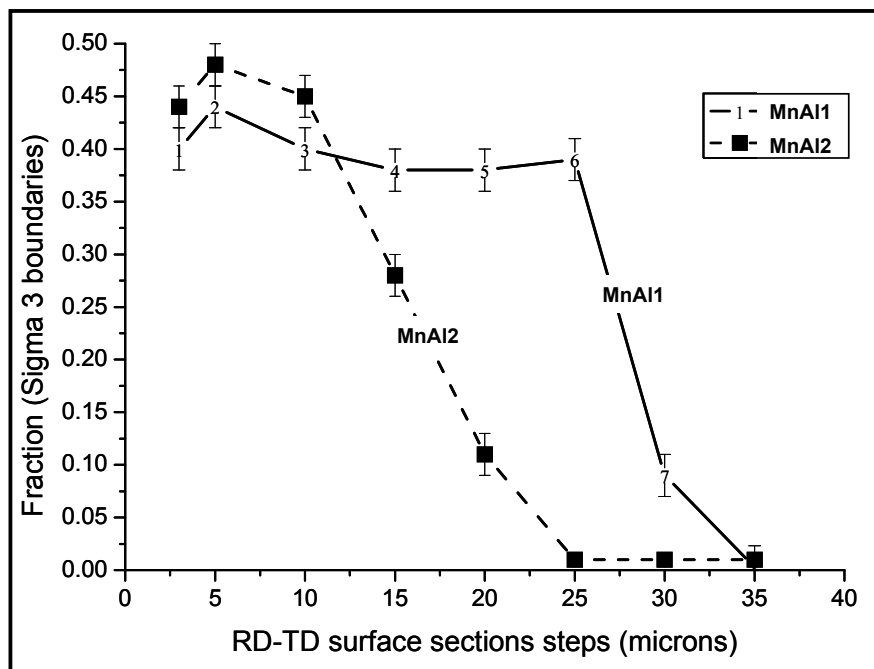


Figure 6.8 Fraction of $\Sigma 3$ boundaries at different sections below the surface.

[†] CSL is short for *coincident site lattice*. This refers to a special type of grain boundaries, i.e. for specific crystal misorientations of the type $\langle hkl \rangle \omega$ a sublattice exists that is common to both neighbouring lattices at either side of the GB. The twin boundary is the most common CSL and is denominated a $\Sigma 3$ boundary.

Figure 6.9 shows, for both alloys MnAl1 and MnAl2, the inverse pole figure maps and the high angle grain boundaries map (resolved for $\Sigma 3$ grain boundaries) at the section 5 μm underneath the surface and at the interface where the surface grains meet the bulk grains, i.e. at 30 μm for MnAl1 underneath the outer surface and at 15 μm for the alloy MnAl1, corresponding to the different depths of the monolayer.

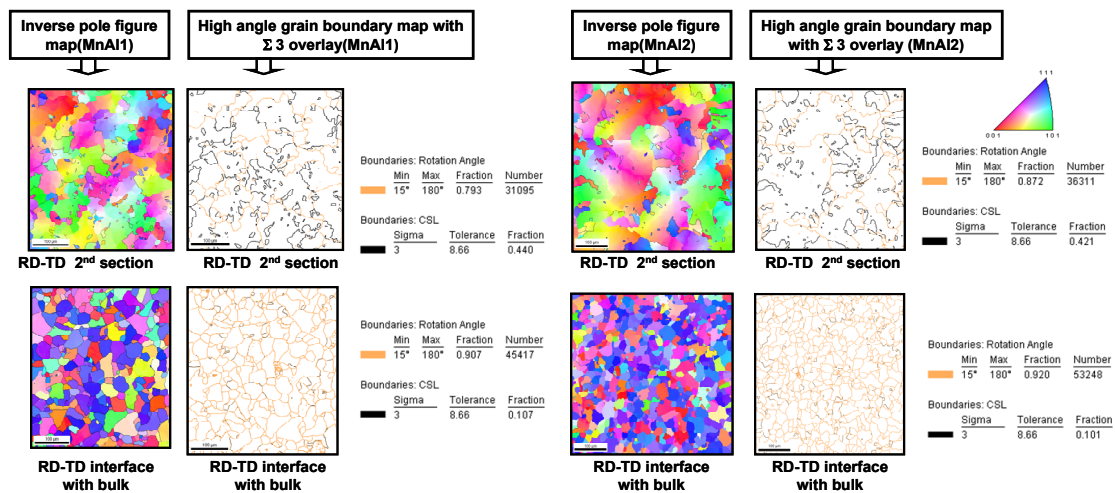


Figure 6.9 Inverse pole figure map and high angle grain boundary map with an overlay of $\Sigma 3$ boundaries in the RD-TD surface sections and in the bulk interface section of the alloys MnAl1 and MnAl2.

It is important to observe that at the interface the grains are polygonal and the grain size is much smaller in comparison to the grain size near the outer surface, Moreover, the bulk grains are predominantly blue in colour representing gamma fibre orientations with no misorientation gradients.

6.5.4. Nucleation and growth of surface (cube) texture

The specific orientation gradient is present in all surface layers with the specific $\{001\}$ dominated texture and it gives a very unusual orientation contrast pattern on the surface in the form of X shaped features. A number of cube grains with cross shaped

internal appearance were selected and cropped. Figure 6.10 shows the two schemes of investigation performed on the cropped areas. In scheme 1 the cube grain was subdivided in four concentric circles. The smallest circle with a radius of $\sim 3\mu\text{m}$ is considered as the nucleus whereas the largest of the concentric circles is nearly enveloping the entire grain. The ODF was calculated for all four circles and the $\varphi_2=45^\circ$ sections are shown in figure 6.10. The $\varphi_2=45^\circ$ section corresponding to circle 1 shows the orientation which is rotated along the Normal Direction (ND) 10° away from the exact cube orientation. The $\varphi_2=45^\circ$ section corresponding to circles 2,3,4 shows that the cube fibre orientation gradually rotates away from the ideal fibre whilst observing a $\langle 110 \rangle$ rotation axis. According to observation scheme 2 the grain edge is compared to the grain centre. The grain edge is considered to be the area covered by the difference in concentric circles 4 and 3 (cf. shaded area in figure 6.10). The nucleus is confined to the area contained in circle 1. It can be seen on figure. 6.10 that the texture corresponding to the edge region deviates from the ideal cube fibre orientation.

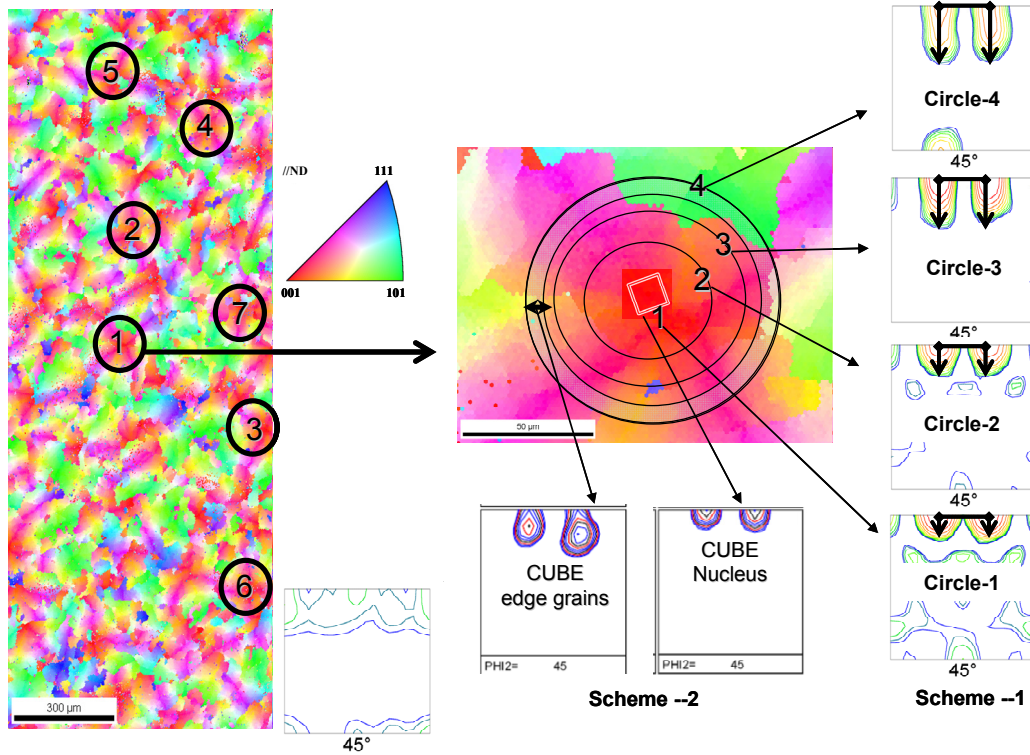


Figure 6.10 Nucleation of cube grains and subsequent grain growth patterns.

Figure 6.11 shows the results of several selected cube fibre grains post-processed according to scheme 2. The $\varphi_2=45^\circ$ section of the grain centre reveals the nucleation orientation which is persistently close to the ideal cube fibre orientation $\langle 100 \rangle // \text{ND}$. However, the $\varphi_2=45^\circ$ sections measured at the grain centre reveal a wide scatter along the cube fibre over the entire range of $\varphi_1 = 0$ (exact cube) to $\varphi_1=45^\circ$ (rotated cube). On the other hand, the $\varphi_2=45^\circ$ sections measured at the edge of the cube grains exhibit rotated orientations which deviate according to a $\langle 110 \rangle \omega$ gradient from the nucleus orientation in the centre of the grain. The present observations suggest that during growth other orientations were selected then during nucleation. This implies that there are two processes of orientation selection involved: first the nucleation event of the cube orientation that takes place at the metal-vapour interface and subsequently during growth of these cube grains a gradual orientation gradient is developed which causes the lattice to rotate along the $\langle 110 \rangle$ axis.

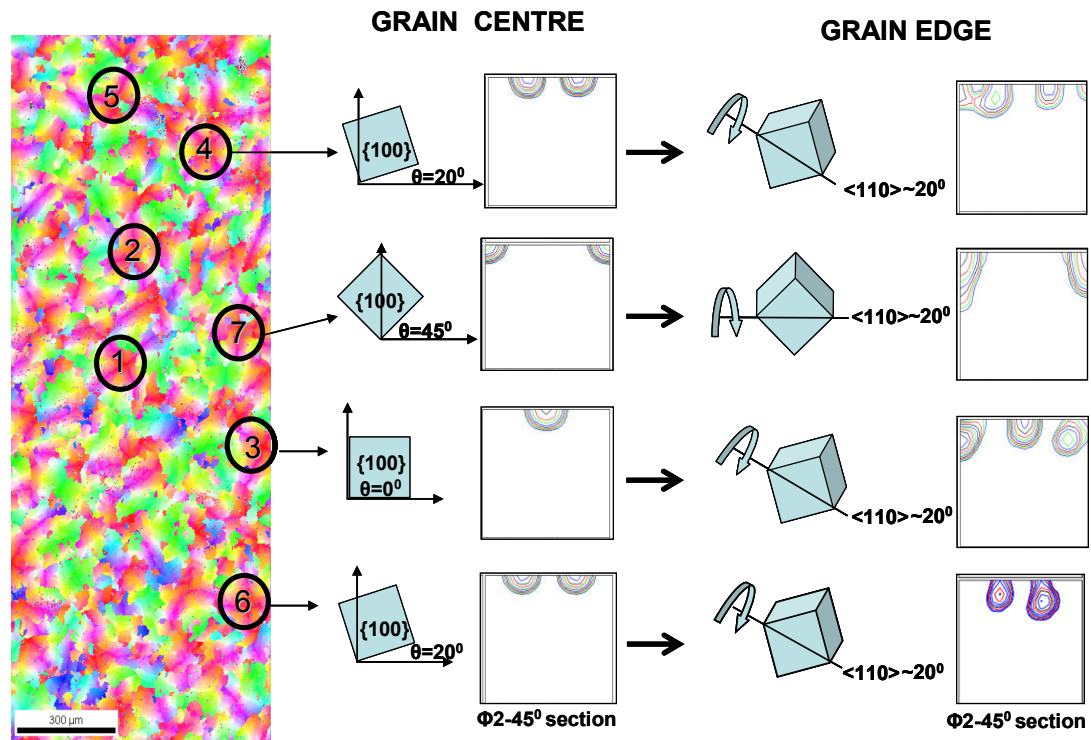


Figure 6.11 $\phi_2=45^\circ$ sections of the cube grain centre and the grain edge.

6.5.5. Simulated texture after double phase transformation

There are 24 crystal variants for the Young-Kurdjumov-Sachs relationship, which implies that one single parent orientation may produce 24 distinctly different product orientations. Hence, for a forward and reverse transformation, i.e. a $\alpha \rightarrow \gamma$ transformation followed by a $\gamma \rightarrow \alpha$ transformation one single parent may produce $(24)^2 = 576$ product orientations.

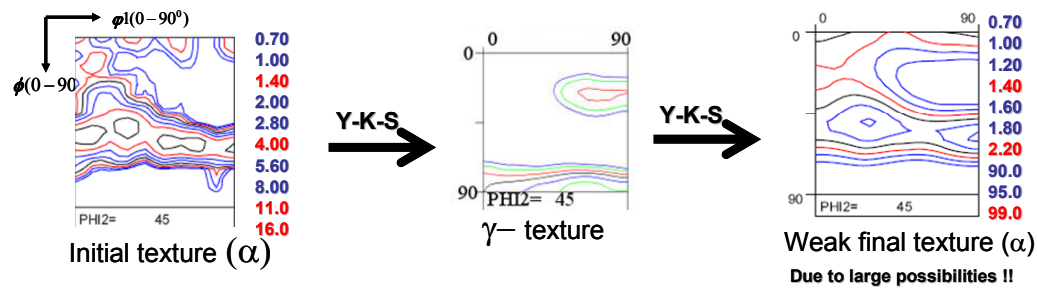


Figure 6.12 Simulated texture during $\alpha \rightarrow \gamma$ and $\gamma \rightarrow \alpha$ transformation according to Y-K-S relations.

Figure 6.12 shows the simulated texture evolution following the forward and reverse transformation according to the Y-K-S orientation relations. The $\phi_2=45^\circ$ section in figure 6.12a is the experimental recrystallisation texture for the alloy MnAl2 after annealing at 800°C for 60 s, which was considered as the initial texture at the onset of the transformation sequence. The $\phi_2=45^\circ$ section of figure 6.12b shows the simulated austenite texture considering all 24 Y-K-S variants. It can be observed that this texture is characterized by the Cu orientation and the $\{110\}$ fibre which includes the Goss and the Brass components. After reverse transformation to ferrite the $\phi_2=45^\circ$ section in figure 6.12 shows the simulated ferrite texture consisting of a weak rotated cube component and a γ fibre. The final ferrite texture after double transformation leads to weakening of the initial ferrite texture due to the large amount of possibilities without variant selection.

6.6. Discussion

The α - γ - α transformation microstructure of the two alloys MnAl2 (high manganese and aluminium) and MnAl1 (low manganese and aluminium) have revealed a typical surface texture containing $\{100\}$ and $\{110\}$ planes parallel to the solid/vapour interface. On the other hand the $\phi_2=45^\circ$ section measured in the mid section of these transformed sheets represents bulk textures with a strong γ -fibre. The texture evolution simulation of the α - γ - α transformation, assuming a YKS orientation relations, exhibits a weak texture which includes the $\{111\}$ fibre but also some $\{001\}$

intensity. When this result is compared to the texture observations in the bulk and at the surface of the sample, it can be argued that the texture components with the highest intensity both at the surface and in the bulk were present in this simulation.

6.6.1. Bulk Texture after phase transformation

With respect to the bulk, a stronger $\{111\}$ fibre texture and low intensities for other components were observed. This could, however, be expected taking into account the texture memory mechanism, as reported by Hutchinson and Kestens [17]. They have indicated that there are three main possible sources of variant selection: (1) stresses generated by the volume change that are retained in the high-temperature phase and bias the transformation behaviour on cooling; (2) thin films of the initial phase surrounding precipitates remaining untransformed at high-temperature, acting as nuclei for growth during cooling; and (3) grain boundaries with specific characteristics for nucleation of ferrite which favour previously present orientations during cooling. The first and second hypotheses were discussed and have been found improbable. However, the third possibility of texture memory associated with cooling rate is closely connected with the final structure of ferrite. They have shown that when the grain structure is polygonal, the texture memory effect is weak and it only becomes perfect when acicular ferrite is formed like in IF-Mn steels. Therefore it was argued that the occurrence of texture memory is intricately related to type of transformation mechanism.

The proposed mechanism by Hutchinson and Kestens for texture memory is schematically represented in Fig. 6.13. It is assumed that during heating two austenite variants nucleate along a single segment of a ferrite grain boundary. Both austenite grains γ_1 and γ_2 are 2 variants of 24 possible product orientations that are allowed by the YKS correspondence. Both grains grow in the neighbour ferrite grain (α_1) by migration of incoherent interfaces and then impinge on each other to create a boundary in the new austenite grain structure, cf. figure 6.13b. As revealed by Landheer et al [19] this grain boundary, on cooling, will be extremely favourable for

nucleation of ferrite and will regenerate the same orientation as the original ferrite grain (α_2) because this specific variant fulfils the double YKS relation with the two neighbouring austenite grains, cf. figure 6.13c. It was reported by Landheer et al [19] that such a two-sided YKS correspondence largely enhances nucleation. Therefore, this is the process that provides the texture memory to the initial ferrite texture at the start of the transformation loop (figure 7.12d). However it is said that it will be much more effective under conditions of displacive rather than diffusional type transformations.

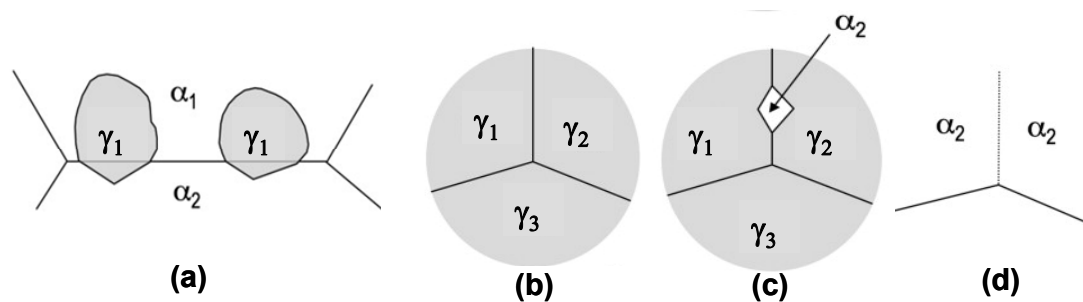


Figure 6.13 Schematic representation of texture memory phenomenon, adapted from Ref. [17]. (a) Two γ grains nucleate at the same α grain boundary, observing a Y-K-S relationship with α_2 ; (b) γ -phase after transformation; (c) favoured nucleation of α grain during γ - α transformation observing a Y-K-S relationship with both γ_1 and γ_2 ; (d) inherited structure after α displacive growth, the orientation α_2 is restored.

In the present study the bulk texture after α - γ - α phase transformation which exhibits an equi-axed ferrite structure is moderately strengthened, with an increase of maximum intensity from 5 random levels initially to 8 random levels after double transformation. This could be attributed to a weak texture memory effect, as expected with polygonal ferrite, cf. report by Hutchinson and Kestens [17]. They argue that a weak texture memory effect is still possible in the case of polygonal ferrite formation if nucleation occurs at triple junctions and further transformation proceeds by migration of the incoherent boundary into the third grain (γ_3).

6.6.2. Surface Texture after phase transformation

The development of the particular surface texture during $\alpha\text{-}\gamma\text{-}\alpha$ transformation shows some remarkable features which may be explained by a selection mechanism on the basis of minimization of metal-vapour surface energy. First, it is noticed that the observed $\{001\}$ and $\{110\}$ orientations precisely correspond to the free surface planes of minimum energy as predicted by the Wulff polyhedron [16]. Second, it is observed that these particular texture components only appear at the very surface of the material, i.e. only the grains which are in direct contact with the metal/vapour interface are of the $\{001\}$ or $\{110\}$ component, whereas the underlying layer of grains which do not possess a metal/vapour interface already exhibit a different texture.

Moreover, at the surface the presence of $\{001\}$ orientations was predicted on the basis of the YKS prediction (cf. figure 6.12), therefore it seems logical that this component exhibits a higher strength in the transformation surface textures than the $\{110\}$ component, which in some cases is entirely absent. Conversely, the fact that the latter component is entirely absent in the simulated result of figure 6.12 does not automatically imply the entire failure of the YKS model. As this model does not include the effect of surface energy anisotropy, it cannot enhance neither the $\{001\}$ nor the $\{110\}$ orientations. The role of surface energy anisotropy has to be considered as an *add-on* that operates in addition to the YKS correspondence, and may enhance or deplete some components that are predicted by the YKS based model.

6.6.3. Surface Energy Anisotropy (SEA)

The precise shape of the surface energy function $E_{\langle hkl \rangle}$ is determined by the anisotropy of the bonding energy in the metallic crystal lattice. If only first nearest neighbour interactions are taken into account, the Wulff polyhedron of bcc iron is known to be a dodecahedron with 8 $\{110\}$ and 4 $\{100\}$ surfaces [12]. The equilibrium shape was experimentally verified by evaporation and solidification of small single crystals at high temperatures in a specific annealing atmosphere [15]. It was reported that ultra fine particles of pure iron produced by evaporation in an inert atmosphere

displayed the dodecahedron shape in figure 1.3 [16]. In a recent investigation, Suklyun Hong et al evaluated the formation energies of low-index surfaces of pure iron on the basis of ab initio calculations [19]. It has been found that the surface energy for {110} planes is 2.36 J/m^2 which is the minimum value, followed by {100} planes with 2.40 J/m^2 and {111} with 2.57 J/m^2 .

The fact that the {001} component is more intense than the {110} component, in spite of its increased surface energy, may be attributed to 3 different reasons:

- (i) The type of initial texture. As the SEA operates on an initial texture of a given type, the final result may be largely dependent on the initial texture;
- (ii) SEA may not be the only active variant selection mechanism. It was already mentioned that if SEA is combined with a YKS orientation relationship, it seems logical that the {001} component is preferred over the {110} component, if the initial texture prior to transformation is a ferrite γ -fibre texture.
- (iii) The effect of surface adsorbed elements like sulphur and oxygen may alter the energy ranking of {110} and {100} orientations normally. The effect of this was observed in a high temperature tertiary recrystallisation experiment [11, 12].

It can also be observed that surface grains display very specific grain boundary morphology in the RD-TD surface. In contrast to the relatively regular GB morphology produced by curvature driven growth, the surface grains display a very irregular almost acicular shape (figure 6.5). From the point of view of crystallography the grain boundaries observed in the RD-TD surface section exhibit a large fraction of $\Sigma 3$ CSL boundaries with the twin type axis angle relationship of $\langle 110 \rangle 70.5^\circ \equiv \langle 111 \rangle 60^\circ$. From the morphology of these GBs it is clear that they cannot be coherent twin boundaries, but even incoherent twin boundaries are known to exhibit a lower GB energy as compared to random high angle GBs. Figure 6.8 shows the fraction of $\Sigma 3$ boundaries on various serial sections underneath the RD-TD surface. These observations of an increased incidence of low-energy $\Sigma 3$ GBs and the presence of {001} and {110} with a reduced solid/vapour interfacial energy strongly indicate that

the creation of the surface structure and texture was controlled by a process of crystallography resolved energy minimization.

6.6.4. In-Grain Orientation Gradients

With the gradual evolution of the $\alpha \rightarrow \gamma \rightarrow \alpha$ transformation, it appears that the {001} grains underwent a crystal lattice rotation during growth that can be accommodated either plastically (by dislocation walls of low angle grain boundaries) or either elastically. A distinction between both cannot be made based on the present data.

It seems that another orientation selection mechanism is responsible for the in-grain orientation gradient in the cube oriented grains with {001} centre and rotating away from this starting orientation from the centre to the edge of the grains.

It is observed that by an orientation shift of $\Delta\Phi \approx 15^\circ$ the {001} fibre orientation is brought into $\Sigma 3$ coincidence with the {111} fibre orientations as shown in Fig. 6.14. Moreover, this very same in-grain rotation of the {001} nuclei also gives rise to a low energy $\Sigma 3$ boundary with the {110} fibre grains that are also present in a more than random quantity at the sample surface, cf. figure 6.14. It remains unclear however what drives the {001} grains towards $\Sigma 3$ coincidence with either {110} or {111} fibre grains according to a strictly linear orientation gradient path (e.g. figure. 6.15).

A possible explanation might be that as the underlying layer (of non-surface grains) is dominated by {111} orientations (cf. texture memory effect), gradually not only the metal/vapour surface energy is of importance but also the metal/metal grain boundary energy starts having an influence. Therefore, as the anisotropy of surface energy at the metal/vapour interface has led to a {001} fibre selection, the anisotropy of surface energy at the metal/metal interface tends towards to the formation of low energy $\Sigma 3$ boundaries. This can be reached by a gradual rotation of the {001} nucleus to a near cube fibre orientation, that forms a $\Sigma 3$ interface with the {111} fibre orientations of the underlying layer. This mechanism is not sustained, though, by the present data because it would imply the presence of $\Sigma 3$ boundaries at the interface of surface and

non-surface grains in a RD-ND section, which is not confirmed by the experimental data.

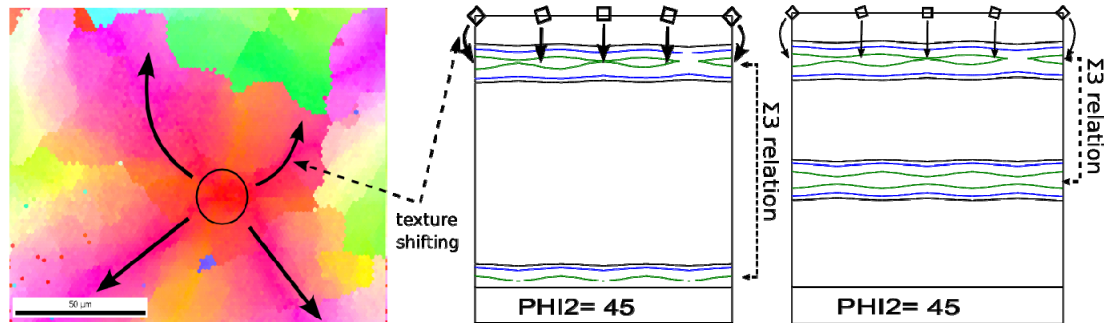


Figure 6.14 Schematic illustration of a possible mechanism. Cube surface grains rotate downwards to match the $\{115\}$ fibre (at $\Phi=15^\circ$) which exhibits a $\Sigma 3$ relation with both $\{110\}$ orientations at the sample surface and $\{111\}$ orientations in the bulk of the material.

In order to understand the mechanism of orientation rotation which has occurred during transformation and leading to a significant fraction of incoherent sigma boundaries, a colour coded crystal direction map was plotted which included the crystal directions $\{100\}$, $\{110\}$, $\{111\}$ and $\{115\}$ as shown in figure 6.15. These crystal directions were plotted with a misorientation spread of 20° and thus the entire area of the inverse pole figure map is covered. The crystal orientations $\{100\}$, $\{110\}$, $\{111\}$ are representing stable orientations nucleated during transformation whereas the $\{115\}$ orientation (plum colour) represents the end orientation resulting from the observed gradient in the cube component. $\Sigma 3$ boundaries (yellow colour) were also included in the crystal orientation map of figure 6.15. It is noticed that the $\Sigma 3$ boundaries formed most frequently when the crystal orientation $\{115\}$ meets the $\langle 111 \rangle$ and $\langle 110 \rangle$ orientation which is expected because with these orientations the emblematic twin orientation match is obtained, cf. figure 6.15. The texture of fig. 6.15 exhibits the orientation distribution of the grains observed at either side of the $\Sigma 3$ boundaries. Unfortunately these detailed observations do not lead to any conclusive evidence on the mechanism of orientation rotation observed in $\{001\}$ grains. Any

potential theory should explain the very gradual (almost linear) orientation shift from $\Phi = 0$ to $\Phi = 15^\circ$ bringing the $\{001\}$ orientations into $\Sigma 3$ coincidence with the neighbours. It remains somewhat of a mystery that the final situation arising in the process appears to match the conditions of a stable energy minimum, although the intermediate structures leading up to this stable minimum cannot be understood.

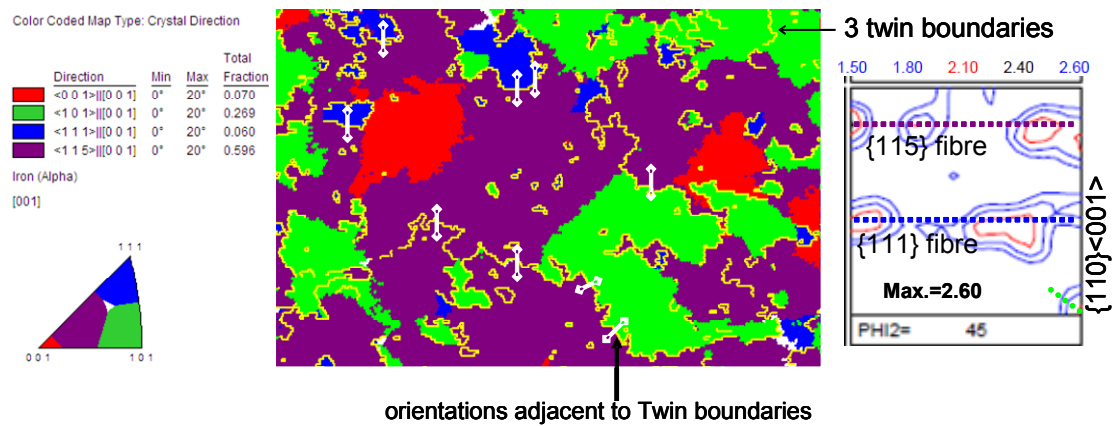


Figure 6.15 Crystal orientations recorded adjacent to $\Sigma 3$ boundaries (left) and plot of these orientations shown in the $\varphi_2=45^\circ$ sections (right).

6.7. Conclusions

The alloy compositions MnAl₂ and MnAl₁ exhibit a specific surface texture and also unique microstructure after α - γ - α transformation on annealing of a cold rolled sheet. The annealed sheet surfaces of the two alloys are characterized by a monolayer of grains in direct contact with the metal/vapour interface and with predominant $\langle 100 \rangle // ND$ and $\langle 110 \rangle // ND$ fibre texture. Simultaneously, the bulk of the sheets display a strong γ - fibre texture.

The RD-TD surface microstructure of the transformation annealed sheet is very unique with large cube grains (~150 μm) with irregular grain boundaries. The grain boundary structure is also very specific with a large fraction (40%) of incoherent $\Sigma 3$ twin boundaries. These boundaries are found mainly when $\{115\}$ orientations meet with $\{111\}$ and $\{110\}$ oriented grains.

A peculiar orientation gradient was observed in the cube fibre grains. It was found that the $\{001\}$ type grains only display the ideal $\{001\}$ orientation in the centre of the grain and rotate away from this ideal $\{001\}$ position with a near linear orientation gradient. The edge of the $\{001\}$ grain is generally $>15^\circ$ off the ideal $\{001\}$ fibre position.

Orientation selection on the basis of minimisation of the metal/vapour interface energy seems to be the most appropriate hypothesis to explain the present results. The observed structure represents a state of optimally reduced energy as both the metal/vapour interfacial energy and the solid state interface energy appear to be minimized. It remains unclear, however, by which mechanism the microstructure has evolved to such a state as the driving force for the gradually accumulating in-grain misorientations could not be determined.

6.8. References

- [1] C.G. Dunn and Walter: Trans. Met. Soc. AIME Vol. 224 (1962), p.518
- [2] O. Hashimoto, S. Satoh, T. Tanaka: Tetsu-to-hagane Vol. 66 (1980), p.102.
- [3] O. Hashimoto, S. Satoh, T. Tanaka: Tetsu-to-hagane Vol 66 (1980), p.112
- [4] R.G. Aspeden, J.Berger and H. E. Trout: Acta Metallurgica, Vol 16 (1968), p.1027
- [5] T. Tomida and Tanaka: ISIJ International Vol. 35 (1995), p.548.
- [6] N.Yoshinaga, L.Kestens and B.C. De Cooman, Mater. Sci. Forum 495 (2005), p.1267
- [7] Romero, M. Preuss, J. Quinta da Fonseca, Acta Materialia 57 (2009) p 5501

- [8] P. Van Houtte: The MTM-FHM Software system Version2 Users Manual (1995)
- [9] C.Goux Mem. Scient. Rev. Metall, 58 (1961) p 661.
- [10] DG Brandon, Acta. Metall., 14 (1966) p 1479
- [11] K. Detert Acta Metallurgica Vol. 7 (1959), p 589
- [12] J.L Walter: Acta Metallurgica Vol. 7 (1959), p 424
- [13] J.K. Mackenzie, A.J.W. Moore and J.F. Nicholas: J. Phys. Chem. Solids Vol. 23 (1962), p 185
- [14] R. Ueda: J. Crystallo.Soc. Japan Vol. 6 (1979), p113
- [15] Y. Sasaki, M.Baghat, M. Iguchi and K. Ishii: ISIJ International Vol.45 (2005), p.1077
- [16] D.A. Porter and K.E. Easterling: Phase transformation in metals and alloys, Stanley Thornes Publishers Ltd, U.K. (1992)
- [17] B. Hutchinson and L. Kestens, Applications of texture analysis, ceramic transactions. 201, (2008) p 281.
- [18] A.C.C. Reis, L Bracke, R Petrov, W. J. Kaluba, and L. Kestens ISIJ International, Vol. 43 (2003), No. 8, p 1260
- [19] S. Hong, Surface energy anisotropy of iron surfaces by carbon adsorption, Current Applied Physics 3 (2003) p 457
- [20] H. Landheer, PhD thesis, Technical University Delft, the Netherlands (2010)

Chapter 7

Inward growth of surface texture components

The final aim of the present work is to develop a scheme which could be useful for the industrial manufacturing of (electrical) steels with an optimized cube texture across the thickness of the sheet. It was shown in the previous chapters that an appropriate surface texture with cube texture components can be achieved by applying α - γ - α phase transformation annealing on the cold rolled sheet. In this chapter an investigation is presented on the inward growth of surface texture components. The mechanism of Strain Induced Boundary Migration (SIBM) has been successfully utilized to grow surface texture components across the thickness dimension of the ultra low carbon low alloyed steels. In low carbon steel the decarburization annealing was explored to the same purpose.

7.1. Introduction

The principal objective of texture control in non oriented electrical steel is to maximize the density of random cube orientations in the bulk of the steel sheet. In Chapter III it has been demonstrated that cube orientations with sizable density can be developed in the bulk of non-alloyed ultra low carbon steel sheet by columnar grains starting at the surface. In ultra low carbon steels sheets, however, alloyed with manganese, aluminium and silicon the favourable texture is restricted only to the surface after the typical phase transformation annealing treatment. The inward growth of the surface texture components is imperative for commercial applications.

Several research papers have been published on inward growth of surface texture during decarburization annealing after temper rolling in semi-processed non oriented electrical steels sheets [1-6]. Temper rolling activates the Strain Induced Boundary

Migration[†] (SIBM) mechanism during subsequent annealing which helps surface grains to grow inwardly. However, no attempt has been reported in the literature regarding inward growth of surface textures in fully processed non-oriented electrical steels. In the method investigated here the role of decarburization will be investigated. The annealing treatment will be (partially) carried out in the austenite phase domain and hence phase transformation can be employed as an instrument of texture control. Additionally, the strain induced by temper rolling (or skin pass reduction) is considered as a crucial process parameter.

7.2. Experimental procedure

Two different experiments were designed to investigate the inward grain growth: (i) by strain induced boundary migration triggered by a light rolling reduction (temper rolling or skin pass) prior to annealing and (ii) by transformation annealing as an intermediate step prior to decarburisation annealing.

Three steel chemistries were selected: two which reveal the specific cube surface texture and one other without specific surface texture. The first two are the two ultra low carbon steels MnAl2 and MnAl1 alloyed with manganese and aluminium in high and low content, respectively. The third alloy is the low carbon steel (Carbon = 470 ppm) which is a low-alloyed semi processed non oriented electrical steel with a Si content of 0.17wt% and denominated as LC. The alloys MnAl2 and MnAl1 reveal a substantial {001} surface texture after phase transformation annealing whereas the alloy LC reveals a surface texture without specific surface texture components.

Figure 7.1 shows the schedule of the annealing treatment to investigate the effect of the intermediate transformation annealing step before decarburization annealing. The cold rolled sheet of the semi processed non-oriented electrical steel (LC) was annealed at 975°C for two minutes. Together with a full hard cold rolled sample this annealed sample was annealed a second time but now in a decarburizing atmosphere

[†] *Strain induced boundary migration* [1] also known as *grain bulging* is a mechanism of grain growth that is driven by a difference in stored energy of plastic deformation at either side of the grain boundary. SIBM is commonly observed after relatively small strains (<10%).

with a mixture of 5% hydrogen and 95% nitrogen with a dew point of 15°C. In the second annealing the sample was reheated and cooled down with a slow rate of ~2°C per minute. Two different annealing temperatures were selected: 950°C (above Ac3) and 885°C (between Ac1 and Ac3) whereas the holding time was maintained constant for 4 minutes. After annealing the surfaces were examined in the x-ray texture goniometer and in the environmental scanning electron microscope for macro and micro texture analysis, respectively.

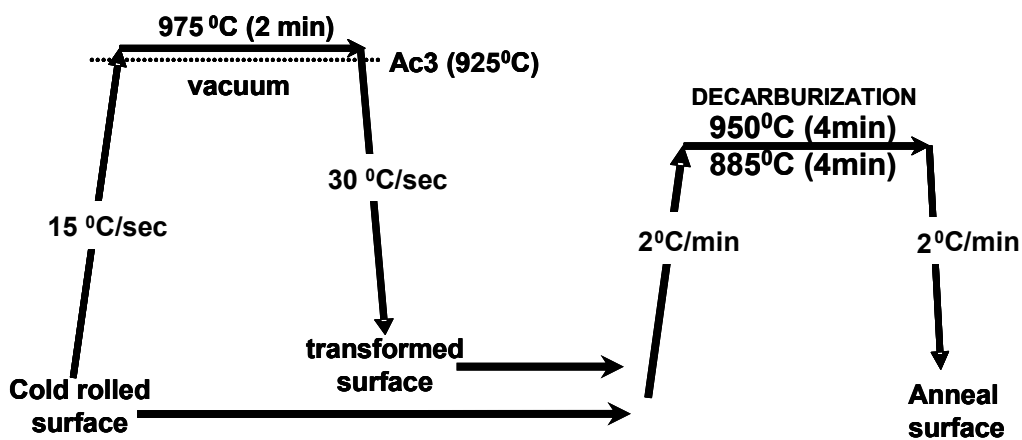


Figure 7.1 Schematic representation of the annealing treatment carried out on the low carbon steel.

In another experiment the ultra low carbon steels alloyed with manganese and aluminium as well as the low carbon steel (LC) were subjected to the transformation annealing treatment in vacuum as shown in the schedule of figure 7.2.

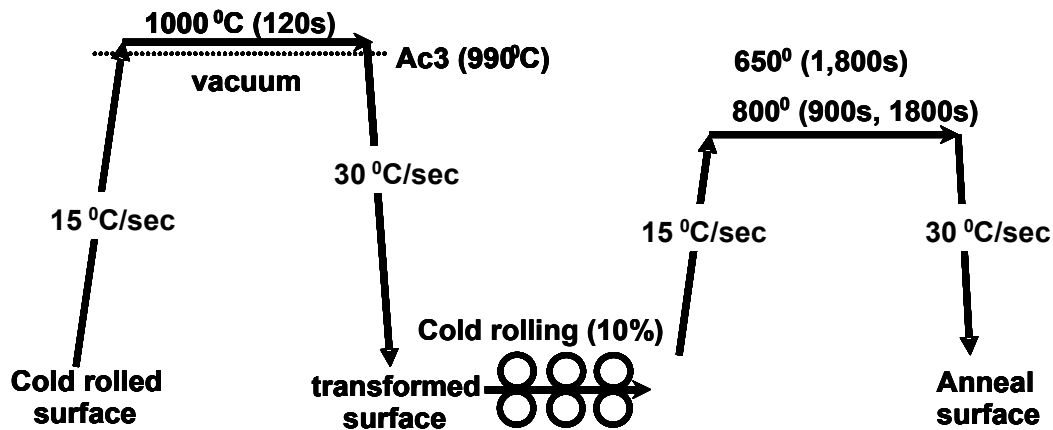


Figure 7.2 Schematic representation of the thermo-mechanical treatment applied on the alloys MnAl1, MnAl2 and LC.

After transformation annealing, the sheets were skin pass cold rolled to reductions of 1, and 10%. After skin pass rolling the sheet surfaces were examined in the x-ray texture goniometer and subsequently subjected to different recrystallisation and grain growth annealing treatments as shown in the figure 7.2. In contrast to the previous trial the 2nd annealing treatment was carried out here without a decarburizing atmosphere and with much faster heating and cooling rates which closely resemble the line speeds of an industrial continuous annealing installation.

7.3. Results

7.3.1. Effect of decarburisation annealing on α - γ - α transformation surface texture

In order to observe the effect of the transformation annealing as an intermediate step prior to decarburisation annealing the semi processed non oriented electrical steel was subjected to the experimental scheme of figure 7.1. The transformation annealing was performed first to develop the cube surface texture as discussed in the previous chapters. Decarburisation annealing is performed afterwards to grow the surface texture components across the thickness of the steel sheet. In order to gauge the effect of the transformation annealing treatment on texture and microstructure evolution

during decarburisation annealing also a full hard cold rolled sheet was subjected to the decarburisation annealing at two different temperatures without a prior transformation annealing step. Figure 7.3 shows the results of X-ray texture at the surface and EBSD texture measurements in the through thickness of the sheet after decarburisation annealing at the inter-critical temperature of 885°C for the LC steel.

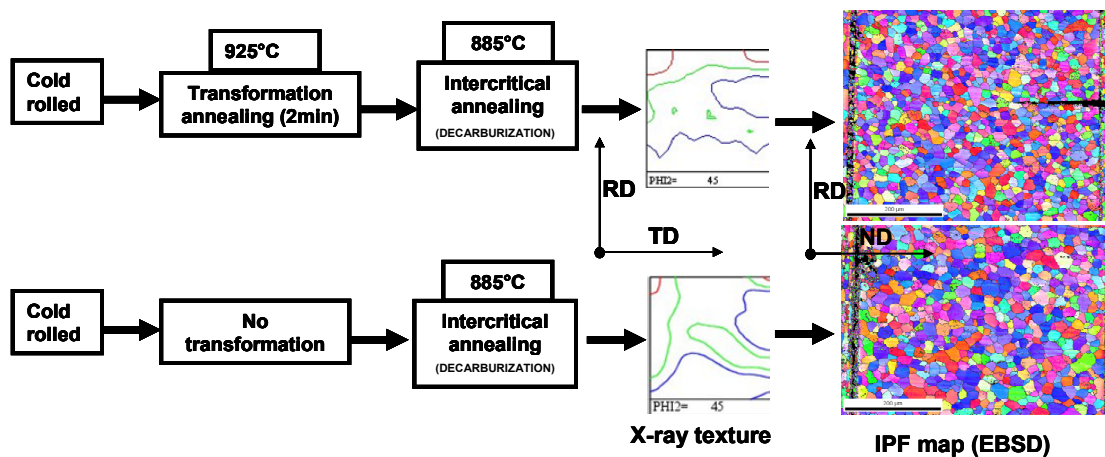


Figure 7.3 X-ray surface texture and through thickness inverse pole figure maps after intercritical decarburization annealing in alloy (LC).

When the transformation annealing is performed prior to decarburisation, the texture obtained after annealing in the intercritical region reveals a relatively stronger cube and a weak γ -fibre. On the other hand, when transformation annealing is not performed in between, then decarburisation annealing leads to a weak transformation texture with alpha and gamma fibre orientations. Figure 7.3 also shows the inverse pole figure map across the thickness for both samples. The grain morphology in both cases is almost identical and it showed an equi-axed structure with a grain size that is nearly identical to the one prior to decarburization. In the present study the carbon concentration profile was not measured before and after annealing, hence it cannot be taken for granted that the said *decarburization* annealing treatment has really produced a decarburization of the sample

In the alternative case decarburisation annealing was performed above the A_{c3} temperature as shown in the schematic representation of figure 7.2. The X-ray texture

and inverse pole figure maps are shown in figure 7.4. The $\varphi_2=45^\circ$ section before annealing shows the typical L shaped deformation texture normally observed after 70% of cold rolling. This cold rolled surface was transformation annealed at 975° C for 2 minutes above the Ac3 temperature. The X-ray texture measured at the annealed surface after phase transformation is shown as a $\varphi_2=45^\circ$ section of figure 7.4. This $\varphi_2=45^\circ$ section shows the texture intensity of 2.5 random levels with a comparatively strong cube fibre and a weak gamma fibre.

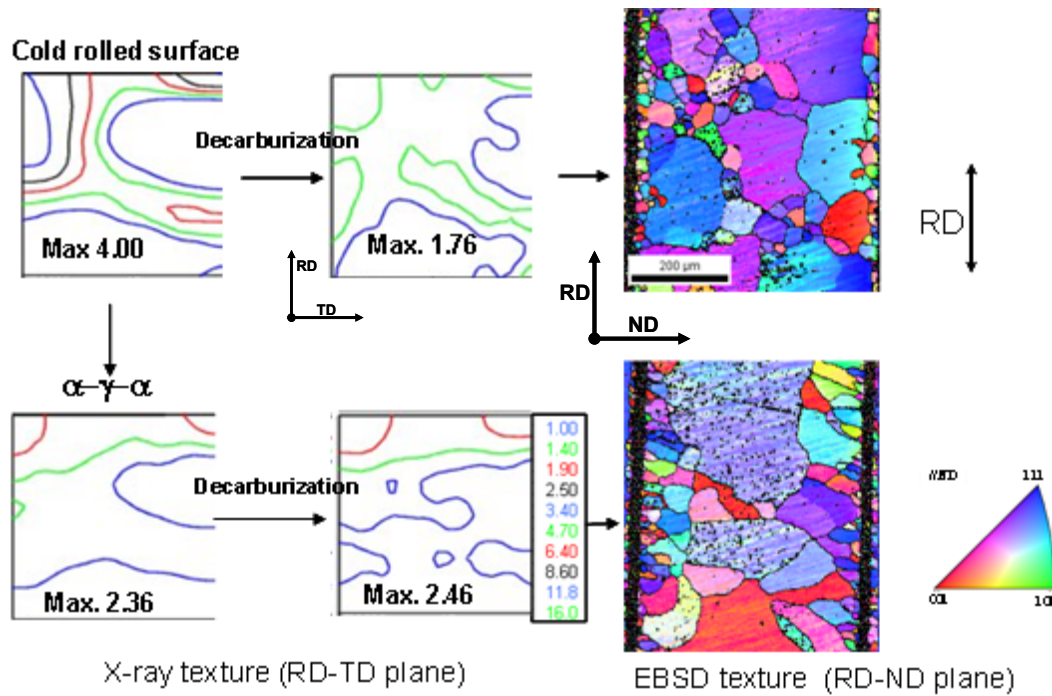


Figure 7.4 X-ray surface texture and through thickness inverse pole figure maps after decarburization annealing (top) and after α - γ - α phase transformation and decarburisation annealing (bottom) in alloy (LC).

The cold rolled steel sheet and the transformation annealed sheet were submitted together to the decarburisation annealing treatment at 950°C (>Ac3) for four minutes. The x-ray surface texture is shown in figure 7.4, together with the orientation scans in inverse pole figure colour coding. When the decarburization annealing is performed without prior phase transformation, the surface texture is a very weak transformation texture with an intensity of 1.76 random levels. On the other hand, when

transformation annealing is carried out before decarburization then the cube component of the surface texture is slightly enhanced. Figure 7.4 shows the through-thickness inverse pole figure map observed after decarburisation annealing above the Ac3 temperature with and without prior transformation annealing. These inverse pole figure maps reveal limited inward grain growth of surface orientations towards the bulk of the sheet during the decarburisation treatment, albeit combined with abnormal grain growth in the bulk of the sheet. The partially columnar (surface) grain structure is typical of an inward growing structure as created by a diffusional transformation process induced e.g. by carbon diffusion. Hence it can be readily assumed that in this case carbon diffusion has really taken place. The original objective, though, of extending the surface texture towards the bulk by inward growth of surface grains could not be obtained via the decarburization annealing treatment as the larger part of the structure still remains occupied by (abnormally grown) bulk grains.

7.3.2. Inward grain growth by Strain Induced Boundary Migration

In another attempt the laboratory cast alloys (MnAl1 and MnAl2) and the non oriented semi-processed electrical steel (LC) sheets were annealed above the transformation temperature. Subsequently, these annealed sheets were skin pass cold rolled to 1, and 10% reduction. After cold rolling these sheets were annealed at different recrystallisation temperatures as shown in figure 7.5. The most significant results are shown in the sections below.

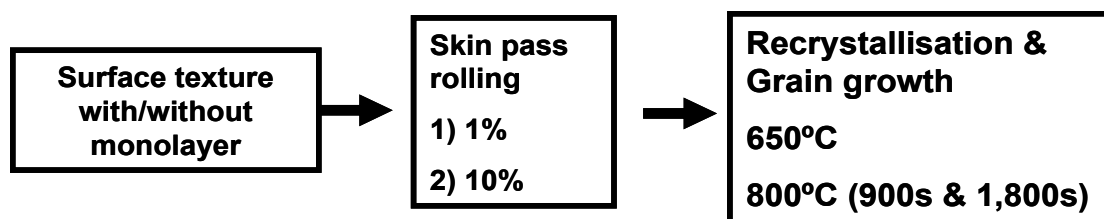


Figure 7.5 Parameters tried for the inward grain growth of surface texture components

First trial

In the first trial the annealed sheets AlMn1 and AlMn2 with the characteristic monolayer were cold rolled to a 1% reduction in order to introduce particular shear strains at the surface.

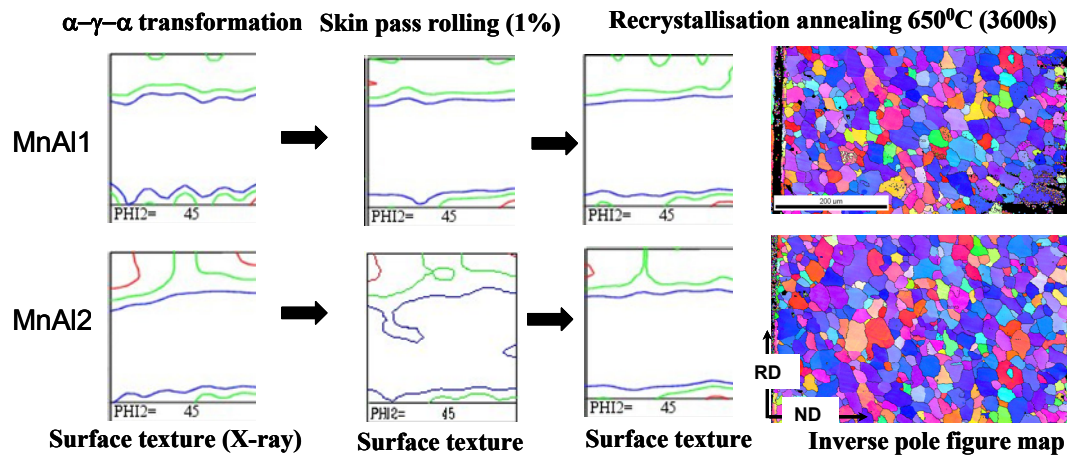


Figure 7.6 X-ray surface texture after phase transformation, skin pass rolling (1%) and subsequent recrystallisation annealing at 650°C for 3,600s.

The surface texture was examined in each stage by X-ray diffraction. The $\phi_2=45^\circ$ sections show the consistent presence of the characteristic $\{001\}/\{011\}$ surface texture through all stages of processing from the transformation annealing treatment onwards. The through thickness examination, however, performed on the recrystallisation annealed sample has given no evidence of grain growth, probably because of lack of driving force to obtain boundary migration at 650°C during 3600s of annealing.

7.3.3. Skin-pass rolling with 10% cold reduction

In another attempt the annealed sheets of the three alloys MnAl1, MnAl2 and LC were cold rolled with 10% reduction after transformation annealing. Subsequently, these sheets were annealed at the recrystallisation temperature of 800°C for 900s and 1800s. The $\phi_2=45^\circ$ sections of the ODFs calculated from the XRD pole figures are shown in figure 7.7 below. The $\phi_2=45^\circ$ sections of the alloys MnAl1, and MnAl2

show the surface texture with a cube fibre whereas the non oriented electrical steel exhibits a cube fibre texture along with a gamma fibre which is slightly less intense. In the second step these annealed sheets were rolled with a reduction of 10%. In figure 7.7 it can be observed that the surface texture intensity, in general, has increased significantly in all three alloys due to cold rolling. This is conventional behaviour when rolling is performed with smooth rolls [11].

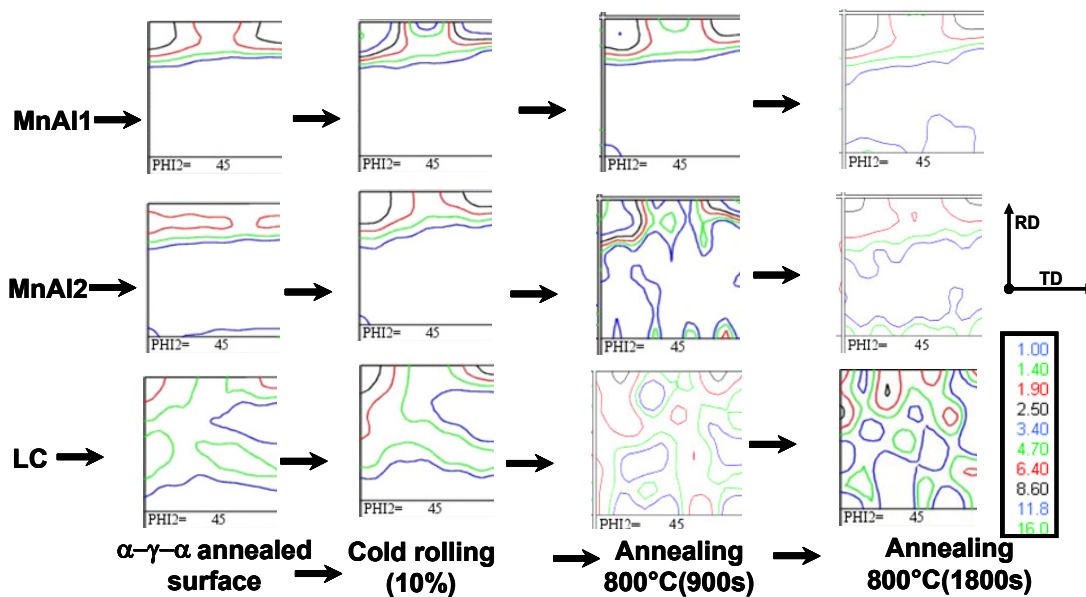


Figure 7.7 $\phi_2=45^\circ$ section obtained after surface X-ray texture analysis of transformation annealed, skin pass rolled (10%) and additionally annealed sheet.

Figure 7.7 also shows the surface texture after annealing at 800°C for 900s and 1800s. The $\phi_2=45^\circ$ sections do not show much change in the surface texture for the MnAl1 and MnAl2 samples, whereas the LC surface texture tends towards a random texture after annealing at 800°C for 1800s. Additionally, the samples were examined across the thickness with orientation contrast microscopy. Figure 7.8 shows the

Kernel average misorientation[‡] map across the sheet obtained after orientation imaging microscopy performed on the samples before and after temper rolling. The Kernel average misorientation has been calculated with third nearest neighbour and 5° misorientation tolerance. This misorientation criterion reveals the lattice curvature change due to small rolling reduction which can be recorded by orientation contrast microscopy. The Kernel average misorientation map before skin pass rolling and after skin pass rolling in through thickness for all three alloys MnAl1, MnAl2, and LC are shown in the figure 7.8. The blue colour represents a uniform lattice whereas the red colour represents a maximum local orientation gradient. The kernel misorientation pattern before skin pass rolling shows almost no deformation except few areas at the edge of the samples.

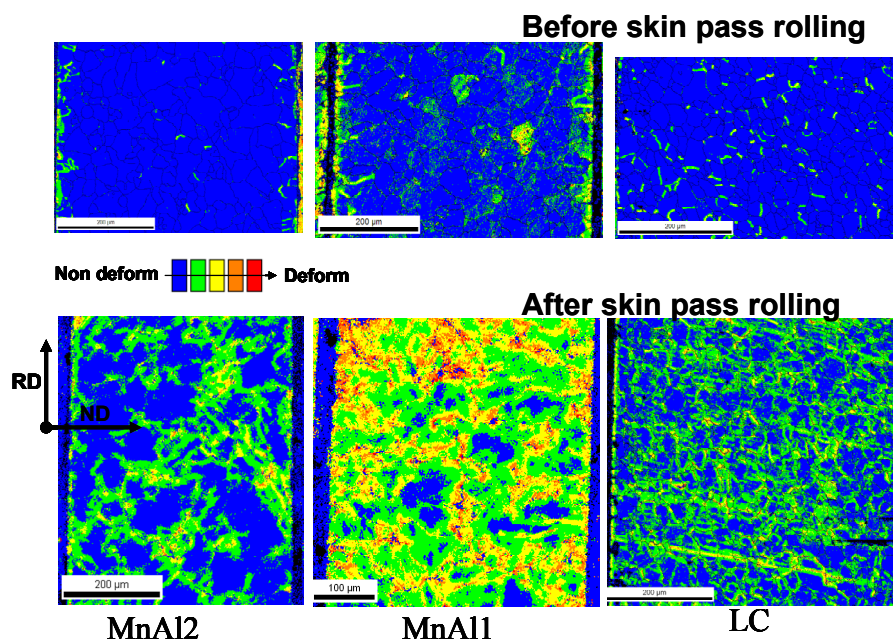


Figure 7.8 The Kernel average misorientation maps (3rd neighbour with 5° tolerance) across the thickness of the sheets of the selected alloys before (top) after skin pass rolling reductions (10%).

[‡] The Kernel average misorientation is the average misorientation of a pixel in the 2D crystallographic data set (acquired by EBSD) with its nearest neighbours; it may also include 2nd and 3rd nearest neighbours. If the misorientation with a neighbour exceeds a certain threshold or tolerance, it is excluded from the averaging because then this neighbour is no longer considered to belong to the same grain as the reference pixel.

The misorientation pattern after skin pass rolling in figure 7.8 suggests that deformation took place not only at surface but also in the interior of the sheet across the thickness during temper rolling. The alloy MnAl1 shows a more intense misorientation profile in comparison to the alloys MnAl2 and LC. This could be due to the large grain size (20 μm) in the alloy MnAl1 which is higher as compared to the alloy MnAl2 (17 μm) and LC (12 μm). It also can be observed in figure 7.8 that for all the three alloys the strained area is not limited to the surface but rather expands across the entire thickness of the sheet.

After skinpass rolling, these sheets were annealed at 800°C for two different soaking times (900s and 1,800s) in order to observe whether or not inward grain growth of surface texture components occurs. The X-ray surface textures shown in figure 7.7 reveal that the specific cube fibre has been retained for the ultra low carbon steel alloys MnAl1 and MnAl2 after annealing at 900s and 1800s with minor differences in intensity. On the other hand, the surface texture of the low carbon steel alloy (LC) exhibits a stable cube fibre and a weak γ -fibre texture after 900s and later it gets randomised after 1800s which could be due to surface decarburisation at this temperature and time in vacuum.

Subsequently, these samples were also investigated in the scanning electron microscope and orientation imaging was performed on the annealed samples. Figure 7.9 shows the inverse pole figure map across the thickness after recrystallisation annealing at 800°C for 900s. One can observe that the surface grains of specific surface orientations have grown inside for all three materials under consideration. The extent of inward grain growth is different, though, and could possibly be attributed to factors like chemical composition, strain heterogeneity and strain energy accumulation.

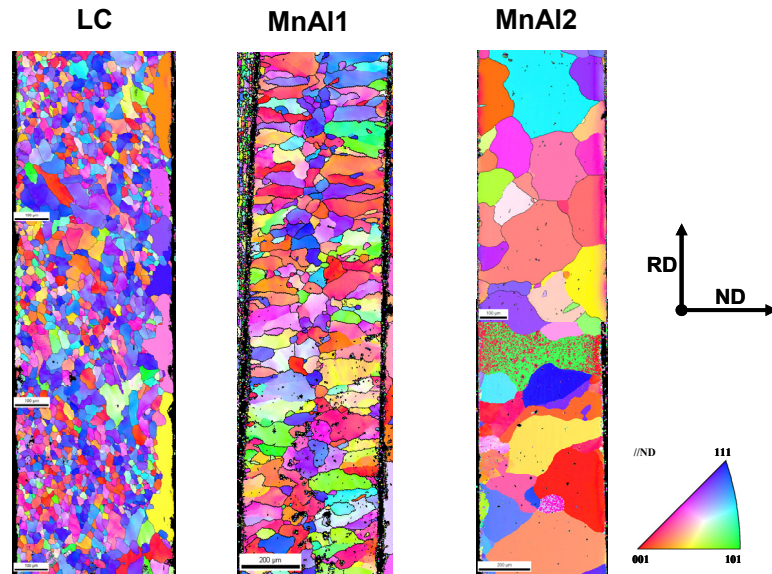


Figure 7.9 Inverse pole figure map of all the three alloys after recrystallisation annealing at 800°C (900s).

In addition recrystallized (or abnormally grown) grains can be observed that have nucleated in the bulk of the sheet. The inverse pole figure map of the alloy LC shows the inward growth of surface orientations on one side of the sheet. Simultaneously there is also some abnormal grain growth in the bulk of the sheet, whereas still a large fraction of grains have not yet recrystallized and continue to exhibit the in-grain orientation gradients that are typical for deformed grains. The alloys MnAl1 and MnAl2 show much deeper inward growth as compared to the alloy LC. The inward growth has reached the middle of the sheet for alloy MnAl1 whereas for alloy MnAl2 inward growth has occurred up to approximately 1/3 of the total thickness of the sheet on both sides. Concurrently abnormal grain growth also took place in the bulk of the sheet.

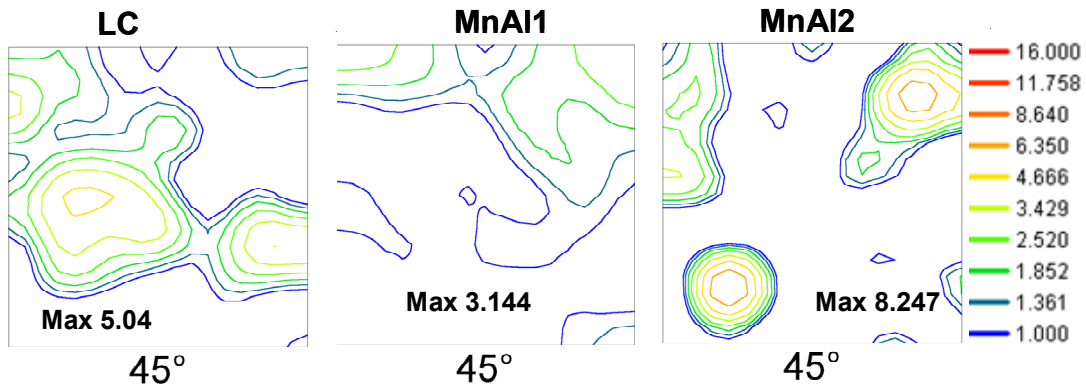


Figure 7.10 $\varphi_2=45^\circ$ section of the ODFs corresponding to the inverse pole figure maps of figure 7.9.

Figure 7.10 shows the through thickness textures corresponding to the inverse pole figure maps of figure 7.9. The LC alloy shows the gamma fibre texture with a strong $\{111\}\langle 112\rangle$ component and a weak intensity of the $\{411\}\langle 110\rangle$ component. On the other hand, the MnAl1 and MnAl2 exhibit stronger cube fibre and rotated cube orientations. The MnAl1 alloy exhibit a less intense texture as compared to MnAl2, but this could be due to the better statistics of the measurement on the MnAl1 sample due to its lower grain size.

Orientation imaging microscopy was also performed on the samples of the second annealing experiment with increased soaking time of 1800s. The inverse pole figure maps of all the three alloys LC, MnAl1 and MnAl2 are shown in figure 7.11. In general it can be observed that abnormal grain growth has occurred during excess soaking time. In general it can be said that some grains have grown from the surface inwards to the bulk whereas other grains have grown abnormally in the bulk.

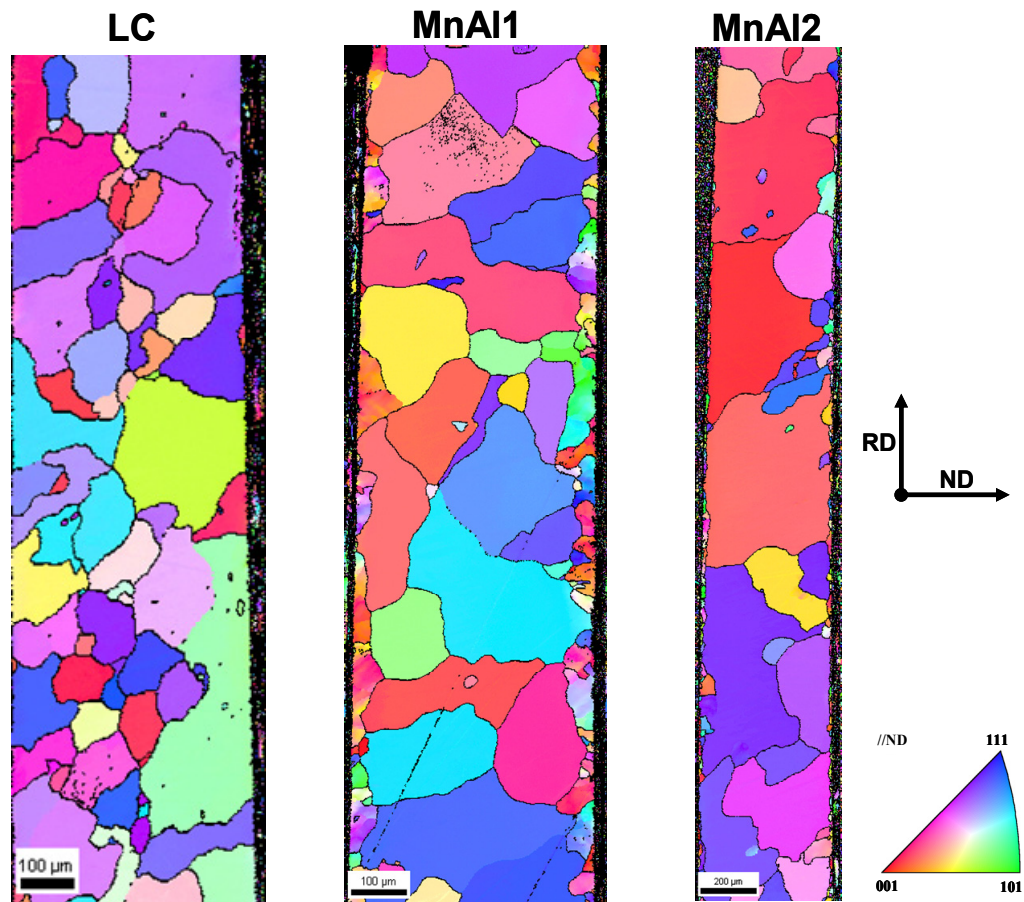


Figure 7.11 Inverse pole figure map after recrystallisation annealing at 800°C (1800s).

The alloy LC with α/γ fibre available at the surface after cold rolling has produced a random surface texture after 30 minutes of annealing (cf. figure. 7.7), but the bulk microstructure and texture is completely different from surface as shown in figure 7.11 and 7.12. The inverse pole figure map of LC alloys shows (figure 7.11) abnormal growth of selective surface orientation towards the bulk of the sheet. The bulk texture exhibits a strong intensity of $\{112\} \langle 110 \rangle$ component and a minor $\{111\} \langle 112 \rangle$ component, cf. the $\varphi_2=45^\circ$ section of figure 7.12. It shows that the surface texture that was created by prior transformation annealing has not played a decisive role in shaping the bulk texture after 10% cold rolling and subsequent annealing.

Figure 7.11 also shows the inverse pole figure map of ULC steel alloys MnAl1 and MnAl2. These inverse pole figure maps reveal an excessive bulk abnormal grain growth process in comparison to the low carbon steel alloy (LC). This excessive grain growth has led to a scattered texture for the alloys MnAl1 and MnAl2 shown in figure 7.12. Apart from big grains the inverse pole figure map of the material MnAl1 and MnAl2 also show small grains at the surface edge. The surface grains might have had the surface texture orientation which did not change during annealing. If we analyse the inward grain growth process in the steels that were annealed for 900s and 1800s, respectively, it appears that either surface orientations have only grown partially or surface grains have grown but were consumed subsequently by the abnormally grown orientations, which originate from the bulk. It appears that a mechanism has occurred of abnormal grain growth starting in the bulk and gradually consuming the structure including the surface grains which may or may not already have started growing. This mechanism might have been instrumental in keeping the surface texture components at the edge of the sheet.

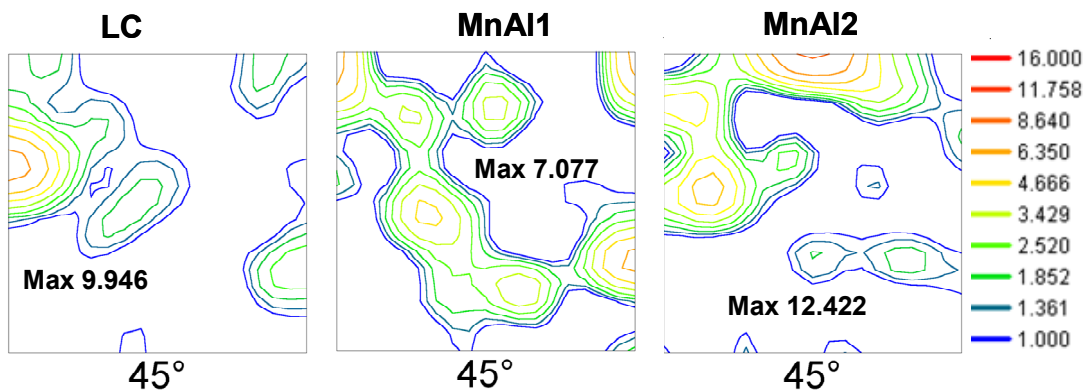


Figure 7.12 $\phi_2=45^\circ$ section of the ODFs corresponding to the inverse pole figure maps of figure 7.11.

7.4. Discussion

The objective was to investigate the inward growth of surface texture components, which were developed during α - γ - α phase annealing, by two different strategies. In the first route, applied on low carbon steels (LC), inward growth of surface texture components was intended by decarburization annealing, whereas in the second route applied on ultra low carbon steel alloys (MnAl1 & MnAl2), it was the intention to activate the mechanism of strain induced boundary migration.

In low carbon steels it is possible to apply a specific thermal treatment that leads to a columnar-grained microstructure of a certain texture, thus avoiding the cross-thickness heterogeneity. The columnar-grained microstructures can be obtained in the solid state either by directional annealing using a temperature gradient [2] or by decarburizing annealing in the intercritical region [3]. The former method is applicable when a reasonably large volume of material is being treated. The latter method is suitable for creating a columnar microstructure in thin sheets, when the microstructure is aligned with normal direction to the sheet plane.

A process reported by Tomida et al. [4] for developing cube-oriented grain growth in silicon steels consists of annealing in an appropriate atmosphere to remove the manganese and subsequent annealing in the γ or $\alpha + \gamma$ two-phase region in a decarburizing atmosphere. Sidor et al [5] have proposed a two step annealing process in the two-phase region enhancing a significant change in microstructure and texture. A similar approach has been adopted in the present study, Prior to decarburization the α - γ - α annealing was performed as an extra step to induce the targeted {001} cube fibre surface texture (c.f. figure 7.4). The inverse pole figure map indeed reveals the importance of the additional transformation treatment which stimulates to some extent the columnar morphology of the microstructure and the simultaneous development of the cube bulk texture. However, the optimum microstructure could not be achieved in the present study due to the inability in controlling the heating and cooling rate during decarburization annealing treatment leading to abnormal grain growth starting in the bulk of the steels sheet. Bulk AGG is not suited for generating the appropriate {001}

bulk texture as {001} grains are hardly present in the bulk of the sheet at the onset of grain growth.

For Mn/Al alloyed ultra-low carbon steels (MnAl1 and MnAl2) the carbon diffusion route cannot be used and another approach is required. Hence, these steels were rolled to a reduction of 10% after a transformation annealing treatment which produced the appropriate {001} cube fibre surface texture consisting of a monolayer of surface grains. The annealing treatment on the 10% cold rolled sheet was intended to initiate a recrystallization (or grain growth) in the surface area which would trigger the surface grains of appropriate orientation to consume the bulk of the sheet. This expectation is based on a number of literature observations [6,7,8,9,10 and 11] in which the surface induced grain growth was attributed to the presence of a strain gradient across the sheet with a concentration of rolling strain in the vicinity of the surface. For reasons of comparison a similar treatment of annealing at 800°C during 900s and 1,800s was also applied on the LC steel.

The main findings have been summarized in figure 7.13. The orientation scans (figure 7.8) do not reveal a strong strain gradient across the thickness of the sheet. Most strain heterogeneities, however, are observed as in-grain (orientation) gradients. It could be observed that the LC steel, with the smallest grain size prior to deformation, exhibits the least in-grain strain heterogeneities, whereas the steel with largest grain size exhibits the opposite tendency. This fits with the general behaviour that larger grains are more prone to developing plastic heterogeneities than smaller grains.

(A) After 10% cold rolling			
	Surface texture	Bulk texture	Microstructure
LC	α/γ fibre	γ fibre	Equiaxed grains (12 μ)
MnAl1	Cube fibre	γ fibre	Equiaxed grains (20 μ)
MnAl2	Cube fibre	γ fibre	Equiaxed grains (17 μ)

(B) After annealing 800°C (900s)			
	Surface texture	Bulk texture	Microstructure
LC	Random	{111}<112>	Abnormal grain growth (surface)
MnAl1	Cube fibre	Cube fibre	Columnar (surface & bulk)
MnAl2	Cube fibre	Rotated cube	Abnormal grain growth (surface & bulk)

(C) After annealing 800°C (1800s)			
	Surface texture	Bulk texture	Microstructure
LC	Random	{112}<110>	Abnormal grain growth
MnAl1	Cube fibre	scattered	Abnormal grain growth
MnAl2	Cube fibre	scattered	Abnormal grain growth

Figure 7.13: Texture and microstructure changes after cold rolling and annealing.

7.4.1. Low carbon steel (LC) Steel

The recrystallisation annealing performed at 800°C for the soaking time 900s and 1800s leads to significant texture and microstructure changes in all alloys under consideration. Figure 7.9 shows that the low carbon steel (LC) shows abnormal grain growth at the surface after an annealing time of 900s. These large recrystallized (or abnormally grown) surface grains rather show a tendency of lateral growth (along RD) than a pattern of inward growth (along ND). If the surface recrystallization is triggered by local strain localization then it is normal that the local driving force (at the surface) is consumed first before the grains start growing towards the surface. It can be observed, however, that the recrystallized surface grains are not exclusively of the targeted {001} fibre. The XRD texture measurements (cf. figure 7.7) reveal a random surface texture after extended annealing. After 1,800s of annealing time a structure is observed which is completely composed of large abnormally grown grains. It is difficult to assert, however, if the grains in contact with the surface have grown from the surface towards the bulk or the other way around. Conversely, the grains not in contact with the surface have certainly started growing from the bulk. It can be seen that these grains in majority are of bluish colour, i.e. they exhibit a $\sim\{111\}$ orientation which is definitely unfavourable for magnetic applications. Hence,

it is very unlikely that this approach is suitable for LC grades to obtain a magnetically suitable texture and microstructure.

7.4.2. Ultra low carbon steels alloyed with manganese and aluminium

In the case of the ultra low carbon steel (MnAl1) with low content of manganese and aluminium a (weak) cube fibre texture is observed both at the surface and in the bulk of the sheet, with a columnar microstructure from the surface inward after annealing during 900 s, cf. figure 7.9. This very much resembles the texture and microstructure that was wanted in the present case, although it can be observed that a tiny ribbon of non-recrystallized grains still survives along the centre line of the specimen. As the latter grains are predominantly of blue colour ($\{111\}$ grains) they will adversely affect the magnetic quality. After 1,800 s of annealing time an entirely different structure arises with large abnormally grown grains (AGG) that have consumed the entire structure. It can be observed that most of these AGGs are not in contact with the outer surface of the sheet. A thin mono-layer of grains separates the AGGs from the surface. It appears that that these surface grains are the reminders of the columnar grains that were present after 900s of annealing time. Hence, the present data suggest that the columnar grains, in a subsequent stage of annealing, have been consumed by the AGGs from the bulk. As these bulk grains have scattered orientations they do not contribute to an improved magnetic properties profile. The fact that data on figure 7.11 show that the surface texture remains of cube type even after 1,800s of annealing can probably be attributed to the presence of the tiny layer of columnar grains, but which is irrelevant for the bulk properties.

The ultra-low carbon steel with increased manganese and aluminium content exhibits a different behaviour as the structure is already composed of AGGs of scattered orientations after only 900 s of annealing. Small surface grains are hardly visible at the surface, although the XRD measured surface texture still reveals a cube surface component which is probably remnant of such a layer.

Two questions are of key importance here: (i) what has caused the columnar structure after 900 s annealing in steel MnAl1, (ii) why this structure has vanished after extended annealing for 1,800s? With regard to the mechanism responsible for the columnar structure two possibilities may be considered: (i) either recrystallization (or strain-induced grain growth) driven by the energy of plastic deformation stored in the matrix after a cold rolling of 10% or (ii) a transformation induced mechanism controlled by surface diffusing of an alloying element. The present data suggest that the first mechanism is rather unlikely to have occurred. There could be thought of two reasons for this. First, as observed and argued on the LC steel (cf. figure 7.9) strain-induced growth structures of this type rather show an elongated microstructure along RD, whereas structures with elongated grains along ND (columnar like) are rather typical for a transformation induced mechanism. Second, it can be observed that the columnar grains are not entirely strain free as they still exhibit some internal strain gradient, which is never observed in recrystallized or abnormally grown grains. The most likely element susceptible here to surface diffusion is manganese.

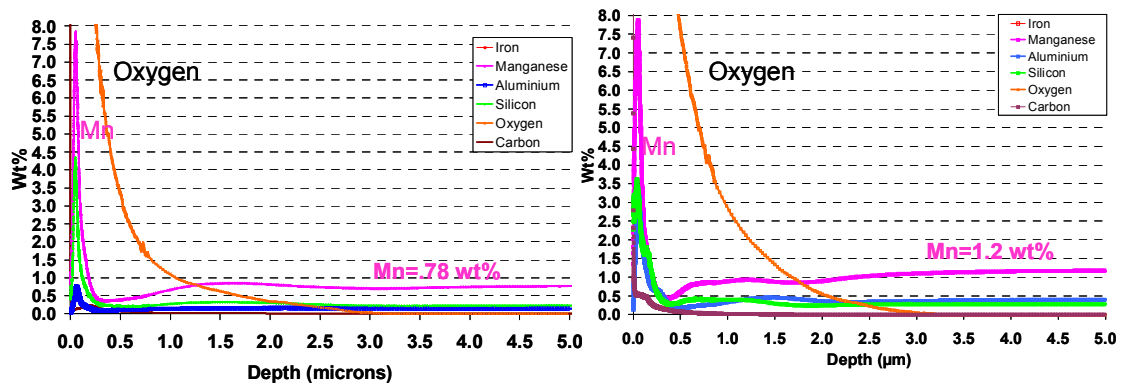


Figure 7.14 Concentration (GDOES) of important alloying elements across the thickness of the annealed sheets of the ULC alloys MnAl1 (left) and MnAl2 (right).

The concentration gradient of manganese created by a diffusion mechanism may have triggered an austenite layer at the surface. The manganese profile measured by GDOES (cf. figure. 7.14 reproduced from figure 4.12) reveals manganese enrichment

at the surface, and a Mn depleted region underneath which is very much compatible with the hypothesis of the presence of an austenite-ferrite interface in the surface area from which grains may start on a columnar growth path during back transformation. The GDOES profiles also show that the MnAl2 alloy shows a shallower Mn profile (extending only over 0.7 μm) as compared to the MnAl1 alloy (extending over 1.5 μm) which may be correlated with the different behaviour of these two alloys in terms of the extension of the monolayer surface grain (cf. chapter 4) and also in the different response to the annealing treatment at 800°C which is considered here.

Another remarkable feature of the columnar structure in figure 7.9 is the fact that the columnar grains still exhibit some internal orientation gradients, which seems to indicate that they have not yet fully recrystallized and hence the structure is still unstable for recrystallization or grain growth phenomena. This may explain why this columnar structure has disappeared in a subsequent stage of strain-induced (abnormal) grain growth and finally has produced the structure of figure 7.11. How the columnar structure may have developed and was capable of preserving an internal misorientation substructure is as yet unclear and need to be subject of further investigation.

7.5 Conclusions

The low carbon steel (LC) was subjected to phase transformation annealing to induce the appropriate $\{001\}$ surface texture prior to decarburization annealing. Unfortunately the decarburization annealing treatment did not produce the wanted bulk texture. Columnar inward growth of surface grains was only observed to limited extent on the samples that were decarburization annealed in the full austenite phase. The process of inward growth was superseded, though, by a phenomenon of abnormal grain growth in the bulk of the sheet which did not produce a satisfactory bulk texture.

Alternatively, the inward growth of surface texture components was also studied by a tentative strategy based on the mechanism of strain induced boundary migration. For

this purpose different cold reductions of 1%, and 10% were applied on transformation annealed sheets with or without the specific {001} surface texture. It was found that the intensity of the surface texture has increased with the application of temper rolling. During subsequent annealing columnar inward growth was only observed on the Mn/Al alloyed ULC steel sheets, whereas a different type of surface growth was observed in the low-carbon steel. The columnar structure had nearly consumed the entire bulk structure only in the ULC sample with moderate additions of Al and Mn (in contrast to the other ULC sample with increased Al/Mn additions), temper rolled to a reduction of 10% and subsequently annealed at 800°C during 15 min. During more extensive annealing these columnar grown grains were outgrown by abnormally grown grains in the bulk of the sheet. Only the sample with columnar grown grains until the mid-thickness exhibited the targeted {001} bulk texture. The abnormally grown grains exhibited scattered orientations more or less randomly distributed in Euler space.

It was argued here that the appearance of surface grown grains in the LC steel was controlled by a mechanism of Strain Induced Boundary Migration, whereas the growth of columnar grains may have been produced by a diffusion phenomenon during annealing.

7.6. References

- [1] F.J. Humphreys and M. Hatherly: Recrystallization and Related Annealing Phenomena (Elsevier Science, UK 1995), p. 207
- [2] F. Assmus, K Detert and G Ibe Z Metallkd 48, (1957) p 341;
- [2] S. Taguchi and A Sakakura Kinzoku Busturi 7, 1968, p 221;
- [3] H Shimanka Y Ito K Matsumura JMMM 26, (1982) p 57
- [4] T. Tomida, JMEPEG, 5 (1996) p 316
- [5] Y. Sidor, F.Kavac and M. Djubinsky, Thermomechanical processing conference proceedings (2004) p 514

- [6] L. Kestens, J.J. Jonas, P. Van Houtte and E. Aernoudt: *Met. Mater. Trans. A* Vol. 27A (1996), p.2347
- [7] S.W. Cheong, E.J. Hilinski and A.D. Rollett: *Proc. of Annual Conf. on Properties and Application of Magnetic Materials*, Chicago, USA, (2001)
- [8] M. Takashima, M. Kurosawa and M. Komatsubara: *Proc. of the 1st Joint International Conf. on Recrystallization and Grain Growth*, (2001) p. 477
- [9] J.T. Park, J.A. Szpunar and S.G. Cha: *Mater. Sci. Forum* Vol. 408-412 (2002), p. 1263
- [10] Y. Kurosaki and T. Shimazu: *IEEE Trans. Mag.* Vol. 35 (1999), p.3370
- [11] B. Bacroix and Z. Hu: *Met. Mater. Trans. A* Vol. 26A (1995), p. 601

Chapter 8

General conclusions & suggestions for future work

Several techniques are reported in the literature on electrical steels to obtain the desired cube fibre texture in these steels. The surface energy anisotropy of crystallographic planes has not been explored in detail, though. In the present research the development of the cube fibre texture by surface texture control and inward growth of surface grain was the main objective.

Investigations were carried out on five compositions which include four ultra low carbon steels alloyed with manganese, aluminium and silicon in various combinations and concentrations. The fifth alloy was a low carbon steel with a carbon content of 470 ppm and with only minute additions of Mn, Si and Al. The annealing experiments were conducted on the cold rolled sheets of 0.5 mm thickness of all five alloy compositions. The two principal tools that were employed for texture investigation in this work are X-ray diffraction and orientation contrast microscopy by means of the Electron Backscatter Diffraction technique. The crystallographic data sets were extensively analyzed and post-processed with the ODF software package developed by Van Houtte and with the TSL[®]-Analysis 5 package.

In a literature survey it was reviewed that the random cube fibre is of prime importance for obtaining the best magnetic properties in rotating electrical machines. Although this is known since long, as yet no industrially viable reference process has been developed. A wide variety of potential processes has been reported in the literature. Among others, it is known that the surface energy anisotropy can be instrumental in developing a cube texture during high temperature annealing in thin sheets by the process of tertiary recrystallisation. Surface texture control via a combination of high temperature annealing in the full austenite stage and surface

energy anisotropy has not yet been thoroughly explored in the literature. Therefore, the prime objective of the present study is to investigate the possibility of surface texture evolution during phase transformation and subsequently the technical application of such surface phenomena by inward growth of surface grains in the bulk of the steel sheet.

A wide variety of process parameters was considered such as annealing temperature, holding time and annealing atmosphere. The ULC steels alloyed with manganese and aluminium MnAl1 and MnAl2 were annealed with a heating rate of 15°C/s and a cooling rate of 30°C/s at different temperatures: either below the Ac1 temperature, in between Ac1 and Ac3 and above Ac3. It has been found that a complete phase transformation annealing (above Ac3) with a soaking time of 120 s is necessary for obtaining a specific surface texture that drastically differs from the bulk and subsurface texture. X-ray texture data reveal {001} and {110} fibre components with a weak intensity of 2 to 3 random levels. It was not possible to improve the strength of the surface texture by increasing the soaking time. On the orientation contrast images it could be observed that the specific surface texture components were present as a monolayer of grains at the outer surface of the sheet.

When similar transformation annealing treatments were carried out in the full austenite domain on an electrolytically pure iron and on an ultra-low carbon steel (ULC) it was observed that not only the cube surface texture appears but these very pure compositions also exhibited a grain structure for which the surface grains had grown towards the bulk of the sheet in a columnar way. The occurrence of inward growth during the α - γ - α annealing treatment could be linked to the (back) transformation mechanism and the Ar3 temperature of γ - α transformation during cooling. Transformation by growth, which is more readily at higher temperatures, enhances the appearance of a columnar structure.

It also was shown that industrially processed alloys, either Si added ULC steels or low-carbon steels do not show any specific surface texture at all after α - γ - α transformation annealing under low vacuum conditions of 10^{-4} Torr. When the Si added ULC steels were annealed under high vacuum conditions (10^{-6} Torr) the specific surface texture also appeared on these compositions. On the other hand the low carbon steel (LC), did not show any improvement under high vacuum. A further modification of the annealing atmosphere, such as annealing under Ar, N₂ or a combination of these gases with 5% H₂, did not cause any significant effect on the transformation surface texture.

The initial texture prior to transformation annealing is a conventionally cold rolled deformation texture with a strong α and γ -fibre. By applying dry cold rolling conditions the deformation texture was changed to a shear type texture in the surface and subsurface area consisting of a Goss component $\{110\}\langle 001\rangle$ and Cu component $\{211\}\langle 111\rangle$. Subsequent short term phase transformation annealing reveals only a slight improvement in the intensity of the $\{001\}$ surface texture in comparison to the conventionally cold rolled sheet.

Compositional depth profiling in the surface and subsurface area was performed by X-ray Photo-electron Spectroscopy (XPS) and Glow Discharge Optical Emission Spectroscopy (GDOES) on the cold rolled sheet and the annealed sheets of five alloys: two Mn/Al added ULC steels, two Si added ULC steels and one low-carbon steel. The compositional depth profiling results of the cold rolled sheets show that the initial conditions are similar for all the five alloys with no contamination in terms of oxides. The XPS and GDOES results show distinctly different oxidation behaviour of the Mn/Al added alloys and the Si alloyed steel. The Mn/Al added steels show less oxidation as compared to the Si added steels. For the former steels the data reveal a Mn enriched zone near the surface in combination with an increased Oxygen activity, which is indicative of the formation of manganese oxide complexes. In the Si added

steels oxide appears to have diffused into the metal to a depth of 0.3 μm . In the same zone also an increased Si activity was observed. These results suggest that Si has been oxidized via the well-known process of internal oxidation. It appears that the formation of an extensive internal oxidation layer at the surface has hindered the action of the low surface energy orientation selection mechanism and hence has impeded the formation of the favourable $\{001\}/\{110\}$ surface texture..

The role of the oxidation layer was confirmed by carrying out in annealing experiments under high vacuum conditions (10^{-6} Torr) on all alloys under investigation here. The results have shown that for the high Si alloys the favourable $\{001\}/\{110\}$ surface texture can only be obtained after annealing in high vacuum conditions. These high vac experiments also reconfirm that a complete $\alpha-\gamma-\alpha$ phase transformation loop is a necessary condition for the formation of the $\{001\}/\{110\}$ surface texture.

In alloys MnAl1 and MnAl2 the surface microstructures with unique low surface energy planes predominantly of $\{001\}$ and $\{110\}$ orientations were analysed by orientation imaging microscopy both on the RD-ND and the RD-TD sections. A very remarkable and unique grain structure was observed on the RD-TD section of the outer surface layer exhibiting very large grains ($\sim 200 \mu\text{m}$) with irregular grain boundaries. Moreover, a peculiar orientation gradient was observed in the cube fibre grains. It was found that the $\{001\}$ type grains only display the ideal $\{001\}$ orientation in the centre of the grain and rotate away from this ideal $\{001\}$ position with a near linear orientation gradient. The edge of the $\{001\}$ grain is generally $>15^\circ$ off the ideal $\{001\}$ fibre position. The grain boundaries features are also very characteristic with a majority of $\Sigma 3$ boundaries (approx. 40% of the total length fraction). These data strongly suggest that the entire surface texture and microstructure is strongly controlled by the features of the crystal dependent surface

energy. Unfortunately the physical mechanism, which controls the orientation rotation from centre to edge in $\{001\}$ grains could not be fully unravelled here.

In an additional series of experiments it was attempted to induce grain growth of surface grains in the ND direction, hence expanding the favourable $\{001\}/\{110\}$ surface texture towards the bulk of the sheet. To this purpose a critical strain of approximately 10% was applied by light cold rolling and subsequently annealing at 800°C for 900s and 1800s was carried out. Unfortunately, the cold rolling strain gradient is not sufficient for allowing only surface orientations to grow. It was observed that grains also grow from the bulk of the sheet leading to a mixed situation of inward grain growth of some orientation and abnormal grain growth of bulk orientations.

When two distinct initial materials (one with the specific $\{001\}/\{110\}$ surface texture i.e. the Mn/Al ULC steel and the other one without specific surface texture, i.e. LC steel) were subjected to an identical treatment of light rolling followed by grain growth, it was observed that the presence of the specific surface texture also gave rise to the better bulk texture in the finished product. It was also observed that inward columnar growth is enhanced by $\gamma \rightarrow \alpha$ transformation conditions at high temperature, i.e. with low undercooling which facilitates transformation by growth rather than by nucleation. Hence it can be concluded that substantial data were gathered for further more applied research that may explore these principles for industrial valorisation.

Suggestions for future work

The observed structure represents a state of optimally reduced energy as both the metal/vapour interfacial energy and the solid state interface energy appear to be minimized. It remains unclear, however, by which mechanism the microstructure has

evolved to such a state as the driving force for the gradually accumulating in-grain misorientations could not be determined. The mechanism by which these specific low energy boundaries are formed should be studied in detail.

Summary

Electrical steels are, with respect to the quantities produced, the most important soft magnetic materials. In 2009, the world market for soft magnetic materials was about 14 million tons, 80% of which were non-grain oriented (“NGO”) and 16% grain-oriented (“GO”) electrical steels. The remaining 4% comprise all other soft magnetic materials such as ferrites, powders, amorphous and nanocrystalline alloys Ni-Fe alloys, etc. At present, the global demand for electricity is increasing strongly, driven mainly by the industrial growth in developing countries such as China and India. The International Energy Agency (IEA) has predicted an increase in the worldwide electrical power generating capacity of nearly 3% or, as an absolute figure, of about 150GW per annum until 2030. New electricity-generating capacities are the main driver for GO electrical steels demand. Today, there are 12 producers of GO in the world and more than 30 companies which fabricate NGO electrical steels. It is a major challenge for them to facilitate this strong increase in electricity generation and transmission capacity by supplying the increased quantities of magnetic core materials required.

With a more stringent energy efficiency standard in full swing for motors, manufacturers are stepping up to the challenge of increasing energy savings in their motor applications. Saving energy is crucial for today's industry, as global greenhouse concerns call for significant reductions in world energy usage and carbon emissions. One area of manufacturing that has felt the pressure is electrical motor-driven applications. Engineers have an implicit goal to design and build efficient equipment. Reducing energy consumption of electric motors driven systems, which accounts for up to 30% of all electricity used in European Union is among the priorities of European Union “intelligent energy for Europe” program. New materials are in great demand for high-efficiency motor cores that need higher magnetic flux density, lower power loss, and lower mechanical hardness.

Despite of many decades of research and continuous improvement of the quality of steel we still cannot be satisfied today with the magnetic properties achieved in the commercial products. The improvement of magnetic properties of electrical steels concerns many metallurgical aspects like microstructures and crystallographic texture. Since Fe-base (body centered cubic) crystals are magnetically anisotropic, crystallographic texture is known to affect significantly the magnetic properties of iron or iron base alloy sheets. The optimum texture of non-oriented electrical sheets is $\{100\}$ plane parallel to the sheet surface because the $\{100\}$ plane has two easy magnetization directions. The anisotropic magnetic behaviour of most ferromagnetic materials requires that controlled crystallographic texture should be developed during the material processing stage. While the $\{100\} \langle 001 \rangle$ (or so called “cube”) texture can be developed in face centred cubic materials through an appropriate schedule of annealing and recrystallisation in BCC metals and alloys this fibre texture is never obtained throughout the thickness of the material unless specific processing is employed such as cross rolling or annealing at high temperature. The conventional methods used to obtain $\langle 100 \rangle$ BCC orientations are basically through preferential recrystallization. In contrast, the austenite to ferrite phase transformation, which is an inherent and significant property of low-carbon steels, has scarcely been investigated for developing appropriate textures in silicon steel sheets for soft magnetic applications. It is well known that the surface energy anisotropy is the driving force for the orientation selection at the metal-vapour interface. This impacts the microstructure and texture evolution at the surface during the phase transformation. Although, the exact value of the interfacial energy between the atmosphere and the steel surface is largely unknown, it is widely accepted that the BCC $\{100\}$ and $\{110\}$ crystallographic planes have a relatively low surface energy, which can stimulate the growth of these orientations in the steels sheets. Therefore, one can expect that through an appropriate selection of the technological parameters of skin pass rolling and annealing, the nucleation and growth of the desired $\{100\} \langle uvw \rangle$ surface texture

can be achieved, which is a prerequisite for obtaining of an excellent soft magnetic material.

This thesis is focussed on the investigation of texture evolution during α - γ - α phase transformation in ultra low carbon steels, low alloyed with Si, Mn and Al with an aim of developing of $\{100\}\langle uvw \rangle$ surface (or through thickness) texture.

The thesis contains 8 chapters which are arranged in the following sequence:

Chapter one includes a general introduction in the subject electrical steels and its correlation with the cube texture. This chapter gives the concise detail on exiting techniques to obtain cube texture with their advantages and disadvantages. The analysis of the exiting techniques also includes the α - γ - α phase transformation phenomenon to develop cube texture by controlling the surface energy anisotropy.

Followed by a general introduction chapter 2 describes the material selection and its thermo mechanical processing as well as the experimental strategy and important equipments used in this investigation. Special attention was paid to the techniques for characterization of the exact chemical composition, microstructure and texture of the surface and in the bulk of the material.

In the third chapter the role of surface free energy anisotropy on surface texture is introduced in a simplified way. The surface morphology at equilibrium conditions may be related to the surface energy per unit area as a function of the crystallographic orientation, because the surface tension of a crystal depends on the crystal orientation. This chapter deals with surface texture evolution during transformation in ULC steel alloyed with Si, Mn and Al taking into account several parameters which could affect the surface texture evolution, like steel composition, temperature, soaking time, atmosphere etc. This chapter includes extensive investigation on the influence of these parameters on the characteristics of surface texture and microstructure.

Fourth chapter discusses possible the role of surface chemistry if any on surface texture evolution. The steel sheet surface was investigated using X-ray Photoelectron Spectroscopy and Glow Discharge Optical Emission Spectrometer, before and after phase transformation. The results show the decisive influence of surface chemistry on the selection of surface texture components at the metal-vapour interface. The available oxygen and impurities in the annealing atmosphere interact selectively with the main alloying elements like Al, Mn Si, and Fe which leads to formation of ultra thin oxide layer on metal surface with a thickness varying from 10nm to 50nm depending on the alloying elements and the annealing conditions. The composition of this thin oxide layer plays a vital role in surface texture evolution during transformation.

From the results of the surface chemistry investigation appears that the subsequent reaction of the alloying elements with the constituents of annealing atmosphere leads to surface texture evolution. The fifth chapter includes the study of effect of vacuum annealing atmosphere quality on the surface texture evolution. The results show that cleanness of the annealing atmosphere and particularly its oxygen content plays a vital role for orientation selection at the metal-vapour interface. This could be due to the fact that the surface energy anisotropy is very sensitive to impurities available at the metal –vapour interface.

The phase transformation leads to development of a specific surface microstructure and texture at the steel/atmosphere interface during annealing. Chapter six discusses in details the surface microstructure and of the very top grain layer based on detailed characterization by EBSD techniques. The development of the surface grain layer and the grain boundaries character distribution in the surface and in the bulk were analysed in the light of the hypothesis for variant selection. The typical microstructural features observed were attributed to the influence-of surface energy rather than the elastic stress relaxation theory of Hashimoto et al.

The seventh chapter discusses the mechanism by which the surface texture components could be grown in the through thickness of the sheet. The laboratory cast alloys show a surface texture and microstructure as thin layer on the edge of the specimen after phase transformation annealing. This thin layer was subjected to skin pass rolling with 5-10% reduction and subsequently recrystallisation annealed at different temperature. The X-ray results shows that intensity of surface texture increases due to skin pass rolling and during recrystallisation selective growth of surface grains occurs along with same surface texture in the through thickness of the sheets. The low carbon alloy (LC) with high amount (500ppm) of carbon also show surface texture and for them inward growth decarburization annealing was performed. The orientation imaging microscopy confirms that better microstructure can be obtained if we do transformation annealing before decarburization.

The general conclusions of the present study and the suggestions for the future work are summarized in chapter 8.

Samenvatting

Elektrische stalen zijn de belangrijkste zacht magnetische materialen wat betreft productievolume. In 2009 bedroeg de wereldmarkt voor zacht magnetische materialen 14 miljoen ton, waarvan 80% niet-georiënteerde (NO) kwaliteiten en 16% korrel-georiënteerde (GO) kwaliteiten. De resterende 4% omvatten alle andere zachte magnetische materialen zoals ferrieten, poeders, amorfe en nano-kristallijne Ni-Fe legeringen. De wereldvraag naar elektriciteit is op dit ogenblik in stijgende lijn en wordt bovenal aangestuurd door de industriële groei in nieuwe groeilanden zoals China en India. Het Internationaal Energie Agentschap (IEA) voorspelt een jaarlijkse stijging van bijna 3 % in de wereldwijde capaciteit in elektrische stoomproductie, wat overeenkomt met een groei van 150 GW per jaar, tot 2030. Nieuwe electriciteitscentrales liggen aan de basis van de vraag naar korrel-geörienteerde elektrische stalen. Vandaag zijn er wereldwijd 12 producenten van GO elektrische stalen en meer dan 30 bedrijven produceren NO elektrische stalen. Het is voor deze bedrijven dan ook een enorme uitdaging deze sterke stijging van stroomproductie- en transmissiecapaciteit te ondersteunen in de voorziening van fluxgeleidende magnetische materialen.

Door de steeds strenger wordende reglementeringen wat betreft energie-efficiëntie voor elektrische machines leggen de producenten steeds meer de nadruk op energiebesparingen bij motortoepassingen. Energiebesparing is van primordiaal belang voor de industrie, zeker nu de klimaatproblematiek een belangrijke daling van het wereldwijde energieverbruik en de koolstofuitstoot noodzakelijk maakt. Ook de elektrische motorenindustrie staat onder druk van de stijgende bekommernis om het milieu. Dit komt o.m. tot uiting in de prioriteiten van het EU programma over Intelligente Energie. Dit programma stelt zich expliciet tot doel een vermindering te realiseren van het energieverbruik van systemen die worden aangedreven door

elektrische motoren, dewelke 30% vertegenwoordigen van het elektriciteitsverbruik in de Europese Unie.

Er bestaat een grote vraag naar nieuwe materialen voor hoog-efficiënte motorkernen die een hogere magnetische fluxdichtheid kunnen dragen met nog minder vermogenverlies en verbeterde mechanische eigenschappen.

Ondanks het jarenlange onderzoek en de voortdurende kwaliteitsverbetering van elektrische stalen blijkt er nog steeds ruimte voor verbetering van de magnetische eigenschappen van commerciële producten. Deze verbetering slaat op verscheidene metallurgische parameters waaronder de microstructuur en de kristalgrafische textuur. Aangezien de kubisch ruimtegecenterde kristalstructuur van het ijzer eenkristal magnetisch anisotroop is, zullen de magnetische eigenschappen van elektrische stalen op basis van ijzer, sterk afhankelijk zijn van de kristalgrafische textuur. De optimale textuur van niet-georiënteerd elektrische staalplaten wordt gekenmerkt door een willekeurige $\langle 100 \rangle$ vezeltextuur, die de dichtheid vergroot van $\{001\}$ kristalvlakken parallel met het plaatoppervlak. Met deze textuur zijn de spontane magnetizatie-richtingen maximaal gericht volgens de magnetische fluxlijnen in de plaat van de kernlamellen. Terwijl de $\{001\}\langle 100 \rangle$ of de zogenaamde kubische textuur op natuurlijke wijze verschijnt in vlakkengecenterde kubische metalen, wordt deze vezeltextuur nooit verkregen in ruimtegecenterde metalen en legeringen tenzij zeer specifieke behandelingen worden toegepast zoals dwarswalsen of gecontroleerd walsen onder specifieke voorwaarden. Voor de productie van NO elektrische stalen werd tot nu toe nog geen industrieel referentieproces ontwikkeld dat wereldwijd gepatenteerd en toegepast wordt. De voorgestelde methoden om een $\{001\}$ BCC textuur te verkrijgen zijn voornamelijk gebaseerd op textuurbeheersing via rekristallisatieprocessen. Daar tegenover staat dat er heel weinig onderzoek wordt verricht naar de impact van de austeniet-ferriet transformatie (eigen aan laaggelegerde laag-koolstof stalen) bij de ontwikkeling van geschikte texturen in silicium staalplaten voor zacht magnetische toepassingen.

Het is welbekend dat de anisotropie van de oppervlakte-energie een drijvende kracht is bij oriëntatieselectie aan het metaal-damp grensvlak, wat een invloed heeft op de microstructuur en de textuurevolutie aan het oppervlak tijdens de fazentransformatie.

Hoewel de exacte waarde van de grensvlakenergie tussen de atmosfeer en het staaloppervlak grotendeels onbekend is, wordt toch algemeen aanvaard dat de BCC {100} en {110} kristallografische vlakken een lagere oppervlakte-energie hebben. Het is daarom te verwachten dat deze {001} en {110} richtingen te voorschijn komen aan het plaatoppervlak na een vaste-stof transformatieproces. Dit onderzoek bevestigt dat kieming en groei van de gewenste {100} $\langle uvw \rangle$ korrels kan bereikt worden als men er bij het proces op toeziet dat de chemische samenstelling en de technologische parameters goed worden gekozen. In dit werk werd ook onderzocht hoe deze gunstige oppervlaketextuur kan uitgebreid worden naar het bulkvolume van de plaat door het materiaal aan een bijkomende thermo-mechanische behandeling te onderwerpen.

De vaste-stof transformatie die hiertoe wordt bestudeerd is de voor- en terugwaartse α - γ - α fasentransformatie in ultralaag koolstofstalen, minimaal gelegeerd met Si, Mn en Al teneinde een optimale chemische samenstelling te verkrijgen voor NO elektrische staalplaat.

De thesis omvat 8 hoofdstukken die als volgt werden gestructureerd.

Hoofdstuk 1 geeft een algemene inleiding over het onderwerp van elektrische stalen en de aanverwante kubische vezeltextuur. Dit hoofdstuk beschrijft in detail de bestaande technieken om deze optimale textuur te verkrijgen, met al de inherente voor- en nadelen. Bij de analyse van de bestaande procédés wordt ook de α - γ - α fasentransformatie bestudeerd, dewelke van groot belang is voor dit onderzoek.

Hoofdstuk 2 beschrijft de materiaalkeuze en de thermo-mechanische achtergrond van de gekozen materialen, alsook de onderzoeksstrategie en de belangrijke experimentele hulpmiddelen die aangewend werden in deze studie. De aandacht werd toegespitst op

de karakterisatietechnieken van de precieze chemische samenstelling, de microstructuur en de textuur van het oppervlak en het bulkvolume van het plaatmateriaal.

In Hoofdstuk 3 wordt onderzocht welke rol de oppervlakteënergie anisotropie speelt bij de vorming van de oppervlaktetextuur. De evolutie van de oppervlaktetextuur wordt nauwgezet gevolgd tijdens de transformatie in ULC stalen gelegeerd met Si, Mn en Al waarbij rekening wordt gehouden met verscheidene parameters die van belang kunnen zijn, zoals staalsamenstelling, gloeikarakteristieken (tijd, temperatuur, atmosfeer) of de toestand waarin het materiaal zich bevindt vóór het gloeien. Dit hoofdstuk beschrijft het uitgebreide onderzoek van de invloed die al deze parameters hebben op de karakteristieken van de oppervlaktetextuur en de -microstructuur.

Hoofdstuk 4 behandelt de mogelijke rol die de chemische samenstelling van het oppervlak speelt. De chemische samenstelling van het staalplaatoppervlak werd onderzocht met specifieke analysetechnieken: X-ray Photoelectron Spectroscopy (XPS) en Glow Discharge Optical Emission Spectroscopy (GDOES). De resultaten tonen aan dat de chemische samenstelling van het oppervlak een invloed kan hebben op de selectie van oppervlaktetextuurcomponenten gedurende de fasentransformatie aan het metaal-damp grensvlak. De aanwezige zuurstof in de gloei-atmosfeer reageert selectief met de belangrijkste legeringselementen zoals Al, Mn, Si en Fe, wat resulteert in de vorming van een dunne oxidelaag op het metaaloppervlak. Uit het onderzoek blijkt dat de samenstelling en de aard van deze oxidelaag een cruciale rol speelt bij de vorming van de oppervlaktetextuur tijdens transformatie.

Hoofdstuk 5 bestudeert de invloed die de vacuümkwaliteit heeft op de vorming van de oppervlaktetextuur tijdens het fasentransformatiegloeien. Uit de resultaten blijkt dat de zuiverheid van de gloei-atmosfeer en in het bijzonder het zuurstofgehalte een grote rol speelt bij de oriëntatieselectie aan metaal-damp grensvlak. Dit kan te wijten zijn

aan het feit dat de oppervlakteënergie anisotropie zeer gevoelig is voor onzuiverheden die voorkomen aan het grensvlak.

Door een vaste-stof fase-transformatie ontwikkelt zich ook een specifieke oppervlaktemicrostructuur aan het staal-damp grensvlak tijdens het gloeien. Hoofdstuk 6 beschrijft de gedetailleerde studie van de oppervlaktemicrostructuur, d.w.z. de buitenste oppervlaktekorrellagen, die verschijnen na de fasen transformatie gloeibehandeling. Er werd een analyse uitgevoerd op de kristallografische kenmerken van deze oppervlaktekorrellagen en de eigenschappen van hun korrelgrenzen. Er werd een heel specifieke en unieke microstructuur vastgesteld in de monolaag van de buitenste oppervlaktekorrels met sterke interne oriëntatiegradiënten. Als gevolg van deze oriëntatiegradiënt zal de centrale zone van een {001} korrel roteren zodanig dat aan de korrelgrens een $\Sigma 3$ ($\langle 111 \rangle 60^\circ$) grensvlak bekomen wordt met een naburige {110} korrel. Dit veronderstelt een rotatiegradiënt van ongeveer 15° .

Hoofdstuk 7 beschrijft de mogelijke behandelingsmethodes waarbij de verschillende componenten van de oppervlaktetextuur kunnen groeien doorheen de staaldikte tot ze het volledige bulkvolume hebben ingenomen. De bestudeerde legeringen vertonen de vooropgestelde {001} oppervlaktetextuur als een dunne oppervlaktelaag na het fase-transformatiegloeien. Deze dunne laag onderging een nawalsbewerking met 1 tot 10% diktereductie, gevolgd door een rekristallisatiegloeibehandeling met variërende gloeiduur en -temperatuur. Uit de resultaten blijkt dat de intensiteit van de oppervlaktetextuur verhoogt door de nawalsbewerking.

Door de juiste keuze van de chemische samenstelling van het staal en van de gloeiparameters werd een kolomnaire inwaarts groei vastgesteld van de oppervlaktekorrels van de gekozen {001} vezeltextuur, dewelke met succes verder werd uitgebreid over het (bijna) volledige plaatvolume. Met dit resultaat werd het bewijs geleverd dat het mogelijk is om de textuur van NO elektrisch staal te

Samenvatting

beïnvloeden door de fysische eigenschappen van het plaatoppervlak te beschouwen als een expliciete procesparameter.

Hoofdstuk 8 omvat de algemene besluiten van dit onderzoek.

List of publications

- [1] Jai Gautam, Roumen Petrov and Leo Kestens, *Surface Texture Evolution During α - γ - α Transformation in Mn and Al Alloyed Ultra-Low Carbon Steel*, **Materials Science Forum** Vol. 550 (2007) pp. 503-508
- [2] Jai Gautam, Roumen Petrov, Leo Kestens and Elke Lunis, *Surface energy controlled α - γ - α transformation texture and microstructure character study in ULC steels alloyed with Mn and Al*, **Journal of Materials Science** 43 (2008) pp 3969–3975
- [3] Jai Gautam, Roumen Petrov, Elke Lunis and Leo Kestens, *Cube texture evolution controlled by gas-metal interface during α - γ - α Transformation in Mn and Al Alloyed Ultra-Low Carbon Steel*, **Proceedings of ISRS 2008** on Metallurgy and Materials science and Engineering, (2008) pp 440-445
- [4] Leo A. I Kestens, Jai Gautam and Roumen Petrov, *Texture and Microstructure Evolution at the Metal-Vapour Interface During Transformation Annealing in a Mn and Al Alloyed Ultra Low Carbon Steel*, Chapter 6, A. Haldar, S. Suwas, and D. Bhattacharjee (eds.), **Microstructure and Texture in Steels**, Springer 2009 pp103
- [5] Jai Gautam, Roumen Petrov and Leo Kestens; Elke Leunis, *Surface Microstructure Evolution during Phase Transformation on Mn, Al and Si Alloyed Ultra Low Carbon Steel* **Defect and Diffusion Forum** Vols. 297-301 (2010) pp 757-763
- [6] Jai Gautam, Roumen Petrov and Leo Kestens; Elke Leunis *Surface Microstructure and Texture Evolution during Interrupted annealing in Ultra Low Carbon Steels*, **Advanced Materials Research** Vols. 89-91 (2010) pp 202-207
- [7] Jai Gautam, Roumen Petrov and Leo Kestens; Elke Leunis *Nucleation and growth of surface texture during α - γ - α transformation in ultra low carbon steel alloyed with Mn, Al and Si* **Solid State Phenomena** Vol. 160 (2010) pp 223-228
- [8] Jai Gautam, Roumen Petrov and Elke Leunis and Leo A.I. Kestens *Heterogeneous phase transformation texture evolution in low alloyed ULC steels sheets*, **Steel research international** accepted for publication
- [9] Jai Gautam, Roumen Petrov and Elke Leunis and Leo A.I. Kestens, *Strain induced inward grain growth during recrystallisation in steel sheets with BCC crystal structure*, **proceedings Rex-GG IV (2010)**,

[10] Edgar Gomes, Kim Verbeken, Jai Gautam, and Leo Kestens, *Evolution of the microstructural surface characteristics during annealing*, **proceedings Rex-GG IV (2010)**,

Acknowledgements

*#“Guru gobind dou khade kake lagun payen
Balihari guru aapne gobind dio batay”*

Saint Kabir, 16th Century, Varanasi, India

Having said the famous quote from saint Kabir I owe my deepest gratitude to my promoter, Leo, whose encouragement, guidance and support from initial to the final level enabled me to develop an understanding of the subject. I would like to thank my daily supervisor, Roumen for his continuous and support and readily availability for the technical discussion whenever it was needed during this PhD project. Also, I would like express my gratitude to my industrial contact, Elke, for her valuable discussion regarding the project and also extending technical support for carrying out vital experiments and measurement at the industry. I would like to express my special thanks my project colleague, Patricia, for her immense support and extended help during all these years. I feel honored and indebted for the special and vital discussions with Bevis and also for being very kind to extend his support for GDOES measurements. Also, special thanks to my colleague Tom at Ghent University for his help to carry out XPS measurement and fruitful discussions.

This PhD project would have not been possible without generous financial support from the industrial partner Arcelor Mittal Global R&D, Ghent. I would like to thank Serge Classenes and Marc de Wulf for their special support and kind attention. I would like to acknowledge specially Yuan Houbaert for extending his personal touch and administrative help during my stay in Ghent. I would like to express my special thanks to Jilt for his motivating support and technical discussion whenever needed.

I would like to acknowledge Jan Penning for the extending his support for hosting Indo-Belgian fellowship as a nucleus start for my research life in UGent. I would like to extend my gratitude to all my colleagues in materials science department at Ghent

English essence “The pupil is standing in front of the God and Guru and he is in dilemma that to whom he should pay his gratitude first”

and also in TU-Delft for their tremendous help and social environment making these PhD years very memorable and special.

Finally, I would like to thank the department secretaries Olga from Delft and Ilse from Gent for their generous help whenever needed during all these years.

Curriculum vitae

Jaiprakash GAUTAM

Born on 4th July 1975 in Lucknow, Uttarpradesh, India

Present	Post doctoral researcher, Materials innovation institute (M2i), Delft, The Netherlands
2006-2008	Technische Universiteit Delft, Doctoral researcher in Materials science and engineering, Delft, The Netherlands
2004-2006	Ghent Universiteit, Doctoral researcher in Materials science and engineering, Ghent, Belgium
2003-2004	Ghent Universiteit, researcher in Materials science and engineering, Ghent, Belgium
2000-2003	Lecturer, Metallurgical Engineering, Institute of Technology, Banaras Hindu University, Varanasi, India
1998-2000	Master of technology in Metallurgical engineering, Institute of Technology, Banaras Hindu University, India
1993-1997	Bachelor of Engineering in Metallurgical Engineering, Visveswaraya national institute of technology, Nagpur, Maharashtra, India
1991-1993	Higher secondary, Colvin Taluqdars college, Lucknow, Uttarpradesh, India
1989-1991	High school, City Montessori college, Uttarpradesh, Lucknow, India